Dissertation

Simon Josef Vitzthum

In-situ Analysis of Elastic-Plastic Characteristics of Steel Sheets

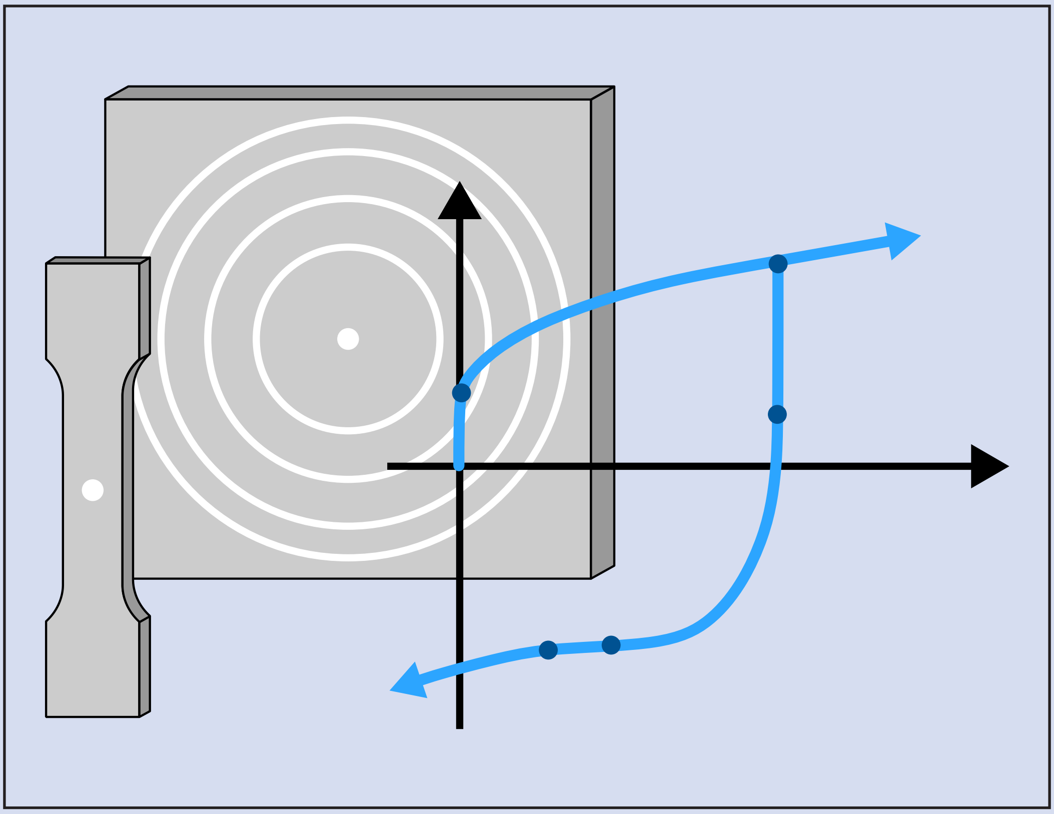

41

Maschinenbau

Lehrstuhl für
Umformtechnik
und Gießereiwesen

KOLLEMOSCH
Verlag & Kommunikation

Schriftenreihe Umformtechnik und Gießereiwesen

Technische Universität München
TUM School of Engineering and Design

In-situ Analysis of Elastic-Plastic Characteristics of Steel Sheets

Simon Josef Vitzthum

Vollständiger Abdruck der von der TUM School of Engineering and Design der Technischen Universität München zur Erlangung des akademischen Grades eines Doktors der Ingenieurwissenschaften (Dr.-Ing.) genehmigten Dissertation.

Vorsitz:

Prof. Dr. techn. Peter Mayr

Prüfer*innen der Dissertation:

1. Prof. Dr.-Ing. Wolfram Volk
2. Prof. Dr. Toshihiko Kuwabara
3. Prof. Dr.-Ing. A. Erman Tekkaya

Die Dissertation wurde am 05.01.2023 bei der Technischen Universität München eingereicht und durch die TUM School of Engineering and Design am 22.05.2023 angenommen.

Dedicated to my parents.

Preface

"In the middle of difficulty lies opportunity."
Albert Einstein

At the beginning of my studies, I would never have thought that I would one day pursue a doctorate in mechanical engineering. Even less would I have thought that I could develop a passion for science. And yet my path led me to a position as a research associate in the field of mechanical engineering. I think the chosen quote from Albert Einstein fits so well, as I faced, let's call it in this context, great challenges at the beginning of my doctoral thesis project. The interdisciplinary nature of the project, which I later came to appreciate so much, required that I also become more familiar with subfields of physics and materials science. In the process, I discovered my passion for materials science investigations and scientific studies. In the end, the project gave me the opportunity to develop my own field of research at the chair. I am very grateful for the wonderful people I have met and the valuable experiences I have gained along the way. Working as a research associate has played a big part in my personal development and this time will always remain a special one.

This research work was done at the Chair of Metal Forming and Casting (utg) in cooperation with the Research Neutron Source Heinz Maier-Leibnitz (FRMII). Special thanks go to my doctoral advisor Professor Wolfram Volk, the chair holder of the utg, who could not have supported me better during my time as a doctoral student. I also would like to thank my examining committee. Thanks to Professor Peter Mayr (Chair of Materials Engineering of Additive Manufacturing, TUM) for taking over the chairman position and the organization of the doctoral examination procedure. I would like to thank Professor Toshihiko Kuwabara (Tokyo University of Agriculture and Technology) and Professor A. Erman Tekkaya (Institute of Forming Technology and Lightweight Components, TU Dortmund University) for taking on the role of examiners. I would like to additionally thank Professor A. Erman Tekkaya for the valuable discussions during the project. Great thanks go to Dr. Joana Rebelo Kornmeier and Dr. Michael Hofmann of FRMII, who supported me in the experimental implementation in my project and were always available to me as important discussion partners. I thank all colleagues at the utg for mutual support and the great time. I want to emphasize Maximilian Gruber and Dr. Matthias Eder, who were a particularly important support for me. Also to be mentioned are Roman Norz, Lorenz Maier, Lorenzo Scandola and Dr. Christoph Hartmann.

This thesis is dedicated to my parents, my mother Waltraud, my father Josef and my stepfather Heinz. As a child, one cannot experience better support than that which they have given me throughout my growing up and education. Without them I would not be where I am today. Great thanks also go to my older sisters Veronika and Elisabeth, who always stood by me as role models, as encouragement and as advisors.

In the end, I am grateful myself, grateful that my time as a research associate at the chair utg has given me much more than my academic education. I had the great fortune to meet my future wife Isabella.

Munich, June 2023 *Simon Josef Vitzthum*

Abstract

This thesis summarizes an experimental study on the elastic-plastic material behavior of industrial steel sheet materials. The overall objective is to deepen the understanding of materials to provide the basis to improve material theories, for example for springback prediction. The fundamental challenge is that the development of new materials is ongoing, and high formability combined with high strength is achieved through advanced microstructures and alloys. As a result, the more complex composition of the microstructure of these materials leads to elastic-plastic characteristics, which deviate significantly from classical theories. Namely, these characteristics are the onset of plastic yielding, elastic modulus, anelastic material behavior and early re-yielding. The study focuses on the experimental investigation at both macroscopic and microstructural levels. Therefore, a single-phase interstitial free low carbon steel and a high-strength dual-phase steel were studied. The macroscopic material characterization is extended by temperature-based determined parameters, which are extensively validated microstructurally. An experimental setup is developed, which allows advanced in-situ synchrotron diffraction measurements in cyclic tension tests and tension-compression tests. Macroscopic parameters such as strain, load and specimen temperature are measured time-synchronously with microstructural quantities such as lattice strains, dislocation densities or specific phase stresses. In this way, it was possible to introduce and validate a new temperature-based determination method for the onset of yielding and the elastic loading modulus, which is based on the thermoelasic effect. Still, strain-dependent elastic behavior and re-yielding after load change represent major challenges for modeling, especially for high-strength dual-phase steels. Therefore, anelastic material behavior and early re-yielding, i.e. the Bauschinger effect, were investigated microstructurally and correlated with the macroscopic material behavior. With the experimental approach, it was possible to confirm existing assumptions and to find plausible explanations. Both dislocation movement and microstructural inhomogeneities were found to be the main drivers for anelastic behavior and the early re-yielding. By separately evaluating the deformation behavior of ferrite and martensite phases of the dual-phase steel, it was possible to confirm that the interaction between the soft and hard phase is mainly responsible for the specific behavior of this material. Finally, the potential of the findings and newly introduced parameters is demonstrated by calibrating a hardening model and evaluating a one-element test.

Contents

Supplementary Information

Prior publications

Several results of this thesis have been published beforehand under my authorship in scientific journals and conference proceedings. These are registered according to the valid doctoral regulations and are not referenced again separately in this thesis. The publications addressed are listed below.

VITZTHUM, S., M. EDER, C. HARTMANN, H. A. WEISS, G. BAUMGARTNER, M. HOFMANN, and W. VOLK (2017). "Determination of crystallographic young's modulus for sheet metals by in situ neutron diffraction". In: *Journal of Physics: Conference Series* Vol. 896.

VITZTHUM, S., M. EDER, C. HARTMANN, and W. VOLK (2018). "Investigation on strain dependent elastic behavior for accurate springback analysis". In: *Journal of Physics: Conference Series* Vol. 1063.

VITZTHUM, S., C. HARTMANN, M. EDER, and W. VOLK (2019). "Temperature-based determination of the onset of yielding using a new clip-on device for tensile tests". In: *Procedia Manufacturing* Vol. 29, pp. 490-497.

VITZTHUM, S., J. REBELO KORNMEIER, M. HOFMANN, M. GRUBER, E. MAAWAD, A. C. BATISTA, C. HARTMANN, and W. VOLK (2022). "In-situ Analysis of the Thermoelastic Effect and its Relation to the Onset of Yielding of Low Carbon Steel". In: *Materials & Design* Vol. 162.

VITZTHUM, S., M. GRUBER, J. REBELO KORNMEIER, M. HOFMANN, and W. VOLK (2022). "Experimental Investigation of Factors Influencing the Determination of the Onset of Yielding by Temperature Measurement". In: *Key Engineering Materials* Vol. 926, pp. 1021-1029.

VITZTHUM, S., J. REBELO KORNMEIER, M. HOFMANN, M. GRUBER, N. NORZ, E. MAAWAD, J. MENDIGUREN, and W. VOLK (2022). "In-situ analysis of the elastic-plastic characteristics of high strength dual-phase steel". In: *Material Science and Engineering: A* Vol. 857.

Note on citation

If the reference is in the sentence or before the period at the end of the sentence, it refers directly to a word, a group of words, or the statement of that sentence. If the reference is placed at the end of a paragraph after the period, it refers to the content of the complete preceding paragraph.

Nomenclature

a	Lattice constant
b	Burgers vector
b_{YU}	Beginning of the reverse bounding surface (Yoshida-Uemori model)
d_{hkl}	Atomic lattice spacing for the (hkl) lattice plane
d^{0}_{hkl}	Initial atomic lattice spacing for the (hkl) lattice plane at stress free state
f	Volume phase fraction
h	Model parameter (Yoshida-Uemori model)
k	Model parameter (Yoshida-Uemori model)
l	Current length
l_0	Initial gauge length
m	Model parameter (Yoshida-Uemori model)
m_{L}	Factor for Lorentz proportion in Pseudo-Voigt function
n	Multiple of wavelength (Bragg's law)
s	Bragg interference
t	Time

A	Current cross-section area
A_0	Initial cross-section area
B	Initial size of bounding surface (Yoshida-Uemori model)
$\mathcal{B}$	Configuration
C	Heat capacity
C_{YU}	Model parameter (Yoshida-Uemori model)
D	Value for crystallite size
DEC_{hkl}	Diffraction elastic constant for the (hkl) lattice plane
E_0	Initial Young's modulus (Yoshida-Uemori model)
E_{a}	Saturated elastic modulus (Yoshida-Uemori model)
E_{av}	Mean elastic modulus (Yoshida-Uemori model)
E_{DIN}	Elastic modulus determined according to the standard
$E_{5-18\mathrm{TS}}$	Elastic modulus determined between 5 - 18 % of tensile strength
E_{YS0}	Elastic modulus determined on basis of temperature measurement
E_{Chord}	Elastic chord modulus
F	Load

$\boldsymbol{F}$	Deformation gradient
G	Gauss function
I	Intensity
I_{BG}	Background intensity
$I_{\max}$	Maximum intensity
K	Constant (Williamson-Smallman model)
L	Lorentz function
PV	Pseudo-Voigt function
R_{sat}	Model parameter (Yoshida-Uemori model)
T_0	Initial temperature
T	Current temperature
$\dot{T}$	Temperature gradient
V_0	Initial volume
Y	Yield strength (Yoshida-Uemori model)
$YS_{0.2\%}$	Equivalent yield strength at 0.2 % plastic strain
YS_0	Yield stress at zero plastic strain
YS_{re}	Yield stress at re-yielding
YS_{Tmin}	Yield stress at temperature minimum
α	Thermal expansion coefficient
β	Integral breadth
β_{exp}	Experimentally observed integral breadth
β_{inst}	Instrumental integral breadth
β_{size}	Integral breadth caused by grain size effects
β_{strain}	Integral breadth caused by microstrains
γ	Grüneisen parameter
ε	Logarithmic strain, or Hencky strain
$\varepsilon_{\mathrm{an}}$	Anelastic strain
$\varepsilon_{\mathrm{el}}$	Linear elastic strain
$\varepsilon_{\mathrm{hkl}}$	Elastic lattice strain for the (hkl) lattice plane
ε_{l}	Strain in longitudinal direction
$\varepsilon_{\mathrm{rec}}$	Total recovery strain
$\varepsilon_{\mathrm{pl}}$	Plastic strain
$\varepsilon_{\mathrm{pl,0}}$	Plastic tensile prestrain (Yoshida-Uemori model)
$\langle\varepsilon^2\rangle$	Microstrain (Williamson-Smallman model)
ζ	Model parameter (Yoshida-Uemori model)

Θ	Bragg angle
λ	Wavelength
ν	Poisson’s ratio
ρ	Density
ρ_{avg}	Mean dislocation density
σ	Cauchy stress
σ_{B0}	Model specific stress value (Yoshida-Uemori model)
σ^{fow}	Forward bounding surface (Yoshida-Uemori model)
σ^{rev}	Reverse bounding surface (Yoshida-Uemori model)
$\sigma_{\mathrm{hkl}}^{\mathrm{ph}}$	Phase stress for the (hkl) lattice plane
$\Delta\sigma_{\mathrm{Ma-Fe}}$	Interphase stress between martensite and ferrite

Abbreviations

Acronym	**Meaning**
AHSS	Advanced high strength steel
bcc	Body centered cubic
BG	Background
DESY	Deutsches Elektronen-Synchrotron
DP	Dual-phase
EBSD	Electron backscatter diffraction
fcc	Face centered cubic
FE	Finite elemente
fow	Forward
FRMII	Forschungs-Neutronenquelle Heinz Maier-Leibnitz
FWHM	Full width at half maximum
HAH	Homogenous anisotropic hardening model
hcp	Hexagonal close packed
HEMS	High Energy Material Science
IB	Integral breadth
IF	Interstitial free
LaB_6	Lanthanum Hexaboride
NIST	National Institute of Standards and Technology
OES	Optical Emission Spectrometer
PT	Platinum resistance thermometer
RD	Rolling direction
rev	Reverse
RMS	Root mean square strain
RT	Room temperature
RVE	Representative volume element
SG	Strain gage
SEM	Scanning Electron Microscopy
SD	Standard deviation
T	Tension
TC	Tension-compression
TE	Thermoelastic effect

TEM	Transmission Electron Microscopy
Temp	Temperature
Tmin	Temperature minimum
TUM	Technical University of Munich
TS	Tensile strength
UL	Unloading
utg	Chair of Metal Forming and Casting
WH	Williamson-Hall
YU	Yoshida-Uemori
ZR	ZwickRoell

1 Introduction

You can have different opinions about Elon Musk, but he has managed to break up the highly segregated car market and build his own car. And he did so with little initial knowledge of cars. Furthermore, founding a startup and successfully entering the car market was considered unrealistic at that time. In an interview about his first principles, he said: "I tend to approach things from a physics framework. Physics teaches you to reason from first principles rather than by analogy" (Clear, 2022). Musk probably means that problems should be reduced to their physical principles and caution should be taken when using comparison models. Why this approach fits so well to the idea behind this thesis will be explained in the following.

Numerical simulation has long replaced the historical trial and error approach to a large extent in the field of sheet metal forming (Tekkaya, 2000). Development and production times could be significantly reduced as a result (Hattalli and Srivatsa, 2018), and this is the only way to keep pace with the increasing demands on products. For example, material behavior must be transferred to models in order to virtually predict springback in forming processes as accurately as possible. In modeling, there are various approaches to do this. In Volk et al. (2019), models were analyzed and classified by their physical interpretation and were divided into theoretical (white) or empirical (black) and further in mathematical-physical, heuristic, phenomenological or statistical ones. Thereby, the theoretical, i.e. mathematical-physical models are based on valid physical relationships and thus correspond to Musk's approach. A so-called white model approach that has been known for a very long time and is fundamental for forming technology is the stress-strain curve. Mathematical equations describe the behavior of a material under uniaxial load, so a physical relationship. Its history or rather its exploration goes back several hundred years and is in relation with some big names in the field of mathematics and mechanics like Leonardo da Vinci, Galileo Galilei and Robert Hooke (Yu, 2018). However, experimental technology has changed tremendously since then and it has long been known that original assumptions such as Hooke's linear-elastic relation (Hooke, 1676) can now only be seen as a strong simplification. Significantly more accurate modeling of the material behavior is necessary to meet the accuracy requirements of today's simulations. And still, especially in the industrial environment, parameters based on the stress-strain curve, such as the Young's modulus, the onset of yielding and the tensile strength, are used according to their determination specified in standards, i.e. the German standard DIN EN ISO 6892-1. However, some of these are surrogate models, such as the equivalent yield strength at 0.2 % plastic strain, which have no physical basis. Also, the determination methods are often strongly dependent on arbitrarily selected boundary conditions and therefore not robust. In general, it has been known in science for a long time that, in contrast to the historical linear-elastic approach of Hooke, elastic material behavior is dependent on the plastic deformation state (Morestin and Boivin, 1996). Especially for high-strength multi-phase steels, which are coming more and more on the market due to their excellent strength-to-weight ratio, the elastic behavior deviates strongly from the original assumptions (Z. Chen, Gandhi, et al., 2016). The classical parameters of the stress-strain curve are no longer able to predict this complex material behavior with sufficient accuracy in the simulation. For example, plastic strain-dependent elastic unloading leads to major problems in accurately predicting the springback, which is crucial for the design of new components and their tools (Wagoner et al., 2013). For this reason, in the research of forming technology, micro-plasticity models (Yoshida and Amaishi, 2020) or topics like anelasticity and early re-yielding (D. Li and Wagoner, 2021) are getting more attention and need to be further investigated. A large number of scientific studies deal with the addressed topics and found explanations are based on microstructural behavior (Cleveland and Ghosh, 2002). Therefore, according to the mathematical-physical approach, a purely macroscopic investigation of the stress-strain behavior, respectively the elastic-plastic material behavior is no longer sufficient to analyze and understand the physical background of the material behavior.

These challenges, in summary the determination of the onset of plastic yielding and initial elastic modulus as well as the anelasticity and early re-yielding are investigated on their physical framework with this thesis. For this purpose, the addressed challenges are investigated by means of in-situ diffraction experiments and can thus be analyzed microstructurally. In-depth material understanding at a micro level is gained, new determination methods are derived and validated, and existing assumptions are experimentally reviewed by correlating the microscopic with the macroscopic behavior. The results of this work in the field of micro material characterization improve the elastic-plastic understanding of sheet metal materials, as well as qualify new experimental methods for the characterization of it. Industrial sheet metal materials are used within this work to keep the benefit for industry high. In the end, a basis is created for extending or improving so-called white models, i.e. mathematical-physical models with regard to the modeling of elastic-plastic material behavior.

2 Fundamentals

In this chapter, the fundamentals of the scientific topic under discussion and the state of the art in its investigation are presented. The material theory on the elastic-plastic behavior of steel sheet materials has a long history and nowadays the determination of material parameters is largely defined in standards. However, it has been shown that given models can only partially reproduce the actual material behavior. This imprecise reproduction of the material behavior has an impact on the prediction of springback for example. Section 2.1 summarizes the principles of material theories concerning the elastic-plastic characteristics of steels and introduces a clear terminology. In Section 2.2, the material theories are reviewed for their validity in materials science, and deviations from classical theories are pointed out. The precise description of elastic-plastic material behavior has major implications, especially for the prediction of springback. It is one of the most important application examples for the material investigations in this thesis. For this reason, springback in the field of sheet metal forming is briefly presented in Section 2.3. Thereafter, the current state of the art for the research of the individual elastic-plastic characteristics is summarized. Temperature measurement and temperature behavior under load, i.e. the thermoelastic effect, are of particular importance in this work. This effect will be dealt with separately and in detail. After this macroscopic summary of the research topic addressed, the microstructure of metallic materials will be discussed due to the objective of this work's correlation of micro with macro material behavior. On the one hand, the composition and behavior of the microstructure under load will be presented. On the other hand, in-situ, non-destructive analysis methods are discussed, which allow the investigation of the microstructural behavior of steel sheet materials.

2.1 Principles of Material Theory

The basis for the material-theoretical description of the elastic-plastic material behavior is the additive decomposition of the strain into an elastic and a plastic part. This can be shown in principle by the multiplicative decomposition of the deformation gradient $\boldsymbol{F}$ into an elastic $\boldsymbol{F}_{\mathrm{el}}$ and a plastic part $\boldsymbol{F}_{\mathrm{pl}}$ (Equation 2.1). For this purpose, an intermediate configuration ${}^{\mathrm{I}}\mathcal{B}$ is introduced between the reference configuration ${}^{0}\mathcal{B}$ and the current configuration $\mathcal{B}$. This relationship is graphically illustrated in Figure 2.1. (Haupt, 2002)

$$\boldsymbol{F} = \boldsymbol{F}_{\mathrm{el}} \cdot \boldsymbol{F}_{\mathrm{pl}} \tag{2.1}$$

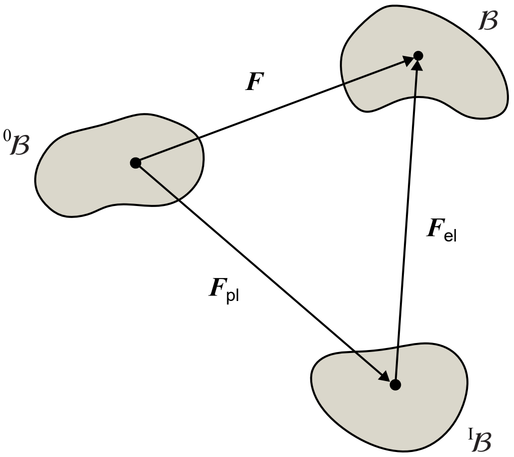

Figure 2.1: Configurations in elastic-plastic formulation.

The true strain ε defined in this work is the logarithmic strain or Hencky strain, which reflects the differential change in length to a given length. For the uniaxial case it is

$$\varepsilon = ln\frac{l}{l_0} \quad , \tag{2.2}$$

with the current length l and the initial length l_0 (Hencky, 1928). According to Vitzthum et al. (2018) and based on Hencky (1924), this strain measure is suitable for describing the deformation, because the additive decomposition of the elastic strain $\varepsilon_{\mathrm{el}}$ and the plastic strain $\varepsilon_{\mathrm{pl}}$ is permissible and can be written as

$$\varepsilon = \varepsilon_{\mathrm{pl}} + \varepsilon_{\mathrm{el}} \quad . \tag{2.3}$$

Furthermore, it is valid that strains of this strain measure can be accumulated to a total strain. It is therefore equal to the sum of the strains of the individual forming steps (Hencky, 1929).

The true stress σ, or Cauchy stress, is the ratio of the load F to the current cross-section area A and is defined as follows for a uniaxial stress state

$$\sigma = \frac{F}{A} \quad . \tag{2.4}$$

The current cross-sectional area in turn is calculated on the basis of the volume constancy assumption and was determined for the results of this thesis with

$$A = \frac{A_0 l_0}{l_0 + \Delta l} \quad , \tag{2.5}$$

with the initial cross-section area A_0, the initial gauge length l_0 and the change in length Δl (Hill, 1950). The Cauchy stress is work conjugated for the logarithmic strain measure and accordingly suitable to use in combination with it (Lehmann et al., 1991).

Commonly, the stress is set in relation to the occurring strain in form of a stress-strain diagram (Banabic and Pöhlandt, 2000). The stress-strain diagram shows the behavior of materials under uniaxial tensile or compressive loading. It can be divided into different sections. These are the elastic loading, the elastic-plastic deformation and the elastic unloading, or in case, the compressive loading. Figure 2.2 shows an true stress versus true strain curve schematically. The mentioned sections and the basic characteristic values in the stress-strain relationship are marked. These are briefly explained in the following.

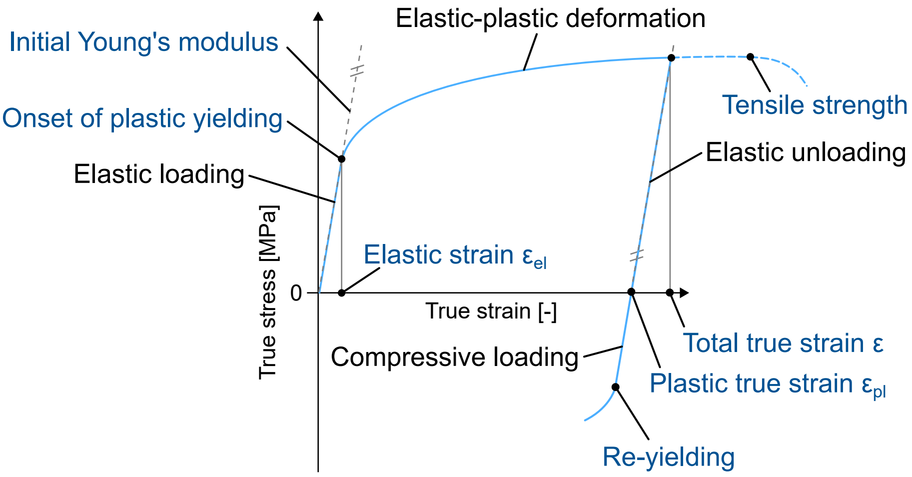

Figure 2.2: Schematic true stress versus true strain curve. The sections in dependence on the load condition and the basic characteristic values are marked.

Hooke's linear-elastic assumption goes back to the 17th century and describes a purely elastic change in shape at the beginning of the loading (Hooke, 1676). This means that the deformation is reversible and the component returns to its original state after the external load is removed. No deformation work is dissipated. With Hooke's law, the elastic strain ε_{el} can be calculated based on the Cauchy stress σ and Young's modulus E for the uniaxial case, assuming ideal linear-elastic behavior (Siegert, 2015). It is defined as

$$\varepsilon_{\mathrm{el}} = \frac{\sigma}{E} \qquad . \tag{2.6}$$

Thereby, the initial Young's modulus E is a material-theoretical description of the proportional stress-strain relation during purely elastic deformation and thus the elastic stiffness of the material (Hooke, 1676).

From a certain point, the onset of plastic yielding, deformation work is dissipated, the material behaves nonlinearly, plastically and cannot return to its original geometry after the load is removed (D. Li and Wagoner, 2021). With further elongation of the material, both elastic and plastic strains are present under load. Hence, the total true strain includes both reversible and irreversible deformation (see Figure 2.2). According to linear-elastic theory, during unloading, the reversible elastic strain component springs back with the same slope as during initial elastic loading. After complete unloading, the remaining plastic deformation reflects the plastic true strain. If the component is now compressed, nonlinear elastic-plastic deformation also occurs in compression when the re-yielding limit is exceeded. This limit can be subject to a direction-dependent change. This phenomenon is called the Bauschinger effect (Bauschinger, 1886). Figure 2.2 also shows the case when the material is not unloaded but is tensioned uniaxially until fracture. The maximum stress that occurs before necking, i.e. before the stress decreases, is referred to as the tensile strength (TS) (Doege and Behrens, 2010). It should be noted here that TS is calculated on the basis of the engineering stress and strain, i.e. in relation to its initial cross-section and length, but the parameter has been included in Figure 2.2 for the purposes of simplicity and completeness.

In summary, the terms true strain and true stress within this thesis always reflect the introduced strain and stress measures for the macroscopic material behavior in tensile or tension-compression tests. This defined terminology is important because microscopic stresses and strains will also be introduced during this thesis. When referring to a true plastic strain, a stress-free state is described, or the elastic part of the strain has been subtracted. In this thesis, the generic term Young's modulus represents the material-theoretical description of the elastic stiffness of a material according to Hooke (1676). It is constant by definition. However, the real material behavior may deviate from this. For this reason, the more general term elastic modulus and, in addition, the terms elastic loading and unloading modulus are used in this thesis. The necessity of the distinction between the moduli is explained in more detail in the following Section 2.2.

2.2 Deviations from Classical Theories

Detailed investigations of the stress-strain behavior have shown long ago that the material behavior can deviate strongly from the ideal linear-elastic assumption according to Hooke (Dalby, 1921). In addition, it was found that parameters based on the mechanically measured stress-strain curve provide a better springback prediction than physically measured values, such as the elastic modulus measured by ultrasonic (Pérez et al., 2005). For this reason, the understanding and description of the actually occurring elastic-plastic behavior of metals in uniaxial tensile and tension-compression tests became more and more the focus of science and still are today.

Figure 2.3 shows the material behavior, possibly occurring in reality compared to the theoretical assumed in Figure 2.2. These are the onset of plastic yielding and the initial Young's modulus, which cannot be determined unambiguously due to nonlinear elastic stress-strain behavior and a steady transition from elastic to elastic-plastic deformation for many materials. Furthermore, the elastic unloading curve often exhibits nonlinear behavior, which leads to a reduction of the unloading modulus and complicates its determination. The initial Young's modulus is therefore not sufficient to describe elastic material behavior. For this reason, a distinction is made in this work between an elastic loading modulus and an elastic unloading modulus. Both are strain-dependent parameters and their determination methods are part of the research results in this thesis. Another frequently discussed issue is early re-yielding, i.e. replasticizing after plastic prestrain even before the load path changes into the compression range.

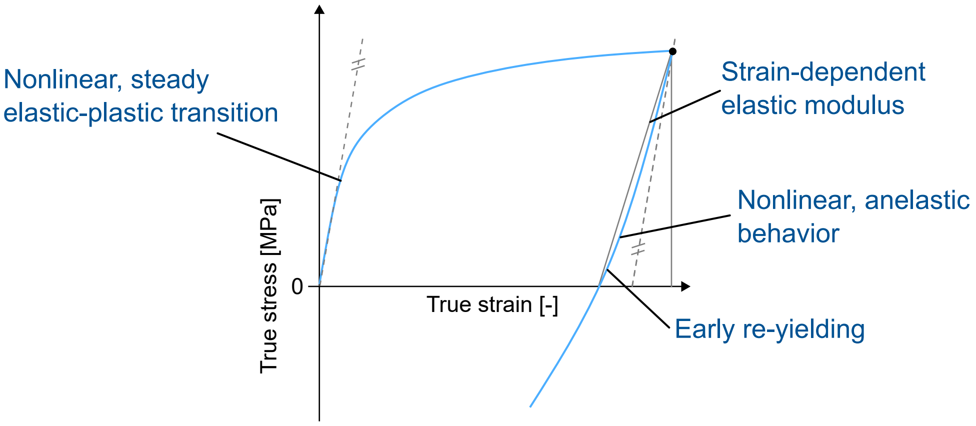

Figure 2.3: Schematic stress-strain curve with possible material behavior in reality.

2.3 Springback in Sheet Metal Forming

The deviations of the material behavior from existing approaches of material theory have an effect in sheet metal forming, especially in the prediction of springback. Springback strongly depends on the elastic-plastic behavior of the material. For this reason, this section briefly discusses springback prediction and the state of the art in research before the individual material characteristics are discussed in more detail. Current challenges in modeling the elastic-plastic material behavior with industrial steel sheets are clarified.

Springback describes the change in geometry after the removal of an external force. In case of a deep drawing process, after opening the press, the sheet metal component changes its geometry until internal residual stresses, which are induced by forming, are in equilibrium (Banabic, 2010). Figure 2.4 shows a deep-drawn U-profile virtually superimposed before and after springback. It can be seen that in this case for a high-strength dual-phase steel, there is a large deviation of the geometry due to springback. This deviation can lead to a geometry that is no longer within the specified component tolerance, which is why springback is also seen as a failure mode in deep drawing (Doege and Behrens, 2010).

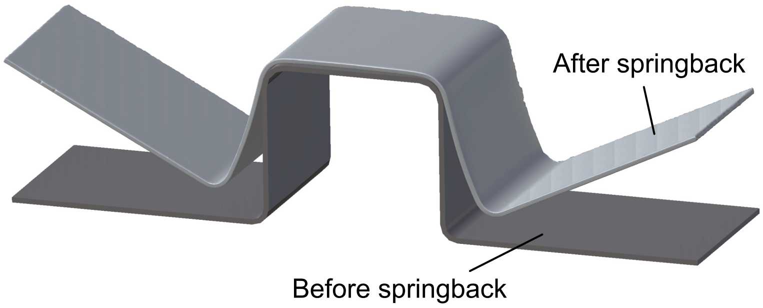

Figure 2.4: Experimental example of a deep-drawn U-profile for the material DP1000 virtually superimposed before and after springback.

There are two main approaches to control or compensate springback in literature, and a large number of studies have been published on these topics over the past decades (P. Chen and Koç, 2007). On the one hand, the sheet tension can be increased (Baba and Tozawa, 1964) and, on the other hand, the tool geometry can be adjusted so that the target geometry is achieved after springback (Hartmann et al., 2021). The prerequisite for implementing the latter is a precise prediction of the springback.

FE simulation is widely used as a tool for this prediction (Hou et al., 2017). S. Lee and Yang (1998) showed in an early stage that FE simulation of springback is very sensitive to its settings and the material model used. The main simulation settings to be mentioned here, are the integration approach (K. P. Li et al., 2002), the solver used, i.e. implicit/implicit (Guo et al., 2002) or explicit/implicit (Papeleux and Ponthot, 2002), the meshing or element size (Banabic, 2010) and the element type (Xu et al., 2004). On the material model side, there are several factors that can have great influence on the numerical prediction of springback and many studies on these can be found in literature (Wagoner et al., 2013). These include the yield strength (Z. T. Zhang and D. Lee, 1995), the strain hardening behavior of the material (Geng and Wagoner, 2000), the unloading behavior and the change in elastic behavior as a function of plastic strain (Yoshida and Amaishi, 2020), plastic anisotropy (Verma and Haldar, 2007), the Bauschinger effect (Kubli et al., 2008) and anelastic phenomena (Cleveland and Ghosh, 2002). These material-specific influencing factors are the subject of the research in this thesis. Their material science basis is analyzed in order to examine the validity of material theory assumptions.

Recently, even more focus has been placed on springback research. This is related to the use of advanced high-strength steels (AHSS), for example dual-phase steels (DP), which are very suitable for lightweight structures due to their excellent weight-to-strength ratio (Wagoner et al., 2013). The mechanical properties allow the use of thinner sheet thicknesses with maintaining strength. But both, the high strength and thus large elastic range and lower sheet thickness, lead to increased springback (Torkabadi, 2018). Furthermore, Wagner et al. (2021) showed for a large number of industrially relevant steels that the material-related influencing factors mentioned, such as the decrease in elastic loading and unloading modulus with increasing plastic strain, occur particularly strongly for high-strength DP steels. Thus, the determination of springback based only on the stress state with constant, linear elasticity leads to large errors for this type of material. Accurate modeling of the elastic and elastic-plastic material behavior and especially of the unloading behavior, is necessary (Torkabadi, 2018). In the following, the addressed elastic-plastic characteristics of industrial steels will be discussed in more detail.

2.4 Onset of Yielding and Elastic Loading Modulus

The relationship between the onset of yielding and the Young's modulus becomes clear if one takes a closer look at the definitions in the respective standards. For example, according to ASTM International standard ASTM E 111-17, Young's modulus is defined as *"the ratio of tensile or compressive stress to corresponding strain below the proportional limit"*. Also the German standard DIN EN ISO 6892-1 defines that Young's modulus should be determined between 10 % and 40 % of the equivalent yield strength. Hence, knowledge of the onset of yielding is necessary. A closer look at the two determination methods according to the standard

reveals that, more precisely, it is a mechanically determined loading modulus.
In theory, Young's modulus is defined as the ratio of stress to strain during purely elastic deformation. In terms of material science, a distinction can be made between the moduli depending on the determination method. Generally, they can be classified in mechanical and physical ones (Münstermann, 2004). For metal materials, mechanical methods are the uniaxial tensile test (DIN EN ISO 6892-1) and indentation test (Oliver and Pharr, 2004), while physical methods are ultrasonic pulse-echo (Droney and Klinman, 1982) and resonance analyzes (Wolfenden and Schwanz, 1995). Pérez et al. (2005) compared the results of the two physical methods with the results of the mechanical tensile test and it was found that the latter are more suitable for springback prediction of sheet materials. In the following, the mechanical determination in the uniaxial tensile test will be discussed in more detail with regard to the scientific objectives of this thesis. Sufficient test and measurement accuracy is a requirement for determining the onset of yielding or Young's modulus from the stress-strain curve of a tensile test. The requirements are defined in the standard and are not discussed in more detail here (DIN EN ISO 6892-1).

2.4.1 Determination of the Onset of Yielding

Approaches to better understand and describe plastic flow have existed for more than a century (Bingham, 1916) and a wide variety of definitions of the onset of yielding can be found in literature (Barnes, 1999). Furthermore, different determination methods can be found in literature. It should be noted that in this thesis only materials with steady elastic-plastic transition are considered. A pronounced yield strength is not addressed. In Sallat (1988), several mechanical methods for determining the onset of yielding by stress-strain curves are explained and examined. Figure 2.5 gives an overview of these approaches schematically. Namely, these are an extrapolation approach, or also called Lode extrapolation, the proportional limit approach, or equivalent yield strength, and an approach using high-precision temperature measurement.

In the extrapolation approach (Figure 2.5 (a)), a regression line is placed through the initial elastic part of the curve and another through the area of linear hardening. The intersection of these lines indicates the onset of yielding. Since the boundary conditions for both regression lines are difficult to define and the point found lies outside of the actual curve, this determination approach is not of great relevance (Sallat, 1988).

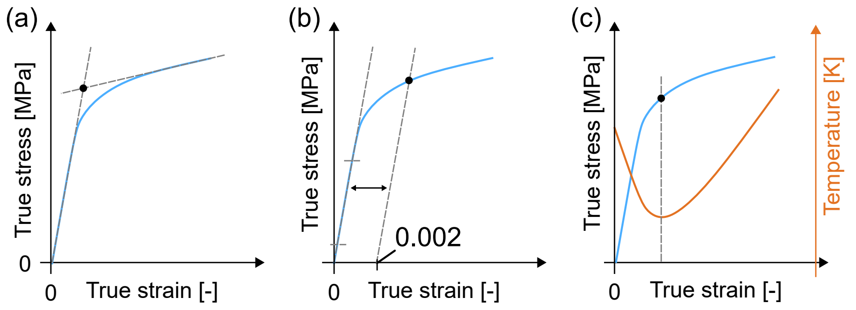

Figure 2.5: Different methods for determining the yield stress, (a) extrapolation approach, (b) equivalent yield stress or proportional limit and (c) temperature approach.

In the proportional limit approach, the point is searched from which the stress is no longer proportional to the strain. It is therefore the deviation of the stress-strain curve from the extended Hooke's line (Figure 2.5 (b)). Consequently, exceeding the yield limit is necessary to be able to determine this point. For many materials, this deviation is difficult to determine due to a smooth transition to nonlinear elastic-plastic deformation. For this reason, the most widely used approach for unambiguous parameter determination is the equivalent yield strength at 0.2 % plastic strain. According to the German standard DIN EN ISO 6892-1, a straight line with the initial slope is shifted backward by 0.2 % residual plastic strain compared to its initial length and the intersection with the stress-strain curve reflects the parameter. It is an equivalent yield strength, since it does not represent the onset of plastic yielding but the state at 0.2 % irreversible deformation (Siegert, 2015). For materials with a continuous change of slope even before the onset of yielding, the determination of the regression line is often ambiguous and depends on the experience of the user (Sallat, 1988).

Another method is the approach via high-precision temperature measurement (Figure 2.5 (c)). Compared to the other approaches, this is not a material theory approach, but a material science approach, since the physical material behavior is utilized. Based on the ideal gas law, the temperature changes as a function of volume (Joule and Thomson, 1852). As this is also valid for solid materials (Weber, 1830), with elastic elongation, the volume is increasing, while the temperature is decreasing. In the case of plastic deformation, the deformation work is mostly dissipated in the form of heat (Pandey and Chand, 2003). This means that the specimen heats up again. These relationships lead to a characteristic minimum between elastic and plastic deformation under tensile load, which can be used to determine the onset of yielding, especially for materials with a particularly smooth elastic-plastic transition (Cardona et al., 1983). Since this approach is one of the main research aspects of this thesis, it will be discussed separately and in more detail in Section 2.6.

2.4.2 Determination of the Initial Elastic Modulus

In this chapter, a distinction is made between elastic modulus types and approaches. The types describe different variants of the elastic modulus description. These types in turn can be evaluated based on different approaches. When determining the elastic modulus in the uniaxial tensile test, a fundamental distinction can be made between different types. The American standard ASTM E 111-17 distinguishes between the Young's modulus, or elastic modulus, the tangent modulus and the chord modulus. Furthermore, the type of a secant modulus can be found in literature (Dean et al., 1995). Figure 2.6 shows these types schematically. The types find application depending on the objective of the analysis and the material behavior. The S-shaped stress-strain curve as shown for the secant modulus (see Figure 2.6), usually indicates inaccuracies in the experimental setup and occurs in the very beginning of the stress-strain curve. For this reason, incorrect assumptions may be made for this type.

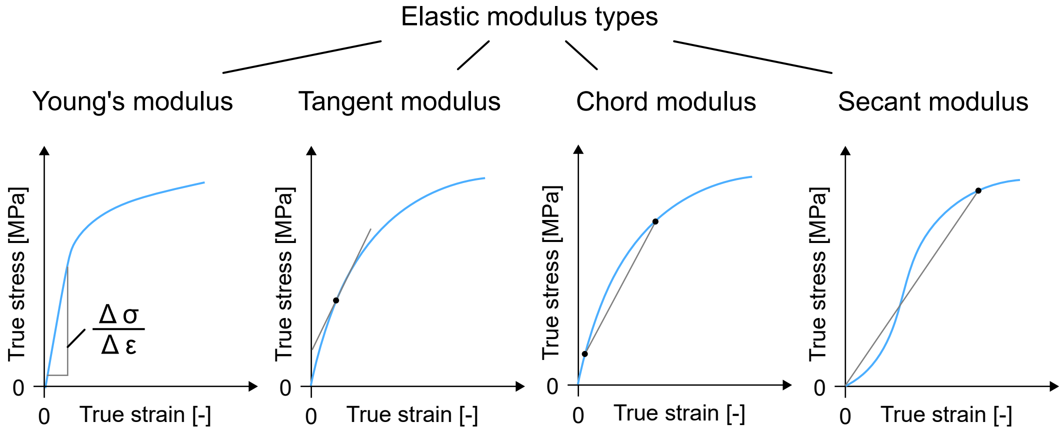

Figure 2.6: Schematic representation of different elastic modulus types (ASTM E 111-17, 2017; Dean et al., 1995).

Based on the types, there are several approaches to evaluate the elastic modulus (Maciolek et al., 2021) and for a better overview, these methods can be classified in limit, fitting and deformation work approaches. Figure 2.7 shows these approaches schematically for better clarity. The basic approaches of these evaluation methods are summarized in the following.

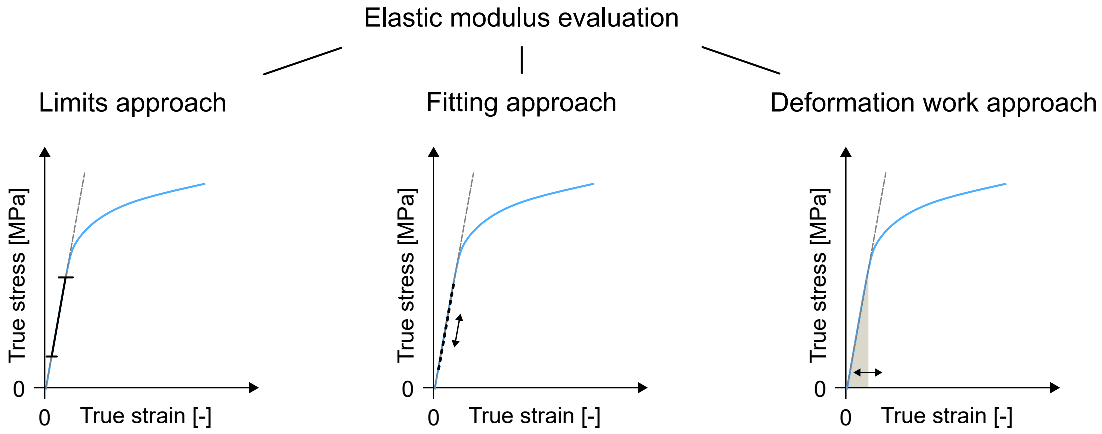

Figure 2.7: Schematic representation of different elastic modulus approaches.

- *Limits approaches*

  The German standard procedure is a typical approach with fixed limits. It suggests to use the range from 10 % to 40 % of the yield strength for a linear regression. Since the yield strength itself depends on the linear range of the initial slope, an iterative process may be necessary (Maciolek et al., 2021). The number of datapoints required and the maximum standard deviation are specified. Nevertheless, it can lead to a user-dependent result, because no real termination criterion is defined for the iterative process. Hence, it depends on the experience of the user.

  The tensile strength (TS) can be determined more clearly compared to the yield strength. Therefore, Sonne (1999) published an evaluation approach where the range between 5 % and 18 % of TS is used for the linear regression. This leads to the fact that for many materials only a small area at the beginning of the stress-strain curve is considered for the determination.

  The approach introduced by McKeighan and Hillberry (1991) also uses the tensile strength for the determination of limits. Therefore, initial values for the upper and lower limits, the step size and an additional stress tolerance value are defined. The definition of these values depends on a try and error procedure and is therefore based on experience. The slope between the lower and upper limit is used to calculate a temporary yield strength at 0.2 % plastic strain. If this value is within the defined stress tolerance with the upper stress limit, the procedure is completed and the elastic modulus corresponds to this slope. A verification approach is also proposed, but this is based on a self-defined accuracy tolerance.

- *Fitting approaches*
  Hesse et al. (1991) used two 3$^{\text{rd}}$ order polynomials in an iterative process where the elastic modulus is determined step by step. This is done by analyzing the curvature of the function curves. The iterative process is terminated when the nonlinear components of the polynomials are negligibly small or a defined minimum value was reached. A detailed description can be found in Hesse et al. (1991).

  The approach by Scibetta and Schuurmans (2004) uses an initial starting value, dependent on the maximum force. Then, a section size and a minimum number of datapoints are defined. This data section size is shifted through the experimental datapoints and a linear regression is performed for each position. In an iterative process, both the number of datapoints and the section size are increased so that the error of the linear fit can be calculated for each area of the stress-strain curve. The slope of the area with the lowest error reflects the elastic modulus.

  Another fitting approach was published by Roebuck et al. (1994). The tangent modulus was calculated using 2$^{\text{nd}}$ order polynomial fit and plotted versus the strain. In this way, a plateau can be searched, which represents linear behavior. For many materials, the plateau cannot be determined unambiguously due to a very soft transition. Furthermore, the evaluation depends on the selected initial parameters for the polynomial as well as on the measurement data acquisition. Hence, user experience is necessary.

- *Deformation work approach*
  Suttner and Merklein (2017) introduced an approach based on the performed deformation work. For this purpose, the triangular work was calculated for each stress-strain pair. During linear behavior, this triangular work corresponds to the deformation work. If the behavior is nonlinear, the deformation work is larger. In this way, taking into account the relationship between the triangular work and the deformation work, the elastic limit and modulus can be determined. However, nonlinear effects led to inaccuracies in the determination of the elastic limit and smaller, nonlinear strains had to be neglected.

In summary, there are a large number of determination methods for Young's modulus and in some cases they differ greatly in their approach (Maciolek et al., 2021). Most methods take the approach of detecting the region of greatest linearity in order to evaluate its slope. Due to the existing nonlinearity for many materials, this often leads to assumptions, which are necessary for the evaluation. Finally, a verification of reasonableness by looking at the fit in the stress-strain curve is necessary.

2.5 Strain-Dependent Unloading Behavior

It has long been known that the elastic unloading behavior after plastic pre-strain can be different from the initial elastic loading (Taylor and Quinney, 1931). For some time, this phenomenon, for example for copper (Lems, 1962), was studied independently of springback prediction without much attention. After it became known that this phenomenon has great influence on springback prediction (Morestin and Boivin, 1996), its investigation became the focus of more and more scientific studies (D. Li and Wagoner, 2021). A variety of different terms can be found in the literature to describe this phenomenon (Torkabadi, 2018). Therefore, a clear classification or terminology is important. Figure 2.8 illustrates the phenomenon by means of an unloading curve of a uniaxial tensile test for a better overview.

At first, the elastic strain composition has to be explained. In literature, it is common to divide the total recovery strain ($\varepsilon_{\mathrm{rec}}$), at 0 MPa external stress, into linear elastic and nonlinear elastic (Cleveland and Ghosh, 2002). The remaining true strain after unloading is referred to a true plastic strain ($\varepsilon_{\mathrm{pl}}$), since it has been corrected for the elastic components. The linear elastic strain ($\varepsilon_{\mathrm{el}}$) is based on the initially measured elastic modulus. Thus, dependent on Equation 2.6, the strain is calculated by the initial elastic modulus and the current stress value at the start of unloading. The nonlinear elastic strain represents the additional strain up to the total recovery strain.

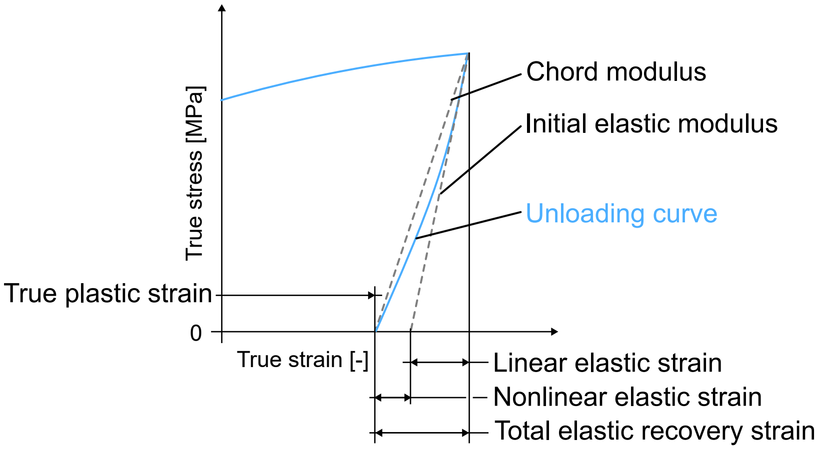

Figure 2.8: Schematic representation of an unloading curve in a uniaxial tensile test to illustrate the elastic components.

In the research area of sheet metal forming and its modeling, there are many different terms for this nonlinear strain component. For example, Sun and Wagoner (2011) refers to this as *"Quasi-*

Plastic-Elastic" strain, Luo and Ghosh (2003) uses the term *"inelastic"* strain and Arechabaleta et al. (2016) specifies the strain as *"anelastic"* strain. Within this thesis, the nonlinear component of the elastic unloading is referred to anelastic strain (ε_{an}) as in most of the publications in this subject area. To avoid confusion it should be noted that in mechanics, anelastic relaxation is also used as a type for internal friction (Blanter et al., 2007) and that a distinction is often made between nonlinear elasticity and anelasticity (Nowick and Berry, 1972). More details about this can be found in Section 2.5.1. Finally, the total elastic recovery strain can be summarized to

$$\varepsilon_{\text{rec}} = \varepsilon_{\text{el}} + \varepsilon_{\text{an}} \qquad , \tag{2.7}$$

(Arechabaleta et al., 2016) or, if describing the total true strain (ε) (Sun and Wagoner, 2011), to

$$\varepsilon = \varepsilon_{\text{pl}} + \varepsilon_{\text{el}} + \varepsilon_{\text{an}} \qquad . \tag{2.8}$$

It has been shown that it is important to consider this behavior for springback prediction. For this purpose, a characteristic value or parameter is necessary, thus, an unloading modulus. Commonly, the slope between the starting point of unloading and the strain value after complete unloading is used. Again, different terms can be found for this parameter in literature, like *"springback modulus"*, *"secant modulus"*, *"chord modulus"* and *"effective modulus"* (Torkabadi, 2018). According to the standard ASTM E 111-17, this type of evaluation is equivalent with the chord modulus (see Figure 2.6) and this term is used within this thesis.

2.5.1 Anelasticity

Definition and classification

The original definition of anelasticity probably goes back to the book *"Elasticity and Anelasticity of Metals"* by Zener (1948) who was the first to create a distinction from general viscoelasticity (Nowick and Berry, 1972). Zener (1948) defines anelasticity as the state in which stresses and strains are not related in a defined way and no permanent deformation occurs. According to this original definition, it was assumed that anelasticity is a time-dependent, nonlinear, additional component besides instantaneous elasticity and it differs from linear viscoelasticity in that it is completely reversible (Nowick and Berry, 1972). The time dependence becomes clear when looking at the defined mechanical standard model for anelasticity (Figure 2.9). With a spring connected in series ((a) and (b)), immediate deformation is possible. By connecting a spring and a dashpot in parallel ((b) and (c)), an additional nonlinear component is added.

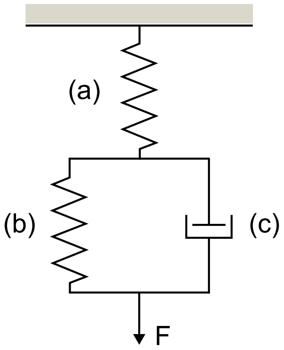

Figure 2.9: Standard three parameter anelastic model according to Nowick and Berry (1972) and Blanter et al. (2007).

Based on the mentioned time-dependency, the model includes so-called elastic after effects (Zener, 1948). Sun and Wagoner (2011) investigated the definition for its validity in an extensive study using uniaxial cyclic tensile tests. A time-delayed material behavior could not be determined, since the obtained stress-strain hysteresis showed no dependency on strain rates in the quasi-static range. Based on the state of the art and a comprehensive experimental study, a revised definition was found in D. Li and Wagoner (2021). There, anelastic behavior is defined as *"a mode of deformation that is recoverable and energy dissipative"* (D. Li and Wagoner, 2021). According to D. Li and Wagoner (2021), the definition does not contradict Zener's original definition as well as the common viscoelastic terminology for polymers. Only the time-delayed material behavior is no longer taken into account, since it could not be proven.

Explanations for anelastic material behavior

Different explanations for anelastic behavior can be found in literature and a summary of them is given by Z. Chen, Bong, et al. (2016). Since anelasticity is a key topic of this thesis, conceivable responsible mechanisms will be explained again. Figure 2.10 shows a graphical summary of the mechanisms, the significance of which will be briefly discussed below.

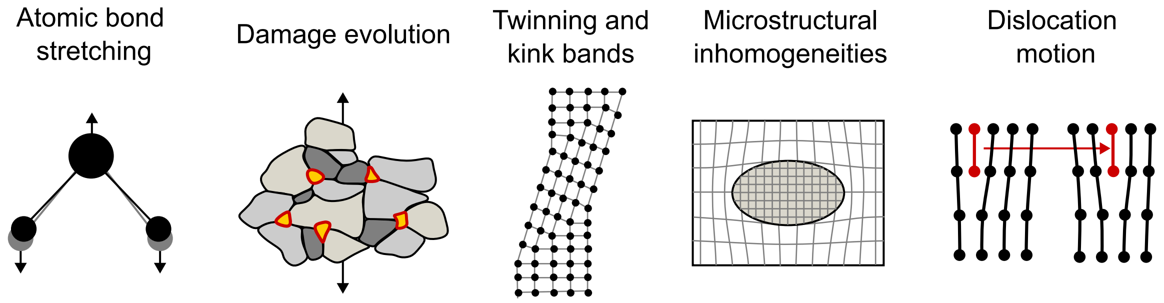

Figure 2.10: Overview of conceivable responsible mechanisms for anelastic behavior.

- *Atomic bond stretching*
  For metals at low temperatures, usually only the deformation mechanisms of dislocation motion and atomic bond stretching occur (D. Li and Wagoner, 2021). It was shown that for ferritic metals and alloys, the atomic bond stretching is linear up to stresses of about 15 GPa (L. Li and Han, 2017). Stresses of this level are not reached in the investigations of this study. Hence, it is assumed that this mechanism is negligible (Z. Chen, Bong, et al., 2016).

- *Damage evolution*
  In Halilovič et al. (2007), the anelastic behavior is explained by decreasing stiffness due to increasing microvoids and microcracks. Experiments of Eggertsen et al. (2011) showed that the elastic stiffness recovers over time. Thus, the elastic modulus increases again over time. As a result, it was shown that the amount of anelastic strain decreases over time at room temperature. The material thus recovers. Furthermore, Torkabadi (2018) showed that after plastic pre-strain, the initial Young's modulus can be achieved again after heat treatment. These experimental results contradict a relationship between damage evolution and anelasticity, since recovery is not expected under the described circumstances.

- *Twinning/detwinning and kink bands*
  Hama et al. (2013) showed a relation between the nonlinear unloading behavior and detwinning. Zhou et al. (2008) found a connection between kink bands and nonlinear behavior. Both studies investigated hexagonal close packed (*hcp*) materials. Since both effects hardly occur in face centered cubic (*fcc*) and body centered cubic (*bcc*) materials, which are investigated in this study, it can be assumed that these mechanisms play only a minor role (Z. Chen, Bong, et al., 2016).

- *Microstructural inhomogeneities*
  Microstructural inhomogeneity refers to different strengths or stiffnesses within the microstructure of polycrystals. On the one hand, this can be different load bearing capacities of grains and microstructural anisotropies, which lead to so called intergranular stresses (Dye et al., 2001). On the other hand, these are interphase stresses in multiphase materials, where the respective phases differ strongly in their strength. The more compliant phase can already enter the pressure range during unloading and thus reverse yielding can occur (Govik et al., 2014). An indication of this was shown in Gardey et al. (2005), who showed a more pronounced Bauschinger effect in dual-phase steels compared to single-phase steels. J. H. Kim et al. (2012) and Govik et al. (2014) published results in a numerical study that indicated that differential phase behavior is the main driver of the Bauschinger

effect, respectively the nonlinear, anelastic unloading behavior. Zecevic et al. (2016) also showed in a numerical study the importance of the behavior of two different phases for the Bauschinger effect.

- *Dislocation motion*
  In literature, the movement of dislocations is most often given as the origin of the strain-dependent, nonlinear unloading behavior. It is assumed that dislocations pile up at grain boundaries and can move differently in opposite directions (Hart, 1984). Cleveland and Ghosh (2002) divided the behavior of these mobile dislocations during unloading into three areas. First, dislocations piled up at obstacles in the lattice during loading, move back and are more mobile in reverse direction. Then, dislocations in the cell wall also begin to move backward. During unloading, more and more piled up dislocations become mobile, which leads to the more compliant elastic behavior near complete unloading. Besides this, bowing out of dislocations between fixed points is named to be a further possible cause for the additional, fully recoverable and nonlinear strain (Pérez et al., 2005). Recently, the correlation between dislocation movement and anelastic behavior could be partially verified. Kupke et al. (2019) was able to show dislocation movement during unloading using electron channeling contrast imaging. Torkabadi et al. (2018) blocked mobile dislocations via heat treatment and thus was able to show a direct correlation with the nonlinear behavior. Arechabaleta et al. (2016) was able to show dislocation movement indirectly by comparing X-ray results with a material model. Using TEM measurements on aluminum, Hasegawa et al. (1975) showed annihilation of 10 - 20 % of dislocation density upon unloading and reverse loading, proving that dislocations can be mobile, or annihilate, and are related to anelasticity and early re-yielding.

In summary, the most plausible explanations for nonlinear anelastic behavior are microstructural inhomogeneities and dislocation motion. Therefore, these two mechanisms will be examined in more detail within this research study.

2.5.2 Reduction of the Unloading Modulus

So far, the specific anelastic behavior of an unloading curve after plastic pre-strain has been considered. Now, the behavior will be described as a function of increasing plastic strain. To describe the springback as a function of plastic strain, an unloading modulus is necessary. Again, there are various evaluation methods. Yoshida et al. (2002) describes the possibility of dividing the unloading curve into four sections in order to determine the slope in each case

(Figure 2.11 (a)). As already mentioned, the chord modulus (Figure 2.8) is the most widely used method for describing the unloading curve. The advantage is that the real springback strain is fully considered with it, because it is evaluated until zero applied stress (Cleveland and Ghosh, 2002). The nonlinearity of the unloading curve is not taken into account, but as the full recovery strain is considered for evaluation of the chord modulus, it is linked with the amount of anelastic strain. Consequently, a reduction of the chord modulus compared to the initial Young's modulus is due to anelasticity.

A large number of studies have analyzed the dependence of chord modulus on plastic strain for a wide range of materials in cyclic loading-unloading tensile tests. Wagner et al. (2021) evaluated the chord modulus dependent on plastic strain in cyclic tensile tests for 27 different steel grades, from mild steels to conventional high-strength steels to high-strength dual-phase steels. The results show that the chord modulus decreases by up to 25 % with uniform elongation. This maximum reduction was found for dual-phase steels. Similar reductions in chord modulus were found for aluminum (Cleveland and Ghosh, 2002), stainless steel (Yamaguchi et al., 1998) and TRIP steels (Mendiguren et al., 2015). In these studies, there was always an initial significant decrease in the chord modulus, which then went into saturation with increasing plastic pre-strain. After showing that the reduction in Young's modulus has large effects on springback modeling (Morestin and Boivin, 1996), several modeling approaches describing this reduction in stiffness with increasing plastic strain were published (Kubli et al., 2008). These ranged from linear approaches (Morestin et al., 1996), to nonlinear analytical (X. Li et al., 2002) and logarithmic ones (Luo and Ghosh, 2003). A widely used exponential approach was introduced by Yoshida et al. (2002) and is

$$E_{\mathrm{av}} = E_0 - (E_0 - E_{\mathrm{sat}})[1 - exp^{-\xi \varepsilon_0^p}] \qquad , \tag{2.9}$$

where E_{av} is an average modulus at the plastic strain ε_0^p calculated with the initial Young's modulus E_0 and a saturated modulus E_{sat} at a large plastic prestrain. The parameter ξ is a material constant. A cyclic tensile test and evaluation of the unloading modulus at several plastic pre-strains is necessary for the calibration of this model. Figure 2.11 (b) shows this modulus approximation according to Yoshida et al. (2002) on basis of four sections of the unloading curve (Figure 2.11 (a)). The range for modulus E_4 is like the chord modulus, since the entire unloading curve is included in the linear regression. For the evaluation shown in Figure 2.11, a dual-phase steel (DP1000) was used and the initial Young's modulus was set to 210 GPa.

In Yoshida (2018), an extension of the modeling approach was presented so that additionally nonlinearity is taken into account. The investigation of the importance of considering chord modulus reduction as well as nonlinearity in hardening models can be found in Yoshida (2022).

In summary, the consideration of a variable elastic modulus has great influence on the result of springback prediction. The additional consideration of the nonlinearity showed a rather small influence depending on the hardening model.

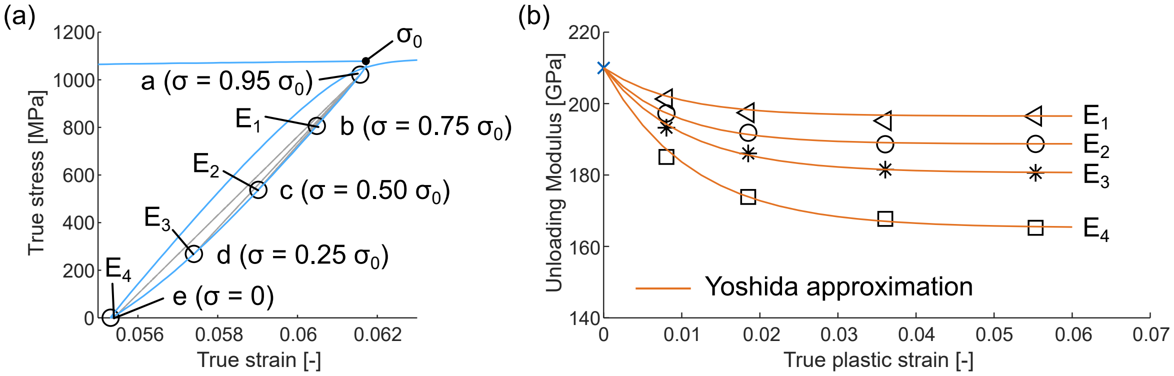

Figure 2.11: (a) Subdivision of the unloading curve into four unloading moduli E_{1-4} and (b) their plastic strain dependency for DP1000. Additionally, the approximations by Equation 2.9 according to Yoshida et al. (2002) are plotted.

2.5.3 Re-yielding and Bauschinger Effect

During the production of sheet metal components, a change in loading direction can occur (Torkabadi, 2018). As already mentioned, the forming behavior differs with load path changes, e.g. with reverse loading after previous plastic tensile loading (Kubli et al., 2008). If a component is subject to loading, unloading and reverse loading, the stress-strain relationship that occurs can be divided into characteristic sections. After a tensile load, nonlinear unloading occurs, which has already been described in detail in the previous sections. When the load changes, the Bauschinger effect or early re-yielding occurs before transient softening takes place. Permanent softening follows this. Figure 2.12 schematically shows a stress-strain path for loading, unloading and reverse loading and highlights the mentioned areas according to Yoshida and Uemori (2002).

The areas addressed are briefly explained in the following and hardening models which can represent these characteristic areas are listed (Torkabadi, 2018). It has to be noted that only a rough overview of the hardening models is given, since the focus of this thesis is not on material modeling, but on understanding material behavior by experimental investigations. A more comprehensive overview of modeling approaches can be found in Wagoner et al. (2013) and Yoshida and Amaishi (2020).

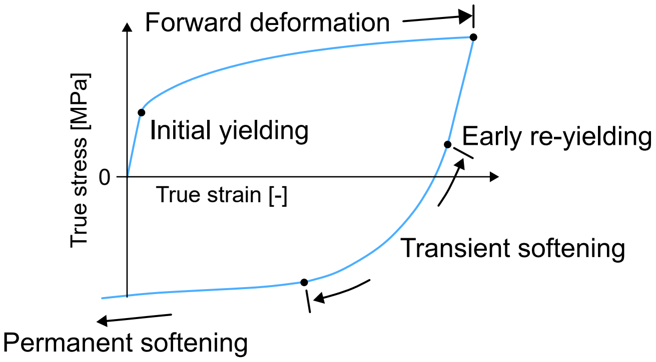

Figure 2.12: Schematic tension-compression stress-strain path. Highlighted are the important areas for modeling the Bauschinger effect according to Yoshida and Uemori (2002).

- *Bauschinger effect, early re-yielding*
  Based on the mechanisms described in Section 2.5.1, early re-yielding occurs in some materials. This means that the material already begins to replasticize during tensile load. As a result, the stress-strain behavior changes significantly. Early re-yielding is thus to some extent related to the anelastic behavior described.

- *Transient softening*
  Transient softening describes the particularly smooth elastic-plastic transition due to the load change.

- *Permanent softening*
  Permanent softening refers to the significantly lower yield curve after load change compared to the yield curve without load change.

For the description of plasticity or hardening behavior, a general distinction can be made between two approaches and their combination. Namely, these are isotropic and kinematic hardening and the combined isotropic-kinematic hardening. For better clarity, the approaches are shown schematically in Figure 2.13 according to Muránsky et al. (2012).

The initial yield surface is a mathematical description of a surface in the space of principal stresses (Banabic and Pöhlandt, 2000). The interior of this three dimensional surface refers to an elastic state and points on the surface refer to a plastic state (Banabic and Pöhlandt, 2000). The different approaches to hardening can be illustrated by the yield surface. In the case of isotropic hardening (Figure 2.13 (a)), the yield surface expands or contracts while the center position, the shape and orientation of the yield surface stay the same (Muránsky et al., 2012). In contrast, the size, orientation and shape of the yield surface remain the same during kinematic hardening (Figure 2.13 (b)) and only the center position changes in the stress space

(Prager, 1955). Isotropic-kinematic hardening combines their properties (Figure 2.13 (c)). The yield surface can expand or contract as well as change in its center position. As illustrated in Figure 2.13 (d), the prediction of the re-yielding point after changing the loading direction is strongly dependent on the chosen hardening model.

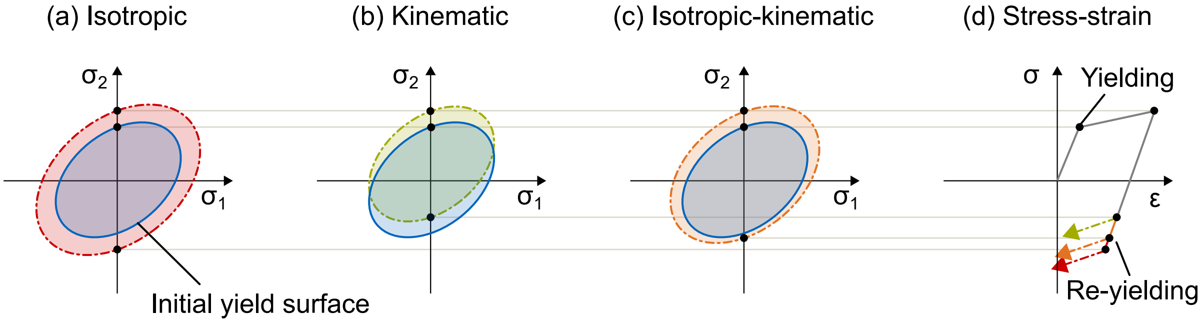

Figure 2.13: Illustration of (a) isotropic, (b) kinematic and (c) isotropic-kinematic hardening and (d) its effect on the stress-strain curve according to Muránsky et al. (2012).

The scientific community agrees that attention to the Bauschinger effect is of great importance for springback prediction (Wagoner et al., 2013; Yoshida and Amaishi, 2020). To model this behavior, the description of the hardening with a simple radially expansion of the yield surface (isotropic) is not sufficient. It has been shown that approaches which consider the translation of the yield surface (kinematic, isotropic-kinematic) are better suited for this purpose (Eggertsen and Mattiasson, 2009). Widely used models that can reproduce the described characteristic features during load changes are nonlinear hardening models (Frederick and Armstrong, 2007), multi-surface hardening models (Yoshida and Uemori, 2002) and models different from the simple kinematic approach (Barlat et al., 2011). The latter, the so-called homogenous anisotropic hardening model (HAH), is becoming increasingly popular. It has been extended to include cross-loading effects (Barlat et al., 2013) and further enhanced for mild steels and high-strength steels (Barlat et al., 2014), and it is still being further adapted and improved (Barlat et al., 2020).

The isotropic-kinematic YU model, published by Yoshida and Uemori (2002), is finding increasing industrial application as it is implemented in several FEM programs (LS-DYNA, Pam-Stamp, AutoForm). It shows high prediction accuracy compared to other models (Grubenmann et al., 2018). For the calibration of the model, three elasticity parameters are determined in a cyclic tensile test (see Equation 2.9) and seven plasticity parameters are necessary, which are determined in a tension-compression test. The YU model is discussed in more detail in Section 8.1.

Generally, experimental, microstructural investigations of the Bauschinger effect for a better understanding of the material behavior are missing and the models mentioned are mainly curve descriptions. This means, the macroscopic stress-strain relationship is reproduced as accurately as possible without knowing the microstructural causes.

2.6 Thermoelastic Effect

In Section 2.4, it has already been shown that there is the possibility to determine the onset of yielding via high-precision temperature measurement (see Figure 2.5 (c)). This method is investigated and further developed in this thesis for the characterization of material behavior. For this reason, the thermoelastic effect (TE) is discussed separately again here. First, a description and short historical summary of the state of the art is given. Then, the thermomechanical basics are discussed.

2.6.1 Description and Historical Summary

The thermoelastic effect describes the temperature change with a volume change in solids. Figure 2.14 illustrates this schematically with a crystal lattice model. According to Vitzthum et al. (2019), the process can be divided into three phases. During elastic tensile loading (phase 1), a stretching or distortion of the lattice occurs. The crystal lattice remains intact, i.e. reversible, and no dislocations are formed, but the distortion leads to an increase in volume. This is also due to Poisson's ratio, which for steel is 0.3 (Doege and Behrens, 2010). The increase in volume leads to a decrease in temperature. Above a certain stress, the material begins to plastically yield (phase 2), the lattice partially breaks up and dislocations form. Most of the energy released in this process is converted into heat (Pandey and Chand, 2003), which leads to a temperature increase and thus to a characteristic temperature minimum in the area of the onset of yielding. During elastic unloading (phase 3), the volume decreases and consequently the temperature increases. However, this can occur with a different gradient than during elastic-plastic deformation.

The thermoelastic effect goes back to the findings of Weber (1830) and Joule and Thomson (1852). They were able to prove that the relationship between the temperature change and the volume change also applies to solids. Thomson (1853) established a theoretical basis and derived a linear relationship between temperature and stress change during reversible deformation (Stanley, 2008). Compton and Webster (1915) published an experimental confirmation of these findings and afterwards several studies were addressed to this topic (Biot, 1955; Rocca and

Bever, 1950). An overview and detailed descriptions can be found in Sharpe (2008). In the beginning, measurement accuracy was the major challenge, because for metallic materials, it is necessary to measure temperature changes of less than one Kelvin (H. Lee and J. Chen, 1991). Belgen (1967) succeeded in measuring the effect with an infrared camera and H. Lee and J. Chen (1991) were able to measure a temperature difference of 0.35 K for steel material using sensitive thermistors. In the meantime, results have been published in literature on stainless steel (Patil et al., 2009; Prakash et al., 2011), on austenitic steel, titanium and aluminum alloy (Oliferuk et al., 2012) as well as on low carbon steel (Jandrlić et al., 2016). The effect was also demonstrated in a biaxial tensile test with welded-on thermocouples (Jocham et al., 2016). A measurement method with a PT1000 sensor has already been presented by the author and will be further modified, improved and validated within this thesis (Vitzthum et al., 2019).

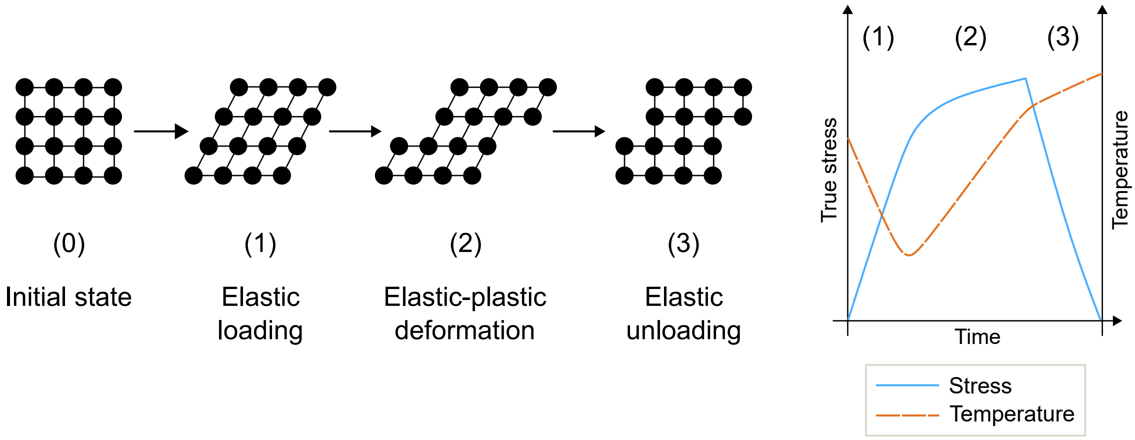

Figure 2.14: Schematic crystal lattice during elastic loading, elastic-plastic deformation and elastic unloading and associated stress-time and temperature-time curve to illustrate the thermoelastic effect.

2.6.2 Thermomechanical Basics

During a uniaxial tensile test, the temperature in the specimen changes. Thus, it is a non-isothermal experiment and the temperature change is related to non-trivial thermodynamic processes in the material. Consequently, elasticity cannot be described only mechanically. Bottani and Caglioti (1982) introduced a thermomechanical description of the temperature behavior during elastic-plastic transition, which can be summarized on basis of Cardona et al. (1983) as follows. During pure elastic deformation, virtually, there is no change in entropy and the material's thermodynamic state is stable. Dislocations cannot move, i.e. are immobile and the material state is almost in equilibrium. It is possible to describe this condition with the strain tensor and the present temperature. If plastic deformation occurs, dislocations form or rearrange themselves and the dislocation density changes. To describe this change another thermodynamic variable is necessary and for this reason, the described purely elastic state gets out of equilibrium. The onset of yielding thus reflects the point at which the prevailing state can no longer be described in conventional thermodynamic terms.

The increase in volume leads to a decrease in temperature and vice versa. The volume during linear elastic deformation can be described with

$$\frac{\Delta V}{V_0} = (1 - 2\nu) \cdot \varepsilon_1 \qquad . \tag{2.10}$$

There, V_0 is the inital volume, ν Poisson's ratio and ε_1 the strain in longitudinal direction. Using Maxwell's relation, the dependency between the initial temperature T_0 and the temperature change ΔT in the elastic range is given with the equation (H. Lee and J. Chen, 1991)

$$\frac{\Delta T}{T_0} = -\gamma(1 - 2\nu) \cdot \varepsilon_1 \qquad , \tag{2.11}$$

where γ is the Grüneisen parameter. This parameter is described by the specific heat capacity at constant volume, the thermal expansion coefficient and isothermal compressibility, but a precise determination of a value for this parameter is not trivial. An extensive investigation of different materials is necessary. (H. Lee and J. Chen, 1991)

Besides this thermomechanical description, there is another, well-known approach to describe the thermoelastic effect. The derivation of the relationship is possible by using the thermoelasticity model of Heinz (1976). After complex derivation (H. Lee and J. Chen, 1991), the relationship between the change in stress $\Delta\sigma$ and in temperature ΔT is given by (Bever et al., 1973)

$$\Delta T = -\frac{\alpha T_0 \Delta\sigma}{\rho C} \qquad . \tag{2.12}$$

Equation 2.12 describes a linear relationship between stress and temperature for elastic deformation. For this relation, the thermal expansion coefficient α, the ambient temperature T_0, the density ρ as well as the heat capacity C are necessary. Consequently, materials like steels with a positive thermal expansion coefficient cool down during elastic tension and heat up during compression. The temperature changes calculated with this formula corresponded very well to those measured experimentally. This could be shown for several materials such as metals, polymers, ceramics and composites (Boley and Weiner, 2012). It was also proofed within this thesis and is shown in Section 6.1.1.

2.7 Microstructural Fundamentals of Metals

The basics of the microstructure of metals are briefly summarized according to Banabic and Pöhlandt (2000), Clemens et al. (2017) and Hornbogen et al. (2019). With this, the terminology used within this thesis is clarified.

Solid materials can be classified by their atomic arrangement and the type of bonding of the atoms (Clemens et al., 2017). Metallic materials are composed of a large quantity of individual grains, also known as crystallites. The grains are separated from each other by grain boundaries and their size can vary greatly depending on the material. The combination of grains, their orientation, possible crystal defects and the grain boundaries is called texture. The structure in a particular grain is given by a periodic arrangement of atoms and their distance to each other, which is also called crystal lattice. The distribution of the grain orientations is thereby random, but each orientation can be defined by their elementary crystal structure (Banabic and Pöhlandt, 2000). For metals, these crystal structures can be divided in body-centered cubic (*bcc*), face-centered cubic (*fcc*), hexagonal closed-packed (*hcp*) and tetragonal (Clemens et al., 2017). Figure 2.15 (a) shows schematically the division of several grains with their crystal lattices of different orientations. In addition, the elementary arrangement of the atoms is shown for *bcc* (Figure 2.15 (b)). Apart from lattice defects, the entire crystal lattice is composed of this structure. Only *bcc* is shown, since within this thesis steels with this lattice structure are investigated. It has to be noted that only the centers of the particular atoms are shown. In reality, the atoms are closely packed together and for *bcc* in diagonal direction in contact to each other. This represents the slip direction. (Banabic and Pöhlandt, 2000)

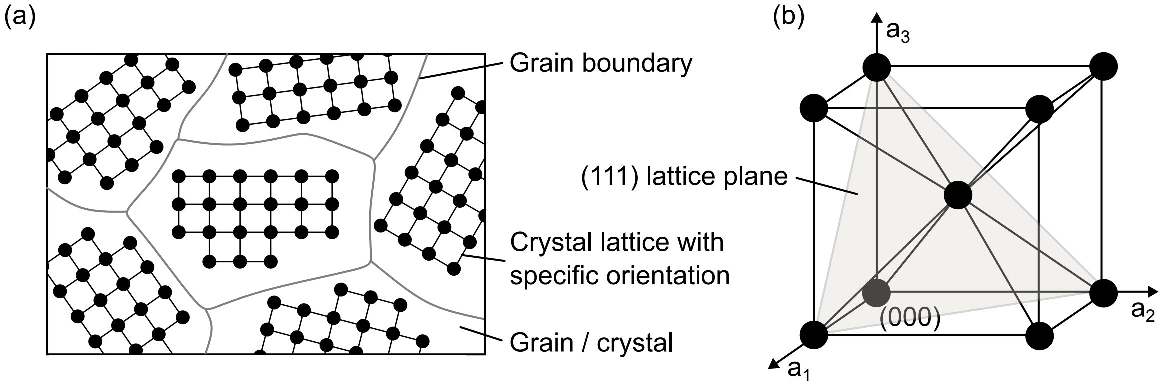

Figure 2.15: (a) Schematic representation of a grain structure of a metal and (b) arrangement of atoms for a body-centered cubic material (bcc). The (111) lattice plane is shown transparent in gray as an example. Illustrations according to Banabic and Pöhlandt (2000) and Jackson (1991).

Miller (1839) introduced the so-called *hkl* Miller indices to define directions and planes within a crystal structure. Based on an initial coordinate system (a_1, a_2, a_3), a direction or plane can be described by the intersection points with the axes (see the example lattice plane (111) in Figure 2.15 (b)). It is specified that the entries for *h*, *k* and *l* must be integers (Jackson, 1991).

In summary, a number of aspects can characterize the microstructure of metals. These are the grains and their sizes, phases present and their compositions or distribution, as well as various types of defects. A distinction is made between zero dimensional defects, namely point defects (e.g. vacancies and foreign atoms), one-dimensional defects such as dislocations and two dimensional defects such as grain boundaries and heterogeneous interfaces. Plastic deformation is based on these defects and mainly on the formation and movement of dislocations. (Clemens et al., 2017)

Dislocations and microstructural stresses are in particular the focus of this thesis, since they are considered drivers of anelastic behavior. For this reason, their fundamentals will be discussed separately.

2.7.1 Dislocations

Dislocations are line defects in the crystal lattice and a general distinction is made between edge dislocations and screw dislocations (Figure 2.16) (Bargel, 2022). The behavior of dislocations has a significant influence on the material behavior, because their movement and formation leads to plastic deformation or hardening. If dislocations encounter obstacles or are blocked, the material hardens. Edge dislocations can move only in the slip direction depending on the lattice, if no thermal activation takes place. The closest packed direction and thus the slip direction for *bcc* materials is $\langle 111 \rangle$ (Jackson, 1991). The Burgers vector represents the distortion of the crystal lattice due to dislocations. The Burgers vector b is calculated via the Burgers circuit, i.e. going from atom to atom in a circuit. In an ideal crystal, the end point is equal to the start point. The position between the start and end point can differ, for example because of an edge dislocation in the crystal (see Figure 2.16 (c)). The Burgers vector represents this distance between start and end point. (Banabic and Pöhlandt, 2000)

The dislocation density usually expresses the dislocation state in a material. It describes the number of dislocations present in a given area. It is the dislocation length per volume and in metallic materials, their range is usually between 10^{10} m^{-2} and 10^{16} m^{-2} depending on the processing history (e.g. heat-treated or cold-formed). (Clemens et al., 2017)

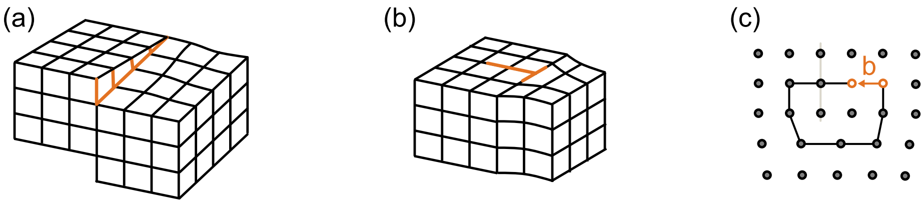

Figure 2.16: Crystal lattice model with (a) a screw dislocation and (b) an edge dislocation. (c) Burgers circuit for an edge dislocation (Banabic and Pöhlandt, 2000).

2.7.2 Microstructural Stresses

Besides dislocations, microstructural stresses are mainly used as a plausible reason for anelastic material behavior. Before microstructural stresses are described in more detail, they are classified in the overall context of residual stresses. Residual stresses are internal stresses within a material or component, which is free from external loads. They are caused by processing or forming and can be divided into three different types (Hauk, 1997). First type are macroscopic residual stresses, which occur over large distances, thus, over numerous crystals and phases within the material or over the entire component length (Repper, 2010). The second and third types are residual stresses within the microstructure. These are intergranular and interphase stresses (2nd type) and intragranular stresses (3rd type) within a grain. Figure 2.17 schematically shows a possible distribution of the three types of residual stresses for a polycrystalline material. If an external force is applied to such a polycrystalline material, the result is a macrostress superimposed of microstresses. These microstresses are acting on individual grains, between grains and within grains as shown in Figure 2.17. (Dye et al., 2001)

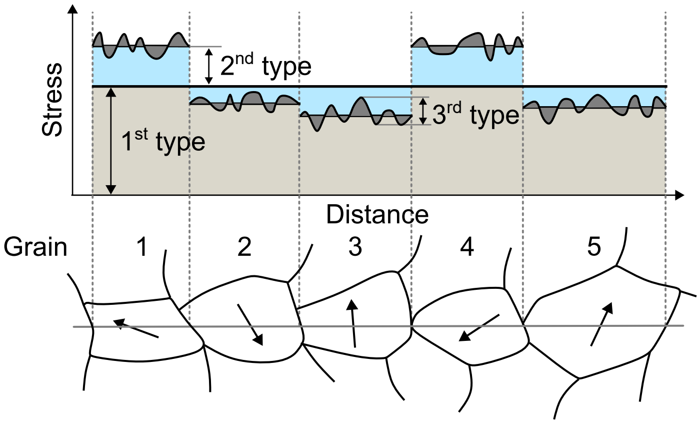

Figure 2.17: Schematic representation of the distribution of residual stresses of 1st, 2nd and 3rd order for a polycrystalline material according to Dye et al. (2001).

Within this work, intragranular, intergranular and interphase stresses are studied. For this reason, these three types will be discussed in more detail in the following.

Intragranular stresses
Intragranular stresses are stress differences within a grain. This type of residual stresses is caused by defects in the crystal lattice, such as vacancies, interstitial atoms, dislocations, etc. (Repper, 2010)

Intergranular stresses
Anisotropic behavior occurs in a single-phase polycrystalline material under elastic and plastic loading, resulting in intergranular stresses (Heyn, 1914). If a uniaxial load is applied to a polycrystalline aggregate, this load is distributed to the individual grains depending on their elastic anisotropy, thus, their stiffness and their orientation to the direction of the load. Elastic stiffer grains absorb more strain then more compliant ones. In the elastic range, this stiffness is called diffraction elastic constant (*DEC*). If the critical stress, which leads to the activation of the slip systems, is exceeded, plasticization occurs. This onset of plasticization also occurs depending on the stiffness of the respective grain family and their orientation to the load direction. Microstructural anisotropy or interactions between grains during plastic deformation can cause individual grains to exhibit different strain states after complete unloading. Figure 2.18 (a) schematically shows the true macroscopic stress versus the lattice strain for two lattice planes. Already during elastic deformation, a difference in slope can be seen, which indicates elastic anisotropy. If plasticization occurs, the plastic anisotropy becomes apparent, which leads to residual strains after unloading. Figure 2.18 (b) shows the corresponding intergranular strains versus the true macroscopic strain. Due to strongly different behavior of the grains at small strains, there is a strong increase in intergranular strains, especially at the beginning. In the further course, the increase depends on the hardening of the material. Clausen et al. (1998) showed that microstructural elastic and plastic anisotropy is crucial for the development of intergranular stresses. (Dye et al., 2001; Stone et al., 1999)

Most studies on intergranular stresses are found for *fcc* materials like stainless steel (Daymond et al., 1997), copper (Clausen et al., 1998) or nickel-base alloys (Holden et al., 1998). In a study of Pang et al. (1998) with pure ferritic *bcc* material, large intergranular strains were observed for the lattice plane (002). Lattice planes with higher multiplicity like (220), (112) and (222) showed smaller intergranular strains, which did not exceed the standard deviation. Furthermore, Tomota et al. (2003) showed in an in-situ neutron diffraction study with single-phase ferritic steel that the (200) lattice plane is highly anisotropic. The DEC_{200} was significantly lower than for the lattice planes (211) and (110). As a result, grains with the orientation of lattice plane (200) behaved more compliant and absorbed more elastic strain, which led to a strongly different plastic yielding behavior between the investigated lattice planes. The range in which some lattice planes are already plasticizing while others are still elastically deformable has been termed grain-to-grain yielding (Tomota et al., 2003).

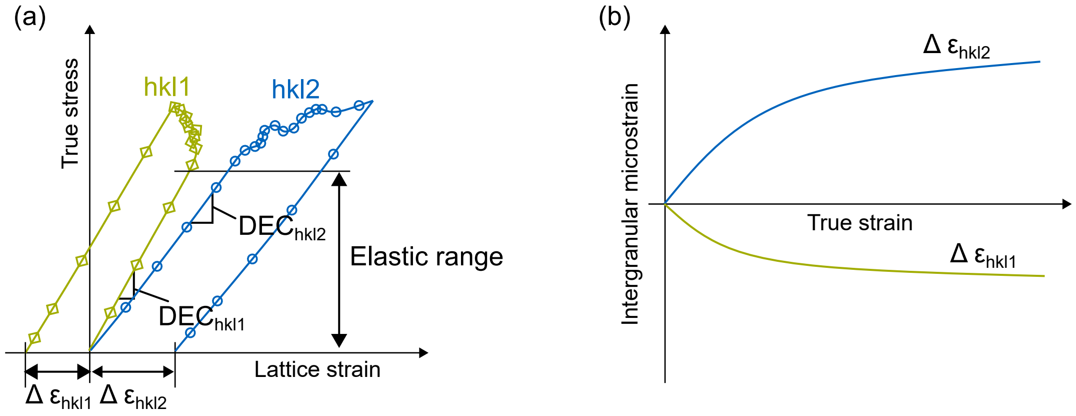

Figure 2.18: Schematic plot of (a) intergranular strains after deformation by the true stress versus lattice strain for two exemplary lattice planes and (b) intergranular strain development with increasing macroscopic strain according to Dye et al. (2001).

Interphase stresses

More and more complex steels are coming onto the market in which multiple phases are present. The background to this is to combine good properties of the respective phases. For example, duplex stainless steels show high strength and yet corrosion resistance due to the smart combination of ferrite and austenite (Gadalińska et al., 2021). Widely used are dual-phase steels, where the hard martensite phase is combined with the soft ferrite phase. In this way, high strength combined with good formability is possible (Bergström et al., 2010). This steel grade is one of the considered steels within this thesis and explained in more detail in Section 4.2.

Large differences in the strength of the phases lead to a strongly different distribution of the load on the respective phases. This in turn leads to different residual microstrains and finally interphase stresses (Stone et al., 1999). Figure 2.19 (a) illustrates schematically the behavior of a harder phase 1 and a softer phase 2 for the same lattice plane. If the material is loaded uniaxial, the phases first deform elastically until the softer phase begins to plasticize. The harder phase then absorbs additional elastic strain, since its onset of yielding is at significantly higher loads. Because the softer phase can no longer absorb any further strain, a residual lattice strain occurs during unloading, which can vary greatly. As exemplary shown in Figure 2.19 (a), one phase may be under compression and the other under tension after complete unloading. This leads to interphase stresses, which are dependent on the true macroscopic strain (Figure 2.19 (b)). (Stone et al., 1999)

Overall, the occurring phase stresses σ_{phase1} and σ_{phase2} are in equilibrium, depending on their volume fraction f_{phase1} and f_{phase2}. Thus, the volume fractions calculated with the phase stresses result in the macroscopic stress σ. It can be calculated with

$$\sigma = f_{phase1} \cdot \sigma_{phase1} + f_{phase2} \cdot \sigma_{phase2} \qquad . \tag{2.13}$$

The characterization of this microstructural material behavior has recently become an important issue in order to calibrate microplasticity models for numerical simulation. For this purpose, representative volume elements (RVE) are established which reflect the behavior of the individual phases and their volume fractions and with which the macroscopic material behavior can be described on a microstructural basis (Torkabadi, 2018).

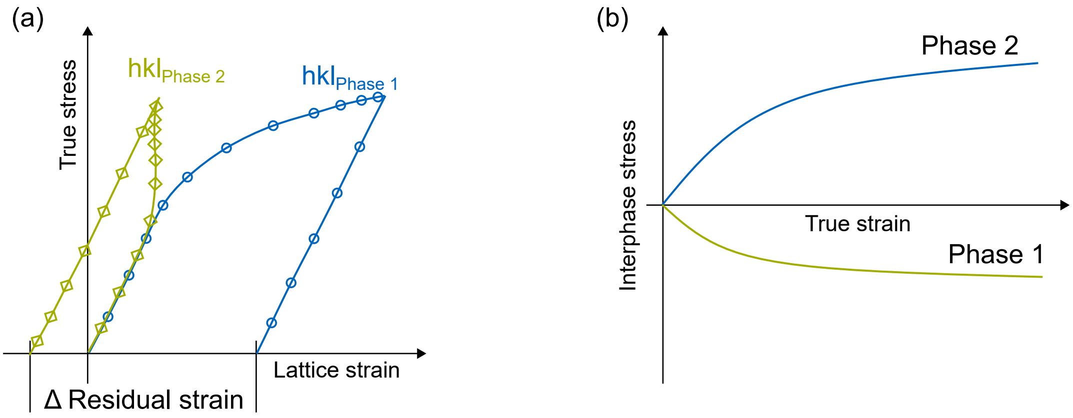

Figure 2.19: Schematic representation of (a) different true stress versus lattice strain behavior of the same lattice plane for two different phases and (b) evolution of interphase stresses with increasing true macroscopic strain according to Stone et al. (1999)

2.8 In-situ Diffraction

In Section 2.7, microstructural basics were given, focusing primarily on dislocations and stresses within the microstructure. In order to analyze these properties, a measurement method is required that can detect individual grains or grain families with the same direction. Diffraction experiments, e.g. with X-ray, neutron or synchrotron radiation, make this possible by evaluating the lattice plane reflections (Dye et al., 2001). In the following, the basics of diffraction experiments with focus on synchrotron diffraction are explained. Subsequently, the state of the art of this kind of measurement method and the considered materials within this thesis is briefly summarized.

Conventional X-ray tubes have the disadvantage that only a minimal portion of around 1 % of the applied energy is converted into ionizing radiation and the rest is released in the form of heat (Falta, 2010). The low radiation energy is followed by a low penetration depth, which in the case of ferritic steel is in the range of a few micrometers (Spieß et al., 2019). Thus, the microstructure of steel materials can only be examined close to the surface and surface defects strongly influence the measurement results. Accordingly, higher energy radiation is necessary for the study of the microstructure of steel sheets with thicknesses in the millimeter range (Spieß et al., 2019). Synchrotron radiation is generated by deflecting electro-magnetically accelerated electrons from their straight trajectory, which results in the tangential emission of high-energy radiation (Wiedemann, 2003). Therefore, a ring-shaped particle accelerator with a diameter of several meters to kilometers is required (Repper, 2010). The benefit of synchrotron radiation compared to conventional X-ray radiation is the much higher energy and brilliance, which allows transmission measurements with steel sheet metals. This is why it is suitable to use synchrotron radiation for the investigations in this thesis. It has to be noted that diffraction tests can only measure values relative to the initial state.

The diffraction experiments for this thesis were performed at the German national laboratory *Deutsches Elektronen-Synchrotron* (DESY) in Hamburg, which is a photon science and particle accelerator (Heinze et al., 2017). The experiments were conducted at the photon science source PETRA III (beamline P07), which is one of the brightest sources in the world. As an example, the generated X-rays are up to 5000 times finer than a human hair. The acceleration ring of 2.3 km length was the largest accelerator in the world when it was inaugurated. Today, PETRA III offers space for almost 60 measuring stations at 23 beamlines. A detailed description of the experimental setup and procedure can be found in Section 5.4. (Deutsches Elektronen-Synchrotron, 2022)

2.8.1 Bragg's Law

Based on the work of Max von Laue, who demonstrated the wave nature of X-rays, W. H. Bragg and W. L. Bragg (1913) studied crystal lattice structures with X-rays (Landesberger, 2022). Bragg's law describes the behavior of waves, respectively radiation, which can amplify each other when passing through a periodically arranged solid, respectively crystal, forming an interference. The diffraction of radiation, i.e. its distribution, provides information about the structure of the solid. Figure 2.20 shows the physical background of this condition. The difference in distance of two waves in phase, which are scattered in the same way by atoms in the crystal, is directly related to the distance between the atoms. Interference (s) occurs, if this delta corresponds exactly to a multiple of the wavelength. (Baker, 2009)

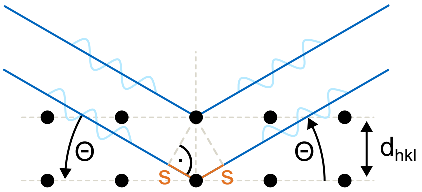

Figure 2.20: Representation of lattice planes with periodically arranged atoms with atomic lattice spacing d_{hkl} and incident radiation leading to interference s according to Bragg's law.

Hence, Bragg's law mathematically gives the relation between the atomic lattice spacing d_{hkl} of the respective lattice plane, the multiple n of the wavelength λ of the radiation and the diffraction angle Θ as follows (Hauk, 1997)

$$n\lambda = 2d sin(\Theta) \quad . \tag{2.14}$$

For a cubic crystal system the atomic lattice spacing d_{hkl} can be calculated with the lattice parameter a and the Miller indices of the respective lattice plane (Borchardt-Ott and Sowa, 2013). It is defined as

$$d_{\text{hkl}} = \frac{a}{\sqrt{h^2 + k^2 + l^2}} \quad . \tag{2.15}$$

2.8.2 Debye-Scherrer Method

Debye and Scherrer (1916) developed a method to investigate and identify crystal structures of materials using X-ray radiation. In a polycrystalline material, according to the condition of Bragg's law, all equally oriented lattice planes reflect at certain 2 Θ angles (Hauk, 1997). Figure 2.21 (a) shows a setup of a transmission diffraction experiment. The beam goes through the specimen. A large part of the beam passes through the sample unreflected and is caught by a beam stop. Some of the radiation is scattered by the crystal lattice, resulting in a scattering cone that can be captured by a detector. The crystal lattice and material behavior in general can be further evaluated by the obtained distribution, form and intensities of the rings (see Figure 2.21 (b)). If, for example, the individual circular segments of the rings are compared with each other, it is possible to obtain information about the texture in the material (Repper, 2010).

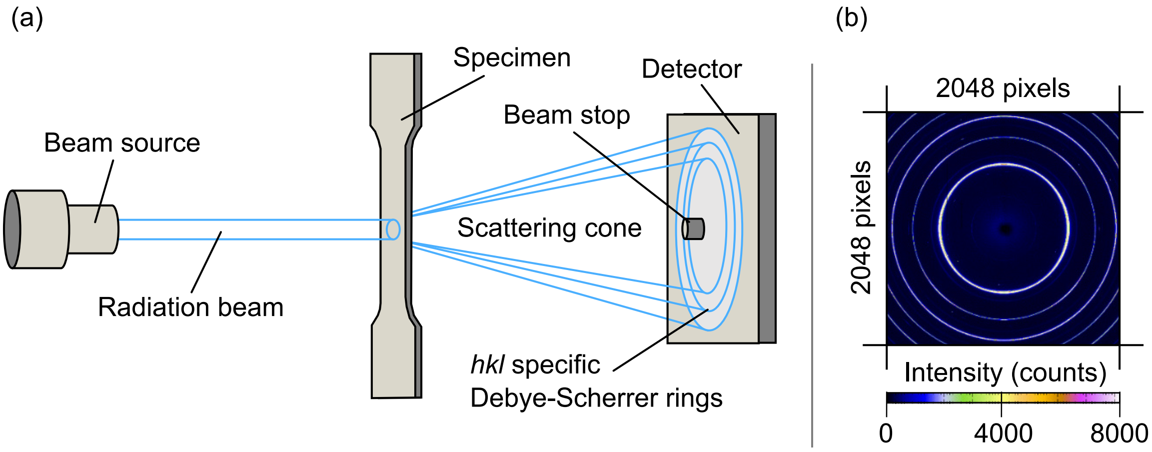

Figure 2.21: (a) Setup of a transmission diffraction experiment for the detection of lattice plane specific Debye-Scherrer rings and (b) exemplary detector image with three complete Debye-Scherrer rings.

For further analysis, the rings can be converted into diffraction profiles. Depending on the objective of the examination, the measured intensities of ring segments in specific orientations can be summed up. This results in a diffraction profile with intensity versus the 2 Θ scattering angle (Landesberger, 2022). Figure 2.22 shows three exemplary Debye-Scherrer rings on a detector which are summed up over the evaluation segment. The summed up intensities are then plotted versus the 2 Θ scattering angle.

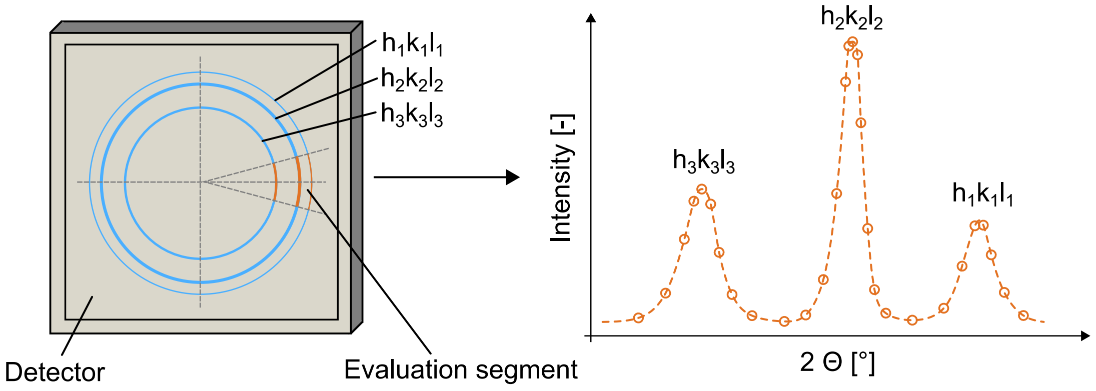

Figure 2.22: Schematic presentation of the evaluation of Debye-Scherrer rings to get a diffraction profile with intensity versus the 2 Θ angle for particular lattice planes.

2.8.3 Diffraction Profile Analysis

It was found that the intensity distribution of a diffraction profile could have different appearance. The shape of the profile depends on micro residual stresses, lattice defects and the size and shape of domains. This is why, the analysis of diffraction profiles is important in the field of materials science. (Spieß et al., 2019)

The background, the maximum intensity, the width and the asymmetry are crucial for the description of a diffraction profile. Their accurate consideration avoid misinterpretations regarding the physical properties. Figure 2.23 illustrates these parameters for the description of a peak profile. Thereby, the parameters are defined according to Spieß et al. (2019) as follows:

- *Background (BG)*
  The background is unavoidable and each material and experiment shows a different amount of background. It is caused by scattering effects, e.g. thermal diffuse scattering and incoherent scattering, as well as further inaccuracies during the diffraction experiment. The existing energy resolution determines the peak to background ratio. Often the background is not parallel to the horizontal measurement axis and it can also deviate from linear behavior. Depending on the shape, the background is approximated with a fit function so that an average value I_{BG} can be determined. This is subtracted from the maximum intensity $I_{\max}$ of the reflection.

- *Full width at half maximum (FWHM)*
  This characteristic value reflects the width of the peak at half the height of the maximum intensity I_0.

- *Integral breadth (IB)*
  The integral breadth is the width of a rectangle whose area is equal to the area of the background-corrected peak at the same intensity maximum.

- *Peak position*
  The scattering angle at maximum intensity $I_{\max}$ is taken as the peak position Θ_0. There are also approaches where the center of gravity is calculated as the position. However, within this thesis the maximum intensity is used.

- *Peak shape*
  The lower part of the peak shape, i.e. the transition of the peak to the background, can be asymmetric and is crucial for the choice of the fit function. Fit functions differ strongly in their goodness of fit for this area.

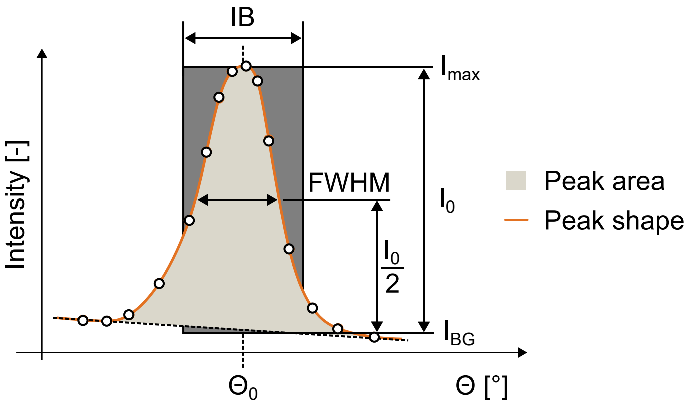

Figure 2.23: Parameters for the description of a diffraction profile according to Spieß et al. (2019).

The shape of the diffraction profile can be approximated by different mathematical methods. It is to distinguish into one-parameter analytical functions like Gauss and Lorentz and composite functions like Voigt or Pearson. These four functions are the most commonly used empirical fit functions (Pecharsky and Zavalij, 2003). It has to be noted that the Lorentz function can also be called Cauchy function in stochastics (Spieß et al., 2019). Within this thesis, however, it is called Lorentz function. Only Gauss, Lorentz and the Pseudo-Voigt function, which is the sum function of Gauss and Lorentz, are considered. A more detailed explanation of this selection for the investigations within this study is given in Section 6.2. The following Equations 2.16, 2.17 and 2.18 give the individual functions.

$$\text{Lorentz} \qquad L(x) = \frac{2}{P \cdot \pi}\left(1 + 4 \cdot \frac{x^2}{P^2}\right)^{-1} \tag{2.16}$$

$$\text{Gauss} \qquad G(x) = \frac{1}{P\sqrt{2\pi}} \cdot exp\left(\frac{-x^2}{2 \cdot P^2}\right) \tag{2.17}$$

$$\text{Pseudo-Voigt} \qquad PV(x) = \left(1 - m_\mathrm{L}\right) \cdot G + m_\mathrm{L} \cdot L \tag{2.18}$$

In these equations, P is equal to FWHM. Using the integral breadth (IB) it has to be adjusted with IB $= \frac{P \cdot \pi}{2}$. The factor m_L reflects the level of Lorentz profile portion in the Pseudo-Voigt function and its value or variation can be an important information for the characterization of the material. (Pecharsky and Zavalij, 2003; Spieß et al., 2019)

Figure 2.24 compares the Lorentz with the Gauss function exemplarily for the (211) lattice plane of a single-phase ferrite steel. It can be seen that the Lorentz function is much tighter than the Gauss function, especially close to the maximum intensity. On the other hand, the lower peak shape of the Lorentz function is larger than the one of the Gauss function. Both functions are symmetric functions. In Figure 2.24, it can be seen that for the single-phase steel (HC260Y) used here exemplarily, the Gaussian function is much closer to the experiment than the Lorentz function. (Pecharsky and Zavalij, 2003)

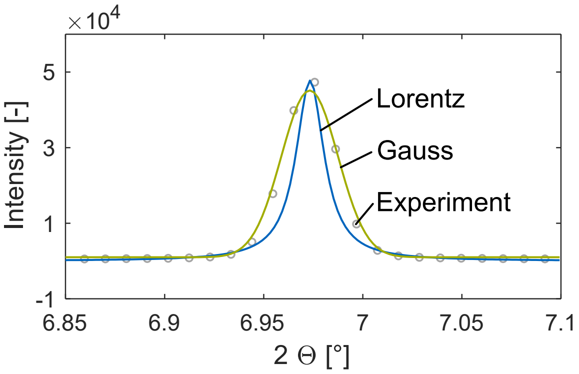

Figure 2.24: Comparison of Lorentz and Gauss fit function exemplary calculated for the (211) lattice plane of a single-phase ferrite steel (HC260Y).

In particular, two properties are valuable for the description of the microstructural behavior of a material. One is the relative change in peak position and the other in peak broadening. With the 2 Θ peak position, the lattice strain can be determined, which gives information about the deformation behavior of particular lattice planes. Peak broadening reflects besides the instrumental resolution physical effects such as crystal lattice defects, or distortions, microstrains, and grain size effects (Zhao and J. Zhang, 2008). The Gauss function describes the amount of distortion, respectively microstrain, while the Lorentz function describes grain size effects due to the different properties (Mittemeijer and Welzel, 2008). However, for a meaningful investigation of grain size effects, the grain size should be smaller than one micrometer (Pecharsky and Zavalij, 2003). In summary, peak broadening analysis can provide much information about material behavior.

2.8.4 Experimental State of the Art

Within this section, major studies in the field of experimental investigation of materials using in-situ diffraction tests are briefly summarized.

Tomota et al. (2003) investigated low carbon and ultra-low carbon steel by means of in-situ tensile tests with neutron diffraction. Beside the evaluation of lattice strains, also the dislocation density was determined and plotted against macroscopic values. This allowed investigating or comparing the onset of yielding for multiple lattice planes. The characteristic of grain-to-grain yielding could be confirmed, because the (200) lattice plane is elastically more compliant than the investigated (211) and (110) lattice planes and begins to plasticize at higher true stresses. In addition, the dislocation density curve for the two steels was compared and a larger increase with increasing plastic deformation was demonstrated for the ultra-low carbon steel. In this study, a comparable material was examined as in the present thesis. For this reason, the study of Tomota et al. (2003) can be used in same extent for verification purposes. However, no investigations were made into the unloading behavior. Measurement stops had to be acquired for neutron diffraction patterns, which can lead to different material behavior due to relaxation effects and the resolution of the results only allowed a rough tendency of the material behavior to be derived.

X. X. Zhang et al. (2021) and Zhong et al. (2015) both performed in-situ synchrotron diffraction experiments with aluminum alloys. They showed comprehensive evaluations of the diffraction profiles and Zhong et al. (2015) introduced a new method for thickness correction on peak broadening effects. Both evaluated the dislocation densities. X. X. Zhang et al. (2021) performed a cyclic tensile test and was able to show that the dislocation density decreases during unloading. This was explained by reverse strain or anelastic strain.

In van Petegem et al. (2016) and Upadhyay et al. (2019), stainless steel was investigated by neutron diffraction for a biaxial loading case. van Petegem et al. (2016) was able to show that lattice strains differ significantly depending on the load case by comparing results of uniaxial with biaxial tests. By observation of the peak broadening during load path changes, a recovery of the material was noticeable. Elastic dependencies, like the elastic unloading dependent on plastic deformation, were not part of the investigations.

Dual-phase steels have been investigated in in-situ diffraction tests. Woo et al. (2012) studied a DP980 steel with neutron diffraction experiments and introduced an evaluation of martensite and ferrite using the volume fractions of the phases. This approach provided the basis for the evaluation method used in this work. The in-situ analysis of DP steel in the study of Woo et al. (2012) was done to calibrate a crystal plasticity model. Elastic behavior was not addressed in their investigations.

Jia et al. (2009) investigated TRIP and DP980 steel. In-situ tensile tests with synchrotron diffraction were performed and the particular phases were evaluated separately for the (200) lattice plane. The results were used for the calibration of a crystal plasticity model. However, due to the significant anisotropic behavior of the (200) lattice plane, it is difficult to consider the results as generally valid for the microstructural behavior. Also, Tomota et al. (2004) investigated the impact of changes in the chemical composition in a TRIP steel by neutron diffraction. But in both studies, the elastic or anelastic behavior was not part of the investigation.

2.9 Conclusions

The state of the art shows that the specific elastic-plastic material behavior leads to difficulties in modeling, especially for widely used high strength steel grades. Classical material theories and parameters, e.g. the mechanical material parameters defined in the standards, are no longer sufficient. They do not reproduce the material behavior accurately enough. Studies have shown that temperature can be used to some extent for determining the onset of yielding, but the correlation between the temperature minimum and the onset of plastic yielding has not yet been validated. Furthermore, no defined determination approach was published. Most explanations for the material-specific characteristics are based on the microstructure. Section 2.8.4 shows that there are approaches to study the microstructural behavior experimentally. However, there are still no studies that focus on the elastic, anelastic and elastic-plastic characteristics described for the materials under consideration. Continuous in-situ cyclic tensile tests and tension-compression tests are missing for this kind of investigation. This type of experiment and its evaluation in terms of elastic material behavior is not found in the literature. Furthermore, there are not really studies on the correlation of microstructural and macroscopic material behavior. Section 2.8.4 shows that there are first approaches to evaluate the dual-phase martensitic-ferritic steel microstructurally. However, the resolution of the measurements and evaluations as well as the performed tests allow only limited conclusions on the elastic-plastic characteristics. Furthermore, for DP steel, phenomena such as early re-yielding or anelastic strain have not yet been investigated mircostructurally using continuous in-situ tests.

3 Objective and Approach

3.1 Challenge

Section 2.2 clearly shows that there are deviations between the theoretically assumed elastic-plastic behavior and that which occurs in reality. There is a certain gap between material theory and material science. Hence, accurate material characterization to provide a suitable database for modeling approaches is of great importance. The determination of the onset of yielding and elastic modulus, the strain dependency of elasticity or anelastic behavior, as well as the Bauschinger effect after changing the load direction make springback prediction a great challenge. In the material characterization according to standard, imprecise and especially unphysically defined limit values or circular references can be found in the determination of material parameters such as the equivalent yield strength and Young's modulus (Section 2.4). Consequently, the results are mostly significant dependent on the experience of the user and thus less robust. Classically defined parameters such as the Young's modulus are no longer sufficient to describe material behavior. This can lead to a situation where the precision of the material characterization is no longer sufficient to meet the increasing demands on the simulation.

The most plausible approaches to explain and describe elastic-plastic behavior have been summarized in Section 2. It is mainly explained by processes in the microstructure (Section 2.5.1), but only a limited number of studies can be found that experimentally investigate relationships between macroscopic and microstructural material behavior. This is a basic requirement for a better understanding of materials and thus for better modeling of increasingly complex materials. In-situ analysis in tensile tests, cyclic tensile tests and tension-compression tests are necessary to better understand the microstructural behavior and these experimental investigations are highly complex. They can only be carried out with great experimental effort and costly measurement technology. In addition, time-synchronous acquisition of microscopic and macroscopic data is of great importance so that correlations can be derived with high precision. However, it is not only on the experimental side that challenges arise. The mentioned elastic-plastic characteristics occur in particular in high-strength, dual-phase steels, whose importance for metal forming is steadily increasing. The dual-phase steel poses the difficulty of evaluating the martensite and ferrite phases separately due to their similar crystal structure.

Why is detailed knowledge of material behavior important? Improving the understanding of materials can start kind of a chain reaction in sheet metal forming. It makes it possible to develop and validate new characterization methods and to improve existing methods. A more precise and comprehensive material characterization in turn leads to the fact that existing modeling approaches can be extended and improved.

3.2 Research Objective and Approach

In this research study, elastic-plastic characteristics of industrial steel sheets are analyzed by advanced in-situ synchrotron diffraction experiments to examine material theoretical assumptions and specific phenomena on their material scientific basis. In this way, the aforementioned gap between materials theory and materials science is to be closed. This is done for a single-phase steel and a high-strength dual-phase steel. For this purpose, an experimental setup and procedure is developed that allows measuring the macroscopic load, strain and temperature simultaneously with microstructural parameters such as lattice strains, phase stresses and dislocation densities. The experiments enable a microstructural analysis of the materials in tensile tests, cyclic tensile tests and tension-compression tests. The elastic, anelastic and elastic-plastic behavior can be analyzed and conclusions about the macroscopic material behavior can be found. In particular, the evaluation of the specimen temperature with regard to extension possibilities in material characterization is one of the main points. An introduced evaluation method for dual-phase steel allows the separate evaluation of individual phases despite their crystallographic similarities. Thus, the physical fundamentals of the occurring elastic-plastic behavior can be analyzed comprehensively in order to create the basis to further improve the characterization and modeling of material behavior in the future.

As summarized in Section 2.4, the determination methods for elastic material parameters are not clearly defined and in some way dependent on each other. Equivalent parameters like the $YS_{0.2\%}$ were introduced, which were chosen more or less arbitrarily and have no physical background. Furthermore, there is a variety of determination methods for the elastic loading modulus and most of them are strongly dependent on the individual user. Especially the definition of lower and upper limits for the elastic range regarding elastic modulus determination poses a challenge. Here, a temperature-based determination method will be introduced for the determination of both, the onset of yielding and elastic loading modulus. It will be tested comprehensively on its experimental robustness, sensitivity and reproducibility. In addition, a microstructural validation of the physical basis of the method and its parameters will be given by in-situ diffraction experiments.

Section 2.5.1 lists the mechanisms responsible for the anelastic behavior. The conceivable reasons are related to the microstructural behavior of the material. An in-situ analysis of these correlations is the subject of this work and a targeted experimental procedure provides information on the material-specific characteristics addressed. The use of high-energy and brilliance synchrotron radiation allows transmission diffraction experiments and lattice strains, phase stresses as well as dislocation densities are determined. Correlations are derived with the relatively high in-situ diffraction measurement frequency (1 Hz) and time-synchronous measurement of the macroscopic material behavior. With the high resolution synchrotron measurements and additional SEM analyses, the phase-specific evaluation of martensite and ferrite is significantly improved in this work. The use of industrial steels in the form of sheets ensures the industrial importance of the study due to the need for accurate springback predictions.

3.3 Structure of the Research Study

A detailed overview of the approach taken in this study and the structure of this thesis is presented in the following. Chapter 2 discusses the basis for and the state of the art in the addressed research field. At the beginning, the principles of the material theory are discussed and it is shown how the actual material behavior deviates from it. This concerns the springback of steel materials and its prediction, which is why springback is introduced in a separate section. After explaining the principles of springback, the mentioned challenges for the description of elastic material behavior are discussed in detail. The state of the art in research is given for each elastic-plastic phenomena. Then, microstructural fundamentals and parameters used in the work are explained. Since the measurement of the specimen temperature and thus the thermoelastic effect plays an important role in this thesis, this effect is explained separately and its state of the art in research is reviewed and classified.

In Chapter 4, the basic mechanical and metallurgical properties of the considered materials are introduced. These are a single-phase and a high-strength dual-phase steel.

Chapter 5 summarizes the experimental methods used within this study. In general, it is about the measurement system and data processing. The basic test procedure for cyclic tensile tests and tension-compression tests is described. Finally, the idea of the developed experimental setups is transferred to a further setup that allows in-situ diffraction experiments in a particle accelerator.

The applied and partly newly developed evaluation approaches are described in Chapter 6. First, the evaluation of the thermoelastic effect is discussed. New determination methods for the onset of yielding and the elastic loading modulus are introduced. Afterwards, the methods for the evaluation of diffraction profiles are described, so that the determination of lattice strains and dislocations can be understood. Since the evaluation of the dual-phase steel is different from the single-phase material, the approach found is explained in a separate section.

All findings with regard to the investigated material behavior are reported in the results, Chapter 7. For better comprehensibility, the presentation of the results and their discussion have been combined in this chapter. Again, the first part deals with the results of the temperature measurement during the tensile tests and tension-compression tests. The main part of this thesis is the correlation of the microstructural results with the macroscopic material behavior described in Chapter 7.2. The chapter is divided into the addressed elastic-plastic characteristics of steel sheets.

Chapter 8 interprets the results of this study and their potential for modeling. For this purpose, a widely used hardening model is calibrated on the one hand with the temperature-based determined parameters and on the other hand conventionally according to the standard. The potential of the new approach is demonstrated in a one-element test. Furthermore, the phenomenon of material recovery and its effect on the elastic behavior is discussed.

Finally, this thesis ends with a summary and outlook (Chapter 9). Possible next steps are discussed to ensure continued improvement in experimental approaches and numerical simulation.

The structure of the research study is shown in Figure 3.1 for a better overview. The key scientific subjects in this work have been highlighted in blue.

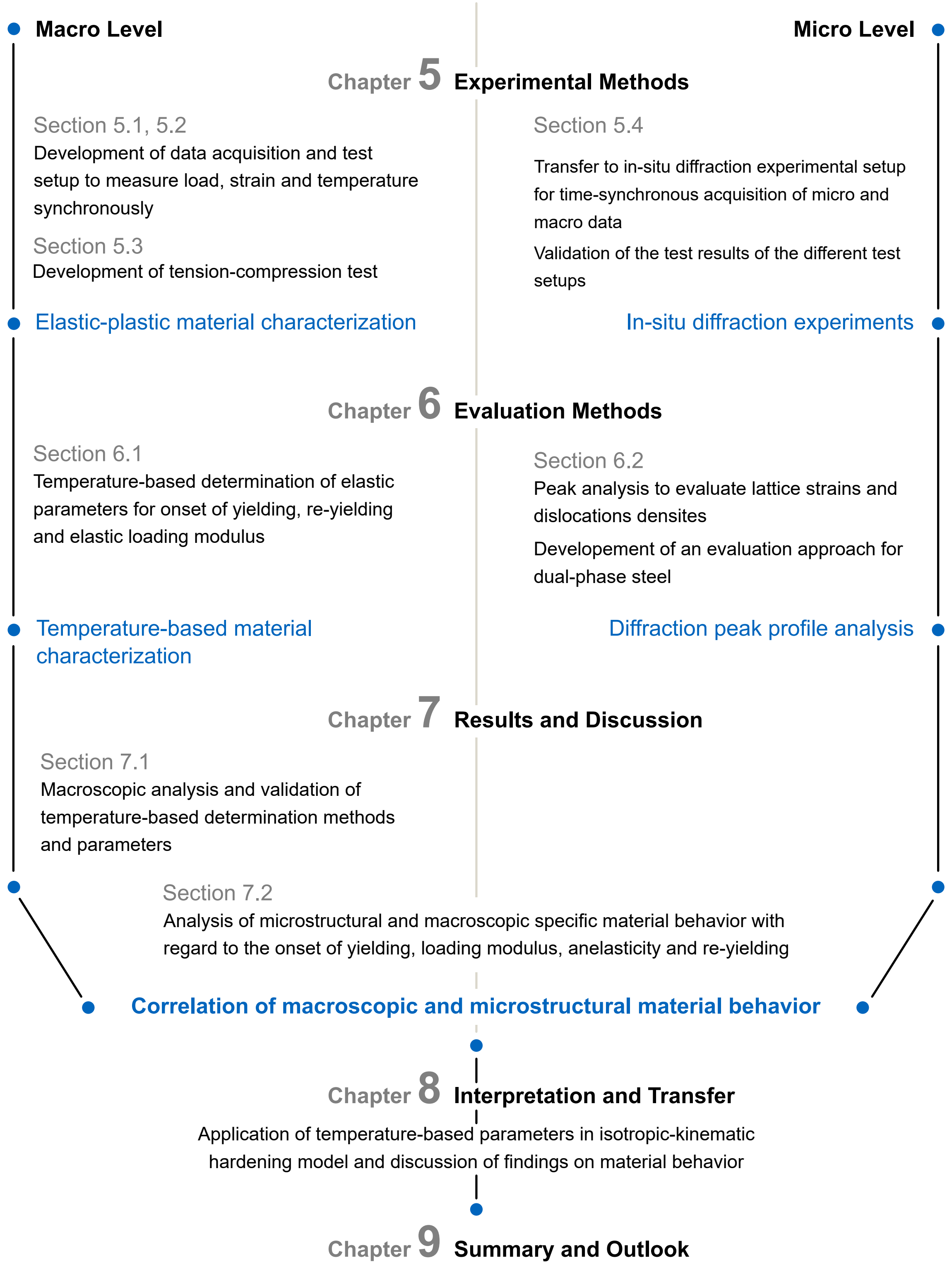

Figure 3.1: Structure of the research project. The particular chapters and sections are assigned to the macro or micro level with the key scientific subjects highlighted in blue.

4 Materials

This chapter summarizes the main metallographic, chemical and mechanical properties of the materials investigated. These are two different types of steel. It is a single-phase, purely ferritic steel (Section 4.1) and a dual-phase martensitic-ferritic steel (Section 4.2). All investigations in this study were carried out on sheet materials.

For metallurgical testing, samples were taken from the materials and embedded in a synthetic resin. Subsequently, the surface was polished in an iterative grinding process. The micrographs were taken with an relfected light microscope.
The shown chemical compositions of the materials are determined by an Optical Emission Spectrometer (OES). A prepared specimen of each material is tested at five different points and the evaluation takes place using iron-based calibration curves.

The basic mechanical properties in the the stress-strain curve were recorded in a tensile test machine (see Section 5.1) in accordance to DIN EN ISO 6892-1. The stress-strain plots shown in Sections 4.1 and 4.2 show the curve averaged from three experiments. Both, the measurement of the mechanical behavior in a quasi-static tensile test and the determination of the parameters were done according to DIN EN ISO 6892-1. For all tensile tests within this thesis, the specimen geometry form H 50 is used according to DIN 50125. Figure 4.1 shows the geometry used. The specimens were taken from the sheet with the long side in the rolling direction (RD) and the dog bone geometry was processed by milling. It should be noted that all tests in this thesis were carried out in the rolling direction.

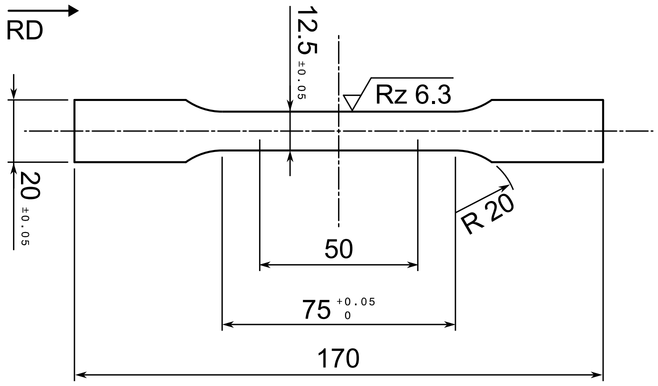

Figure 4.1: Technical drawing of the used specimen geometry. Lengths are given in millimeters.

4.1 Single-Phase Steel

A low carbon, interstitial free (IF) and purely ferritic *bcc* steel with a sheet thickness of 1 mm was investigated. It is called HC260Y according to DIN EN 10268 or CR240IF according to VDA 239-100. Within this thesis, the designation HC260Y is used. The properties of the material are briefly discussed in the following.

Interstitial free means that this material has only a low content of alloying elements such as carbon and nitrogen embedded in interstitial lattice positions, which enhances the dislocation movement and thus plastic deformation (Bode et al., 2000). The material is stabilized by titanium and niobium and the strength classes are produced by the addition of solid solution strengthening alloying elements (Stahl GmbH, 2018b). Despite the increased costs of processing, the material is widely used because of its insensitivity to aging (Bode et al., 2000). In addition, it exhibits good forming properties but with increased yield strengths compared to classical mild steels (Stahl GmbH, 2018b). Table 4.1 gives the chemical composition of the material used for this study. Figure 4.2 (a) shows the microstructure of this steel grade. The mean grain size is below 20 µm, which is significantly smaller than grain sizes of classical mild steels (e.g. DC06) and beneficial for the counting statistics of the diffraction experiments. In Figure 4.2 (b), the true stress versus true strain curve can be seen. The equivalent yield strength is 292 MPa and the tensile strength 425 MPa.

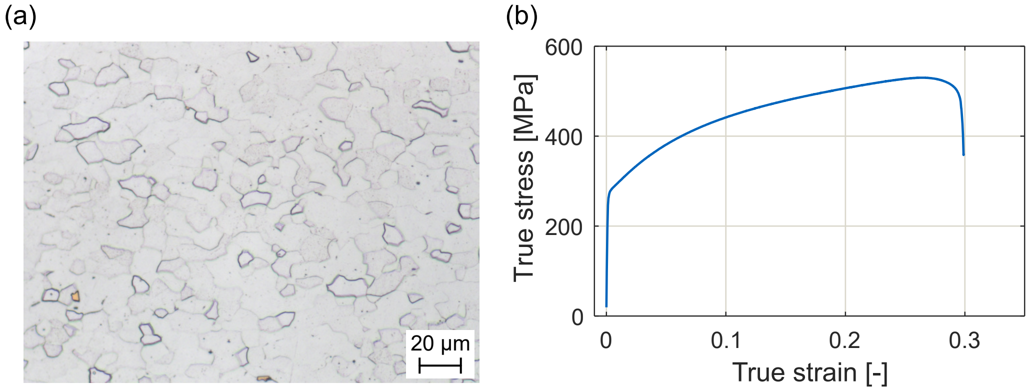

Figure 4.2: (a) Microstructure and (b) true stress versus true strain curve for HC260Y in RD.

Table 4.1: Chemical composition of HC260Y in [%] - mass fraction according to DIN EN 10268.

	C	Si	Mn	P	S	Al	Ti	Nb
HC260Y	0.004	0.123	0.770	0.063	0.007	0.046	0.046	0.030

4.2 Dual-Phase Steel

The mechanical properties of multiphase steels are mainly based on the properties of the phases present. This is unlike HC260Y, where the strength depends on inclusions and the solid solution. Due to a special procedure (heat treatment) during rolling of the material, austenite is accumulated, which is transformed into martensite during rapid cooling. To achieve this, a suitable ratio of about 80 % ferrite and 20 % austenite is required. During the transformation from austenite to martensite, there is an increase in volume. This deforms the surrounding ferrite. This leads to a particularly smooth elastic-plastic transition. (Berns and Theisen, 2008)

It has already been mentioned that this type of steel is getting more and more in focus of industry. This is due to the comparatively low yield strength with high tensile strength, hardening and elongation at fracture (Stahl GmbH, 2018a). The good strength-to-weight ratio qualifies this material in particular for crash-relevant components in the car body (kloeckner metals, 2021). There are several designations for the DP steel studied in this work. According to VDA 239-100, the designation is CR590Y980T. According to DIN EN 10338, the steel grade is called HCT980X. For simplicity, the material is designated DP1000 in this work. Table 4.2 summarizes the chemical composition of the material used. Figure 4.3 (a) reflects the micrograph of the microstructure. The material is fine-grained compared to HC260Y. The dark spots show the martensite, while lighter areas reflect the ferrite phase. The larger white areas are ferrite segregations. On average, this steel grade has a grain size of 2 µm (Liu et al., 2020). Figure 4.3 (b) shows the true stress versus true strain curve. The aforementioned soft transition from elastic to plastic deformation is clearly visible. Due to the high equivalent yield strength of approximately 700 MPa, a large elastic range occurs with this material. This property consequently leads to a large recovery, respectively springback strain. The tensile strength is 1047 MPa.

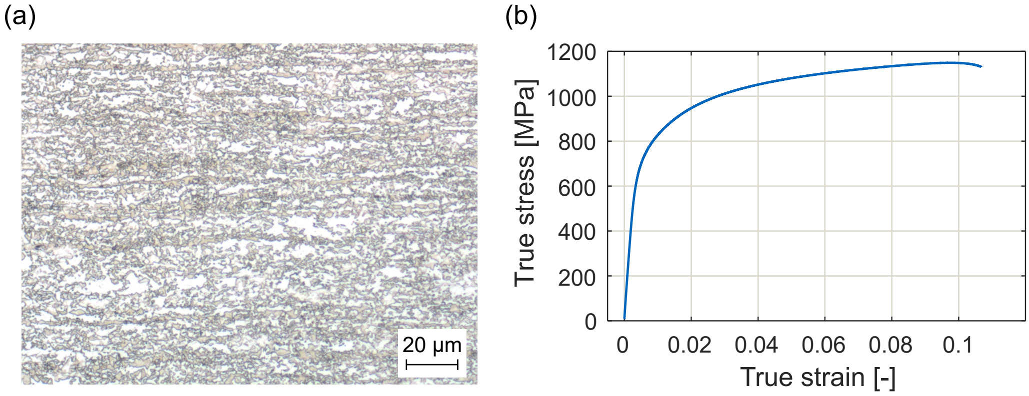

Figure 4.3: (a) Microstructure and (b) true stress versus true strain curve for DP1000 in RD.

Table 4.2: Chemical composition of DP1000 in [%] - mass fraction according to DIN EN 10338.

	C	Si	Mn	P	S	Al	Cr+Mo	Nb+Ti	V	B
DP1000	0.12	0.20	2.00	0.02	0.01	0.18	0.40	0.07	0.01	0.01

5 Experimental Methods

This chapter describes the experiments performed for this thesis. Besides comprehensive studies on a macro scale in cyclic tensile tests and tension-compression tests, synchrotron diffraction experiments were performed to investigate the material on a micro scale.

5.1 Measurement Systems and Data Acquisition

Regarding the experiments, two aspects are especially important for the analysis in this thesis. These are a highly accurate measurement of the signals and a suitable data processing, i.e. time-synchronous acquisition of the data. A comparison of the macroscopic behavior with processes in the microstructure in a continuous experiment is only meaningful if time-synchronous measurement of the parameters is ensured.

This work distinguishes between two different experimental setups. This is the experimental setup for macroscopic experiments (*utg* setup) and the experimental setup for the synchrotron diffraction experiments (*DESY* setup). Both setups allow for cyclic tensile and tension-compression testing. Table 5.1 gives an overview of the used experimental and measurement systems for the two different setups.

Table 5.1: Overview of experimental setups and measurement systems used.

Setup name	(a) utg	(b) DESY
Test machine	ZwickRoell (ZR) Z150	Self-developed test machine
Strain	LaserXtens (optical)	Strain gages (tactile)
Load	Load cell (max. 150 kN)	Load cell (max. 50 kN)
Temperature	PT1000 (Class B) applied with plastic clip	
Data acquisition system	QuantumX MX840B	
Data acquisition software	HBM Catman	

In setup (a), the universal test machine ZwickRoell Z150 is used. This corresponds with the latest standards in material testing and is characterized by high positioning accuracy of the crosshead. Due to a clearance-free mandrel, a reasonable measurement is also possible during load path changes. The built-in load cell measures up to a maximum load of 150 kN in both compression and tension. In setup (b), a self-developed test machine is used. This machine was developed especially for diffraction experiments and is characterized by its flexible application and small size (Hoelzel et al., 2013). The load cell used can measure up to 50 kN in tension and compression.

The ZR LaserXtens measures elongation via a laser speckle pattern and two markers that are tracked during the test. It is therefore an optical extensometer. This measuring system is permanently installed on the test machine (*utg* setup) and cannot be used in the *DESY* setup. For this reason, the strain is measured in the *DESY* setup using strain gages. Here the strain gages KYOWA KFGS-02-120-C1 for strains up to 8 % and KYOWA KFEM-05-120-C1 for strains up to 15 % are used. In Section 5.4, the experimental setup for the in-stu diffraction experiments is described in detail. To ensure that both experimental setups provide the same results, the entire test machine from *DESY* setup was installed in the ZR test machine. This made it possible to match the test machines and their strain measurement systems.

The specimen temperature was measured for both setups using a platinum resistance thermometer (PT) of the type Heraeus Nexensos M222 PT1000. This sensor has a measuring range of -70 °C to +500 °C and accuracy class B. The electrical resistance is at 1000 Ω and the temperature can be converted by means of a linearization table, since the electrical resistance of platinum to temperature is approximately linear (Bernhard, 2004). It is defined in the standard DIN EN 60751.

Figure 5.1 (a) shows the PT1000 sensor used for the experiments within this thesis graphically. The platinum base is 2.1×2.3 mm^2. The sensor can be connected to the data acquisition system via the solder pins. In Figure 5.1 (b), the plastic clamp used for the application of the PT1000 sensor on the tensile specimen can be seen. It is a commercially available clip.

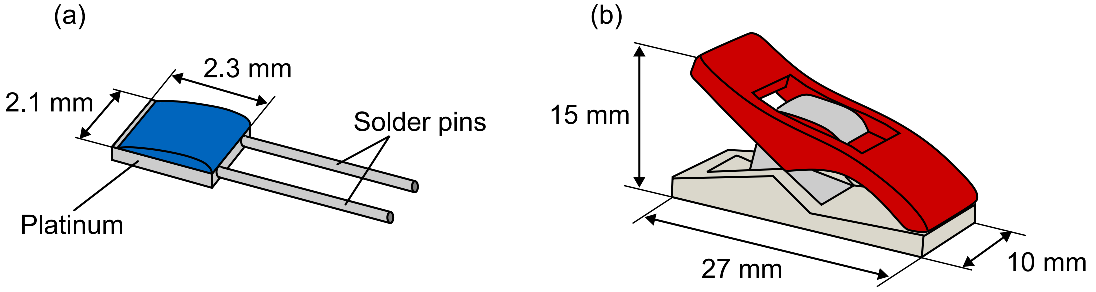

Figure 5.1: Graphical illustration of (a) PT1000 sensor and (b) commercially available plastic clip used for the application on the tensile specimen.

The universal measuring amplifier QuantumX MX840 from HBM was used for signal processing. This has an accuracy class of 0.05 % and a maximum measurement frequency of 40 kHz. The data was processed using HBM's Catman software. This software offers the possibility to convert the sensor signals into the desired unit. It has already been emphasized that time-synchronous measurement is essential for the study. For this reason, the load and strain were taken in the form of 0 ... 10 V signals directly from the machine and read into the measuring amplifier. In addition to the stress and strain, the specimen temperature was also recorded in the same way. With this approach, time delays caused by triggers, e.g. between the machine control and the data acquisition, are avoided.

Figure 5.2 shows an overview of the experimental setup and the data acquisition approach. The macroscopic parameters load, elongation and temperature were directly connected to the amplifier. In the *DESY* setup, the acquisition of the diffraction profiles was additionally synchronized with the data acquisition system.

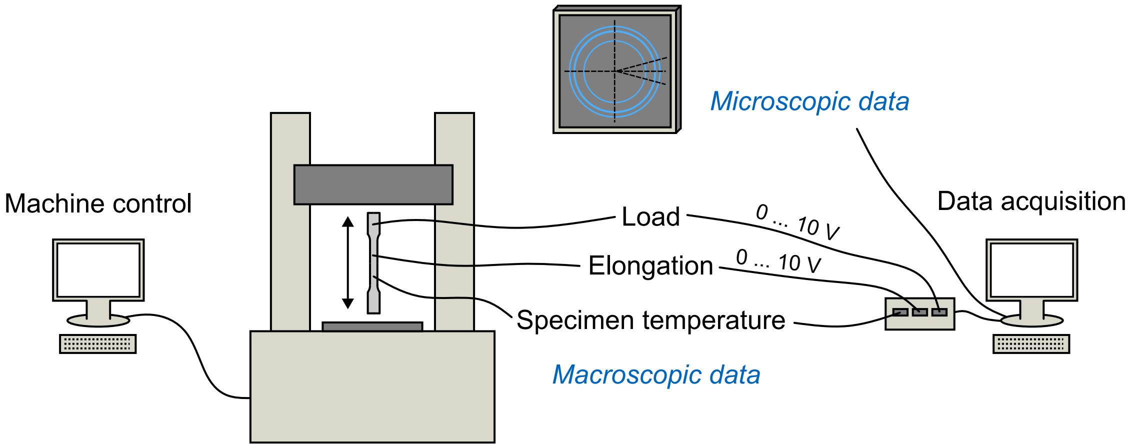

Figure 5.2: Overview of the data acquisition for both utg and DESY setup.

5.2 Cyclic Tensile Test

Cyclic tensile tests are suitable for investigating the plastic strain dependency of elastic material behavior due to multiple unloading-reloading cycles at increasing plastic strain. This is a variant of the classic tensile test in which the specimen is tensioned to certain elastic-plastic strains and then unloaded, usually to zero stress. Afterwards, the specimen is tensioned again to the next strain value. Thus, it is possible to analyze both the elastic unloading curve and the reloading curve as well as to assign the behavior to a true plastic strain value. Figure 5.3 exemplary shows the true stress versus true strain curve of a cyclic tensile test for DP1000. An unloading-reloading cycle was performed every 1.5 % engineering strain. Within this work, a distinction is made between initial loading, unloading and reloading (Figure 5.3 (b)).

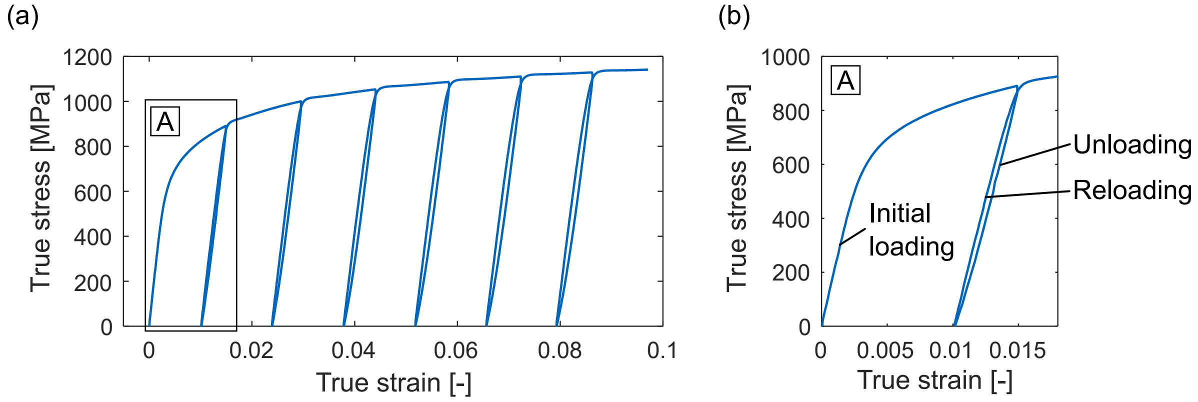

Figure 5.3: (a) True stress versus true strain curve of a cyclic tensile test for DP1000 and (b) enlarged view of area A with classification of curve sections.

Anelastic material behavior affects in particular the lower part of the unloading curve. The basic requirement for the investigation of this area is that the test setup, respectively the clamping of the specimen, is as stiff as possible. For this reason, wedge grips, which are usually used for clamping the specimens in tensile tests, are not suitable because they first tighten during the test. For the tests in this study, horizontally clamping specimen grips were developed (Figure 5.4). The clamping force is applied via four screws and positioning is ensured via guiding pins. Specially knurled and hardened clamping inserts ensure high friction between specimen grips and tensile specimen so that no slippage occurs. The grips can be used in both test setups.

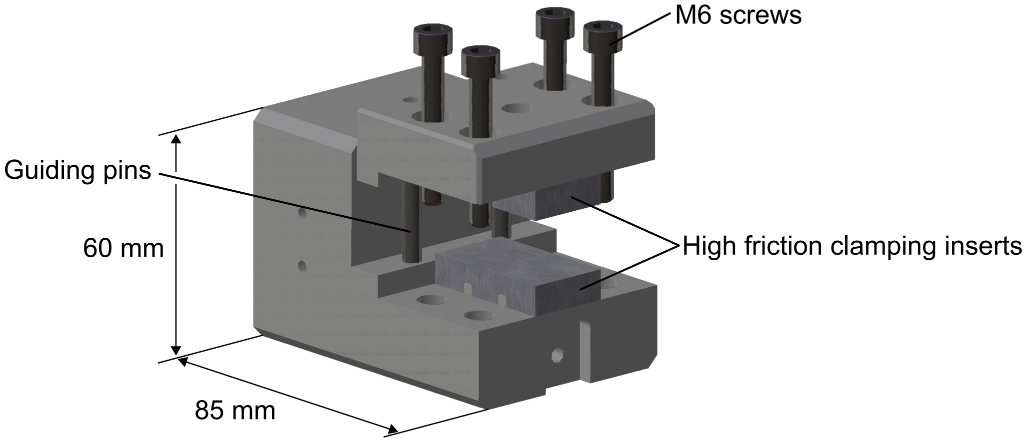

Figure 5.4: Horizontal clamping specimen grips, specially designed for cyclic tensile tests.

5.3 Tension-Compression Test

A variety of different experimental approaches for the investigation of the material behavior after load path change, respectively the Bauschinger effect, can be found in literature (Gau and Kinzel, 2001). Marciniak (1961) investigated the Bauschinger effect for copper using an in-plane torsion test, which was further developed by Tekkaya et al. (1982) and Yin et al. (2015). In Weinmann et al. (1988), pure bending tests were performed to characterize the Bauschinger effect. Miyauchi (1992) investigated the effect by means of a shear test named after him. A widely used approach is the uniaxial tension-compression test. This type of test has the disadvantage that the specimen tends to buckle in compression. Buckling can be prevented by adjusting the specimen geometry (Hetz and Merklein, 2019). For this, the gauge length is chosen small and the width of the measuring area is only slightly larger than the thickness of the sheet. Thus, the geometry is similar to a bar, which is more stable in terms of buckling. Another approach is to use a buckling support. Here, the specimen is supported perpendicular to the load axis by a suitable fixture (Kuwabara et al., 2009).

In the context of this work, a classical uniaxial tension-compression (TC) test will be used to investigate the Bauschinger effect, or the re-yielding behavior. This type of test was chosen because the results will be compared with the results of the cyclic tensile tests. The usage of the same specimen geometry (Figure 4.1) for both tests ensures good comparability. On the other hand, only a small amount of construction space is available, in particular for the in-situ tests. The requirements for the TC test setup can be summarized as follows:

- Use of specimen geometry Form H 50×12.5 according to DIN 50125
- It must be ensured that the specimen does not buckle during the test
- Can be installed in *utg* setup as well as *DESY* setup
- Possibility for optical strain measurement and simultaneous measurement of specimen temperature with PT1000 sensor in the *utg* setup
- Possibility of synchrotron transmission measurement and simultaneous strain measurement with a strain gage as well as temperature measurement with a PT1000 sensor in *DESY* setup

5.3.1 Test Setup

The following describes the test setup developed based on the requirements for the tension-compression tests in this study. The test setup for the tensile test (see Section 5.2) was extended so that compressive loading of the flat specimen is possible. Therefore, additional parts are necessary, which prevent the specimen from buckling. In literature, anti-buckling supports can be found, which are directly attached to the specimen (Cao et al., 2009) and approaches, which are combined with the specimen grips (Chang et al., 2020). One of the latter was presented by Kuwabara et al. (2009) and was the basis for the experimental setup developed in this study. This system is based on interlocking teeth, which allow elongation or compression of the specimen, but prevent buckling. Figure 5.5 shows the setup developed for the TC tests within this thesis.

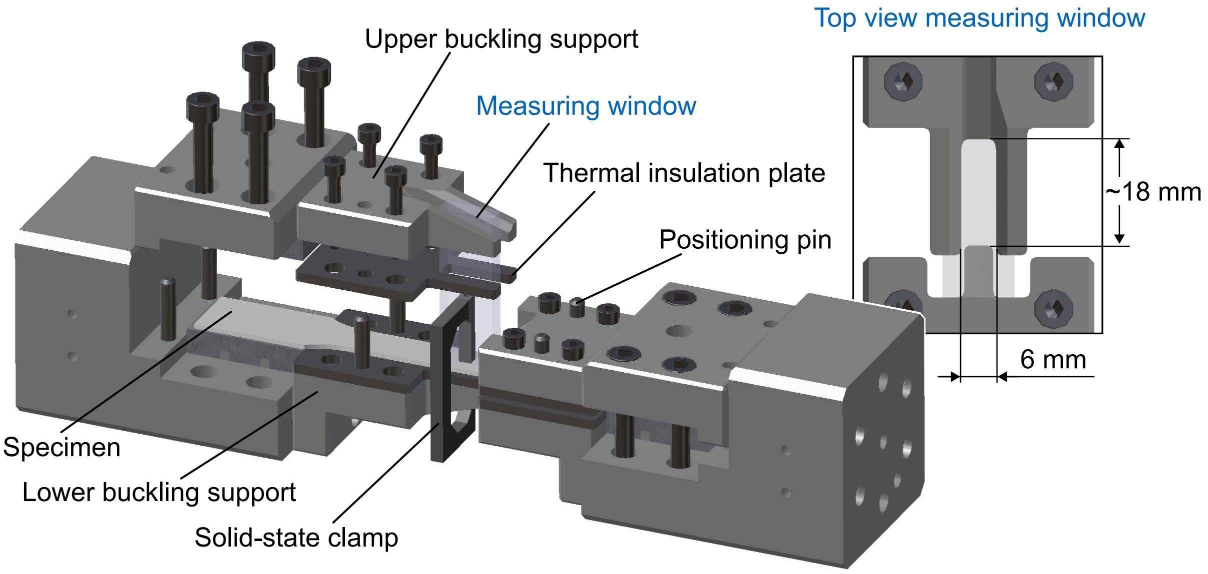

Figure 5.5: Specimen grips including anti-buckling support with thermal insulation plates for the TC test. Additionally, a top view of the measurement window is shown. PT1000 sensor can be applied via the solid state clamp in the measurement window.

The specimen grips of the standard tensile tests and cyclic tensile tests are used for clamping the specimens (see Figure 5.4). Buckling supports are mounted to these on both the lower and upper sides. Positioning pins ensure precise positioning during assembly. Interlocking teeth support the specimen perpendicular to the direction of loading. The supporting force can be adjusted via four screws and a torque wrench. A measuring window with a size of 18 × 6 mm^2 in the initial state enables the attachment respectively the use of measuring equipment. In the *DESY* setup, the strain gage KYOWA KFGS-02-120-C1 is applied in this. In the *utg* setup, an optical extensometer with a gauge length between 8 mm and 12 mm is used. Between the two optical markers, the PT1000 sensor is clamped onto the sample with a 3D printed solid state clamp (see Figure 5.5). In addition, thermal insulation plates with a thickness of 3 mm are inserted between the buckling support and the specimen in the *utg* setup for temperature measurement. These are intended to reduce influence on the temperature signal due to thermal conduction between the specimen and the steel anti-buckling supports. The insulation material (KV3) with a thermal conductivity coefficient of 0.25 W/mK and a maximum compressive strength at room temperature (RT) of 700 N/mm^2 was used (Brandenburger Isoliertechnik GmbH & Co. KG, 2022). In comparison, the thermal conductivity coefficient of steel is around 50 W/mK (A. Böge and W. Böge, 2021). The effects of the insulation plates and their necessity for temperature measurement in the TC tests are clarified in Section 7.1.4. To keep the friction between the specimen and the plates low, they were specially coated. Furthermore, a lanolin-containing lubricant is used to reduce friction between specimen and isolation plates in the *utg* and specimen and anti-buckling support in the *DESY* setup.

5.3.2 Test Procedure

A precise test procedure for the TC test is of particular importance due to the complicated installation of the specimen and attachment of the measurement equipment in the limited area of the measuring window. Possible influences due to buckling or friction must be excluded or precisely detected. In addition, it is challenging to obtain consistent results with two different experimental setups (*utg* and *DESY* setup), which is mandatory for the analysis within this thesis. The detailed procedure is described in the following.

1. Before the test, the milled edges of the specimen are deburred, as the burr could increase friction and the cross-sectional area of the specimen is measured.
2. The specimen is placed in the specimen grips, levelled vertically, and clamped. Therefore, 15 Nm are applied to each of the four clamping screws of the specimen grips.
3. In case of the *DESY* setup, the strain gage has to be applied so that it fits into the measuring window, when the specimen is mounted.
4. Lubricant is applied to the areas of the specimen that are in contact with the buckling support.
5. After clamping, the specimen is loaded to 100 N.

6. Now, the buckling support is attached and the four screws are each tightened with 0.4 Nm. These values are based on preliminary tests, which were compared with standard tensile tests without anti-buckling support on the one hand and examined for possible buckling on the other. Via a groove with a fit in the specimen grips and the positioning pins, the anti-buckling supports are aligned with each other.
7. In case of temperature measurement (*utg* setup), the PT1000 sensor is placed in the center of the measuring window with the solid state clamp.

Figure 5.6 shows a comparison of the true stress versus true strain curves of a TC test with the material HC260Y of the *utg* and the *DESY* setup. The curve of a standard tensile test was additionally plotted as a reference in order to investigate a possible influence of the buckling support on the stress-strain behavior. It has to be emphasized that two different test machines including load cells and two different strain measurement systems were used. The stress-strain curves for both the cyclic tests and the TC tests were obtained reproducibly without significant scatter.

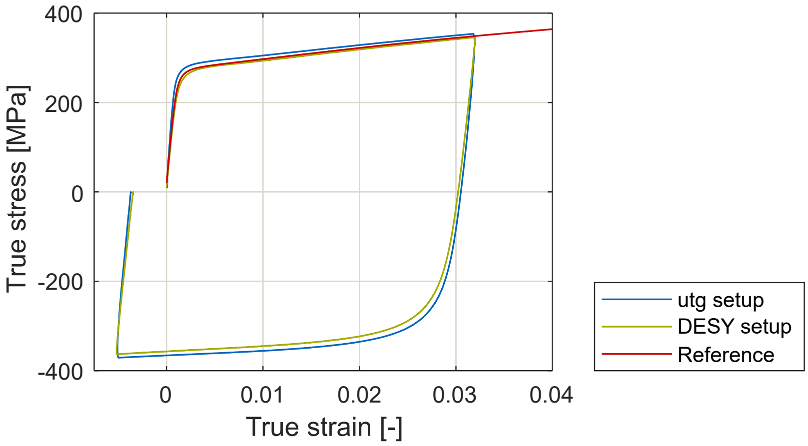

Figure 5.6: HC260Y - Comparison of the TC test with utg and DESY setup and with a reference stress-strain curve of a standard tensile test.

5.4 Synchrotron Diffraction Experiments

In the following, the synchrotron measurements at DESY are discussed in more detail. As already mentioned, a separate experimental setup was necessary for the measurements, which is referred to as the *DESY* setup.

Figure 5.7 shows the experimental setup for the in-situ tensile tests. The setup for the TC tests is analogous, except that the buckling support is mounted. The setup consists of the beam source, the detector and the tensile test machine, which was mounted on a xyz displacement stage.

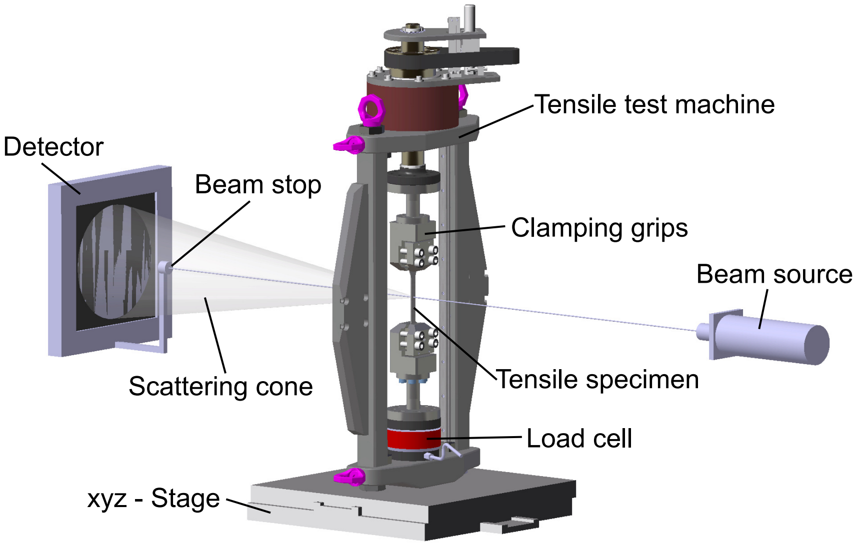

Figure 5.7: Tensile test setup of in-situ synchrotron diffraction experiments at HEMS (DESY, Hamburg).

The synchrotron beam comes tangentially out of the acceleration ring and was monochromatized by a single bounce monochromator. With a flat water-cooled Laue crystal Si (220), a wavelength of 0.14235 Å was achieved. The resulting beam had an initial cross section of 0.7×0.7 mm^2. Six Debye-Scherrer rings could be completely detected with the distance set to 1062 mm between the specimen and the detector. For a higher resolution study of the DP steel, the specimen to detector distance was increased to 1605 mm. With this setting, only three lattice planes could be imaged, but with better resolution and statistics. All specimen to detector distances were determined with Lanthanum Hexaboride (LaB_6) measurements. In addition, the beam was reduced to 0.5×0.5 mm^2 for DP1000 measurements. The detector used was a Perkin Elmer XRD flat panel with a resolution of 2048×2048 pixels. The pixel size was 200×200 µm^2. While measurement stops in the range of minutes were necessary for diffraction experiments with neutrons and a similar material (Vitzthum et al., 2017), synchrotron measurements take only a few seconds. The aim was to measure the sample temperature synchronously in order to compare it with the microstructural behavior. For this reason, a continuous tensile test was required, since a meaningful, simultaneous measurement of the thermoelastic effect would not have been possible with measurement stops. The highest possible measuring frequency of the detector of 1 Hz was set in order to manipulate the data as little as possible.

The tensile test machine was specially developed for diffraction experiments (Hoelzel et al., 2013). The specimen grips, PT1000 sensor, sensor application clamp and general data acquisition system used were the same as in the *utg* setup and an overview is given in Table 5.1. To measure the macroscopic strains, strain gages (KYOWA KFGS-02-120-C1) with a capacity of about 8 % engineering strain were used for the dual-phase steel, and special strain gages (KYOWA KFEM-05-120-C1) for high strains (up to around 15 %) were used for the single-phase steel. The strain gages were directly connected to the data acquisition system. In order to evaluate the thermoelastic effect for several elastic loadings and unloadings dependent on true plastic strain, mainly cyclic tests were performed, as described in Section 5.2. TC tests according to Section 5.3 were conducted for the microstructural investigation of the Bauschinger effect. Since the test setup did not allow defined strain values to be approached for the individual cycles, the first cycle was performed after 1.5 mm and all further cycles after 3 mm crosshead travel in each case. As strain rate, 1.5×10^{-4} s^{-1} was chosen, which is as low as possible to detect a high number of diffraction profiles during the experiment and at the same time high enough to measure the specimen temperature still reliably. In order to perform a locally accurate measurement, the xyz stage was moved in the opposite direction at half speed during the test. The diffraction profiles were recorded synchronously in time with the macroscopic data acquisition (see Section 5.1) using the instrument control. The temperature in the laboratory was kept constant at 20 °C by an air conditioning system.

6 Evaluation Methods

In this chapter, the evaluation methods used in this work are described in detail. As already shown in the big picture in Figure 3.1, a distinction is made between methods at the macro and micro level. At the macroscopic level, the temperature-based determination of parameters is presented. At the microscopic level, the approach to the determination of microscopic quantities based on diffraction data is explained. The dual-phase steel is dealt with separately in Section 6.2.4 due to the increased complexity in the evaluation.

Some of the evaluation methods are developed by the author such as the temperature-based determination of the onset of yielding and the elastic loading modulus. Some are based on already known approaches, such as the determination of the dislocation density according to Williamson and Hall (1953).

6.1 Temperature-based Determination Methods

The evaluation of temperature-based elasticity parameters using the thermoelastic effect is discussed in this section. While the thermoelastic effect has been known for a long time, the author has newly introduced evaluation methods for the onset of yielding and the elastic loading modulus. The basic parameter is the yield stress at temperature minimum, which is called YS_{Tmin} in the following. The parameter to describe the onset of plastic yielding is the yield stress at zero plastic strain, or YS_0. First, the hypothesis on which the evaluation methods are based is presented. Then, the determination of the onset of yielding and loading modulus will be discussed in detail.

6.1.1 Hypothesis

The thermoelastic effect has already been explained in detail in Section 2.6. It is an interaction of elastic cooling and plastic heating that leads to a characteristic minimum in the case of tensile loading. Now, to evaluate the plastic onset of yielding based on the temperature change, the relationship between the temperature and the elastic-plastic strain must be understood. For this purpose, a hypothesis was found.

Figure 6.1 shows the true stress versus true strain curve and the corresponding relative temperature versus true strain curve of a uniaxial tensile test for HC260Y. To better understand the relationship between temperature and the elastic-plastic transition, it is necessary to think about the state at temperature minimum (Tmin). This state has to be the balance between elastic cooling and plastic heating, like illustrated in Figure 6.1. This means that plastic yielding has already started before. In Section 2.6, it was already discussed that during pure elastic deformation, the temperature change is linear. Hence, the real onset of plastic yielding must be the deviation from linearity in the temperature signal.

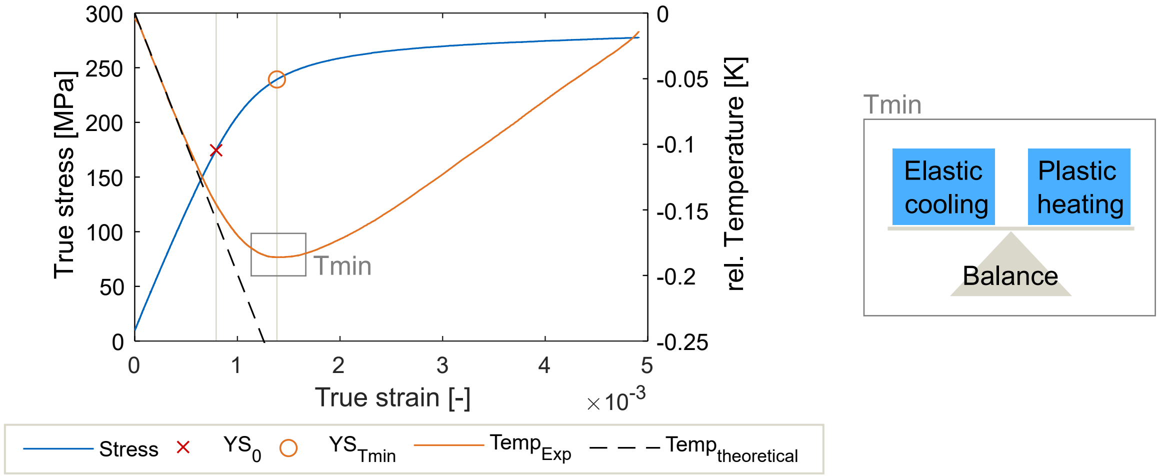

Figure 6.1: Stress-strain curve with relative temperature and theoretically calculated temperature for HC260Y. Parameters YS_0 and YS_{Tmin} are marked. The hypothesis on the relationship between Tmin and onset of yielding is shown. (strain rate 0.00015 s^{-1})

Figure 6.1 additionally shows the theoretical slope of the temperature decrease calculated with the linear thermoelastic Equation 2.12 in Section 2.6.2. For the material-specific parameters required for this purpose, literature values for steel were used. The thermal expansion coefficient α was set to $12 \cdot 10^{-6} \mathrm{K}^{-1}$ (Weißbach et al., 2015). The specific heat capacity C was assumed to be 481 J $\mathrm{kg}^{-1}\mathrm{K}^{-1}$ and the density of steel 7850 kg m^{-3} (Doege and Behrens, 2010). The initial temperature T_0 was set to 293.15 K, which corresponds to the room temperature. It can be seen that at the beginning of the deformation, the slope of the experimental temperature curve is similar to the theoretical one. Equation 2.12 is only valid for linear elastic behavior. Accordingly, heating due to plastic deformation cannot be reproduced. Thus, if the experimental and theoretical curves differ, it can be assumed that plasticity sets in. The comparison of the experimental and theoretical curves confirms that plastic deformation is already present before Tmin. Furthermore, the initially similar slopes of the experimental and theoretical temperature curve suggest that thermal convection and conduction are negligible for the experiment shown.

In summary, this means that during purely elastic deformation, the temperature decreases linearly until the onset of plastic deformation causes the linearity to be lost, since it leads to heating. The influence of the temperature by plastic deformation could be shown by comparison with the theoretically calculated temperature. In Tmin the elastic cooling and plastic heating are around equilibrium and after that the plastic deformation is predominant and thus the specimen heats up again. Therefore, if one wants to define the onset of yielding via the temperature signal, one has to determine the time of the end of the linear temperature behavior.

6.1.2 Onset of Yielding

Figure 6.2 (a) shows exemplarily the true stress versus time and relative temperature versus time curves for HC260Y. Plotted are the initial loading and one unloading-reloading cycle of a uniaxial tensile test. The parameter YS_{Tmin} is the stress value at the time of Tmin and can accordingly be determined directly without additional evaluations. It can be seen that the parameter YS_{Tmin} is in the transition range between the initial elastic slope and the slope in the elastic-plastic range. This indicates that plastic deformation already occurs before Tmin as hypothetically assumed.

The temperature signal is approximately linear during elastic loading (*el*), elastic-plastic deformation (*pl*) and elastic unloading (*eul*) (see Figure 6.2 (a)). Only the slopes of the signal for these conditions are different. For the test shown in Figure 6.2, the temperature behavior in the individual conditions *el*, *pl* and *eul* can be clearly distinguished. The initial decrease and the minimum can be seen, as well as a slope change between elastic-plastic deformation and elastic unloading. The first derivative or gradient of the signal is suitable for the determination of these slope changes. Linear behavior means constant slope and thus a horizontal line in the first derivative. Figure 6.2 (b) shows the temperature gradient curve to the temperature curve in (a). The approach of finite differences was used for the derivation in order to manipulate the data signal as little as possible and smoothing was omitted to avoid errors. The temperature gradient $\dot{T}$ was calculated by

$$\dot{T}_j = \frac{T_{j+1} - T_{j-1}}{t_{j+1} - t_{j-1}} \quad , \tag{6.1}$$

with the temperature T and the time t. Small fluctuations in the temperature signal lead to a more significant noise in the temperature gradient, which can be seen in Figure 6.2 (b). However, since the corresponding data ranges are fitted with linear regression lines (comparable with a low pass filter), an influence of the noise is negligible.

As described in Section 6.1.1, it is assumed that the first deviation from linear behavior occurs due to the onset of plastic deformation and this point in time is to be determined by means of an evaluation method. For this purpose, a time-dependent evaluation method according to Volk and Hora (2011) is used. The idea behind this is that the change in slope is determined by means of two regression lines. Their intersection point, respectively an angle bisector on the data signal is then assumed as beginning of the slope change.

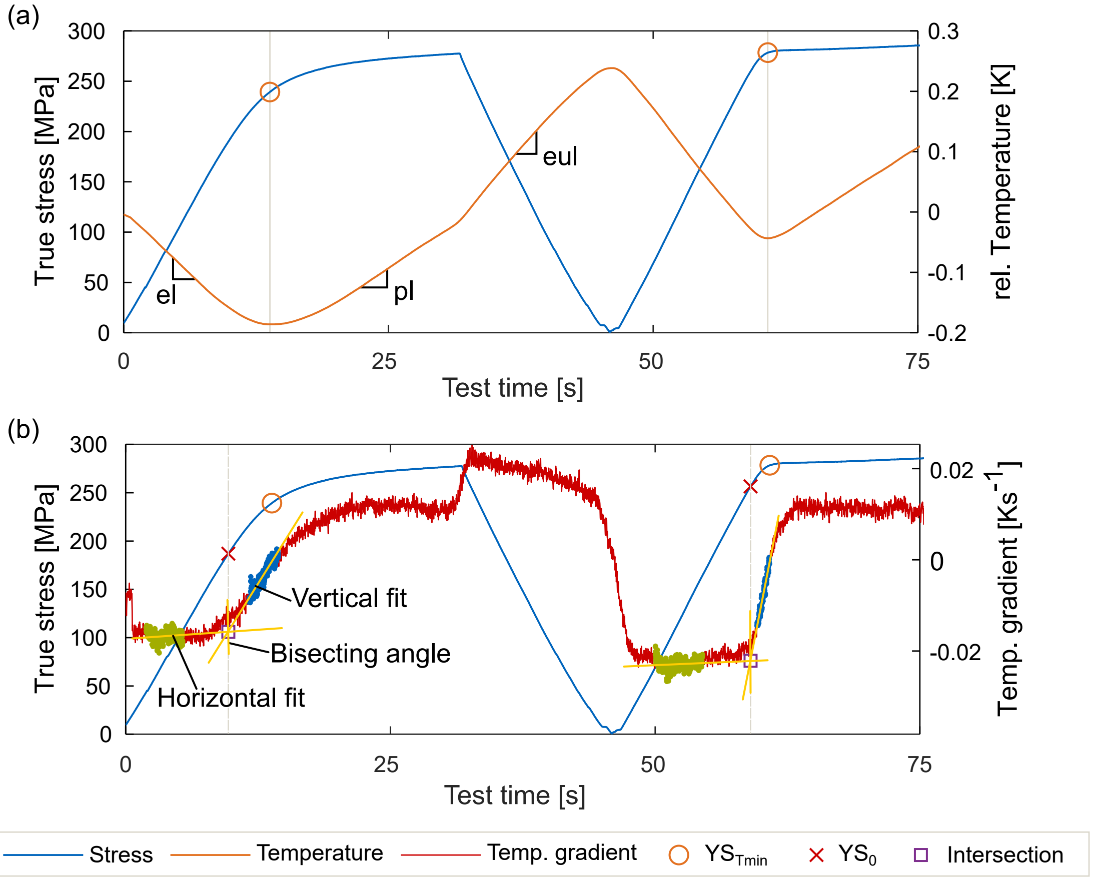

Figure 6.2: HC260Y - (a) True stress versus time and relative temperature versus time curves with Tmin and YS_{Tmin}. (b) True stress versus time and temperature gradient versus time curve. The linear regression lines for the determination of YS_0 are marked.

In Figure 6.2 (b), the horizontal and vertical linear regression lines are plotted. They are determined on basis of the green (horizontal) and blue datapoints (vertical). The evaluation method is developed in such a way that the size of these datapoint ranges depend on the respective measurement frequency of the test and can be adjusted by the user if necessary. The datapoints are then shifted through the temperature gradient data curve using a step size, which also depends on the measurement frequency of the experiment. For each step, the slope and the goodness of fit are calculated. To determine the intersection point, the regression line with the largest slope for the vertical fit and the one with the smallest slope for the horizontal fit are selected. The sensitivity of this evaluation is further discussed in Section 7.1.2. After the intersection point is found, an angle bisector is calculated on the data signal and the time point for the yield stress at zero plastic strain YS_0 in the stress curve is determined.

6.1.3 Elastic Loading Modulus

Various approaches for the determination of the loading modulus have already been discussed in Section 2.4.2. A distinction was made between limits, fitting and deformation work approaches. Now, based on the method in Section 6.1.2, a temperature-based approach is explained that can be assigned to both limits and fitting approaches. Most of the methods described have in common that no upper limit for purely elastic behavior can be defined for a continuous elastic-plastic transition. With the temperature-based method, it is now possible to determine this value with YS_0. Using this parameter as an upper limit, the entire purely elastic range is used for the determination of the loading modulus. Thus, the method has a physical and material-specific background. In order to avoid possible experimental errors in the evaluation, the value of 5 % of TS is defined as the lower limit according to Sonne (1999). A linear regression is formed with the datapoints between the lower limit and YS_0. Its slope represents the temperature-based determined loading modulus E_{YS0}. Figure 6.3 shows this determination exemplarily for a cyclic tensile test with HC260Y.

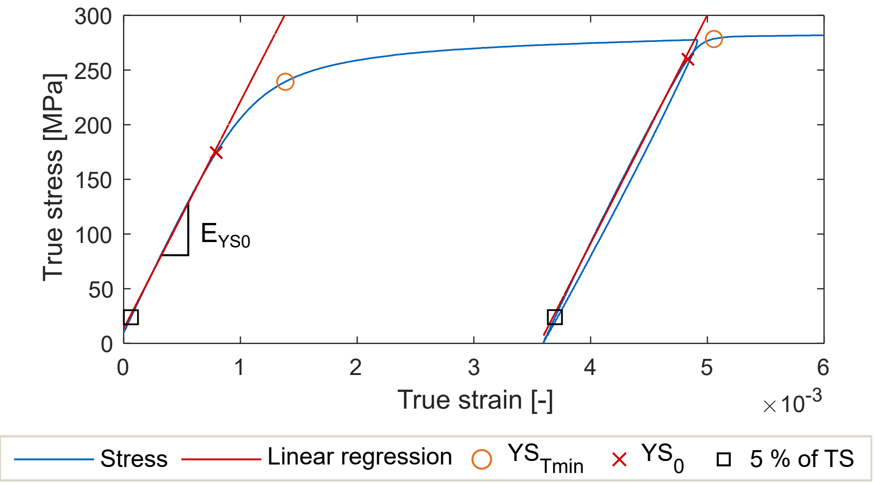

Figure 6.3: HC260Y - Example of the temperature-based determination of E_{YS0} for the initial and first reloading in a cyclic tensile test.

6.2 Microscopic Evaluation Methods

In the following, the evaluation procedure of the diffraction profiles detected in the synchrotron experiments (Section 5.4) is described specifically in context with this study. The principles for the evaluation of Debye-Scherrer rings and the corresponding peak profiles were described in Section 2.8. With the chosen settings, the measurement system provides full Debye-Scherrer rings for five lattice planes for the single-phase HC260Y and three lattice planes for the dual-phase DP1000. The evaluation of DP1000 differs from that of HC260Y. For this reason, it is discussed separately in Section 6.2.4.

6.2.1 General Profile Analysis

The relevant peak information, the center position, integral peak intensity, maximum peak intensity, the background and the shape are extracted from the Debye-Scherrer rings. Figure 6.4 shows this procedure schematically. First, the Debye-Scherrer rings are detected from the synchrotron transmission measurements. Then, the intensity of sectors with a specific angular range (±10°) of the Debye-Scherrer rings is integrated up longitudinally (blue) and transversely (green) to the loading direction with the profile analysis software Fit2d (see Figure 6.4) (Hammersley, 1997). This means that the individual Debye-Scherrer rings are radially summed up. The intensity is equivalent to the counts of detected radiation dependent on the $2\ \Theta$ angle. This results in one dimensional diffraction profiles. The same angular range was used for all evaluations in this study. To increase counting statistics for precise evaluation of the dual-phase material, the lower sector (shown blue dotted in Figure 6.4 in the schematic detector image) was summed with the upper longitudinal sector. A diffraction profile is obtained for each individual measurement and the particular peaks can be evaluated for the corresponding $2\ \Theta$ range, respectively (hkl) lattice planes.

Figure 6.4 shows the diffraction profile for the upper longitudinal sector for HC260Y. Five peaks are visible in the profile. These can be assigned to the lattice planes on basis of a powder diffraction table. The lattice plane (110) shows the highest intensity. In contrast, the lattice plane (200) shows the lowest intensity, but zoom A in the figure shows that this peak is still well defined and can be evaluated. For this material, the five lattice planes shown were evaluated. Due to the larger specimen to detector distance, only the lattice planes (110), (200) and (211) could be evaluated for DP1000.

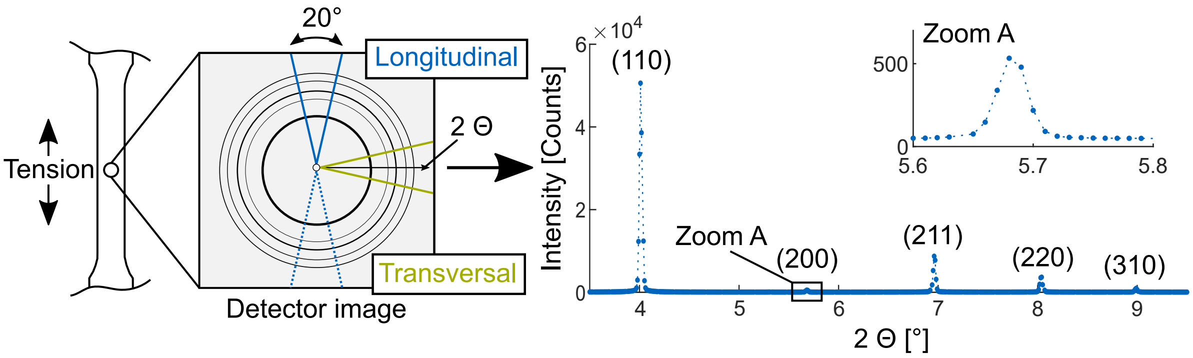

Figure 6.4: General procedure for the evaluation of Debye-Scherrer rings and diffraction profile for HC260Y.

It has already been described in Section 2.8.3 that microstrains in the form of distortions, respectively dislocations can be evaluated by comparing the peak width of individual Gauss peak fits. Both the HC260Y and the fine-grained DP1000 have grain sizes >1 µm. For this reason, an evaluation of additional grain size effects by means of a Lorentz function is not reasonable (Pecharsky and Zavalij, 2003). Hence, all peak fits within this study are performed with a Gauss function. In Figure 2.24, a Gauss fit function was compared with a Lorentz one for HC260Y. Besides the reasons already mentioned for choosing a Gauss fit, it was shown that the Gauss functions fits the experimental results better than a pure Lorentz function. Several peaks were evaluated using a Pseudo-Voigt function to check again whether the application of the Gaussian function is permissible. The Pseudo-Voigt curve is the additive mean of Gauss and Lorentz. Hence, if it is similar to the Gauss curve, it shows that the Lorentz component is negligible. Figure 6.5 (a) shows a comparison of a Gauss and a Pseudo-Voigt fit for HC260Y and the lattice plane (211). The fit functions are almost identical. The lower part of the peak shape and the width of the peak are fitted equally well with both functions. There are no differences in the values for FWHM and the center position, only the intensity maximum differs slightly. These findings were analogous for the other lattice planes. Accordingly, the use of the Gaussian fit is assumed to be adequate. Finally, the Gauss function was chosen because it is suitable for the planned evaluation with the considered materials and thus there is no need to use the more complicated Pseudo-Voigt function. In this way, the number of fit parameters can be kept low.

Figure 6.5 (b) shows the comparison of the peak in the initial state at 0 MPa and after the 6th loading cycle, at around 12 % true plastic strain, also at 0 MPa. The experimentally measured points and their Gauss fit functions are plotted. For better comparability, the intensity was normalized and the respective center positions aligned in their 2 Θ range. It can be seen that the reflection increases in width with increasing plastic strain. Furthermore, the Gaussian function fits the experimental points well, also at higher plastic strains.

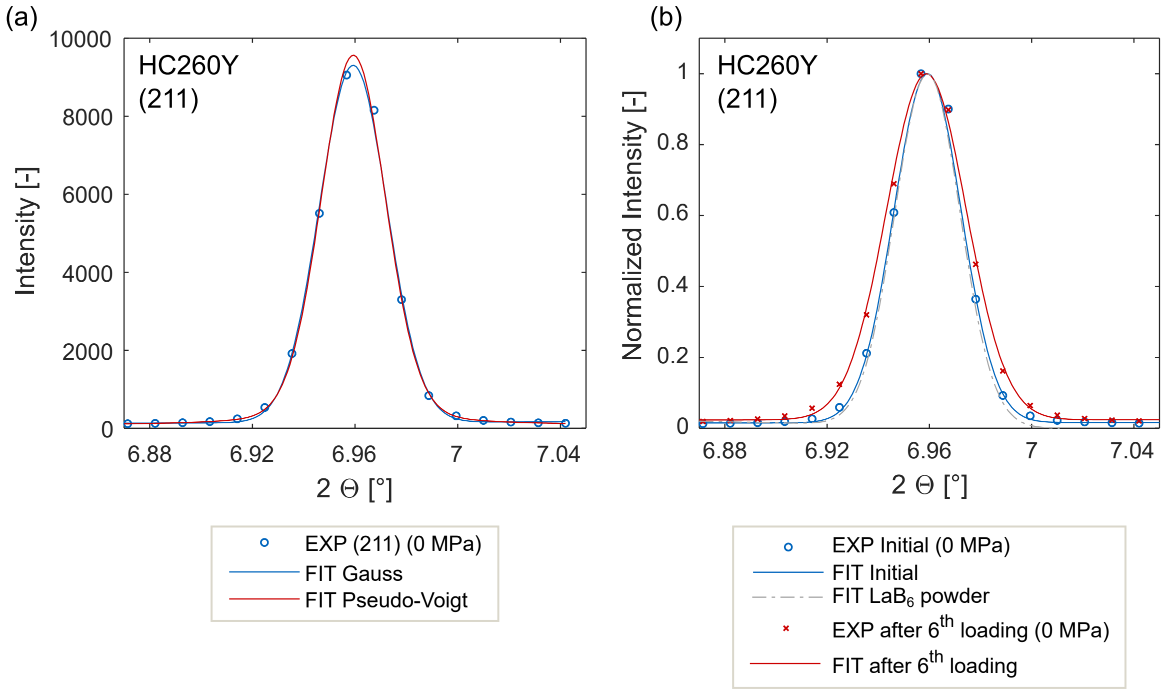

Figure 6.5: (a) Comparison of the fit results of a Gauss and Pseudo-Voigt function. (b) Comparison of the Gauss fit for the initial state and after the 6th loading cycle. Additionally, the fit for the LaB$_6$ reflection is shown. Intensities were normalized and the peaks were adjusted in their 2 Θ value.

For specific evaluations of the peak shape, e.g. integral breadth methods (see Section 6.2.3), it is necessary to correct the peak shape for the instrumental resolution. For this purpose, lanthanum hexoboride (LaB$_6$) samples with approximately the same thickness as the specimens are measured using the same experimental setup and test conditions. The LaB$_6$ material used is a reference material certified by the National Institute of Standards and Technology (NIST). It is specifically made for the investigation of instrumental aspects of diffraction experiments (Black et al., 2020). The material is prepared to show minimal peak broadening. Therefore, the measured peak broadening of this reference material can be assigned to the instrumental contribution to the detected peak profiles. By knowing the 2 Θ peak positions of the LaB$_6$, the diffractometers can be calibrated. For example, it is possible to determine the specimen to detector distance. (Black et al., 2020)

In Figure 6.5 (b), the corresponding LaB$_6$ reflection is shown. The LaB$_6$ peak closest to the respective peak of the material in the 2 Θ range is used. There is hardly any difference between the initial reflection and the instrumental resolution. This also indicates that grain size effects have no influence on this material and these measurements. For the calculation of the dislocation densities, the instrumental resolution is subtracted from the respective peak area.

6.2.2 Elastic Lattice Strains and Diffraction Elastic Constants

Elastic lattice strain is based on the change in atomic lattice spacing d_{hkl} due to macroscopic and possibly microscopic stresses. The atomic lattice spacing d_{hkl} can be calculated by the peak center position and the wavelength using Bragg's law (see Equation 2.14). If the measured atomic lattice spacing d_{hkl} is now set in relation to the initial atomic lattice spacing d^0_{hkl} of the macroscopic stress-free state, an elastic lattice strain $\varepsilon_{\mathrm{hkl}}$ can be calculated for that specific lattice plane (Agnew et al., 2013).

$$\varepsilon_{\mathrm{hkl}} = \frac{d_{\mathrm{hkl}} - d^0_{\mathrm{hkl}}}{d^0_{\mathrm{hkl}}} \tag{6.2}$$

Only those lattice planes whose orientation fulfills the criteria of Bragg reflection contribute to the measured reflection. Accordingly, the lattice strain $\varepsilon_{\mathrm{hkl}}$ represents the average strain of these particularly oriented lattice planes (Dye et al., 2001). The determination of the lattice plane specific DEC_{hkl} is similar to the determination of the macroscopic loading modulus. It is defined by the slope of the macroscopic stress versus the lattice strain. Here, the stress value YS_0 is used as an upper limit as described in Section 6.1.3. Thus, good comparability with the macroscopic E_{YS0} is given. For the DEC_{hkl}, the following relationship results with the macroscopic true stress σ and the lattice strain $\varepsilon_{\mathrm{hkl}}$

$$DEC_{\mathrm{hkl}} = \frac{\sigma}{\varepsilon_{\mathrm{hkl}}} \quad . \tag{6.3}$$

6.2.3 Dislocation Densities

In addition to the elastic lattice strain, further information about the microstructural material behavior is obtained from the peak broadening. The peak broadening can be evaluated with the full width at half maximum (FWHM) or the integral breadth (IB) (Spieß et al., 2019). IB methods are suitable for a qualitative analysis of the peak broadening and are therefore often used for analysis (Klug and Alexander, 1976). Especially, if tendencies in the material behavior are to be analyzed on a microscopic scale, these methods are appropriate (Scardi et al., 2004).

Based on the IB, the dislocation density can be estimated using the classical Williamson-Hall plot (WH-plot) (Williamson and Hall, 1953) and the Williamson-Smallman model (Williamson and Smallman, 1956). This procedure is described in the following.

The dislocation behavior is attributed to intergranular microstrain (Bindu and Thomas, 2014). Using a Gaussian fit, the relationship of the integral breadth β is as follows

$$\beta_{\mathrm{exp}}^2 - \beta_{\mathrm{inst}}^2 = \beta_{\mathrm{size}}^2 + \beta_{\mathrm{strain}}^2 \quad , \tag{6.4}$$

where β_{exp} is the experimental observed IB, β_{inst} the instrumental resolution, β_{size} the IB caused by size effects and β_{strain} due to microstrains. For the correction of the IB by the instrumental resolution, the measurement of LaB_6 is used as described in Section 6.2.1. For simplicity, the corrected experimental IB by the instrumental resolution is called β in the following. With the assumption that the crystallite size does not change and is therefore an independent quantity, Williamson and Hall (1953) showed an approach that expresses IB in terms of a linear equation, equal to $y = ax + t$, where the slope a is related to the microstrain and the intercept t to size-effects. Adapted to a pure Gaussian function (squared) (Bindu and Thomas, 2014), this linear equation can be written as follows in the reciprocal space

$$\left(\beta^*\right)^2 = \left(2 \cdot e \cdot d^*\right)^2 + \left(\frac{1}{D}\right)^2 \quad . \tag{6.5}$$

There, e represents the microstrain and d^* the $2\,\Theta$ range. To apply this equation to experimental data, it has to be transferred to real space with the following relations $\beta^* = \beta cos(\Theta) \cdot \lambda^{-1}$ and $d^* = 2 \cdot sin(\Theta) \cdot \lambda^{-1}$ (Williamson and Hall, 1953). Furthermore, the root mean square microstrain (RMS) $\langle \varepsilon^2 \rangle^{1/2}$, which is necessary for the calculation of the dislocation density later, can be determined by the relation $\langle \varepsilon^2 \rangle^{1/2} = (2\pi)^{1/2} \cdot e$ (Mittemeijer and Welzel, 2008). Here, $\langle \varepsilon^2 \rangle$ reflects the intergranular microstrain, which is based on the peak broadening. By substituting and solving, one arrives at the following equation for the real space

$$(\beta \cdot cos(\Theta))^2 = 8\pi \cdot \langle \varepsilon^2 \rangle \cdot (sin(\Theta))^2 + \frac{\lambda^2}{D^2} \quad , \tag{6.6}$$

where Θ is the Bragg angle, λ the wave length and D a value for the crystallite size. By plotting $(\beta \cdot cos(\Theta))^2$ versus $(sin(\Theta))^2$ of each diffraction pattern for at least two lattice planes of different orders, the RMS can be determined by the slope of the linear regression through these values (see yellow lines in Figure 6.6 (a)). With the intercept, the crystallite size D can be evaluated for small particles in the nanometer range (Pecharsky and Zavalij, 2003). If the linear regression curves pass through the origin or are close to the origin, i.e. the intercept is close to zero, it can be assumed that peak broadening is only due to intergranular microstrain (Christien et al., 2015).

Figure 6.6 (a) shows the WH-plot obtained with the procedure described for the lattice planes (110), (211), (220) and (310) of HC260Y. In principle, the calculation is performed for each individual diffractogram, but for better illustration, only seven strain states were plotted in Figure 6.6 (a). The strain states plotted are shown in (b) in the true stress versus true strain curve. The individual values for the lattice planes do not give exactly a linear relation. This is due to microstructural anisotropy. Furthermore, it can be seen that the anisotropy also increases with increasing plastic strains, because the deviations from the linear regression curve become more pronounced. In summary, the linear regression lines pass approximately through the origin. This indicates that the peak broadening is predominantly due to microstrain rather than grain size effects (Christien et al., 2015). This was already expected due to the grain sizes, which are larger than one micrometer and the shape of the Bragg peaks.

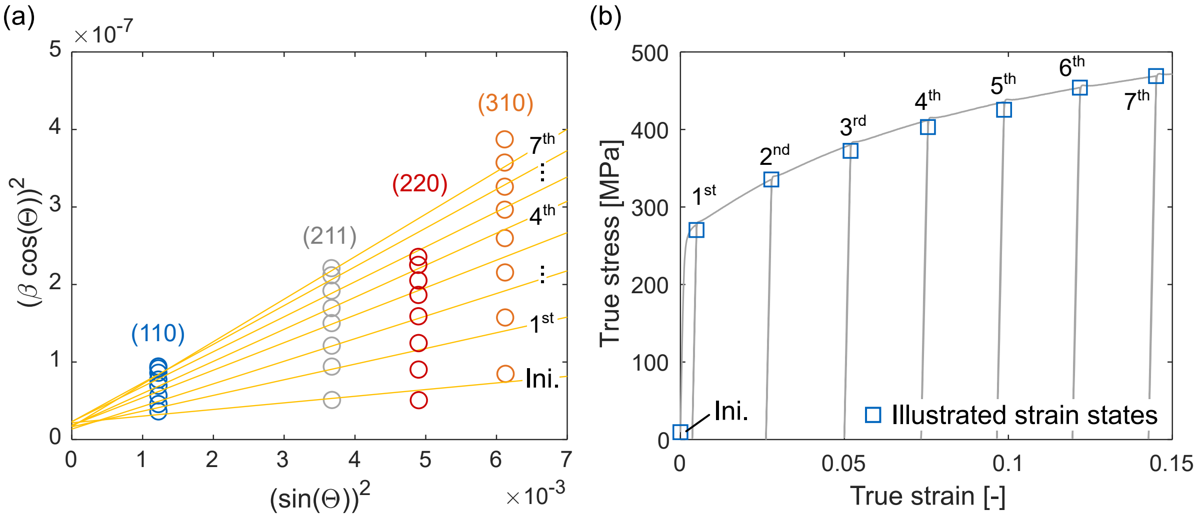

Figure 6.6: HC260Y - (a) Williamson-Hall plot for four lattice planes. Illustrated are the initial state and the seven strain states before unloading shown in (b).

The model according to Williamson and Smallman (1956) can now be used to estimate the dislocation density ρ_{avg} as a function of microstrain $\langle \varepsilon^2 \rangle$ with

$$\rho_{avg} = \frac{K \cdot \langle \varepsilon^2 \rangle}{D \cdot b^2} \quad . \tag{6.7}$$

In this equation, K is a constant and can be substituted with 6π for *bcc* materials (Williamson and Smallman, 1956). The Burgers vector b is calculated from the lattice constant and the slip direction of the lattice system. Here for a *bcc* material, the direction $\langle 111 \rangle$ is used. The parameter D reflects the coherent domain size, but as mentioned, size-effects are negligible. In this study, the relative behavior of the dislocation density as a function of plastic strain is investigated. Hence, the simplest way of calculating the dislocation density is sufficient. According to Williamson and Smallman (1956), D can be assumed to be 1 for the simplest way of calculating the dislocation density. This was chosen in this study.

6.2.4 Evaluation of Dual-Phase Steel

The major challenge in evaluating diffraction profiles of DP steel is the overlap of the peaks of the martensite and ferrite phases, which occurs due to the very similar crystal structure and similar lattice constants (Woo et al., 2012). The highest possible resolution of the peaks is required for a reliable evaluation of the diffraction profiles. For this reason, a different setting was used for DP steel as described in Section 5.4. The three lattice planes (110), (200) and (211) can be evaluated with this setting. The Matlab toolbox LIPRAS was used for the evaluation of the profiles (Esteves et al., 2017). It was chosen because it can process the sector data from the Debye-Scherrer rings integrated with the Fit2D software (Hammersley, 1997). Additionally, the fitting function can be chosen freely and multiple peaks can be fitted within one experimental reflection profile. The order of the files can be reversed so that profiles with high strains can be evaluated first. This can be helpful because it can be easier to distinguish between individual peaks at higher plastic strains. It will be explained in more detail later on. It is also possible to define lower and upper limits for the respective fit, so that boundary conditions for the intensities and the FWHM can be specified. Since the intensity of the reflections is related to the volume phase fractions (Popović, 2020), the fractions can be taken into account in the evaluation.

Figure 6.7 gives an overview of the procedure for the separate evaluation of martensite and ferrite for the dual-phase steel. The evaluation is divided into three steps. The first step is the determination of the phase fractions by means of Scanning Electron Microscopy (SEM) images and a gray scale analysis. The second step is the processing of the diffraction data and the third step is the evaluation of the individual reflections.

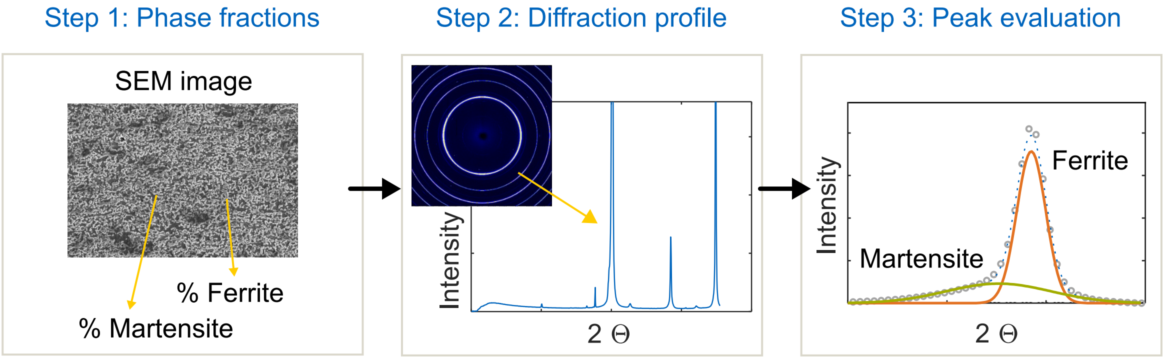

Figure 6.7: Approach for the separate evaluation of martensite and ferrite for dual-phase steel.

Phase fraction determination

Gray scale analysis based on SEM images was performed to determine the phase fractions. The images were taken parallel to the rolling direction of the material. For the analysis, specimens had to be prepared beforehand. First, the specimens were mechanically grinded in an iterative process (sandpaper up to P1200) and then polished in a diamond suspension (6 µm, 3 µm and 1 µm). Finally, the specimens were in a vibratory polisher in a silica suspension for 2 hours. The settings of the SEM analyses are summarized in Table E.1 in the Appendix E.1. The grain and sub-grain microstructure were analyzed by the Matlab toolbox MTEX (Bachmann et al., 2010).

Figure 6.8 (a) shows the SEM image for DP1000. The lighter gray areas are martensite. The slightly darker areas are ferrite. The individual grains are delimited by grain boundaries, which are not taken into account for the evaluation, since they play a minor role regarding the volume fractions in DP1000. There is almost no retained austenite left in DP1000, which was also confirmed by checking the diffraction profiles. As no austenite reflections were detectable, retained austenite was excluded from the evaluation. The threshold value for the differentiation of the gray values was set in such a way that the black and white image is as congruent as possible with the SEM image (see Figure 6.8 (b)). This evaluation was performed using a Matlab script and the black and white image was superimposed on the SEM image for verification. By counting the black and white pixels, the proportion of each area was determined. For this purpose, five images were checked at five different locations. These evaluations resulted in an average of 36 % martensite and 64 % ferrite with a standard deviation below 2 %. This agrees very well with the result of Woo et al. (2012), who used a similar method also for a DP1000 steel.

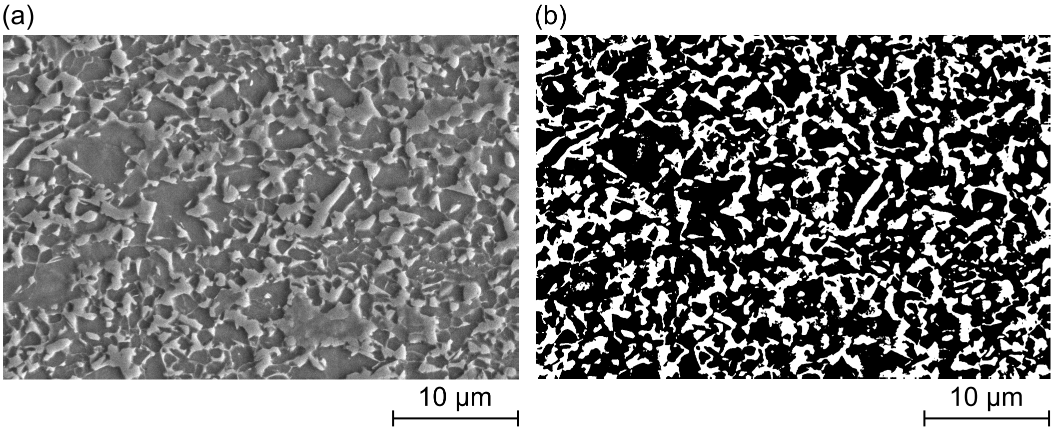

Figure 6.8: DP1000 - (a) SEM image and (b) result of corresponding gray scale value analysis for the determination of the volume phase fractions.

Diffraction profile

As indicated in Figure 6.4, the angular evaluation sectors of the Debye-Scherrer rings were summed up for the DP steel at the top and bottom in longitudinal direction. This leads to an increase in the intensity of the reflections and a more precise evaluation is possible. The software LIPRAS does not interpolate between experimental datapoints when fitting peak profiles. Therefore, to increase the fit accuracy, linear interpolation was performed between the experimental datapoints to create more input values for the fitting.

Figure 6.9 (a) shows the obtained diffraction profile for the DP1000 in-situ experiments for the initial unloaded state. The three reflections of the lattice planes (110), (200) and (211) are clearly visible. Again, the reflection of the (110) lattice plane shows the highest intensity and that of the (200) lattice plane the lowest. Figure 6.9 (b) zooms in the reflection of the lattice plane (211). The experimentally detected datapoints for the upper and lower angular sector of the Debye-Scherrer ring are plotted as well as their sum. It can be seen that there is almost no difference between the datapoints from the upper and the lower sector. Also, the linearly interpolated datapoints are plotted.

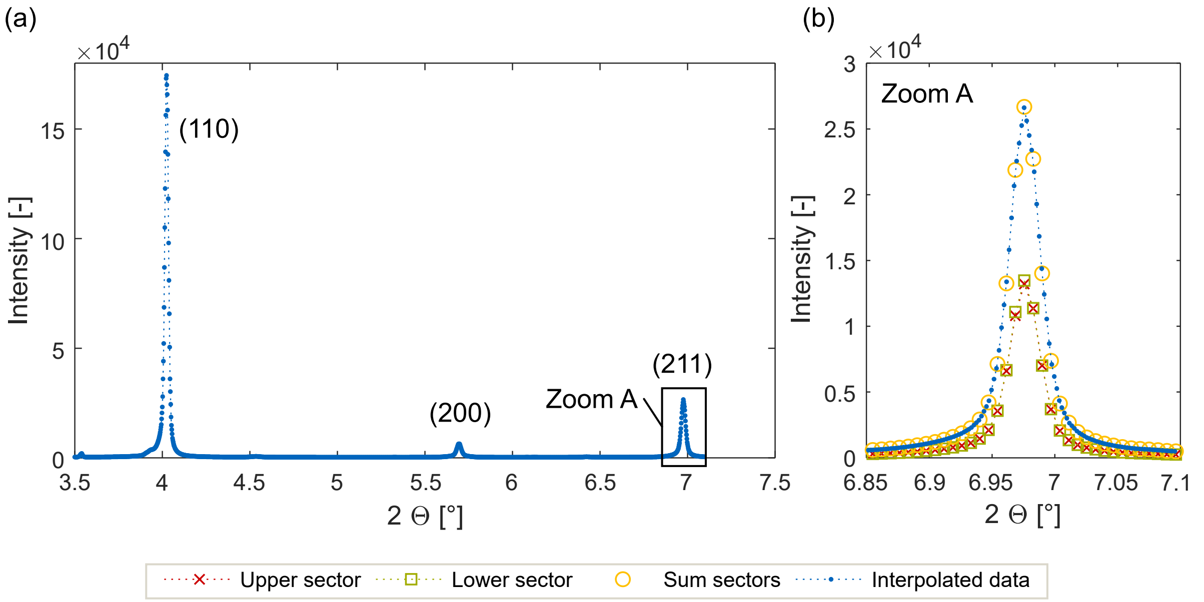

Figure 6.9: DP1000 - (a) Integrated diffraction profile from Debye-Scherrer rings for the initial unloaded state. (b) Presentation of experimental datapoints for the upper angular sector, the lower angular sector and their sum as well as the interpolated datapoints.

Peak evaluation

The volume fractions of martensite and ferrite are already known. These proportions also correspond to the intensity ratio of the two peaks. However, it is not known what shape the peaks have. Therefore, the shape and especially the change of the shape of the experimentally measured reflections were analyzed during the experiment. Because of the strong overlap of the two reflections, the experimental datapoints represent the intensity sum of the two reflections. It was found that at higher plastic strains the lower region of the reflection becomes strongly asymmetric. It is assumed that this occurs due to the 2 Θ displacement of the two basically symmetrical reflections with respect to each other. Previous studies also showed that separation of the two peaks is more feasible at higher strains (Jia et al., 2009).

Figure 6.10 shows the experimentally measured datapoints for the reflection of the lattice plane (211) at 5.5 % true plastic strain. It can be seen that the lower part of the experimental peak shape is asymmetric. Assuming that the phase fractions correspond to the intensity distribution of the two peaks, the two peaks can be fitted to the experimental data as indicated in Figure 6.10. In the initial state, the peaks of the martensite and ferrite are at almost the same 2 Θ position, so it is hard to distinguish between them. For this reason, the fitting is done inversely starting from the highest plastic strain back to the initial state.

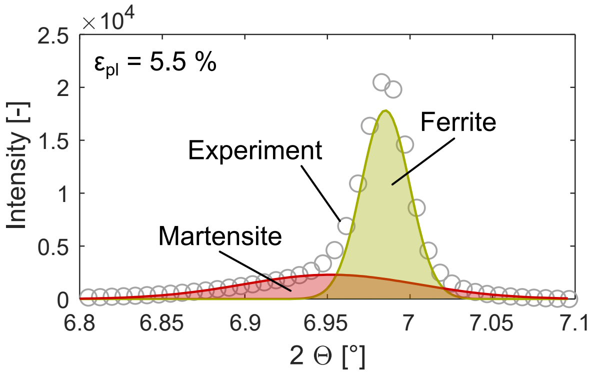

Figure 6.10: DP1000 - Experimental datapoints for the reflection of lattice plane (211) at 5.5 % plastic strain. Indicated is the partitioning of the experimentally observed reflection into a martensite and ferrite reflection.

Figure 6.11 shows some stages of the fitting process. The Bragg reflections are of the lattice plane (211). In (a-c), the states at 0 %, 1.85 % and 5.53 % plastic strain are plotted which were obtained during the cyclic tensile test after complete unloading. Based on the phase fraction ratio, the intensity ratio between ferrite and martensite was given as a boundary condition for the Gauss fits made. No further boundaries were assigned to the ferrite. As can be seen, the reflection of the martensite is located in the lower part of the total experimentally observed reflection and is clearly wider than the ferrite reflection. A minimum FWHM was assigned to the martensite to avoid illogical errors in the fitting. In the initial state, it can be seen that the peaks are strongly overlapping. When comparing the experimentally observed reflection with the Gaussian fit of the ferrite, it is noticeable that there is a large deviation from the Gaussian curve, especially in the foot region of the peak. This is attributed to the second phase with lower intensity, i.e. the martensite peak. By observing this foot region at higher strains, it becomes clear that this assumption is valid, since one can clearly see the 2 Θ movement of the martensite peak compared to the ferrite peak. This dissimilar behavior of the two phases can be explained by their different behavior under load. It can also be seen that the total shape area decreases with increasing strain. Phase transformation can be practically excluded with the present DP1000 and thus the shape area would have to remain the same during transformation. Thus, this decrease comes from peak broadening due to plastic deformation.

In Figure 6.11 (d-f), three states during the TC test are shown. These are the initial state at 0 % strain (d), the tensile state at 3 % true strain right before unloading (e) and the compressive state at -0.4 % true strain. The two initial states (a) and (d) are from two different specimens and show an almost identical diffraction profile including peak fits. It seems that the diffraction behavior is well reproducible. In (e), lower intensity and peak broadening can be obsevered, which is in good agreement with the results for tensile loading of the cyclic tensile test (b-c). The behavior of the measured Bragg reflection during compressive loading (f) must be mentioned. It can be seen that the experimental peak and consequently the two peak fits become narrower again. This indicates a material recovery, for example in the form of dislocation annihilation, which will be discussed in more detail in Chapters 7 and 8.

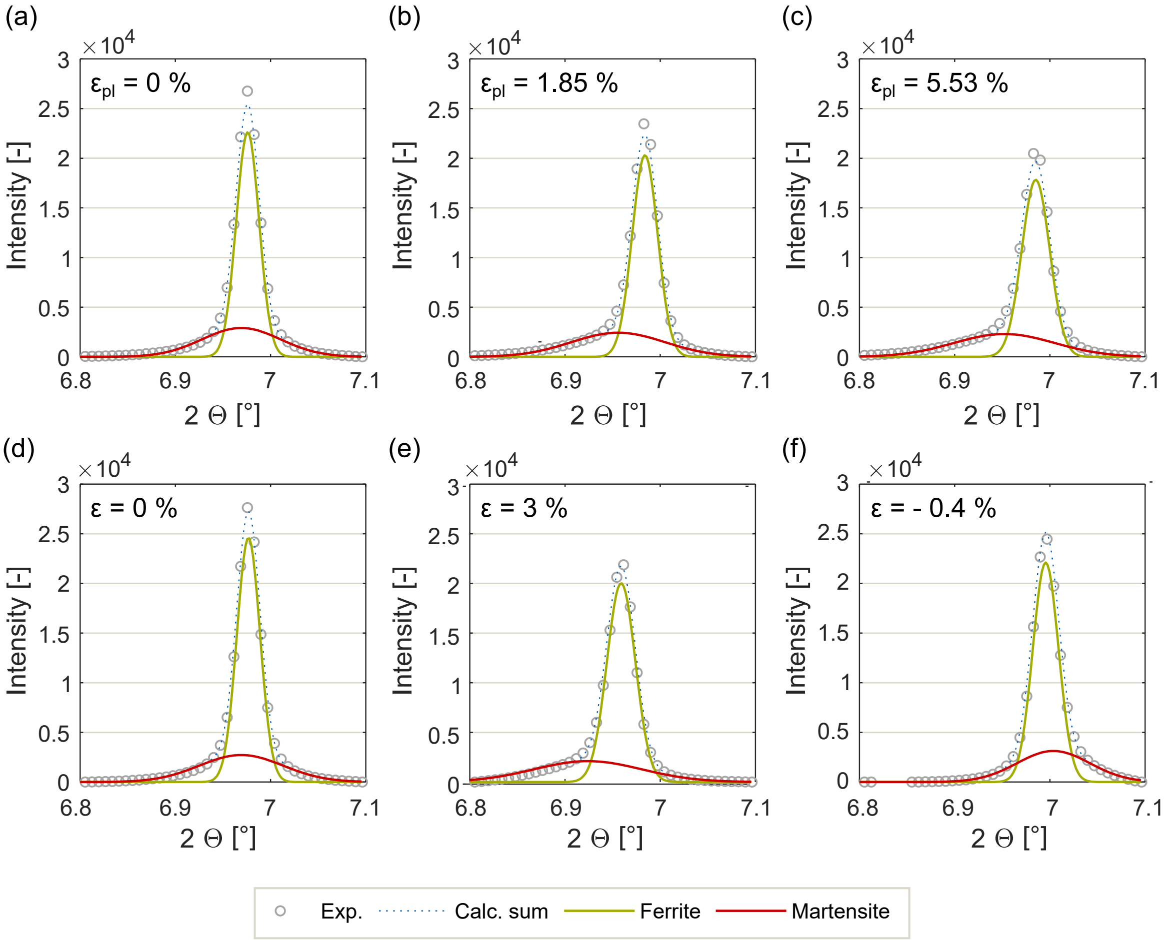

Figure 6.11: DP1000 - Experimentally measured intensities for the lattice plane (211) plotted versus 2 Θ. Shown are the particular Gauss fits for ferrite and martensite and their sum curve for different strain states during the cyclic tensile test (a-c) and the TC test (d-f).

7 Results and Discussion

Chapter 7 summarizes all results obtained in this work. The results are divided into two parts. The first part deals with the qualification of the temperature measurement in tensile and tension-compression tests for the characterization of elastic-plastic material parameters. This represents an important part of this work and therefore the measurement accuracy, sensitivity and reproducibility of the newly found methods are extensively analyzed. The second part of the results is the main part of this research project. It deals with the correlation of the macroscopic material behavior with the microstructural behavior. The presentation of results is structured according to the elastic-plastic characteristics. These are the onset of yielding and elastic loading modulus, anelastic behavior and the re-yielding behavior or Bauschinger effect.

7.1 Temperature Measurement

The historical and thermomechanical basics are given in Chapter 2.6. The hypothesis about the relation between the thermoelastic effect and the onset of yielding is formulated in Section 6.1. Now, the measurement accuracy and robustness (Section 7.1.1), the sensitivity of the evaluation (Section 7.1.2), the reproducibility and strain rate sensitivity (Section 7.1.3) as well as the temperature measurement in tension-compression tests (Section 7.1.4) are analyzed. The tests were carried out with the *utg* setup.

7.1.1 Measurement Accuracy

To investigate the accuracy of the measurement system, four temperature sensors (T_I-T_{IV}) were positioned as close as possible to the center of the specimen (Figure 7.1 (a)). In this way, the extent to which different sensors and their plugs differ is determined. HC260Y was used for this investigation. To investigate the influence of the position of the sensor on the specimen, the sensors were arranged as shown in Figure 7.1 (b). Sensor T_0 was applied directly in the center of the specimen. Sensors T_1 and T_2, 15 mm above and below this, i.e. symmetrically. Sensor T_3 was positioned 35 mm below the center, which was already outside the measuring length of 50 mm of the optical extensometers. In this way, it is possible to analyze the temperature behavior across the specimen.

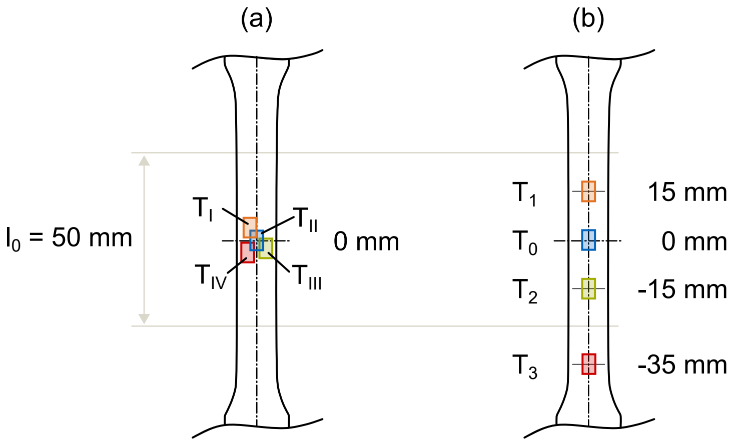

Figure 7.1: Arrangements of four PT1000 sensors for the analysis of the measurement accuracy (a) and the thermal behavior within the specimen with regard to the influence on Tmin (b).

Figure 7.2 shows the results of the experiment with setup (a) in Figure 7.1. The test was evaluated until uniform elongation. An unloading-reloading cycle was performed in steps of 3 % engineering strain. The four sensors show almost identical behavior and hardly any deviations from each other. The maximum deviation is less than 0.2 K at the end of the evaluation. For the evaluation of YS_{Tmin} for all four sensors, a standard deviation of 0.9 MPa over all cycles can be achieved.

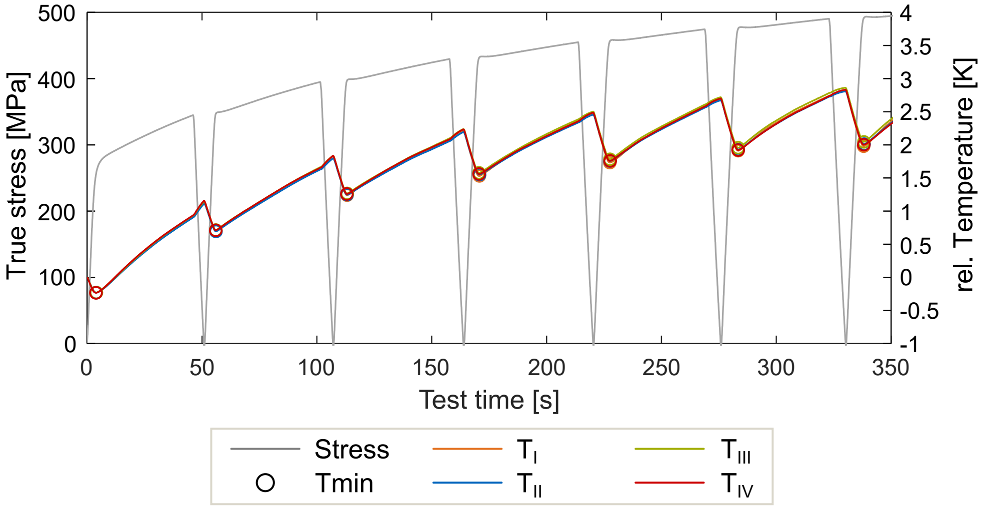

Figure 7.2: HC260Y - Comparison of the sensors T_I-T_{IV} at the center position of the specimen. (strain rate 0.0007 s^{-1})

In Figure 7.3, the results for the sensor positions of setup (b) in Figure 7.1 are shown, now for HC260Y and DP1000. Before the parameter YS_{Tmin} is discussed in more detail, the temperature behavior is described in general. DP1000 shows clearly a larger elastic range compared to HC260Y. This leads to a more significant decrease in temperature until the minimum is reached due to the onset of yielding and plastic heating. The decrease in temperature during elastic deformation is about 0.5 K for DP1000 for the strain rate of 0.001 s^{-1}. For HC260Y, on the other hand, it is 0.2 K. For both materials, the temperature increases linearly during the elastic-plastic range between the unloading-reloading cycles. During unloading, the temperature behavior differs for the materials. For the first four unloadings, the temperature increase is even higher than during elastic-plastic deformation for HC260Y. Afterwards, the temperature still increases during unloading, but less than during elastic-plastic deformation. In the case of DP1000, the gradient of temperature increase during elastic unloading continues to reduce across the experiment. This is attributed to thermal convection and conduction, which become stronger with a larger temperature difference between the periphery and the specimen.

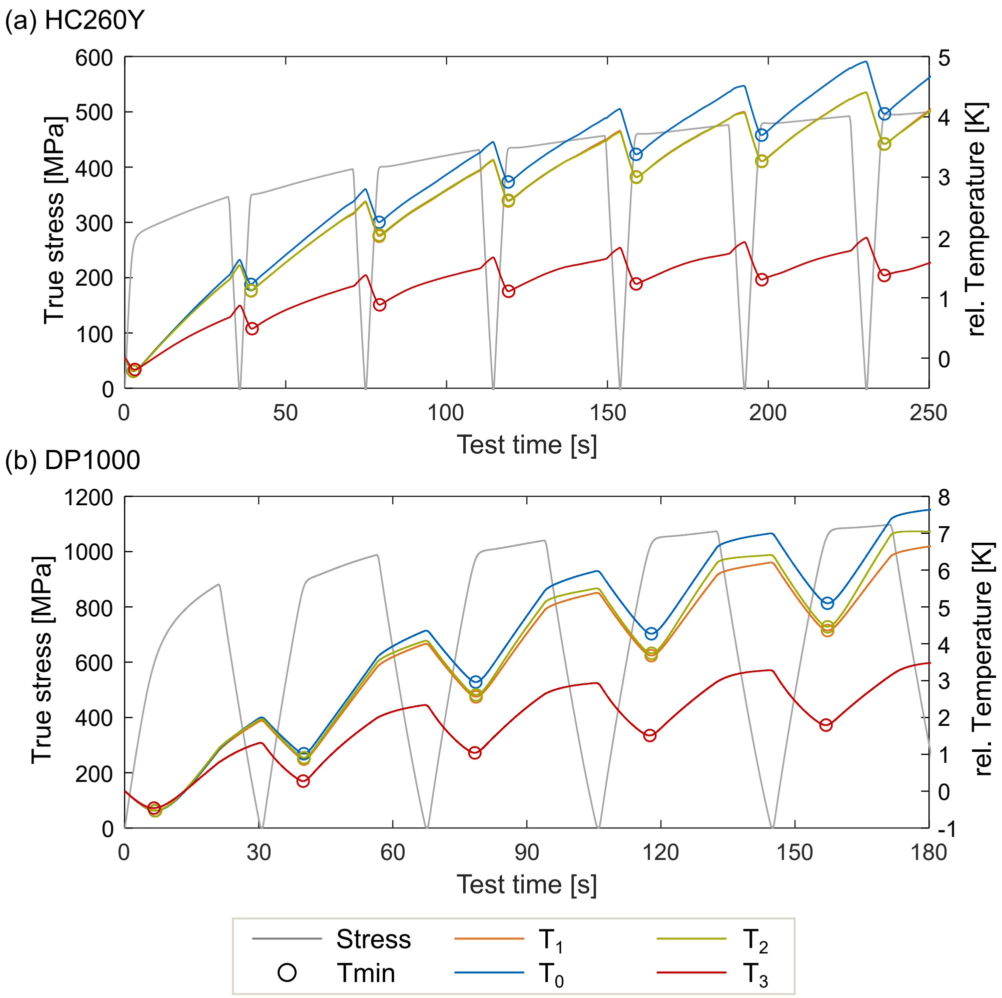

Figure 7.3: Comparison of sensor positions T_0-T_3 and their temperature minima for (a) HC260Y and (b) DP1000. (strain rate 0.001 $^{-1}$)

Now the individual sensor signals are compared. For both materials, it can be seen that the sensor in the center of the sample (T_0) shows the greatest heating during the experiment. The sensors T_1 and T_2, which are positioned symmetrically to the center, show a lower heating, but similar behavior. Sensor T_3 shows a significantly lower heating for both materials. In summary, the sample becomes warmest in the center and then the heating decreases towards the clamping. For HC260Y, the sensors T_0, T_1 and T_2 heat up around 4 to 5 K, whereas the sensor T_3 shows a warming of around 1.5 K. This is an indication that the steel specimen grips, which are in direct contact with the specimen, reduce the temperature from the specimen by thermal conduction. The decisive factor for the temperature-based evaluation method is whether this behavior has an influence on the temperature minimum. Therefore, YS_{Tmin} is evaluated for all sensors and all unloading-reloading cycles. For the comparison of the sensors, the difference to the sensor in the center (T_0) was calculated in each case. The standard deviation was determined over all cycles. This calculation was done for the strain rates 0.0004 s^{-1}, 0.001 s^{-1} and 0.004 s^{-1} to be able to exclude any effects due to the strain rate. Table 7.1 shows the results of the deviations for three repetitions each. No trends are discernible for HC260Y. For all three strain rates investigated, the deviations are in the range of 1 MPa. Only at the low strain rate of 0.0004 s^{-1} and sensors T_0 and T_3, an increased standard deviation of more than 2 MPa was found. For DP1000, the largest deviation of 7.34 MPa occurs also between sensors T_0 and T_3. Here, it should be noted that T_3 is outside the gauge length and for this reason does not reflect a permissible value. Nevertheless, for example for DP1000, the deviation of 7.34 MPa in relation to its TS is still only 0.7 %. Thermal conduction is clearly visible, but this does not seem to have an influence on Tmin and hence, YS_{Tmin}. This suggests that it is indeed related to the onset of yielding, which assumed to occur homogeneously over the parallel length of the tensile specimen.

Table 7.1: Standard deviations (SD) for the parameter YS_{Tmin} between the PT1000 sensors at different positions on the specimen calculated over all cycles.

	Strain rate [s^{-1}]	$T_0 \leftrightarrow T_1$ SD [MPa]	$T_0 \leftrightarrow T_2$ SD [MPa]	$T_0 \leftrightarrow T_3$ SD [MPa]
HC260Y	0.0004	0.32	0.19	2.05
	0.001	0.62	0.19	0.36
	0.004	0.34	0.73	1.23
DP1000	0.0004	1.31	1.08	7.34
	0.001	3.21	0.96	2.11
	0.004	4.6	2.22	1.58

7.1.2 Sensitivity

From here on, only one sensor is used, which is applied in the center of the specimen (cf. sensor T_0). In Section 6.1.2, the temperature-based determination of the onset of plastic yielding, thus the parameter YS_0 was introduced. Figure 7.4 again shows the temperature gradient versus time curve, which is the basis for this determination approach. Shown are the curves for the initial loading as well as 1st reloading for both materials, HC260Y and DP1000. The horizontal and vertical data array, which are decisive for the horizontal and vertical regression lines, are plotted. Furthermore, the line for the bisecting angle is plotted, which finally determines the point in time of the slope change. The slope change in the initial loading is not as pronounced compared to the 1st reloading. This can be explained by the fact that the elastic-plastic transition is smoother at initial loading than at reloading, where the slip systems have already been activated. This behavior is also reflected by the macroscopic stress-strain curve. For the detection of YS_0, i.e. the change in slope of the temperature curve, the arrays for the two regression lines must be defined. This must be done specifically for the material investigated. As can be seen in Figure 7.4, the curve shape may differ slightly for different materials. The evaluation method searches step by step in an iterative process in a given range the minimum and maximum slope, so that the horizontal and vertical fit are found as shown. Nevertheless, the reliability of the intersection found must be checked.

Therefore, the influence of the user, i.e. how the start values for the horizontal and vertical data arrays are set, in this determination method was investigated in a sensitivity analysis. Initial values were determined for the two arrays and are shown in Figure 7.4. Then, the sizes of the arrays were decreased in 5 % steps to 65 % and increased to 135 % of the initially defined datapoints for the following regression. All resulting intersections were calculated in a full factorial design. In the Appendix, Figure E.1 gives an example of the full factorial analysis of the initial loading for DP1000. The resulting scatter of the values for YS_0 was checked for its distribution. A normal distribution (Gauss) was found, so that the calculation of the standard deviation (SD) and the arithmetic mean is permissible. Figure 7.5 shows the respective SD in relation to the mean value of the parameter YS_0 for 6 loadings. In total, 225 values per loading were conducted for the SD and mean value. The highest deviations occur for the initial loading with 4.95 % for HC260Y and 2.39 % for DP1000. This reflects absolute deviations of 8.9 MPa (HC260Y) and 10.5 MPa (DP1000) for the average YS_0 values of 178 MPa (HC206Y) and 455 MPa (DP1000). For all further loadings, the deviations are less than 1 %. The low deviations in the temperature-based evaluation method for the determination of YS_0 proof that it is robust with respect to the initial values for the line fit method and thus to the user.

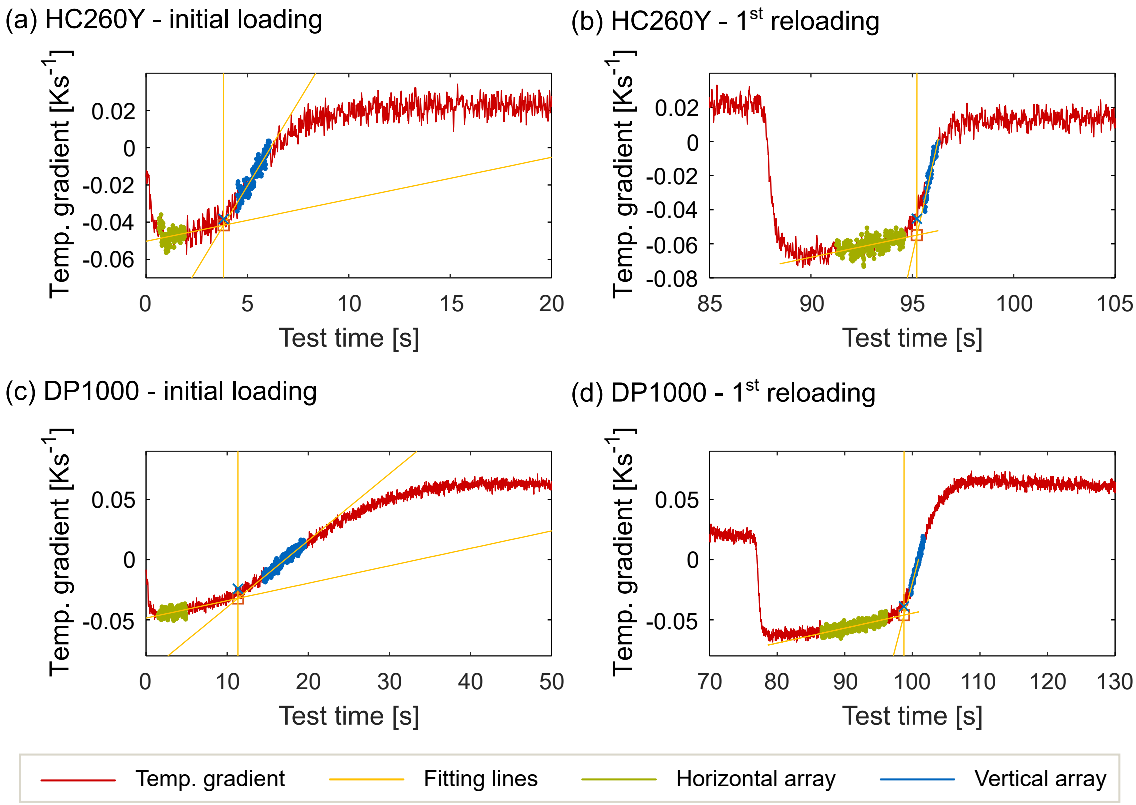

Figure 7.4: Temperature gradient curves with temperature-based determination method for YS_0 *for the initial loading and* 1^{st} *reloading for HC260Y (a-b) and DP1000 (c-d). (strain rate 0.0004* s^{-1}*)*

.

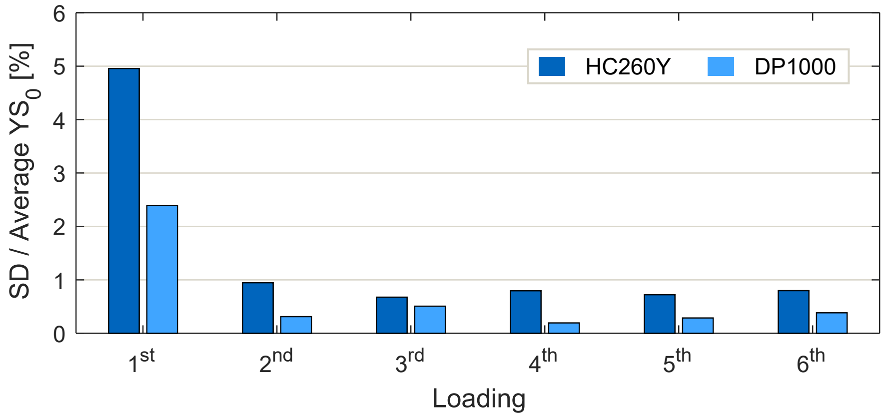

Figure 7.5: Standard deviation (SD) of full factorial analysis in percent of the average YS_0 *of the particular loading for HC260Y and DP1000. (strain rate 0.0004* s^{-1}*)*

7.1.3 Reproducibility

The robustness and reproducibility of the measurement and temperature-based evaluation are investigated in this section. Therefore, different strain rates are considered and the deviations of the parameters YS_0 and YS_{Tmin} are compared from three experimental repetitions each. For the YS_0 determination, the horizontal and vertical data arrays were fixed and not changed during the repetitions. The initial loading and five additional reloadings after every 1.5 % (DP1000) and 3 % (HC260Y) engineering strain were evaluated for five different strain rates. Figures 7.6 and 7.7 summarize the standard deviation as a percentage of the mean value. In general, it can be observed that the deviations are smaller for YS_{Tmin} than for YS_0. This is, because of the high temperature measurement accuracy and the fact that YS_{Tmin} can be determined directly without an additional evaluation. The deviations for YS_{Tmin} are smaller than 2.5 % for both materials and all loadings. Thereby, the initial loading show the highest deviations. All deviations of YS_0 are below 7.5 %. Again, the highest deviation occurs for the initial loading. This can be explained by the smooth initial elastic-plastic transition and the less pronounced slope change in the temperature gradient curve (see Figure 7.4). The deviations of the reloadings are less than 5 %.

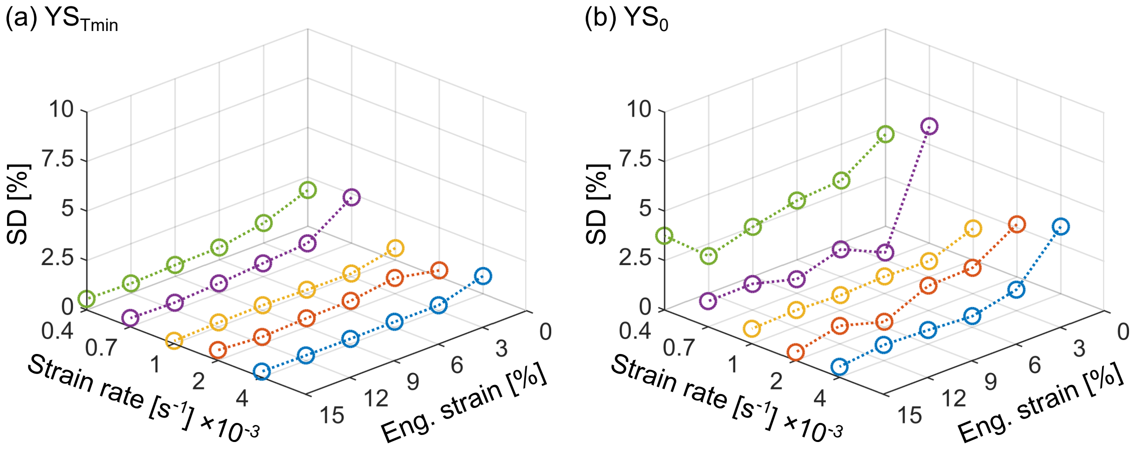

Figure 7.6: HC260Y - Standard deviations relative to its mean value of three experimental repetitions for five strain rates and the parameters (a) YS_{Tmin} and (b) YS_0.

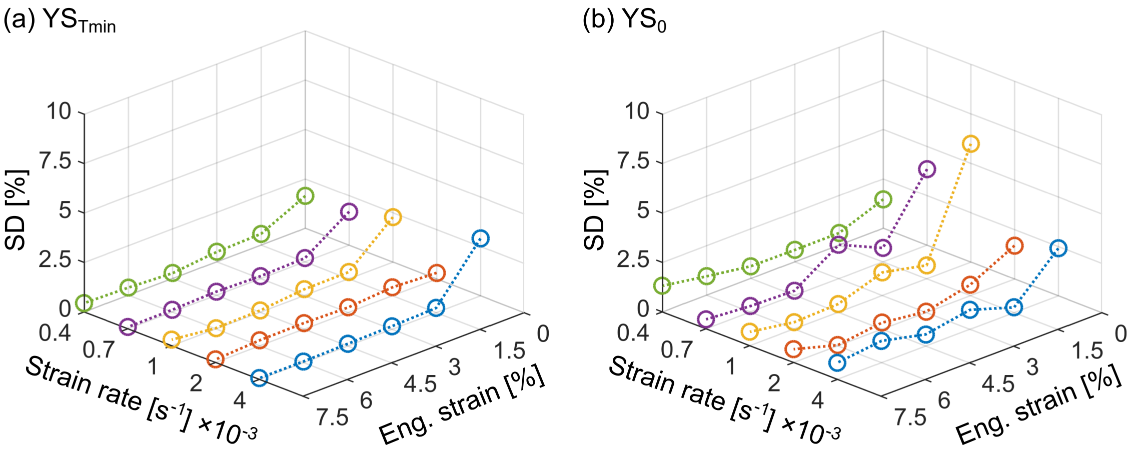

Figure 7.7: DP1000 - Standard deviations relative to its mean value of three experimental repetitions for five strain rates and the parameters (a) YS_{Tmin} and (b) YS_0.

The initial onset of yielding is of particular importance, as it determines the beginning of the flow curve for FEM material models for example. Furthermore, the YS_0 is the upper limit for the temperature-based determination of the initial loading modulus E_{YS0}. For a better classification, the absolute values are shown separately for the five strain rates and a comparison is made with the conventionally used equivalent yield stress $YS_{0.2\%}$. Therefore, $YS_{0.2\%}$ was determined by the slope between 5 % of TS and YS_0. A parallel to this slope was shifted to 0.2 % true plastic strain and the intersection with the stress-strain curve gives the value. Figure 7.8 shows the results for both materials. In all evaluations, the value for $YS_{0.2\%}$ is the highest. According to the hypothesis in Section 6.1.1, there is already plastic deformation at YS_{Tmin}, but this deformation seems to be below the 0.2 % plastic strain, which is the defined value for the determination of $YS_{0.2\%}$. The difference between each parameter remains approximately the same for all strain rates. There is no evidence of strain rate sensitivity in DP1000. It is known that the mechanical properties of low carbon steel, like the HC260Y, show strain rate sensitive behavior (Jandrlić et al., 2018). This can be seen by the increased values for the strain rates 0.002 s^{-1} and 0.004 s^{-1}. The strain rate sensitivity is captured by all three parameters.

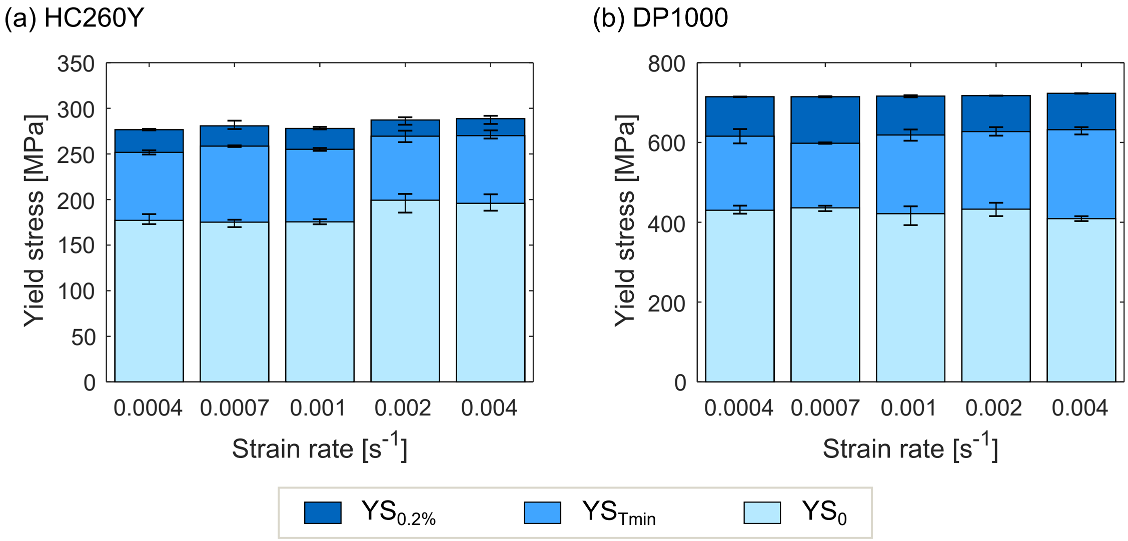

Figure 7.8: Comparison of the parameters $YS_{0.2\%}$, YS_{Tmin} and YS_0 for the initial yielding and five strain rates for (a) HC260Y and (b) DP1000.

.

7.1.4 Temperature Measurement in Tension-Compression Tests

One of the challenges in this study is to determine not only the onset of plastic yielding but also the re-yielding after load path change when using the specimen temperature as indicator. It is known that during elastic-plastic deformation the specimen temperature increases. During elastic unloading and compressive loading, there is a reduction in volume. Due to the thermoelastic effect, this also leads to a heating of the specimen. In contrast to the determination of the onset of yielding in tension, where there is a clearly pronounced temperature minimum, there is only a change in gradient in the compression range. The evaluation of the transition in the temperature gradient is therefore more difficult, since the heating also depends on the strain rate. Before showing the determination of the yield stress at re-yielding YS_{re}, the characteristics of the temperature measurement in the TC test are explained.

In Figure 5.5, the experimental setup was shown. The PT1000 sensor is applied in the measurement window by a solid state clamp. The influence of thermal conduction has already been demonstrated earlier. Due to the direct contact of the specimen with the voluminous grips, heating decreases from the center of the specimen towards the grips. During the TC test, the specimen surface is in direct contact not only with the grips but also with the anti-buckling support. Accordingly, a larger area of the specimen is affected, which most likely results in a greater impact due to increased thermal conduction. Therefore, additional thermal insulation plates are mounted between the anti-buckling support and the specimen to minimize the effect of thermal conduction. Figure 7.9 shows the true stress versus time curves with their corresponding temperature for two TC tests with DP1000. One test (Exp1) was done without thermal insulation plates, so that there was a steel to steel contact between specimen and anti-buckling support. The other one (Exp2) was performed with insulation plates. It is clear that there is a significant difference when comparing the temperature curves. In Exp1, the entire temperature curve is significantly damped and not even Tmin at initial tension is clearly visible. The temperature curve in Exp2 shows a pronounced minimum during the tensile onset of yielding and in total a larger change in the temperature during the test. Thus, with the insulation plates, there is a significant improvement. From here on, all tests shown were performed with thermal insulation plates.

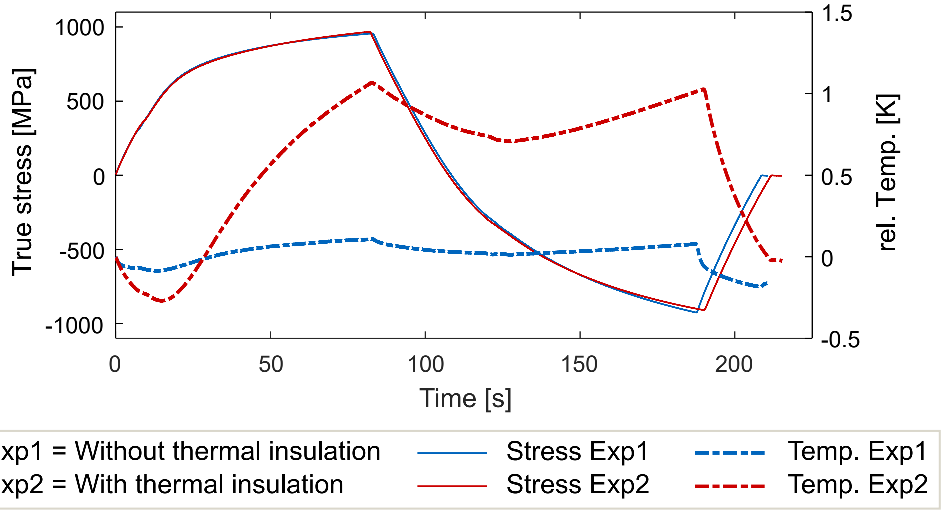

Figure 7.9: DP1000 - True stress versus time and relative temperature versus time curves for two TC tests. Experiment 1 was performed without and experiment 2 with thermal insulation plates.

Figure 7.9 shows for Exp2 that during elastic unloading the temperature decreases, which seems to be in conflict with theory. Only after complete elastic unloading in the compression range, the temperature starts to rise again. This behavior can be attributed to thermal conduction despite the insulation, since there is a temperature difference between the specimen and the periphery at this time. The heating during elastic unloading is not sufficient to counteract the cooling due to this temperature difference. For this reason, tests were carried out, in which a holding time after tensile loading was introduced until the specimen temperature had adjusted to the ambient temperature again. Only then, the specimen was elastically unloaded and compressed. During the holding time, the experiment was stopped displacement controlled. With this procedure it could be shown that, as theoretically expected, a temperature increase occurs also during elastic unloading. That is why for all TC tests with temperature measurement, a holding time of seven minutes for DP1000 and of five minutes for HC260Y was carried out before elastic unloading and compressive loading.

Figure 7.10 shows the true stress versus true strain curves of three repetitions for (a) HC260Y and (b) DP1000. Furthermore, the temperature curves are plotted. For clarity, these are shown only for elastic unloading and compressive loading and have been zeroed at the starting point of UL. The stress-strain curves of the repetitions show almost no deviation for both materials. Hence, the experiment is reproducible. Also the temperature curves show similar behavior. For HC260Y, a transition in the slope of the temperature curve during compressive loading can be seen. In the beginning of the unloading, the temperature increases rapidly and then transitions to a slower rate of heating. The temperature curves for DP1000 show different behavior. From the beginning on, the temperature behaves highly nonlinear. The slope changes also during compression, but there is no significant point of transition determinable.

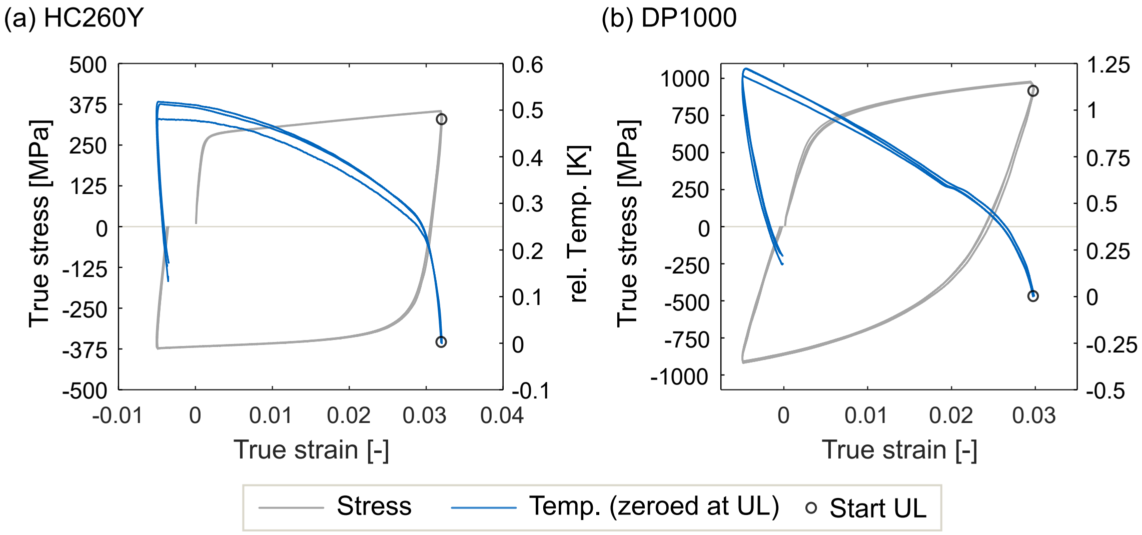

Figure 7.10: (a) True stress versus true strain curves and relative temperature curves of three repetitions for (a) HC260Y and (b) DP1000. Only the temperature curves for UL and compression are plotted and zeroed at the start of UL. (strain rate 0.0004 s^{-1})

In the following, an attempt is made to transfer the idea of the temperature-based evaluation method for the onset of plastic yielding YS_0 to the re-yielding parameter YS_{re}. For this purpose, the temperature gradient is derived for the range of elastic unloading and subsequent compressive loading and shown in Figure 7.11 (a) for HC260Y. In the gradient, the transition of the slope is even more obvious. Two regression fits are performed, like for the determination of YS_0 described in Section 6.1.2. One for the vertical array in the beginning of unloading and a second one for the horizontal array during compressive plastic deformation. The size of the arrays was set manually by the user. To better classify the location of the arrays in the overall test, they are also plotted in the stress-strain curve in Figure 7.11 (b). The vertex of the gradient change is determined with an angle bisector. This value is taken as YS_{re} and is also marked in the stress-strain diagram in (b). Looking at the shape of the stress-strain curve, the location of the determined value seems to be reasonable. An average stress value of -177 MPa was determined for YS_{re} with a standard deviation of 10 MPa for three repetitions and a prestrain of around 3 % true strain. For comparison, the average YS_0 value for a tension reloading without load change after the same prestrain is 322 MPa. Hence, there is a significant difference between YS_0 and YS_{re}. The lower value for re-yielding can be attributed to a Bauschinger effect. In Section 7.2.5, the YS_{re} value is correlated with the microstructural behavior. In this way, on the one hand, the evaluation method can be validated and, on the other hand, the material behavior after load change can be analyzed in more detail.

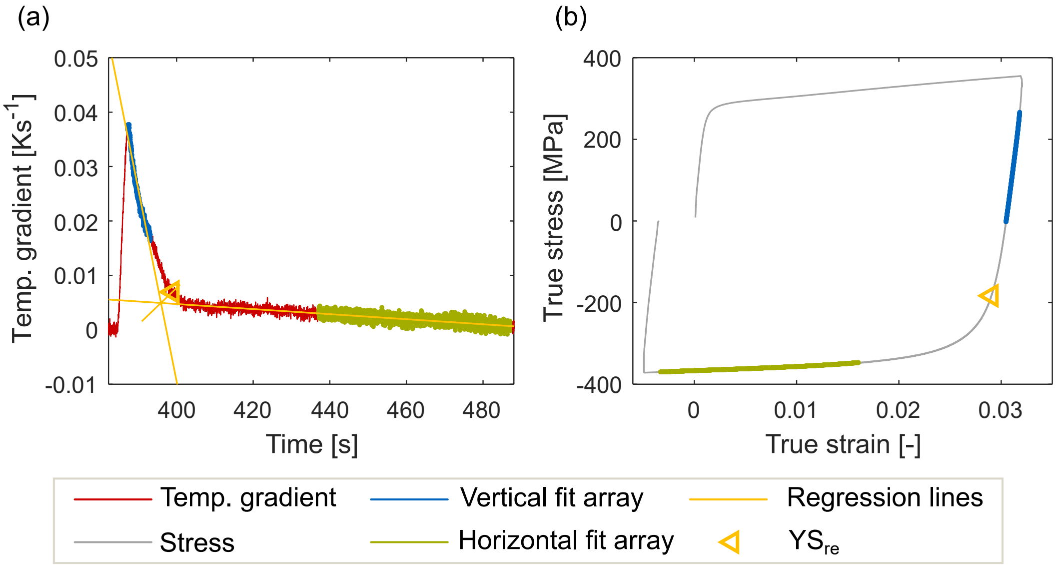

Figure 7.11: HC260Y - (a) Temperature gradient curve for the temperature during unloading and compressive loading. The used arrays and regression lines for YS_{re} determination are plotted. (b) True stress versus true strain curve. Plotted are the arrays, used for the regression in (a) and the determined parameter YS_{re}.

For DP1000, an evaluation with the described approach was not possible. Due to the highly nonlinear behavior, no slope transition could be detected. The microstructural behavior is also investigated in Section 7.2.5 and provides information about the re-yielding behavior of the material. The temperature measurement needs to be further improved in future, so that a temperature-based evaluation of YS_{re} may also be possible for this kind of material.

7.2 Correlations with Microstructural Material Behavior

In this chapter, the macroscopic elastic-plastic behavior of the steels studied is correlated with their microstructural behavior. The results are divided into the elastic-plastic characteristics, namely the onset of yielding, the loading modulus, anelastic behavior and re-yielding. The previous results for temperature-based material characterization are examined microstructurally. Before discussing the individual characteristics, the general microstructural behavior of the two materials is discussed for a better overview.

7.2.1 General Microstructural Behavior

Figure 7.12 (a) shows the macroscopic true stress versus the lattice strains for five lattice planes for HC260Y. The lattice strains were determined based on their 2 Θ peak shift as described in Section 6.2.2. These results were obtained in a standard tensile test until 15 % engineering strain without cyclic unloading and reloading with the *DESY* setup. Each circle represents a diffraction measurement. Considering the value for YS_0, the material shows elastic deformation up to about 180 MPa. The different slopes of the curves until this stress value indicate the microstructural anisotropy of the material. Tomota et al. (2003) showed for a similar low carbon steel that the lattice plane (200) is the most compliant one. This result can be confirmed as the lattice strain for the (200) lattice plane has the lowest slope in Figure 7.12 (a). In Figure 7.12 (b), the lattice strains are plotted versus the macroscopic true strain. Lattice strain, determined on basis of Bragg's law, can only be determined during elastic deformation. That is why, this plot better show the onset of plastic yielding. The lattice strain increase rapidly in the beginning and at a certain point, the lattice planes can hardly absorb any more strain. This condition reflects the microstructural onset of yielding, which is individual for the lattice plane. It will be discussed in more detail in Section 7.2.2. It can be seen in Figure 7.12 (b) that the lattice planes can absorb different amounts of elastic strain, which again indicates the microstructural anisotropy. The lattice plane (200) clearly absorbs the most strain.

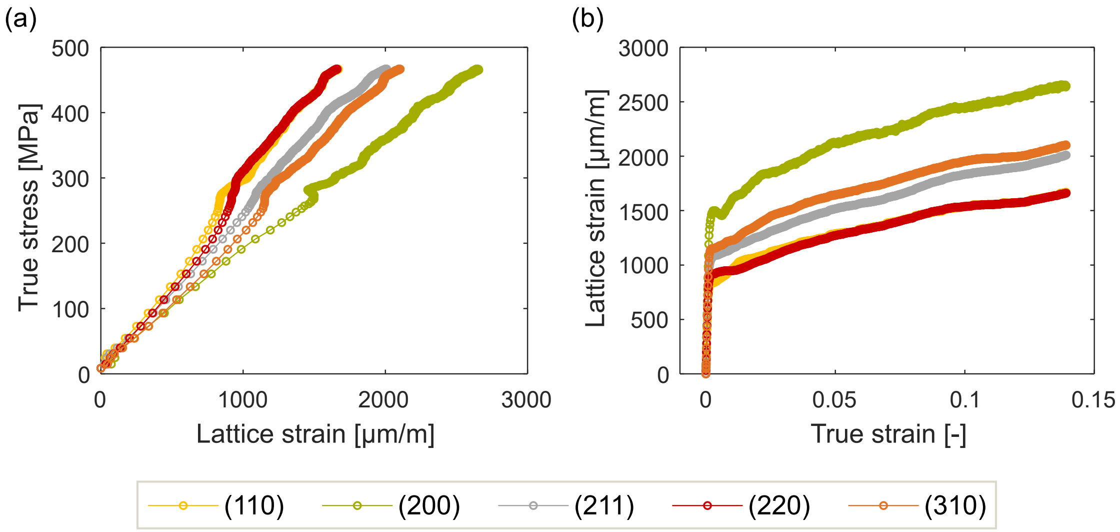

Figure 7.12: HC260Y - (a) Macroscopic true stress versus lattice strain and (b) lattice strain versus macroscopic true strain for five lattice planes.

Figure 7.13 shows the results for DP1000 plotted in the same manner as in Figure 7.12. The standard tensile test was evaluated until 8 % engineering strain. The lattice strains for three lattice planes are shown separately for ferrite and martensite. Figure 7.13 (a) shows that during elastic deformation up to YS_0 of 430 MPa, the ferrite and martensite behaves similarly. Then, ferrite and martensite start to behave differently. Whereas martensite absorbs even more strain, ferrite plasticizes and hardly absorbs any more strain. Again, the different slopes during elastic deformation indicate microstructural anisotropy. In Figure 7.13 (b), the mentioned differences in the strain absorption of the particular phases and lattice planes become obvious. The ferrite hardly absorbs any more strain when it is plasticized. This can be seen from the horizontal asymptotic behavior.

It is noticeable that the ferrite in the DP steel begins to plasticize at significantly higher stresses compared to the ferrite in HC260Y. Figure 7.12 (a) shows plasticization occurring between 200 - 300 MPa, while in Figure 7.13 (a) plasticization of the ferrite occurs at above 500 MPa. In Choi et al. (2001), nanoindentation was used to show that ferrite near grain boundaries has higher strength. It was shown that finer grain sizes led to a significantly increased elastic modulus in ferrite. Grain boundaries act as a kind of barriers to dislocations. Thus, the higher strength of ferrite compared to the single-phase material is because it is embedded in a harder martensite phase and that the significantly finer grain size results in a greater influence by grain boundaries. This grain boundary strengthening is also known as Hall-Petch strengthening (Callister and Rethwisch, 2008). Compared to ferrite, martensite absorbs significantly more strain. It seems that the martensite of lattice plane (200) can absorb strain during the whole experiment. Hence, it is not fully plasticized. The martensite of the lattice planes (110) and (211) show asymptotic behavior at the end of the experiment for higher true strains. This indicates plasticization of the martensite. In literature, the degree of plasticization of the martensite and its effect on anelastic behavior is often discussed (Bergström et al., 2010). This is further analyzed in Section 7.2.4.

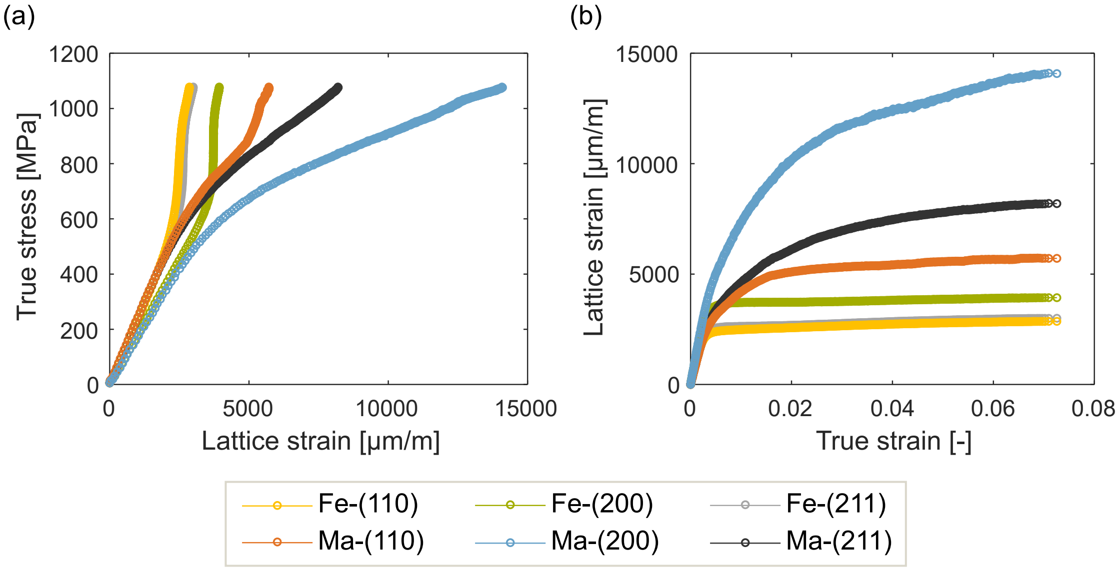

Figure 7.13: DP1000 - (a) Macroscopic true stress versus lattice strain and (b) lattice strain versus macroscopic true strain of ferrite (Fe) and martensite (Ma) for three lattice planes.

In summary, when true stress is plotted versus lattice strain, vertical behavior reflects plastic deformation. When lattice strain is plotted versus true strain, horizontal behavior reflects plastic deformation. This is important for understanding the further results. True stress and true strain always refer to the macroscopic values. In the following, the two materials are analyzed by means of cyclic tensile tests and tension-compression tests.

7.2.2 Onset of Yielding

A new temperature-based determination method was introduced to determine the onset of plastic yielding. The parameters yield stress at zero plastic strain (YS_0) and yield stress at temperature minimum (YS_{Tmin}) are now analyzed on a micro level. This means that the onset of plastic yielding in the crystal lattice is investigated and conclusions are drawn about the macroscopic behavior. The investigation of the onset of yielding is divided in analysis by lattice strains, FWHM and dislocation densities as well as irreversible macroscopic strain.

Lattice strains

Figure 7.14 shows the initial loading for HC260Y. In (a), lattice strains of five lattice planes are plotted versus the macroscopic true strain. In (b), the true stress versus true strain and specimen temperature curve are shown. Vertical lines mark the parameters YS_0 and YS_{Tmin}. At the beginning of the loading, purely elastic deformation is assumed and the lattice strains show similar linear behavior. Microstructural anisotropy leads to different slopes. All lattice strains show a smooth transition from initial slope to horizontal behavior. From the vertical YS_0 line onwards, the first lattice strains start to deviate from the linear behavior and approach a horizontal line. This can be seen in particular for the strains of the lattice planes (110), (211) and (220). The strain of lattice plane (310) shows similar behavior shortly thereafter. Grains of lattice plane (200) show the most compliant behavior and absorb more elastic strain, since even after exceeding YS_0, the lattice strain increases linearly. At approximately YS_{Tmin}, it begins to approach a horizontal one. From YS_{Tmin} onwards, all lattice planes seem to be plasticized, because from this point on hardly any strain is absorbed. It can be seen that lattice plane specific plasticization occurs starting at YS_0 and ending at approximately YS_{Tmin}. In Tomota et al. (2003), this was referred to as grain-to-grain yielding.

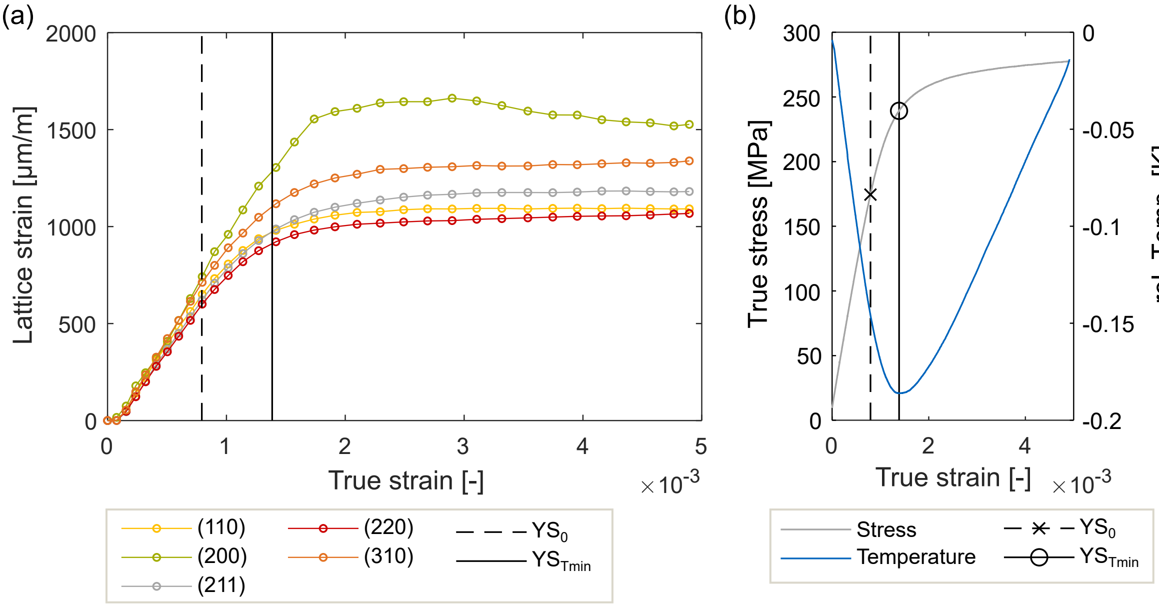

Figure 7.14: HC260Y - (a) Lattice strain versus true strain for five lattice planes in longitudinal direction for the initial tensile loading. Marked are YS_0 and YS_{Tmin}. (b) True stress versus true strain and temperature with YS_0 and YS_{Tmin}.

Figure 7.15 shows the lattice strains versus true strain for the 3rd, 5th and 7th loading of the same experiment. Again, the lattice strain start to change their slope beginning at YS_0 and seem to be fully plasticized from YS_{Tmin} on. Compared to the initial loading in Figure 7.14 (a), the lattice strains show similar behavior, but the grain-to-grain yielding is less pronounced. This fits well with the explanation of slip systems already activated. The results shown are in longitudinal direction. The behavior of the lattice strains in transversal direction is analogous and can be seen in the Figures E.2 and E.3 in the Appendix E.3.

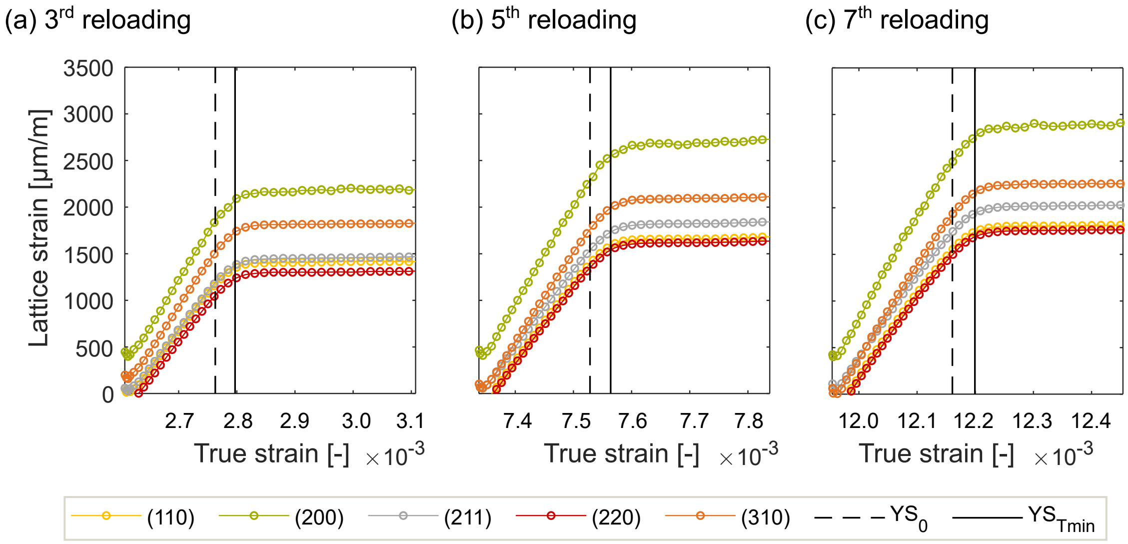

Figure 7.15: HC260Y - Lattice strain versus true strain for five lattice planes in longitudinal direction for the (a) 3^{rd}, (b) 5^{th} and (c) 7^{th} reloading. Marked are YS_0 and YS_{Tmin}.

It can be summarized that lattice plane specific grain-to-grain yielding occurs and it is particularly pronounced during initial loading. The parameter YS_0 indicates the macroscopic stress value at which the first lattice planes seem to start plasticizing. When the stress YS_{Tmin} is exceeded, all lattice planes appear to be plasticized.

Figure 7.16 presents the same evaluation for DP1000. The lattice strains of the lattice planes (110), (200) and (211) are separately plotted for the ferrite and martensite phase. The material shows highly anisotropic behavior and again, the lattice plane (200) is the most compliant one. Above the stress value YS_0, the ferrite phase begins to plasticize, as is the case with HC260Y. The three ferrite lattice strains show similar behavior. After exceeding YS_{Tmin}, the ferrite phase seems to be plasticized, so the findings with HC260Y for ferrite can be confirmed. The martensite phase shows identical behavior to the ferrite during purely elastic deformation until YS_0 and then absorbs further elastic strain with a different slope when the ferrite phase is plasticized. The martensite of lattice plane (200) can absorb significantly more elastic strain. The results in Figure 7.16 indicate a direct correlation with the two temperature parameters and the microstructure for this material. The parameter YS_0 again reflects the onset of plastic yielding, which in DP1000 is related to the plasticization of the ferrite phase.

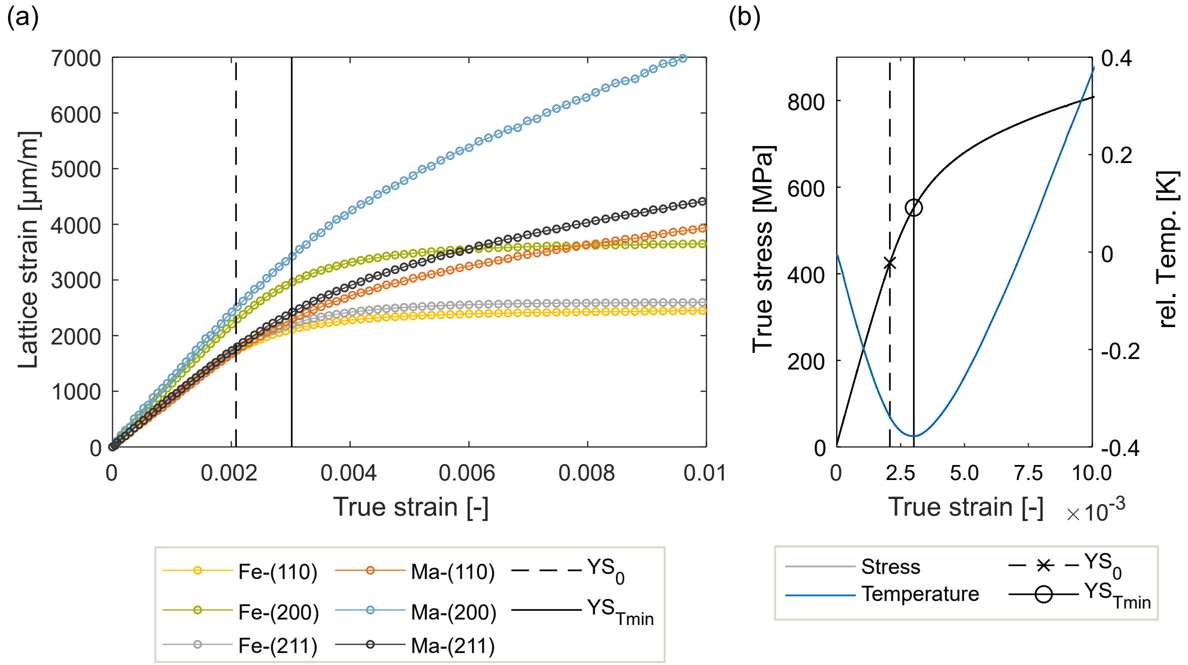

Figure 7.16: DP1000 - (a) Lattice strain versus true strain separated for ferrite and martensite for three lattice planes in longitudinal direction for the initial tensile loading. Marked are YS_0 and YS_{Tmin}. (b) True stress versus trues strain and temperature with YS_0 and YS_{Tmin}.

Dislocation density and FWHM

Dislocation density provides another way to analyze the onset of yielding at the micro level. Unlike lattice strains, the dislocation density evaluation depends on peak broadening and represents intragranular microstrains. Figure 7.17 shows the relative dislocation density behavior evaluated for HC260Y for the initial loading and three reloadings of a cyclic tensile test. Plotted is the true stress versus the root mean square of the dislocation density, like suggested in Tomota et al. (2003). Vertical lines mark the parameters YS_0 and YS_{Tmin} again. In order to better visualize the position of YS_0, a horizontal line has been added. During ideal elastic deformation, the dislocation density does not increase. When the yield stress is exceeded, and thus after activation of the slip systems, new dislocations form and the density increases. This behavior is reflected in Figure 7.17. During initial loading (a), the dislocation density increases slightly, but a clear increase can then be seen after exceeding YS_0. It has to be noted that the peak width for the initial loading is the smallest and, due to the instrumental resolution, greater inaccuracies can therefore occur than for the subsequent reloadings. The reloadings (b-d) indicate that the dislocation density hardly changes during elastic loading and there is a significant increase from YS_0 onwards. Each circle in Figure 7.17 represents one measurement. On closer examination, it can be seen that there is a jump in dislocation density after YS_0. From YS_{Tmin} on, the dislocation density appears to increase continuously. It is assumed that this jump is due to the activation of the slip systems. In addition, there is a slight decrease in dislocation density upon reloading. At YS_0, the density is approximately equal to the value at complete unloading. It is assumed that the initial decrease upon reloading is due to dislocations encountering opposing dislocations and thus annihilating each other. With increasing plastic strain, this effect appears to become more pronounced. This behavior is discussed again in Section 7.2.4.

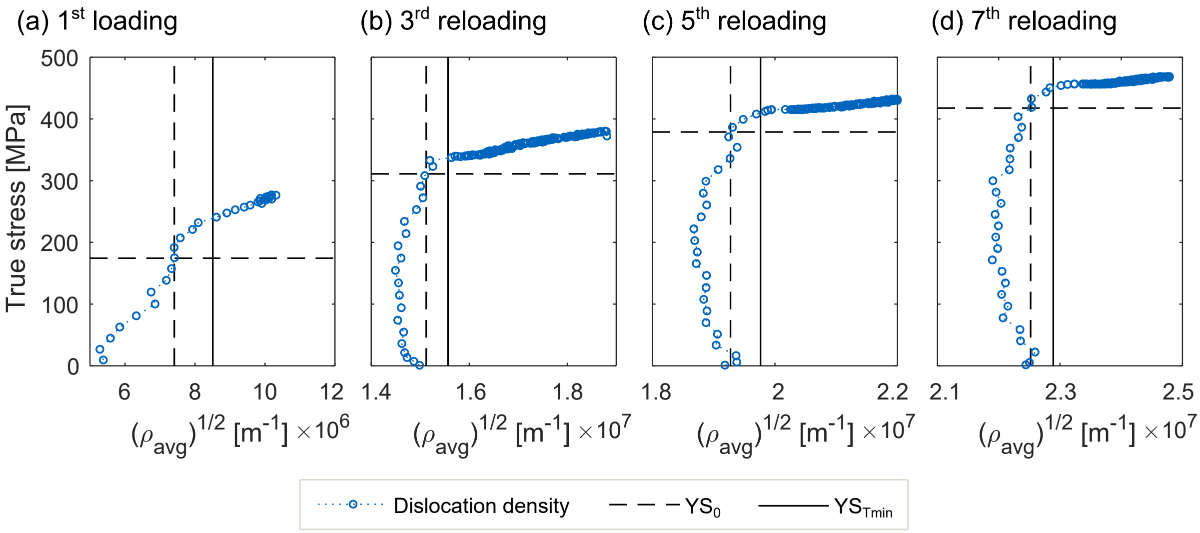

Figure 7.17: HC260Y - True stress versus the root square of the dislocation density ρ_{avg} in longitudinal direction for the initial loading (a) and three reloadings (b-d).

Based on these results, the relationship between the parameter YS_0 and the onset of yielding is clearly evident. Accordingly, YS_0 can be considered a material specific parameter based on physical behavior. The dislocation density in transversal direction shows the same trends and correlation with YS_0. These results can be found in Figure E.4 in the appendix.

Due to the more complex dual-phase microstructure of DP1000, an evaluation of the dislocation density according to Williamson and Smallman (1956) was not possible. Since the peak broadening is correlated with intragranular microstrain, the relative observation of the FWHM can also be meaningful. Here, only the FWHM of the ferrite peaks is evaluated, since it is less affected by the martensite peaks, which are located in the foot region of the ferrite reflections (see Figure 6.11). Figure 7.18 shows the FWHM for the lattice planes (110), (200) and (211) for the initial loading in longitudinal direction. The FWHM of lattice plane (110) increases significantly after exceeding YS_0. For (200) and (211) lattice planes, the FWHM increases slightly from the beginning, but changes the slope after exceeding YS_0. The plasticization of the DP steel depends on the softer ferrite phase. The results of the lattice strains (Figure 7.16) as well as the FWHM (Figure 7.18) show that YS_0 reflects the onset of yielding also for this material, since a correlation between the ferrite behavior and YS_0 can be recognized. However, the correlation is not as evident as for the single-phase material HC260Y. This is due to the more complex microstructural behavior of the DP steel. Martensite absorbs significantly more strain and thus dampens the elastic-plastic transition of the ferrite. Since martensite remains elastic beyond the plasticization of ferrite, it leads to an increase in volume and, in turn, a cooling of the temperature. This also dampens the temperature signal around the temperature minimum.

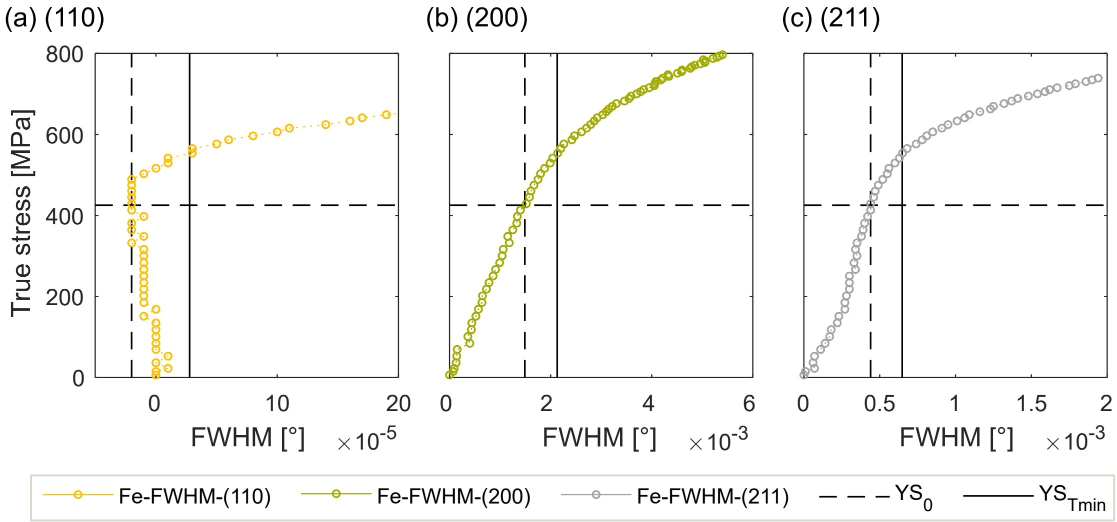

Figure 7.18: DP1000 - True stress versus FWHM of ferrite in longitudinal direction for the initial loading for the lattice planes (a) (110), (b) (200) and (c) (211).

Irreversible macroscopic strain

The onset of yielding at the micro level was investigated and a correlation with the parameter YS_0 was shown. Finally, the question arises whether macroscopic irreversible deformation also occurs when YS_0 is exceeded. For this purpose, cyclic tensile tests were carried out with both materials. In case of DP1000, unloading-reloading cycles were absolved and the maximum load was increased stepwise by 500 N, starting at 5 kN. For DP1000, 5 kN corresponds to a stress of about 260 MPa for the given specimen geometry and is well below YS_0 with around 430 MPa.

HC260Y was cycled with load steps of 100 N starting at 1 kN, which is also well below its YS_0 value. Figure 7.19 shows the stress-strain curves of the considered test.

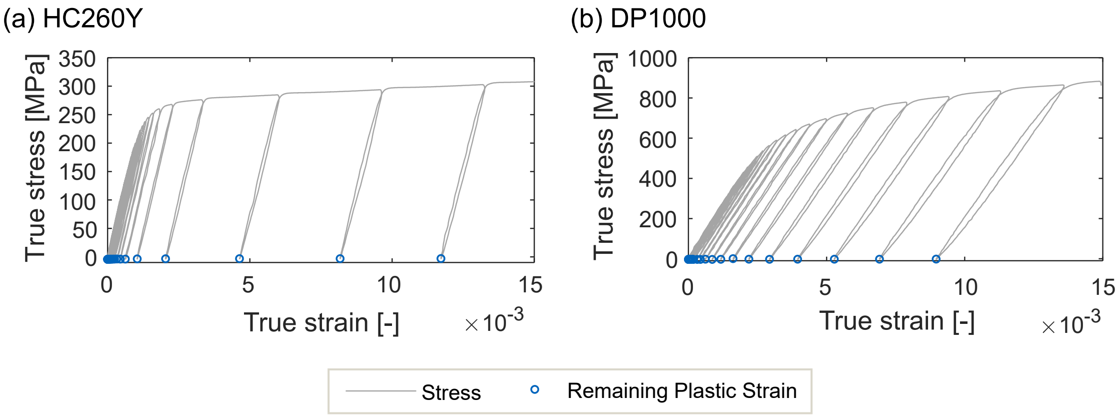

Figure 7.19: True stress versus true strain curves of cyclic tensile tests to investigate the initial onset of irreversible plastic strain for (a) HC260Y and (b) DP1000.

The remaining true plastic strain after each unloading was evaluated. Then, the corresponding true stress was plotted versus the remaining plastic strain to see when an irreversible deformation occurred (Figure 7.20). For both materials, it can be clearly seen that no irreversible strain occurs up to YS_0, and plastic deformation starts when this stress is exceeded. It can be concluded that YS_0 reflects the plastic onset of yielding for HC260Y and DP1000. This confirms that plastic strain is already present at the stress YS_{Tmin}.

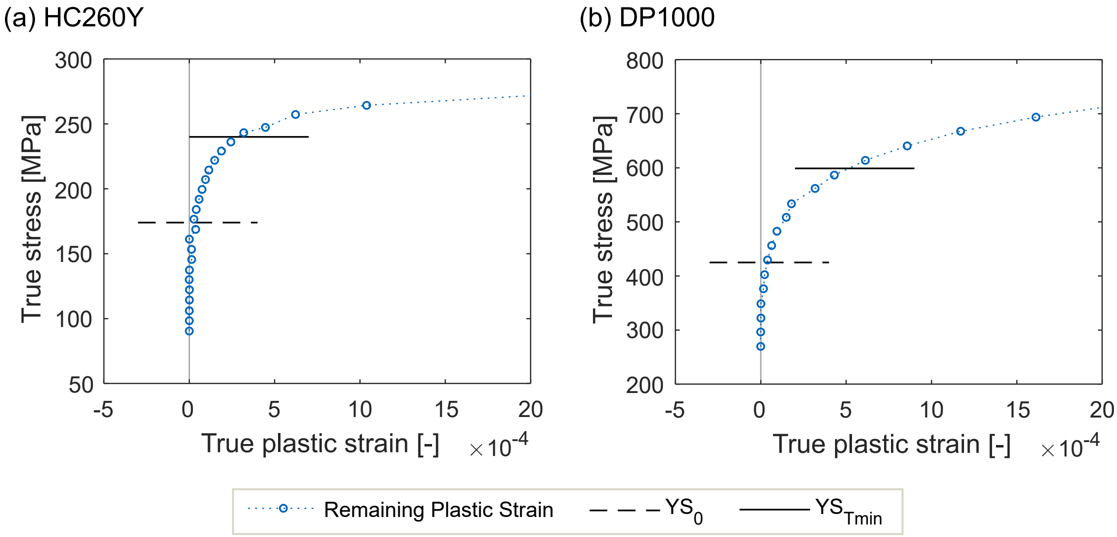

Figure 7.20: True stress versus remaining plastic strain for (a) HC260Y and (b) DP1000. Marked are YS_0 and YS_{Tmin} by horizontal lines.

7.2.3 Elastic Loading Modulus

In this section, the temperature-based determined elastic loading modulus E_{YS0}, which was introduced in Section 6.1.3, is analyzed and compared with two other determination approaches. For this, the elastic modulus according to the standard DIN EN ISO 6892-1 (E_{DIN}) and according to (Sonne, 1999) ($E_{5-18\mathrm{TS}}$) were selected. These are selected, because the standard approach is widely used, in particular in industry, and the approach according to (Sonne, 1999) has clearly specified limits. According to the standard DIN EN ISO 6892-1, the term Young's modulus is only referred to when the strain and force measurement, as well as the strain rate and test method, meet certain requirements. For this reason, as it is no standardized test and evaluation procedure, the modulus is called loading modulus here. This leads to a clear distinction from the unloading modulus E_{Chord}. The onset of yielding, or its equivalent parameter is necessary for several loading modulus determination methods. Figure 7.21 shows the initial loading in a tensile test for (a) HC260Y and (b) DP1000. Marked are the parameters YS_0, YS_{Tmin} and $YS_{0.2\%}$, which clearly differ. As expected, YS_0 is at the upper end of the linear region of the stress-strain curve, YS_{Tmin} is in the elastic-plastic transition, and $YS_{0.2\%}$ is clearly in the plasticized part of the stress-strain curve. Grain-to-grain yielding is more pronounced for the initial plasticization, i.e. the initial activation of the slip systems, which leads to a smoother elastic-plastic transition. Hence, YS_0 is significantly lower than YS_{Tmin}. The results for subsequent loadings in a cyclic tensile test can be seen in the appendix in Figure E.5.

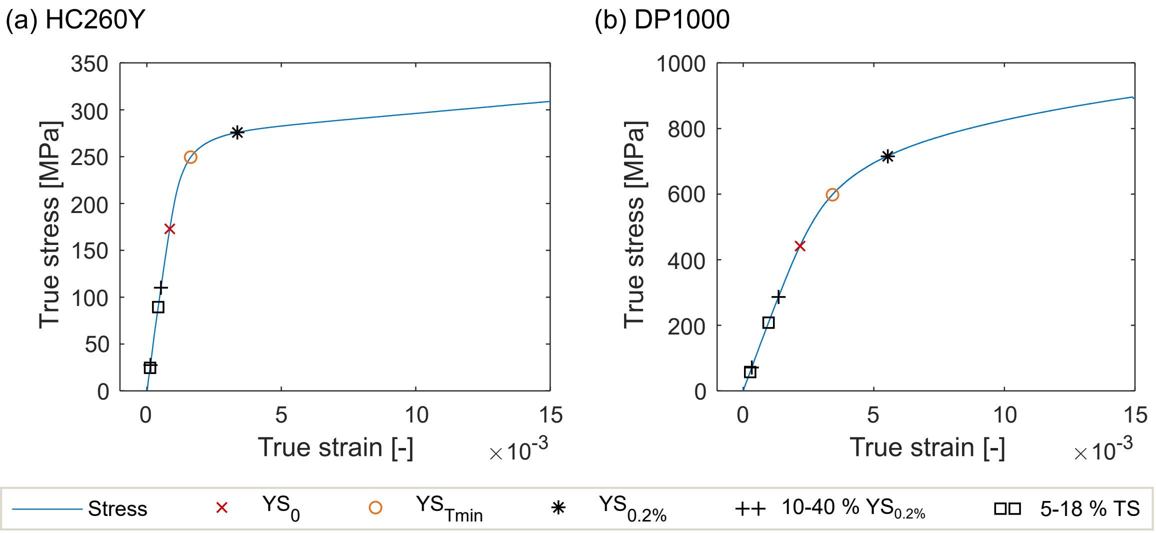

Figure 7.21: Comparison of the initial loading with YS_0, YS_{Tmin} and $YS_{0.2\%}$ for (a) HC260Y and (b) DP1000. Additionally, the areas for the determination of E_{DIN} and E_{5-18TS} are marked.

Figure 7.21 additionally shows the evaluation ranges for E_{DIN} between 10 - 40 % of $YS_{0.2\%}$, and $E_{5-18\text{TS}}$ between 5 - 18 % of TS. It gets evident that the evaluation ranges for the loading moduli E_{DIN} and $E_{5-18\text{TS}}$ lie in the lower range of the stress-strain curve. In comparison, the evaluation range for E_{YS0} from 5 % of TS to YS_0, considers a larger part of the loading curve for the evaluation.

In Section 7.1.2, the sensitivity of the determination of the parameter YS_0 was investigated and maximum deviations of 4.95 % for HC260Y and 2.39 % for DP1000 were found for the initial loading. The influence of this deviation on the temperature-based determination of E_{YS0} has to be analyzed. Therefore, the value for YS_0 of the initial loading was varied between 90 % and 110 % for HC260Y and 95 % and 105 % for DP1000, which is around twice as large as the deviation found in the sensitivity analysis of YS_0 for the particular material. Table 7.2 shows the results for this variation for the initial loading. For both materials, the standard deviation is between 1 % and 1.5 %. Therefore, one can conclude that the parameter E_{YS0} shows little sensitivity to the variation of YS_0. Furthermore, the elastic modulus values of around 202 GPa of both materials are in good agreement with the expected value for steel materials.

Table 7.2: Variation of E_{YS0} dependent on YS_0 for the initial loading in [MPa] and its standard deviation (SD) in [%].

	0.9 × YS_0	0.95 × YS_0	YS_0	1.05 × YS_0	1.1 × YS_0	SD in [%]
HC260Y	204.02	202.70	201.21	199.44	197.37	1.31
DP1000		203.17	201.24	198.92		1.06

In Section 2.4, several determination approaches for the loading modulus were presented. Now, the approaches E_{DIN} and $E_{5-18\text{TS}}$ are compared with E_{YS0}. This is done for both materials, the strain rate 0.0004 s^{-1} and three repetitions. A cyclic tensile test is performed to be able to analyze the evolution of the loading moduli as a function of plastic strain. The necessity of an initial slope for the determination of $YS_{0.2\%}$ has already been discussed. In this study, the slope up to YS_0 was used for this purpose. Figure 7.22 shows the results for (a) HC260Y and (b) DP1000. For comparison, the chord modulus E_{Chord} is plotted additionally. The moduli E_{DIN} and $E_{5-18\text{TS}}$ are higher than the values for E_{YS0} for all loadings. For all three methods, the scatter is largest at the initial value. In the further course, the loading modulus E_{YS0} shows little scattering. The moduli E_{DIN} and $E_{5-18\text{TS}}$ show significantly larger deviations for the three repetitions. In addition, $E_{5-18\text{TS}}$ shows a slight increase with increasing plastic deformation for HC260Y, which cannot be explained physically in this way and can therefore be attributed to measurement inaccuracy. Only the lower region of the stress-strain curve is used for the regression and this area can be suspect to inaccuracies in the tensile test due to the clamping of the specimen for example. For the approach according to the standard, it is up to the user whether these values are trusted or whether the limits for the determination are changed again so that other values for the loading modulus are obtained. This is a clear disadvantage of this approach, since no precise specifications are made and it is significant user-dependent. With E_{YS0}, a clear decreasing trend of the loading modulus with increasing plastic strain can be seen, which is closer to the values for the unloading curves E_{Chord} for both materials. The advantage of E_{YS0} is that the limits are fixed and now depend directly on the onset of yielding.

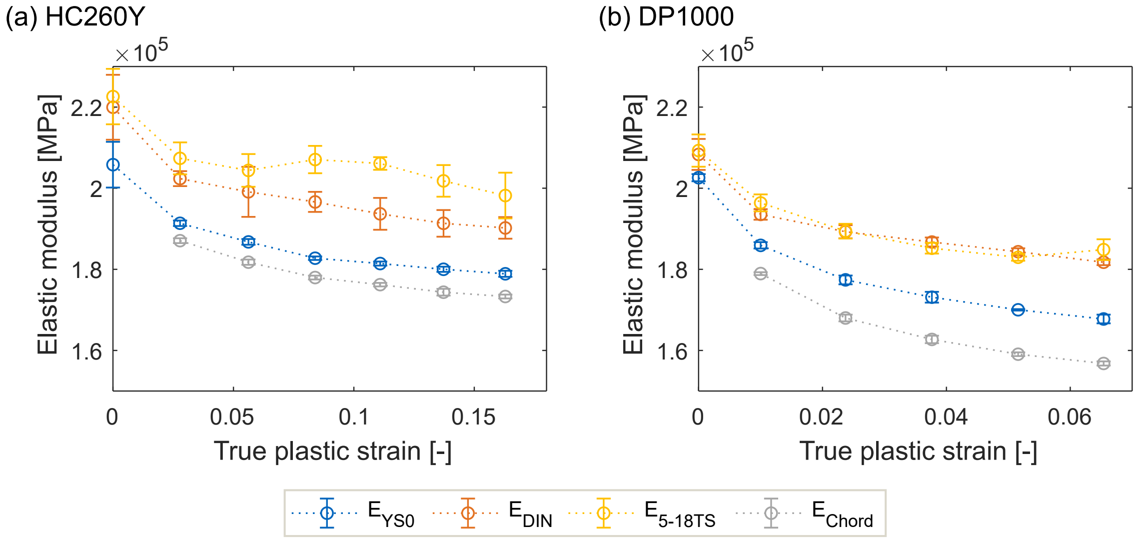

Figure 7.22: Comparison of different elastic modulus determination approaches in a cyclic tensile test for (a) HC260Y and (b) DP1000. (strain rate 0.0004 s^{-1})

Now the values for E_{YS0} are to be compared with the DEC_{hkl} of individual lattice planes. The DEC_{hkl} are based on the stiffness of the lattice planes and thus the lattice structure of the materials. For their evaluation, the same determination approach was used as for E_{YS0}. The value of YS_0 was taken as an upper limit and 5 % of TS as a lower limit. Figure 7.23 shows the results. In (a), E_{YS0} is compared to DEC_{hkl} of five lattice planes for HC260Y. The DEC_{hkl} for HC260Y are between 180 GPa and 250 GPa, with the lowest value for the lattice plane (200) and the highest for (220). The DEC_{hkl} values for all lattice planes do not show strain-dependent behavior, as they hardly change with increasing plastic strain. Hence, the strain-dependent behavior of the loading modulus E_{YS0} is related to other material effects. In (b), it is compared to the DEC_{hkl} of three lattice planes, separately for martensite and ferrite, for DP1000. The DEC_{hkl} for both phases for the lattice planes (110) and (211) show similar results at around 240 GPa. Again, no plastic strain-dependency is evident. The values of the DEC_{hkl} for the lattice plane (200) are significantly lower. For ferrite, it is stable for all plastic strains around

180 GPa. For martensite, it is around 170 GPa with a slight change with increasing plastic strain. The lattice plane (200) shows a high level of strain anisotropy and the difference between the DEC_{200} for ferrite and martensite can be explained by polycrystalline grain interactions (Cong et al., 2009). Additionally, it has to be noted that the lattice plane (200) has the lowest intensity, which means that the counting statistics is worse compared to the others. This aspect leads to a lower accuracy, thus the measurement of lattice plane (200) is more prone to errors than for the other two lattice planes and less reliable. Overall, the effect of the decreasing elastic modulus is not evident in the DEC_{hkl} for DP1000 (Figure 7.23 (b)), if one neglects the martensite lattice plane (200).

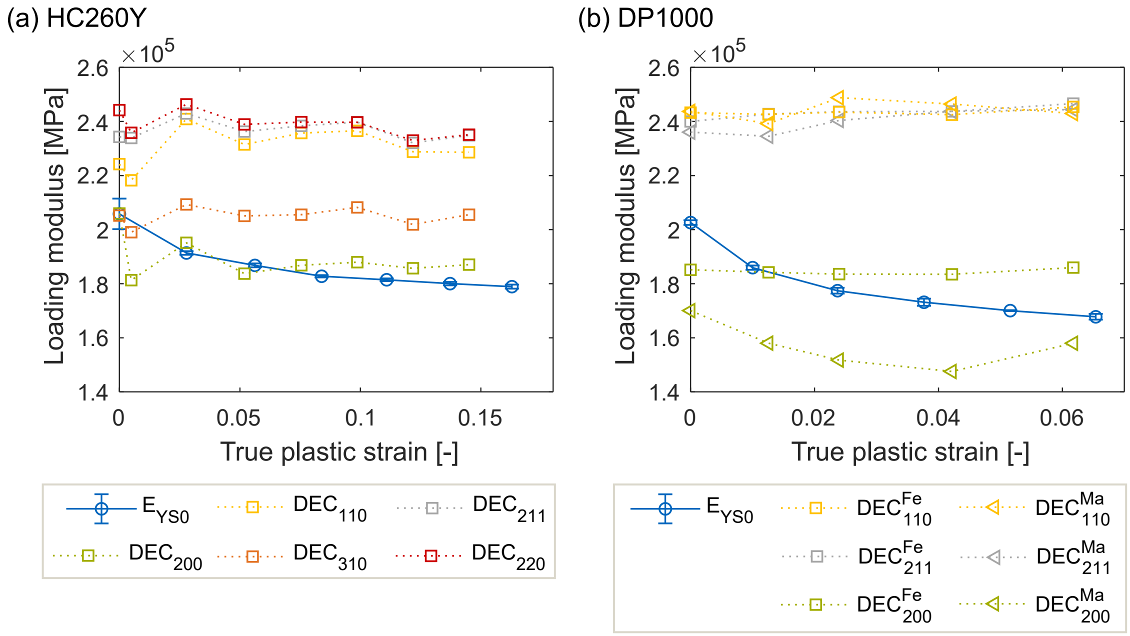

Figure 7.23: Comparison of E_{YS0} with DEC_{hkl} as a function of true plastic strain for (a) HC260Y and (b) DP1000. For DP1000, DEC^{ph}_{hkl} are differentiated into ferrite and martensite.

7.2.4 Anelasticity

Dislocation motion and microstructural inhomogeneities are most plausible reasons for anelastic behavior (Torkabadi, 2018) and were discussed in Section 2.5.1. Hence, the anelastic behavior has to be correlated with microstructural behavior. However, in a first step, the macroscopic anelastic behavior of the two steel materials is compared. Figure 7.24 (a) shows the anelastic strain proportion relative to the total recovery strain (see Section 2.5.1). In this way, materials of different strength can be compared with each other. It can be clearly seen that the proportion of anelastic strain is significantly higher for DP1000 than for HC260Y. However, anelasticity is also present for HC260Y. Accordingly, neither mechanism can be excluded and it appears that both mechanisms occur. In the case of the DP1000, it is noticeable that the proportion of anelastic strain increases significantly at the beginning. This increase reduces with increasing plastic strain. HC260Y shows an approximately linear increase of anelastic strain.

Figure 7.24 (b) reflects the chord modulus E_{Chord} and the temperature-based loading modulus E_{YS0} as a function of true plastic strain. There is no initial value for E_{Chord}, therefore the initial value of E_{YS0} was used here. The chord modulus is directly related to the anelastic behavior, since it is determined by the complete unloading curve. This can be seen by the inverse behavior compared with its anelasticity. It decreases strongly in the beginning and seem to saturate with increasing plastic strain, which is in good agreement with the findings of Yoshida et al. (2002). The loading modulus is determined on basis of the loading curve. Thus, it is independent from the anelastic strain from unloading. For both materials, E_{YS0} is slightly higher than the E_{Chord}. This difference is smaller for HC260Y. Since both, the unloading modulus and the loading modulus show a relationship with anelasticity, it can be assumed that the mechanisms responsible for anelastic behavior influence the overall elasticity of the material.

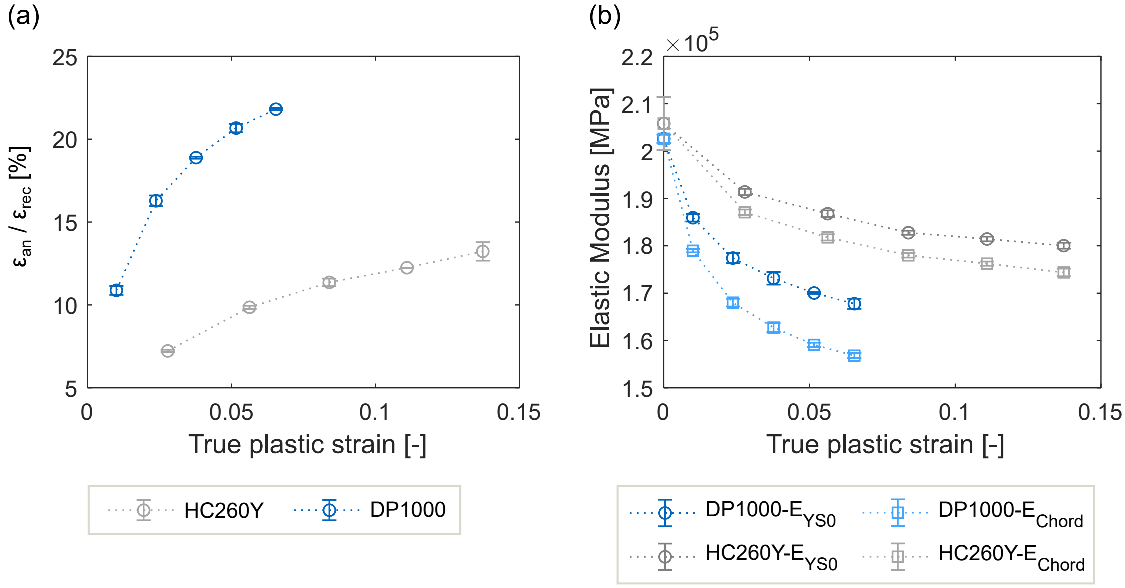

Figure 7.24: (a) Proportion of anelastic strain (ε_{an}) to total recovery strain (ε_{rec}) and (b) comparison of E_{YS0} and E_{Chord} for HC260Y and DP1000.

Anelastic analysis of HC260Y

According to the Bailey-Hirsch relation, the square root of dislocation density is linearly proportional to the hardening of the material (Bailey and Hirsch, 1960). This was analyzed using a standard tensile test. Figure 7.25 shows the true stress versus square root of dislocation density curve. A linear regression line through the range of elastic-plastic deformation approximately confirms the linear proportion between hardening and dislocation density. This is a further validation of the evaluation of dislocation density within this study. It is again in good agreement with the results of Tomota et al. (2003), where the Bailey-Hirsch relation was also proven for a low carbon steel material, but with less experimental datapoints. Furthermore, YS_0 and YS_{Tmin} are marked in Figure 7.25 and the correlations with the onset of yielding found in Section 7.2.2 can be confirmed again. The dislocation density starts to increase after exceeding the YS_0 value.

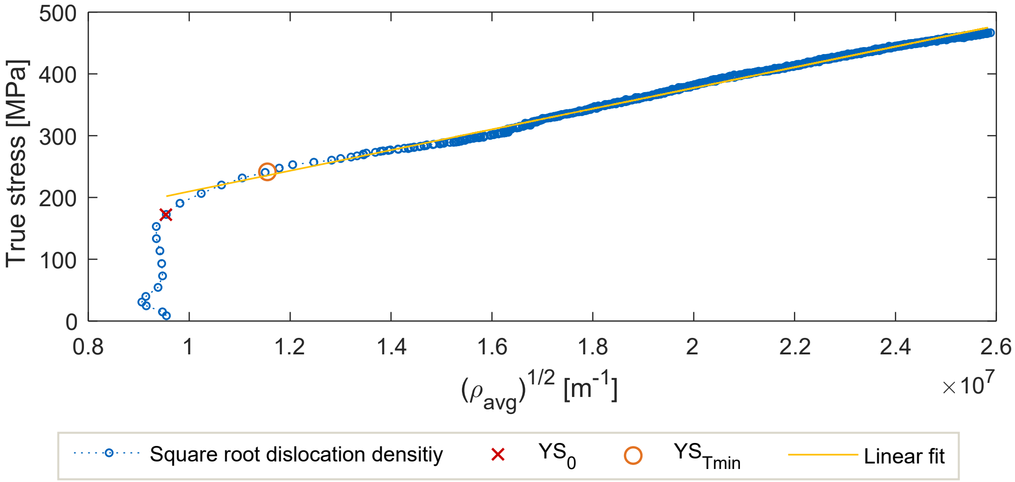

Figure 7.25: HC260Y - True stress versus square root of discloation density. Marked are YS_0 and YS_{Tmin} as well as a linear fit line through the elastic-plastic range.

The motion of dislocations is seen as a driver of anelastic behavior. However, the experimental determination of this motion is still a major challenge. With the in-situ diffraction approach used, it is possible to determine the relative dislocation density. That is, the total line length of dislocations per measured volume (Zhuang et al., 2019). The motion of individual dislocations cannot be identified. Thus, a correlation with anelastic behavior is only possible to a limited extent.

In order to establish a possible connection between the anelasticity and the dislocation density, the behavior of dislocations during deformation must be discussed in more detail. Dislocations are directly related to the hardening of the material, as they act as obstacles, creating a back stress (Ashby, 1970). Due to the back stress, there is a backward movement of the dislocations during unloading (X. X. Zhang et al., 2021). This backward motion can cause dislocations to be annihilated if they are absorbed at their source (Mompiou et al., 2012). In addition, opposing dislocations that encounter each other during unloading can annihilate (Monavari and Zaiser, 2018). All of these effects lead to a decrease in dislocation density. Figure 7.26 shows the dislocation density as a function of test time in (a) longitudinal and (b) transversal direction to the loading. For clarity, three unloading-reloading cycles at higher plastic strains are shown. The reflection is significantly wider than the instrumental resolution (measured by LaB_6 powder) for this plastic strain range and so the dislocation density signal is less noisy. When unloading, the dislocation density decreases unambiguously for all cycles in longitudinal as well as in transversal direction. Furthermore, the dislocation density before unloading is higher than after plasticization in the subsequent reloading. This can be interpreted as reversible plastic strain and thus corresponds to the definition of anelasticity of D. Li and Wagoner (2021).

Comparing the values of dislocation density at the beginning of reloading and the beginning of yielding (YS_0) in longitudinal direction, one finds that these values are approximately the same. It is noticeable that the dislocation density seems to decrease further in between. This decrease in between is hard to explain at this stage. Bowing of dislocations can also lead to a change in dislocation density, since it has an influence on the total length of the dislocations (Mompiou et al., 2012). In addition, dislocations that are mutually aligned can annihilate each other again during reloading. The dislocation density change between the start of reloading and the onset of yielding is not as pronounced in transversal direction. Here, it seems that the density slightly increases. Effects based on dislocation motion are therefore conceivable, because a directional dependence of the dislocation density is recognizable. Further experiments with better instrumental resolution are needed for a more precise explanation of this effect.

In summary, with the change in dislocation density, a dislocation movement can be assumed. Furthermore, it was shown that there is dislocation annihilation during elastic unloading and thus plastic strain can be reversible. This can be seen as anelastic strain, which was shown in Figure 7.24.

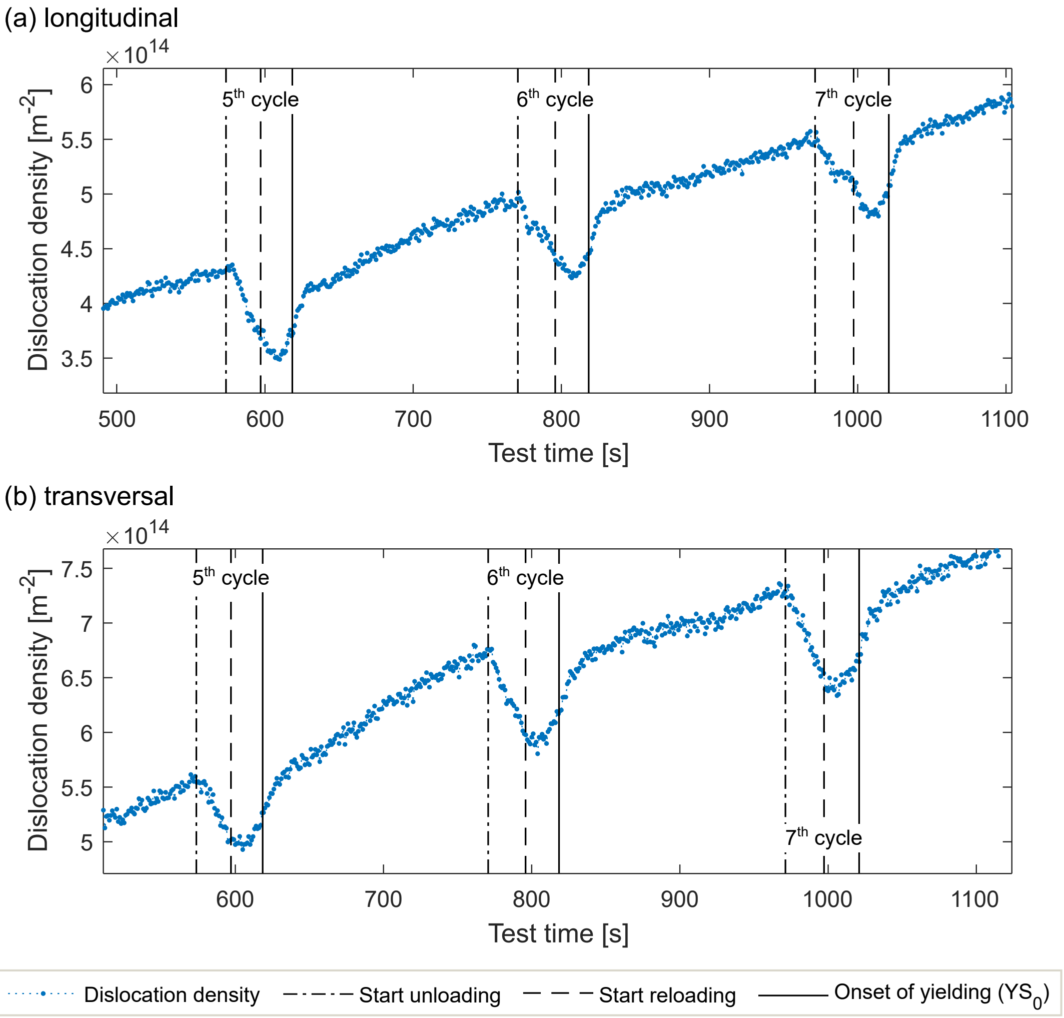

Figure 7.26: HC260Y - Dislocation density versus test time. Shown are the 5th, 6th and 7th loading-unloading cycles of a cyclic tensile test. Vertical lines mark the start of unloading, reloading and the onset of yielding.

Intergranular microstrains can also lead to specific macroscopic behavior and potentially cause anelastic behavior. For this reason, this was also investigated. Figure 7.27 shows intergranular strains as a function of true plastic strain in (a) longitudinal and (b) transversal direction. Intergranular strains are present, which are negative for the lattice planes (110) and (220) and positive for the lattice plane (200) after complete unloading. These intergranular strains can influence the macroscopic behavior. However, since hardly any changes with increasing plastic strain can be seen in both the longitudinal and transversal directions, these cannot explain the increasing anelastic strain.

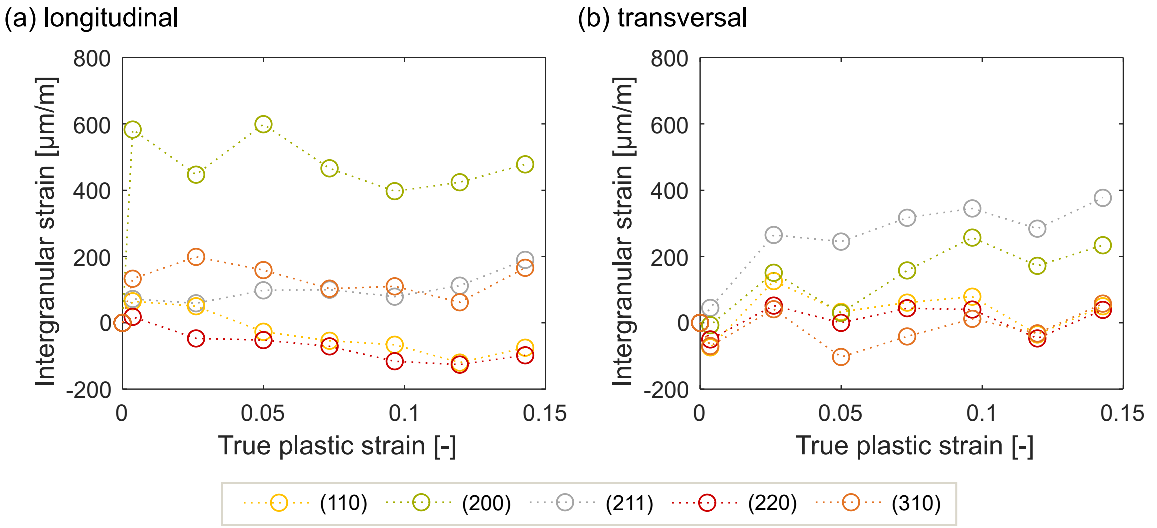

Figure 7.27: HC260Y - Intergranular strain versus true plastic strain for five lattice planes in (a) longitudinal and (b) transversal direction to the loading.

Anelastic analysis of DP1000

Due to the more complex evaluation of the overlapping peaks, a precise evaluation of the integral breadths was not possible, in particular for the martensite phase. Accordingly, no dislocation density could be determined for DP1000. In J. H. Kim et al. (2012) and Govik et al. (2014), it was stated that in DP steel, interphase stresses in particular are responsible for the anelastic behavior. For this reason, the focus here is on the evaluation and analysis of the stresses in the ferrite and martensite phases. The lattice plane (211) is used for this purpose, because it is hardly subject to microstructural anisotropy and more representative for the majority (Woo et al., 2012). It is also proposed by the standard DIN EN ISO 21432 for this kind of analysis. The phase specific stress $\sigma_{\mathrm{hkl}}^{\mathrm{ph}}$ can be calculated on basis of the phase specific $DEC_{\mathrm{hkl}}^{\mathrm{ph}}$ and lattice strain $\varepsilon_{\mathrm{hkl}}^{\mathrm{ph}}$ by the following relation

$$\sigma_{\mathrm{hkl}}^{\mathrm{ph}} = DEC_{\mathrm{hkl}}^{\mathrm{ph}} \cdot \varepsilon_{\mathrm{hkl}}^{\mathrm{ph}} \quad . \tag{7.1}$$

This evaluation of DP1000 can be inversely validated, since the sum of the phase stresses, calculated proportionally with their volume phase fractions, should reflect the macroscopic stress (see Equation 2.13). This validation is shown in Figure 7.28. The martensite phase stress increases up to 1500 MPa, whereas ferrite hardly absorbs stresses above its yield stress of around 600 MPa. The combined sum curve, calculated with Equation 2.13, is in good agreement with the experimental true stress-strain curve.

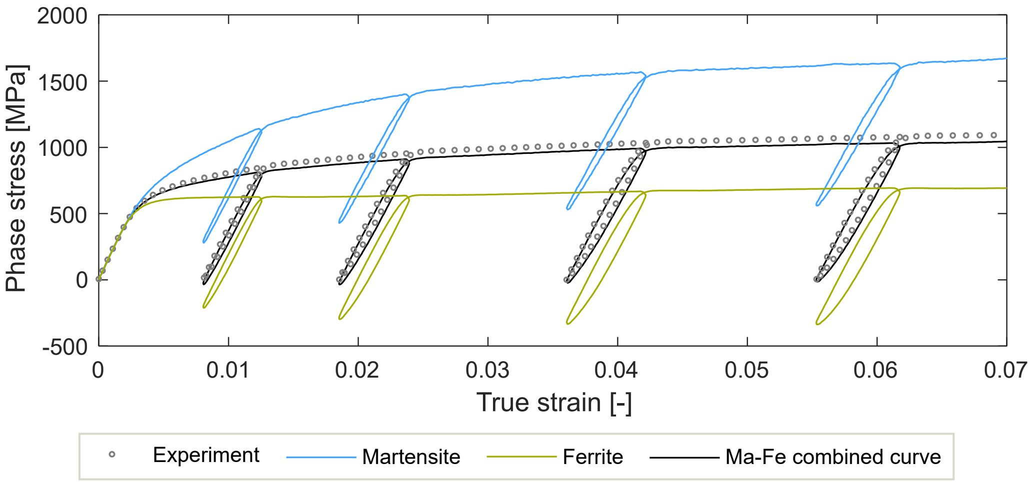

Figure 7.28: DP1000 - Comparison of the macroscopic experiment with phase stress of martensite and ferrite for the lattice plane (211) and their combined curve calculated with their phase fractions.

In general, three deformation states can be defined in the microstructure:

1. *el-el* state: Both, ferrite and martensite are in a purely elastic state (*el*)
2. *pl-el* state: Ferrite is in an elastic-plastic state (*pl*) while martensite is still elastic (*el*)
3. *pl-pl* state: Both phases are in an elastic-plastic state (*pl*)

The transition from the first state to the second is at the onset of yielding (YS_0) and thus can be determined relatively accurately. The transition from the second to the third state cannot be determined exactly due to the smooth transition of the martensite. This can be seen from the hardening behavior of the martensite in Figure 7.28. It slowly approaches a horizontal line and no transition point can be identified. Furthermore, Figure 7.28 clearly shows that martensite absorbs much more stress than ferrite and remains essentially elastic. This results in the martensite phase placing the ferrite phase under compressive stress during unloading. Figure 7.29 (a) shows the martensite and ferrite phase stress again. Additionally, the residual stress state after complete macroscopic unloading is marked. The orange area reflects the interphase stress ($\Delta\sigma_{\mathrm{Ma-Fe}}$), i.e. the difference between the residual martensite phase stress and ferrite phase stress at macroscopic stress free state. In Figure 7.29 (b), $\Delta\sigma_{\mathrm{Ma-Fe}}$ is determined for each unloading-reloading cycle and plotted versus the true plastic strain. The curve clearly shows that the interphase stress increases strongly at the beginning, and its increase becomes less with increasing plastic deformation. This can be explained by the fact that the ferrite phase plasticizes at around 600 MPa, while the martensite phase remains elastic (*el-el* and *pl-el* state).

Due to this condition, $\Delta\sigma_{\mathrm{Ma-Fe}}$ increases significantly until the martensite also starts to plasticize at around 1500 MPa (*pl-pl* state). If this is the case, the ratio between the residual phase stress in ferrite and martensite stabilizes and hardly changes during the unloading-reloading cycles. The progression of interphase stresses with increasing plastic deformation is in good agreement with the progression of anelasticity (see Figure 7.24 (a)). This indicates that the anelastic behavior is strongly dependent on interphase stresses.

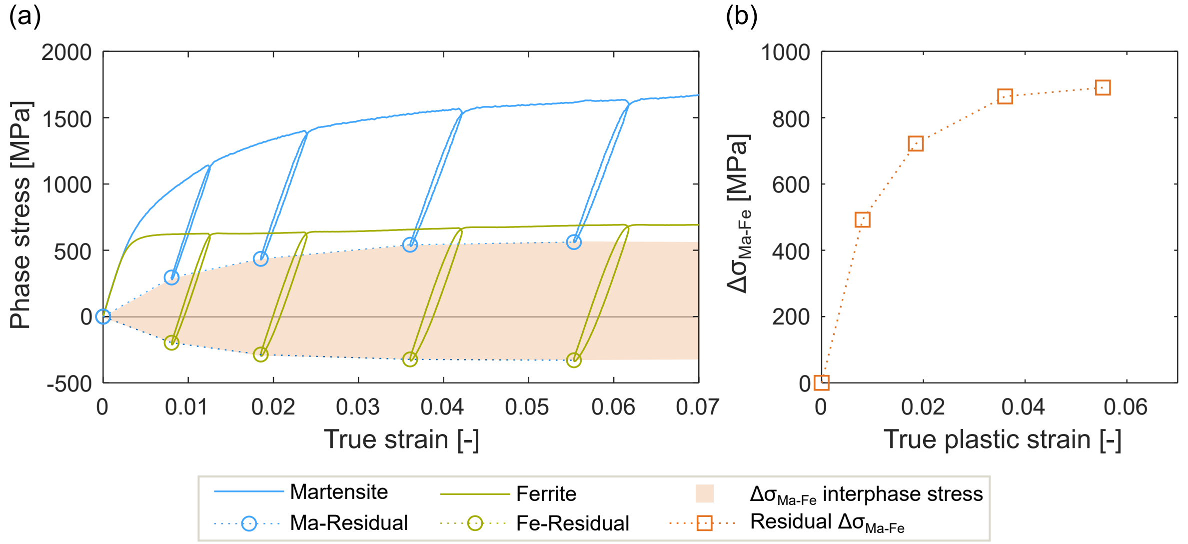

Figure 7.29: DP1000 - (a) Phase stresses and their residual stresses at complete unloading versus true strain and (b) residual interphase stresses versus true plastic strain.

A closer look at the unloading-reloading cycles in Figure 7.29 (a) reveals that ferrite shows clearly a more pronounced hysteresis than martensite. It is also noticeable that the curve becomes more nonlinear, especially in the lower part of the unloading curve, i.e. when ferrite enters the compressive range. The instantaneous tangent modulus for the phase stresses of the ferrite and martensite as well as the macroscopic stress was calculated for four unloadings to investigate this behavior in more detail (see Figure 7.30). The instantaneous tangent modulus gives the slope for each measuring point to the respective neighboring measuring points. This means that a change in the tangent modulus during the unloading corresponds to nonlinear behavior. For better clarity, a vertical line is added at the state, where ferrite enters the compressive range during unloading (Figure 7.30 (a)). The tangent modulus in ferrite shows a significant decrease with compressive loading. At the first unloading, the tangent modulus decreases to about 120 GPa, at the second already to below 100 GPa. Between the second, third and fourth unloading, there is no big difference. This again corresponds to the anelastic behavior, which increases significantly in particular at the beginning of plastic deformation. Martensite shows less nonlinearity (Figure 7.30 (b)). At the end of unloading, there is a slight decrease, but it is much smaller than with ferrite. It can be assumed that this is related to the residual phase stresses, which remain in the tensile range in the case of martensite. Figure 7.30 (c) shows the tangent moduli for the macroscopic true stress. The behavior reflects a combination of that of ferrite and martensite. It is in good agreement with the results in Cleveland and Ghosh (2002), where a similar evaluation was done for high-strength steel, but only macroscopically.

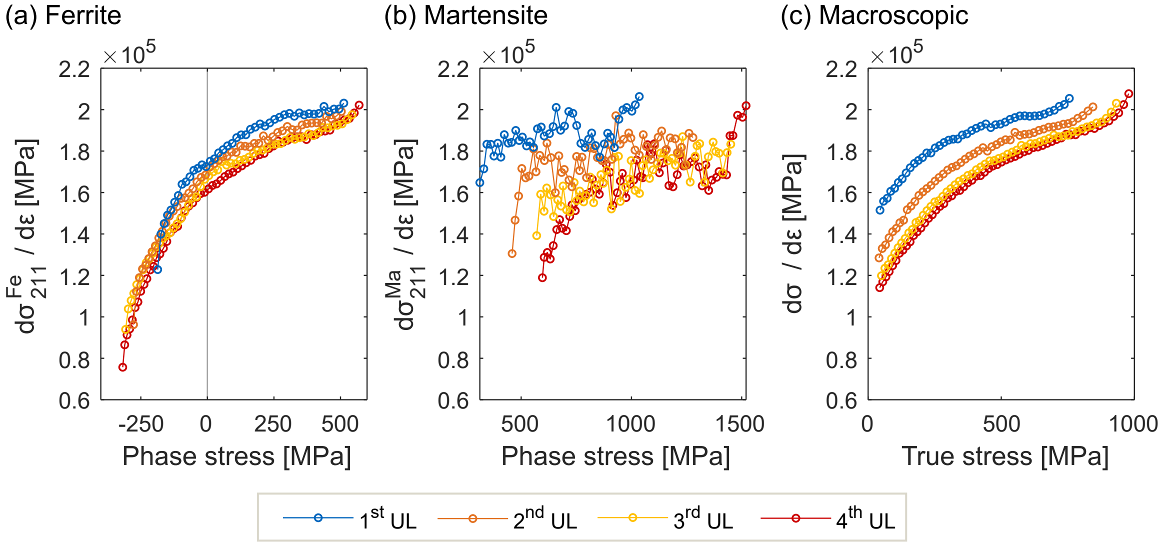

Figure 7.30: DP1000 - Instantaneous tangent modulus during UL for (a) ferrite phase stress, (b) martensite phase stress and (c) macroscopic true stress. The tangent moduli are calculated for four unloadings.

In summary, anelastic behavior occurs in both HC260Y and DP1000. It is much more pronounced in DP1000. Dislocation motion could be detected in the HC260Y by the analysis of the dislocation density and a correlation is conceivable. For DP1000, it was shown that interphase stresses occur in the same way as the anelastic strain. It is assumed that in particular the different behavior between martensite and ferrite can be seen as a main driver for the significant anelasticity in this material. It has also been shown that the ferrite is subjected to compressive stress by the much harder martensite phase when unloaded. This compressive loading leads to significant increasing nonlinear behavior, which is in good agreement with the nonlinear behavior of the macroscopic curve. Therefore, the anelasticity arises due to the compressive loading, and thus the load change in the ferrite.

7.2.5 Re-yielding

In this section, the re-yielding behavior for both single-phase and dual-phase steel is analyzed at microstructural and macroscopic levels. Based on these investigations, conclusions are drawn on the material behavior after changing the load direction. As in the previous sections, lattice strains, peak widths, dislocation densities and phase stresses are used in this analysis. To identify a possible tension-compression asymmetry, additional compression tests were performed. In the end, by correlating the results with the temperature measurements (see Section 7.1.4), conclusions are drawn about the temperature measurement in the TC test.

Analysis of tension-compression asymmetry
In order to be able to attribute differences between the tension and compression behavior to the Bauschinger effect, the influence of a possible TC asymmetry must be known. In theory, the onset of yielding during uniaxial tension and compression is assumed to be the same, but this assumption could be disproved for several materials (Maeda et al., 2017). For example, for magnesium materials, a pronounced tension-compression asymmetry was demonstrated (*hcp*) (Lou et al., 2007). For materials with *bcc* or *fcc* lattice structures, it is known that they do not show such asymmetry (Mehrabi et al., 2020). However, there are studies that showed asymmetric tension and compression behavior also for low carbon steel (Koizumi and Kuroda, 2018) and high-strength dual-phase steel (J. Kim et al., 2022).

Compression tests were performed to investigate the asymmetry using the *utg* setup. The stress-strain curves of the compression tests were then compared with those of the tensile test. Figure 7.31 shows the results for this investigation for (a) HC260Y and (b) DP1000. For better comparability, the compression curves are plotted inversely. The compression stress-strain curve of HC260Y is clearly higher than the tensile curve. Hence, the onset of yielding is at higher stresses and asymmetric TC behavior occurs. The compression and tensile stress-strain curves for DP1000 hardly differ. At approximately 0.5 % true strain, it slightly starts to deviate and the compression stress-strain curve shows slightly higher stresses. This indicates a minor TC asymmetry for DP1000 and the yielding seems to be not affected.

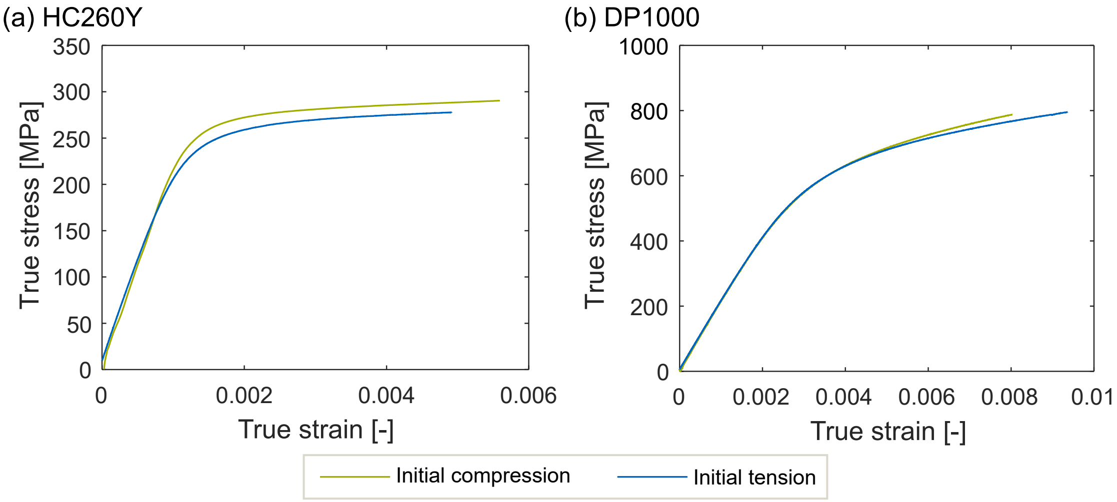

Figure 7.31: Comparison of stress-strain curves of compression and tensile test for (a) HC260Y and (b) DP1000. The compression curves are plotted inversely.

HC260Y

Macroscopic stress-strain curves of the TC test of HC260Y have already been shown in Section 7.1.4. There, it was also shown that a temperature-based determination of the re-yielding was possible. Now the focus is, whether the determined stress value YS_{re} also shows a correlation with the microstructural behavior.

Figure 7.32 (a) shows the true stress versus true strain curve for a TC test performend under synchrotron radiation (*DESY* setup). YS_{re} is marked. YS_{re} is -177 MPa with a standard deviation of 10 MPa. In comparison, the average YS_0 value for this material is 178 MPa. Hence, the temperature-based determined parameters for yielding show similar results for initial yielding and re-yielding after load path change at around 3 % true tensile prestrain. Figure 7.32 (b) reflects the dislocation density for the unloading and compression range, highlighted in blue in (a). The dislocation annihilation during UL has already been addressed and can be confirmed here. During compressive loading, the dislocation density hardly decreases any more, and above a certain stress range, a clear increase can be seen. This range reflects the re-yielding. For better estimation of the YS_{re} parameter, it is plotted on the dislocation density curve. In fact, the value is in the range from which the dislocation density starts to increase again. Thus, also for the temperature-based determination of the re-yielding, at least for the single-phase material, a direct correlation with the microstructural material behavior can be established.

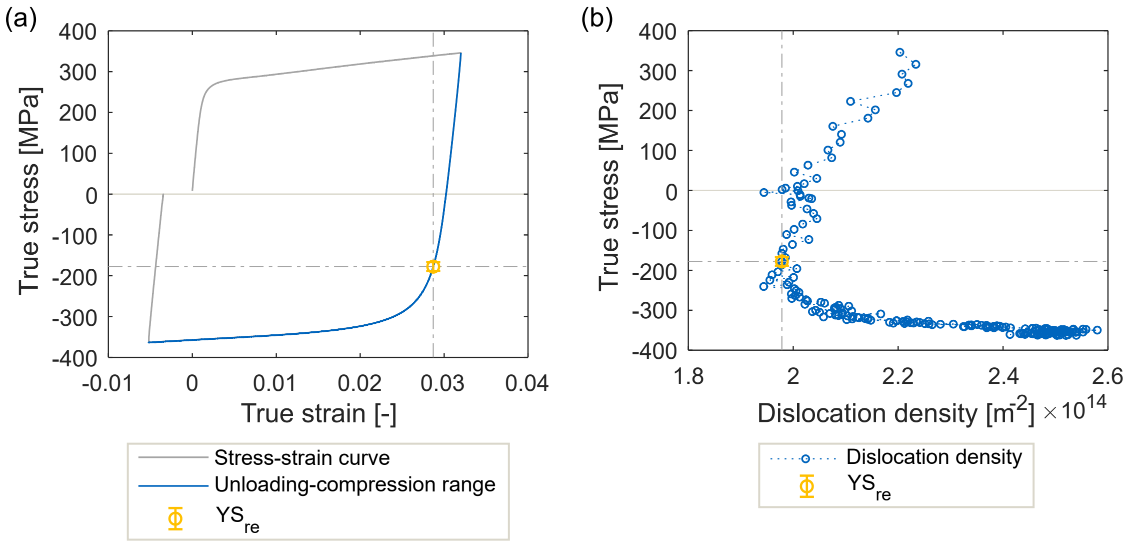

Figure 7.32: HC260Y - (a) True stress-strain curve of TC test and (b) true stress versus dislocation density for the unloading-compression range. Additionally, YS_{re} is marked in both plots.

In addition to the dislocation density, the relationship between re-yielding and lattice strains is analyzed. Figure 7.33 shows the lattice strains for four lattice planes versus the true strain. Again, only the unloading and compression range is plotted (see Figure 7.32 (a) blue range). The different values at the start of unloading indicate intergranular strains, i.e. microstructural anisotropy. The lattice strains show a smooth elastic-plastic transition under compressive loading and the individual lattice strains differ in their yielding behavior. This different yielding behavior was already discussed in Section 7.2.2 and is called grain-to-grain yielding.

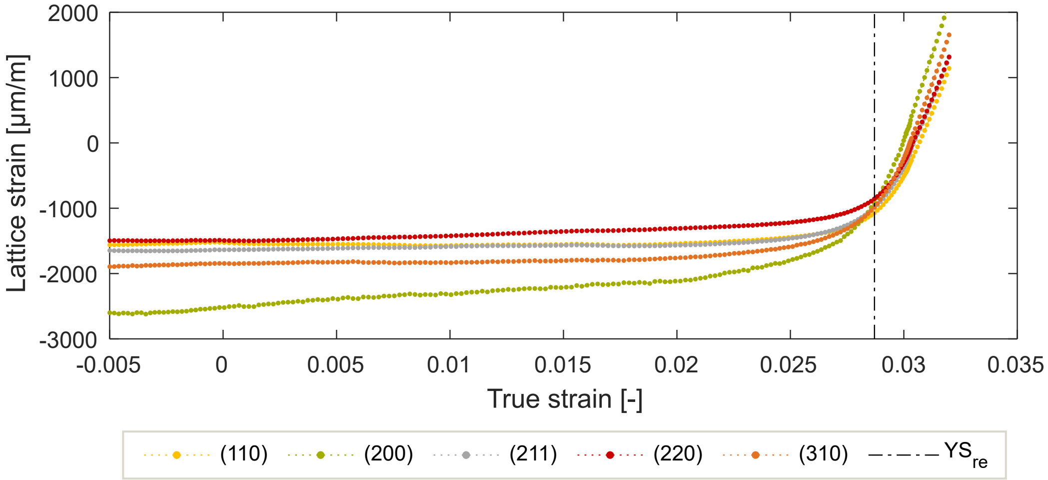

Figure 7.33: HC260Y - Lattice strain versus true strain for five lattice planes with YS_{re}.

In order to evaluate the extent of grain-to-grain yielding, it is necessary to compare yielding with and without change of load direction. Figure 7.34 shows this comparison. In (a), the tensile loading of a cyclic tensile test after around 2.6 % true tensile prestrain is presented. In (b), the compressive loading of a TC test after 3 % true tensile prestrain is plotted. In order to compare the relation of lattice strains with the macroscopic TC curve, the areas in which the macroscopic curve is in tension and compression are colored in (b). Vertical lines highlight the parameters YS_0 and YS_{Tmin} for tension and YS_{re} for TC. Without changing the load direction, there is a sharp transition from elastic to elastic-plastic behavior. Almost no grain-to-grain yielding is evident, since there is hardly any difference between the particular lattice strains (see Figure 7.15). This is explained by the fact that slip systems have already been activated in the respective load direction and, if the same direction of reloading is used, they can be reactivated more easily. When compressive loading is applied to the material after initial tensile loading (Figure 7.34 (b)), it can be seen that a particularly smooth transition occurs. The lattice planes appear to plasticize differently and thus, a pronounced grain-to-grain yielding can be seen. The results show that the Bauschinger effect also occurs at the microstructural level.

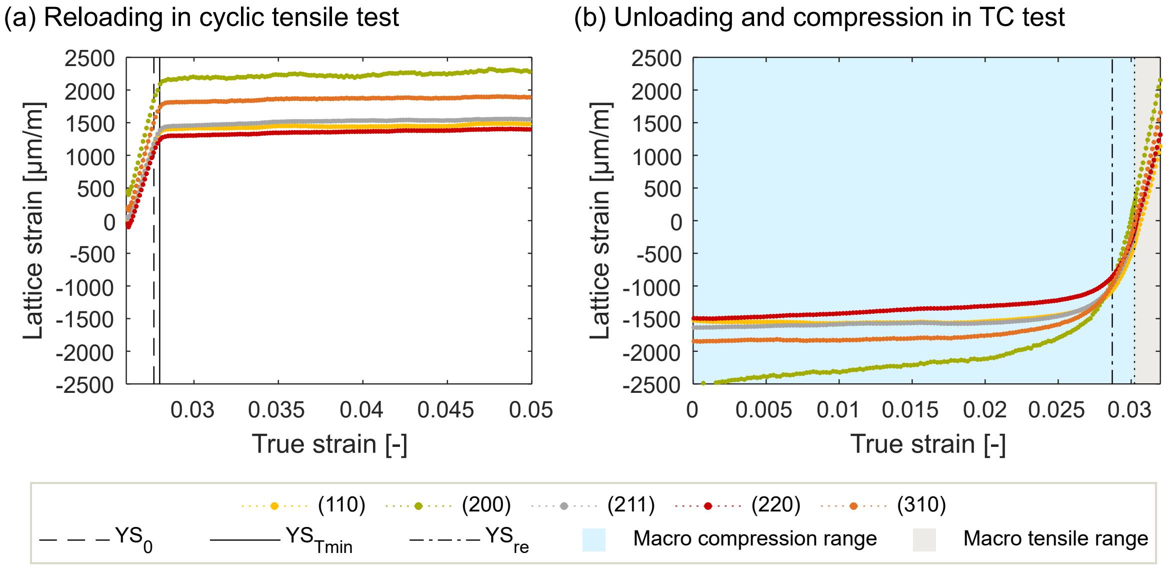

Figure 7.34: HC260Y - (a) Lattice strain versus true strain for tensile loading and (b) for compressive loading. Vertical lines highlight YS_0, YS_{Tmin} and YS_{re}. Plot (b) is divided in the macroscopic tensile and compression range.

The stress value YS_{re} reflects the beginning of re-yielding well. Without changing the load direction and after around 3 % true strain, the lattice strains show values between 1300 µm/m and 2300 µm/m. With the change in load direction, values between -1500 µm/m and -2500 µm/m are reached for the five considered lattice planes. During compression, the microstructure seems to be able to absorb more strain and hence, resist higher stresses. This can be explained by the TC asymmetry investigated and shown in Figure 7.31 (a). It should be noted here that not exactly the same tensile prestrains are compared.

In summary, there is no early re-yielding in HC260Y as early re-yielding is defined as plasticization under macroscopic tensile load here. The re-yielding occurs in the macroscopic compressive range. Nevertheless, there is a clear difference in grain-to-grain yielding compared to without load change, which confirms the Bauschinger effect also at the microstructural level. Temperature-based evaluation of the YS_{re} parameter shows good agreement with microstructural plasticization. Thus, the temperature-based evaluation method could also be validated for re-yielding, at least for the single-phase steel.

DP1000

For DP1000, the re-yielding analysis is more complicated due to the interaction of the two phases. On the one hand, it has already been established that the ferrite phase plasticizes at higher stresses than for a single-phase ferritic material. On the other hand, the ferrite is exposed to the much harder martensite, which absorbs further elastic strain and thus further prestresses the ferrite.

Figure 7.35 shows for a first overview in (a) the macroscopic true stress-strain curve and in (b), the true stress versus lattice strain curve for the lattice plane (211). For better clarity, characteristic points are marked in the microstructural curves as well as in the macroscopic curve. As in the cyclic test, ferrite and martensite lattice strains increase equally under tensile loading until plasticization of the ferrite occurs, which is reflected by YS_0. Martensite then absorbs additional elastic strain. In Figure 7.35, the start of elastic unloading is shown with a black dot in the macroscopic curve and correspondingly in the ferrite and martensite curves. The significantly larger elastic strain absorbed in the martensite causes the ferrite to enter a compression state during unloading already under macroscopic tensile stress (see red circle "Fe-Zero"). The martensite enters the compressive state later (see red square "Ma-Zero"). At this point, the macroscopic stress is already negative. In the macroscopic compression range, no linear behavior is recognizable for both phases. The ferrite seems to plasticize directly and influences the behavior of the martensite, similar to its behavior in tension.

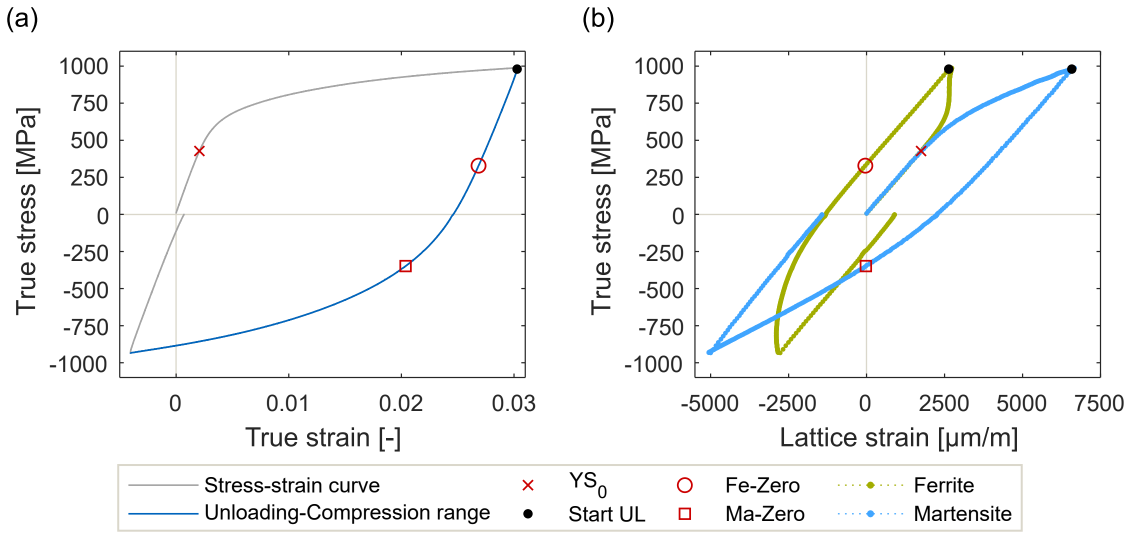

Figure 7.35: DP1000 - (a) True stress-strain curve of TC test and (b) true stress versus lattice strain separated for ferrite and martensite for the lattice plane (211). Additionally, the characteristic states zero ferrite lattice strain (Fe-Zero), zero martensite lattice strain (Ma-Zero) and start of unloading (Start UL) are marked in both, (a) and (b).

Figure 7.36 shows true macroscopic stress versus lattice strain curves for three lattice planes. Plotted is the unloading-compression range (see Figure 7.35 (a) blue range) for ferrite and martensite. The curves are zeroed at the beginning of the unloading for better comparability. The slope differences again confirm strong microstructural anisotropy. Furthermore, it can be seen that after macroscopic stress zero crossing, the curves become nonlinear. This indicates plasticization. The curves for ferrite converge to a vertical line, i.e. they can no longer absorb any further strain and plasticize completely. Martensite, on the other hand, does not appear to plasticize, since lattice strain can be absorbed over the entire compressive loading.

The ferrite phase already changes to compression during macroscopic tensile stress. Due to the significantly lower onset of yielding compared to martensite, the softer ferrite has a significant influence on the macroscopic yielding and re-yielding behavior. For HC260Y, in Figure 7.34, the comparison of tensile and compression curve at a similar tensile prestrain was shown. The ferrite showed comparable behavior for both cases. Similar lattice strain values were obtained, slightly higher in compression, possibly due to the TC asymmetry. This means that the onset of yielding of ferrite is comparable in compression and tension. Only the grain-to-grain yielding was significantly different due to the change in load direction. Accordingly, for DP1000, ferrite can be expected to start plasticizing in compression at values similar to those in tension.

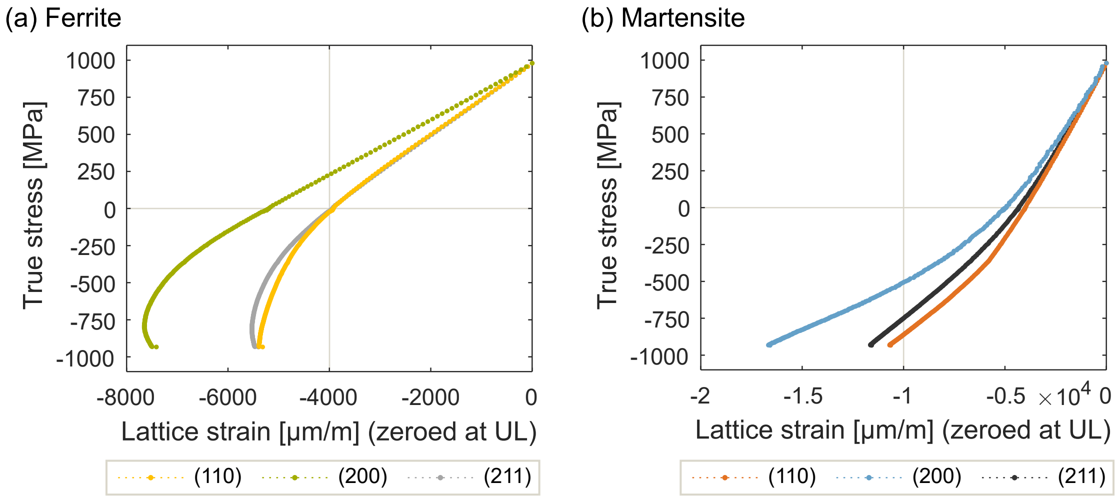

Figure 7.36: DP1000 - True stress versus lattice strain for three lattice planes plotted for the unloading-compression range for (a) ferrite and (b) martensite.

Figure 7.37 shows a comparison of (a) a reloading in a cyclic tensile test and (b) an unloading and compression in a TC test for similar true strain values. As assumed on basis of the results for HC260Y, comparable values are achieved in tension and compression. The lattice strain of the lattice plane (200) converges at close to 4000 µm/m in tension and in about -4000 µm/m in compression. The absolute values for the lattice planes (110) and (211) are between 2500 µm/m and 3000 µm/m in both tension and compression. Furthermore, the significant difference in grain-to-grain yielding can be confirmed for DP1000 ferrite as well. After changing the load direction, a significantly smoother transition from elastic to elastic-plastic deformation takes place. The macroscopically prevailing stress state is shown by the background colors in Figure 7.37 (b). Due to the harder martensite, the macroscopic zero stress state for ferrite is near the onset of its compressive yielding. The lattice strain curves indicate that plasticization has even started before the macroscopic zero stress state. This means, that the onset of yielding in DP1000 depends on the ferrite phase, both in tension and in compression. The prestressing of the ferrite by martensite means that ferrite is already at the onset of yielding when macroscopic compressive stress is reached. This interaction explains the significant Bauschinger effect in this material and again suggests that microstructural inhomogeneity is one of the main drivers for anelastic and re-yielding behavior. The shift of the onset of yielding of the ferrite relative to the macroscopic stress-strain state can be seen as microstructural confirmation for the necessity of a kinematic hardening model in the FEM simulation.

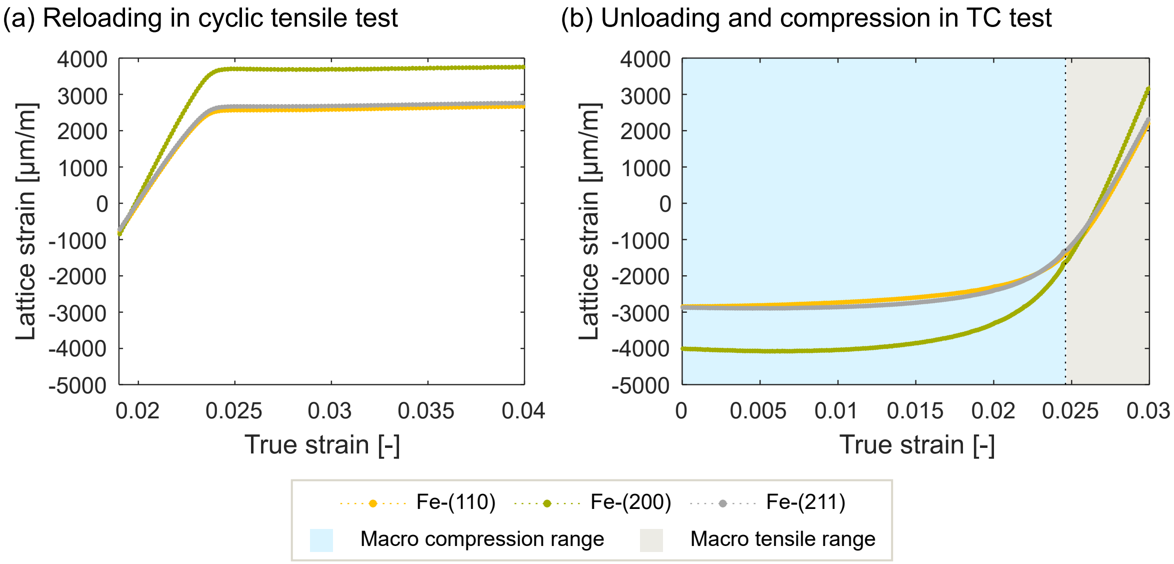

Figure 7.37: DP1000 - (a) Ferrite lattice strain versus true strain for tensile loading and (b) for compressive loading. Plot (b) is divided in the macroscopic tensile and compression range.

8 Interpretation and Transfer

In Chapter 7, the results from various experiments were shown. The objective was to gain deeper understanding of materials in order to better understand springback. New temperature-based material characterization methods have been presented. With these, it was possible to determine the plastic onset of yielding, the loading modulus and the re-yielding (for HC260Y) based on the specimen temperature during tension and tension-compression tests. In the following, it is discussed how these findings and new parameters are suitable for modeling springback and, in particular, hardening behavior.

In Section 2.5.3, several hardening models were addressed. The results of this study confirmed a significant Bauschinger effect for dual-phase steel. It was found that due to the influence of the harder martensite, the onset of yielding of ferrite is shifted relative to the macroscopic onset of yielding. The usefulness of using a kinematic hardening model could thus be demonstrated by the ferrite, whose yield surface was shifted relative to the macroscopic one due to the martensite. In Chaboche and Rousselier (1983), a nonlinear kinematic hardening model was introduced. Therefore, the kinematic hardening rule was combined with a nonlinear isotropic model. This model was the basis for the mixed isotropic-kinematic model of Yoshida and Uemori (2002). The model was extended by work hardening stagnation and early re-yielding (Grubenmann et al., 2018). The YU model has been shown to be very useful for predicting springback and hardening in high-strength materials, like the dual-phase steel (Kessler et al., 2008). The disadvantage of this model is that ten parameters are necessary for it and their determination is not trivial. On the other hand, cyclic tension tests and tension-compression tests, which are necessary for the determination of the parameters, are nowadays part of the standard repertoire in material characterization. Furthermore, software, like LS-Opt from DYNAmore GmbH, allow a simulation-based determination of the values.

In this work, the plastic onset of yielding YS_0 and the loading modulus E_{YS0} were determined in a novel way. Both parameters are directly included in the YU model and have an influence on the determination of the other parameters. For this reason and due to the good suitability of the model for DP steel, the YU model was chosen for the discussion of the influence of the parameters on existing modeling approaches. A one-element test is performed using FEM software LS-DYNA. The parameter identification is done classically according to Yoshida and Uemori (2002) and is summarized in Section 8.1. To investigate the influence of the temperature-based determined parameters, these are compared with the parameters determined according to the standard DIN EN ISO 6892-1.

8.1 Application in Yoshida-Uemori Hardening Model

Three elasticity parameters and seven plasticity parameters have to be determined for the YU model. A detailed description of the backstress equations to describe the re-yielding behavior as well as the determination approach of the parameters can be found in Yoshida and Uemori (2002). Table 8.1 summarizes the parameters necessary. Two parameter sets are determined. One based on the equivalent onset of yielding ($YS_{0.2\%}$) and loading modulus according to the standard (E_{DIN}) and one based on the temperature-based onset of yielding (YS_0) and loading modulus (E_{YS0}).

Table 8.1: Elastic and plastic parameters necessary for YU hardening model.

Elasticity			Plasticity						
E_0	E_a	ζ	Y	B	R_{sat}	b_{YU}	C_{YU}	m	h

8.1.1 Parameter Identification

The determination of the three elasticity parameters with a cyclic tensile test has already been explained in Section 2.5.2. For the initial loading modulus E_0 and the saturated elastic modulus E_a, the values for E_{DIN} and E_{YS0} can be used directly. The material constant ζ can be determined with Equation 2.9.

In the following, the parameter identification of the plasticity parameters is described. Parameter Y reflects the onset of yielding and thus the initial size of the yield surface. It is constant for all plastic deformations. Here, the equivalent onset of yielding ($YS_{0.2\%}$) is originally used. This is compared with the use of YS_0 instead. The remaining plasticity parameters must be determined on basis of the yield curve of a uniaxial TC test. Figure 8.1 shows a schematic representation of a TC curve. Highlighted are the model parameters, necessary for the calibration of the YU model. For better understanding, the stress-strain curve in Figure 8.1 has been divided into areas labeled (a) to (g). In the uniaxial case, the yield curve has to be calculated with the corresponding elastic loading modulus and onset of yielding. This results in different yield curves for the approach according to DIN EN ISO 6892-1 with E_{DIN} and $YS_{0.2\%}$ and the temperature-based approach with E_{YS0} and YS_0. The two parameters influence the values of all other parameters in this way. The yield curve of the TC test has to be divided in a forward (fow) and a reverse (rev) bounding surface. The forward curve starts at Y (point (a)) and ends at the maximum plastic strain $\varepsilon_{\mathrm{pl,0}}$ before unloading (point (b)). The reverse curve starts at the re-yielding point (point (c)), which is defined to $2 \cdot Y$ subtracted from σ_0 and ends at $\varepsilon_{\mathrm{pl}} = 0$ (point (e)).

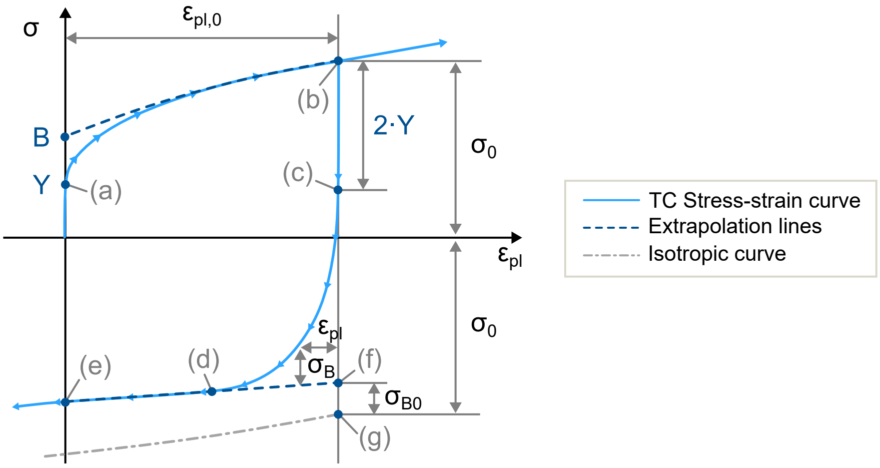

Figure 8.1: Schematic overview of YU parameters in the TC yield curve according to Yoshida and Uemori (2002).

To determine the initial size of the bounding surface B, a range of datapoints starting from $\varepsilon_{\mathrm{pl,0}}$ (point (b)) is fitted backwards with the following equation,

$$\sigma^{\mathrm{fow}} = B + (R_{\mathrm{sat}} + b_{\mathrm{YU}})(1 - e^{-m\varepsilon_{pl}}) \qquad . \tag{8.1}$$

The range of datapoints must be chosen to match the stress-strain curve and is user-dependent. This fit provides the parameters m and $R_{\mathrm{sat}} + b_{\mathrm{YU}}$. The parameter b_{YU} is determined in the next step to obtain separate values for R_{sat} and b_{YU}. Therefore, the area of permanent softening has to be defined. This is done with a linear regression line in the section (c) to (e) of the stress-strain curve, starting from (e) backwards. The number of datapoints considered for this linear regression must be chosen to match the area of permanent softening as good as possible (see range (d) to (e)). The parameter b_{YU} reflects the beginning of the reverse bounding surface and can be determined by

$$\sigma_{\mathrm{B0}} = 2b_{\mathrm{YU}}(1 - e^{-m\varepsilon_{\mathrm{pl,0}}}) \qquad . \tag{8.2}$$

In this equation, σ_{B0} represents the difference between the linear regression line of the permanent softening in the reverse bounding surface (point (f)) and the value for isotropic hardening at $\varepsilon_{\mathrm{pl,0}}$

(point (g)). For m, the value from Equation 8.1 is taken.

The parameter C_{YU} describes the rate of kinematic hardening and is identified in the range of the transient softening of the material (points (c) to (d)). To determine it, the ratio of σ_{B} to $\varepsilon_{\mathrm{pl}}$ is formed from the re-yielding (point (c)) to the intersection with the linear regression line (point (d)) used before. This ratio is fitted with Equation 8.3 and thus C_{YU} can be determined. The parameter k in Equation 8.3 is a constant, which is not further considered in the YU model.

$$\sigma_{\mathrm{B}} = 2ke^{-C_{\mathrm{YU}}\varepsilon_{\mathrm{pl}}} \tag{8.3}$$

Material parameter h is used to adjust the modeling results to the cyclic stress-strain curves (Yoshida and Uemori, 2002) and can be determined via experiments and simulations. It reflects the expansion of non-isotropic hardening and its value can vary between 0 and 1 (Thaweesak Phongsai et al., 2016). According to Thaweesak Phongsai et al. (2016), this parameter shows only little influence in the LS-DYNA solver and is therefore set to the default value of $h = 0.5$.

The data ranges for the extrapolation in the forward bounding surface with Equation 8.1 and for the linear regression line to determine the area of permanent softening in the reverse bounding surface have been chosen to be 50 % here, for both parameter sets. Table 8.2 shows the parameters identified with this approach and settings.

Table 8.2: Parameter sets for YU hardening model identified with values according to the standard (Set DIN) and temperature-based values (Set Temp) for DP1000.

Set	E_0 GPa	E_a GPa	ζ -	Y MPa	B MPa	R_{sat} MPa	b_{YU} MPa	C_{YU} MPa	m -	h -
DIN	208.3	181.8	76.0	714.7	760.8	65.7	240.7	256.4	59.0	0.5
Temp	202.6	167.8	76.4	430.2	704.9	48.1	308.8	363.3	62.0	0.5

8.1.2 One-Element Test

The influences of the temperature-based parameters on the YU model are investigated. The one-element test is suitable for this investigation, since other influences such as meshing, friction or the stress state of a component in the FEM simulation can be excluded. For the calibration in Section 8.1.1, the DP1000 TC test (*DESY* setup) discussed in Section 7.2.5 and shown in Figure 7.35 (a) is used. The element was defined and constrained as shown in Figure 8.2 (a) and a fully integrated shell element was used. The side length was defined as 100 mm and a sheet thickness of 1 mm was set. The displacement was set to match the displacement of the experiment. The element was first stretched 3.07 % and then compressed to -0.41 % before being unloaded to 0.07 %. This corresponds to the strain at 0 MPa after testing in the experiment. All strain values given are engineering strains. Throughout the simulation, 300 calculation steps were performed and Figure 8.2 (b) shows the displacement versus calculation step curve for the one-element test. MAT_125 was used as the material card for the YU calculations. MAT_036 (Barlat 89) was used for the calculation of the isotropic curve. The yield curve for MAT_036 was defined in tabular form, calculated conventionally with E_{DIN} and $YS_{0.2\%}$.

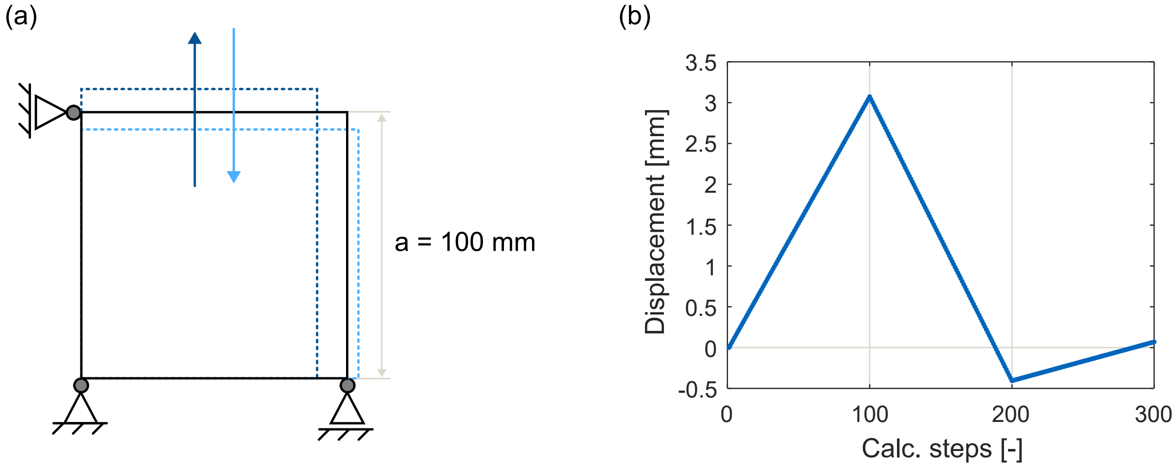

Figure 8.2: (a) Schematic illustration of the one-element test performed in LS-DYNA and (b) displacement versus calculation steps used for the simulation.

Figure 8.3 shows the results for the one-element tests. Shown are the curve of the experimental data, the calculated isotropic curve (Barlat 89), the calculated isotropic-kinematic YU curve identified with standard values (YU - DIN) and the calculated YU curve identified with temperature-based parameters (YU - Temp-based).

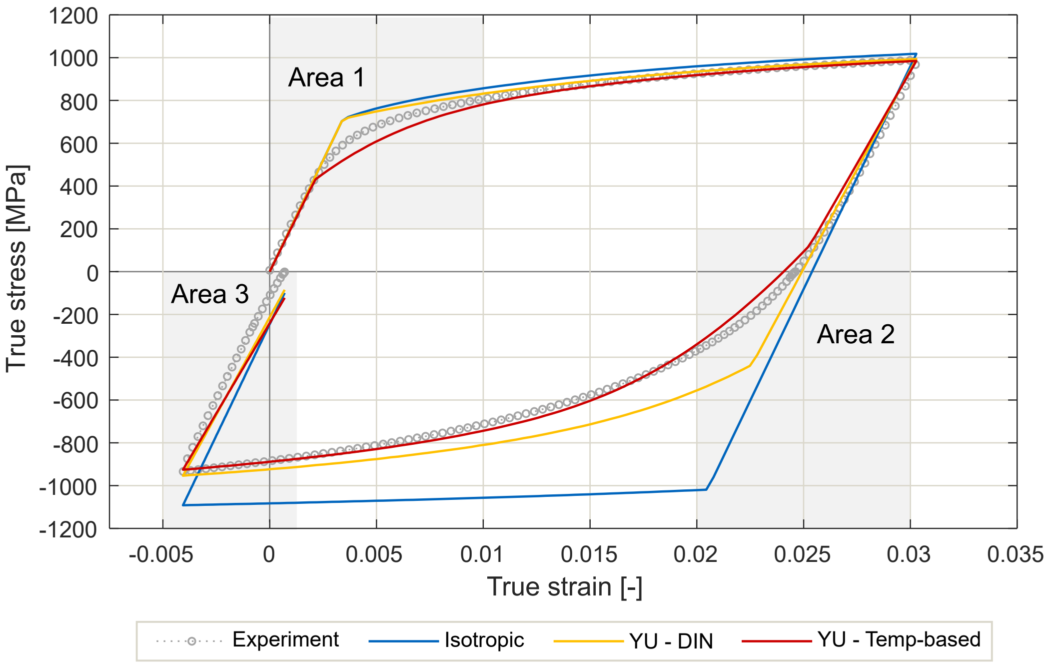

Figure 8.3: DP1000 - Experimental stress-strain curve of a TC test in comparison with the results of the one-element test (LS-DYNA). Shown are the results for an isotropic material model and two differently calibrated YU material models. One uses the values determined according to the standard (DIN) and the other one, the temperature-based determined values (Temp-based).

The curves are explained below on the basis of three characteristic areas (see Figure 8.3).

- *Area 1: Onset of yielding*
  In this area, deviations between the calculated curves and the experiment occur. The temperature-based curve starts at a significantly lower value ($Y = YS_0 = 430.2$ MPa) than the conventional YU curve and the isotropic curve (both $Y = YS_{0.2\%} = 714.7$ MPa). This results in the temperature-based curve being below the experiment at the beginning. The other two curves are above the experimental data curve. It seems that an earlier onset of yielding at lower stress values results in a smoother beginning of the elastic-plastic transition in the model. It is conceivable that such an early onset of plastic yielding for the type of material was not considered when developing the model. Therefore, this smooth elastic-plastic transition cannot be accurately reproduced. The marginally different initial Young's modulus has no influence on the results. In future, it is conceivable that the onset of yielding could be calibrated similarly to transient softening. With the temperature-based method, three parameters are now available for the onset of yielding. These are

YS_0, YS_{Tmin} and $YS_{0.2\%}$. Using these three parameters, which can be determined directly in the same experiment, the elastic-plastic transition can be modeled more precisely. This can lead to advantages in particular for materials with a large and smooth elastic-plastic transition, such as DP1000. All three calculated curves agree well with experiment as the tensile load progresses.

- *Area 2: Re-yielding*
  This kind of material shows a strong Bauschinger effect, i.e. re-yielding occurs early. As shown, this can be attributed to the interaction of the phases. The particularly smooth elastic-plastic transition after changing the load direction is due to strong grain-to-grain yielding. This behavior cannot be reproduced by the isotropic curve, which is why there is a very large deviation from the experiment. No variable elastic modulus is implemented which leads to an underestimation of the springback after tensile unloading. In addition, the isotropic curve approaches the experimental curve only slightly in the further course of the compression, because permanent softening is not considered. The necessity of a kinematic model becomes clear. Comparison of the two YU curves shows that both reflect early re-yielding. However, the curve based on the temperature-based parameters reproduces this behavior much better and is closer to the experimental data. By using YS_0, which is much lower than $YS_{0.2\%}$ for this material, re-yielding is also earlier as it is dependent on Y in this model. This seems to agree very well with the behavior of the macroscopic curve. It is in good agreement with the onset of yielding in ferrite and thus, the use of $2 \cdot Y$ in the model can be seen as reasonable. Another aspect may cause the temperature-based curve to give a better result. Similar to tension, using YS_0 instead of $YS_{0.2\%}$, a larger area of the experimental curve is considered when calculating the reverse plastic yield curve. Thus, more data is considered for the parameter identification in the critical area and the round behavior can be better represented. The YU-DIN curve approaches the experimental curve only in negative strain region, while the YU-Temp-based curve shows good agreement for the whole compression range.

- *Area 3: Elastic unloading after tension-compression*
  It is noticeable that none of the calculated curves can reflect the elastic unloading after TC loading. The experimental curve is steeper than the calculated curves. However, for a component, this elastic unloading would also be important for springback prediction. The YU curves take into account a variable Young's modulus. Thus, the unloading after tension can be mapped more precisely. However, this modulus is also used in the subsequent unloading from compression. A possible increase of the modulus under compression is not taken into account. The isotropic curve shown uses the initial elastic

modulus for all three areas. The experimental curve indicates that the elastic modulus decreases under tensile loading and increases again under compressive loading. This behavior has been studied microstructurally and is discussed in the following Section 8.2.

In summary, the use of temperature-based elasticity parameters in the YU model leads to a significant improvement in the mapping of experimental data. In particular, the area of re-yielding and the elastic-plastic transition in compression after initial tensile loading can be better represented. On the other hand, when using YS_0 as Y, the assumption of Yoshida and Uemori (2002) to calculate the re-yielding with $2 \cdot Y$ proves to be reasonable. Furthermore, the additional parameters YS_0 and YS_{Tmin} for the onset of yielding offer great potential to further refine the model.

8.2 Recovery of Elastic Modulus

When comparing the experimental data with the YU model, it is obvious that the elastic unloading after TC loading could not be reproduced well. The experiment shows that the elastic modulus increases again. It was shown in Section 7.2.4 that the decreasing elastic modulus significantly depends on the difference of martensite and ferrite phase stresses. In the case of tensile loading, this delta increases strongly at the beginning and then saturates. The decrease of the elastic modulus behaves in the same way.

Figure 8.4 shows this analysis for a TC test. In (a), the martensite and ferrite phase stresses are plotted versus the true strain. Furthermore, the phase stress state at 0 MPa macroscopic stress is marked for both, ferrite and martensite. In (b), the true stress versus true strain curve is shown and the initial loading modulus, the chord modulus after tension and after tension-compression are highlighted.

On basis of the markers used for ferrite (circle) and martensite (square) in Figure 8.4 (a), it is already noticeable that the interphase stress $\Delta\sigma_{\mathrm{Ma-Fe}}$ is reversed after TC compared to after tension. Table 8.3 gives the absolute values for the specific states. After around 3 % tensile strain, $\Delta\sigma_{\mathrm{Ma-Fe}}$ is at 846 MPa, which leads to a significantly decreased chord modulus compared to the initial value of around 202 GPa. After subsequent compression to around -0.4 % strain, it is -552 MPa (see Figure 8.4 (a)). Now the martensite has a residual compression state and the ferrite has a tensile state. The measured chord modulus after TC with 191.7 GPa is clearly higher than after tension with 173.4 GPa, but does not reach the inital value (see Figure 8.4 (b)). These results show that the elastic modulus can recover. Furthermore, a connection with interphase stresses is again conceivable, since these are reversed in compression. It is possible that the stress built up by the martensite on the ferrite leads to this behavior.

In addition, a recovery of the material in the form of annihilation of dislocations cannot be excluded here. For this purpose, the FWHM or IB of the martensite and ferrite as well as their peak shapes would have to be investigated in more detail. The profiles shown in Figure 6.11 (d-f) indicate that their width decreases again under compressive loading. Experiments with higher instrumental resolution are necessary for this.

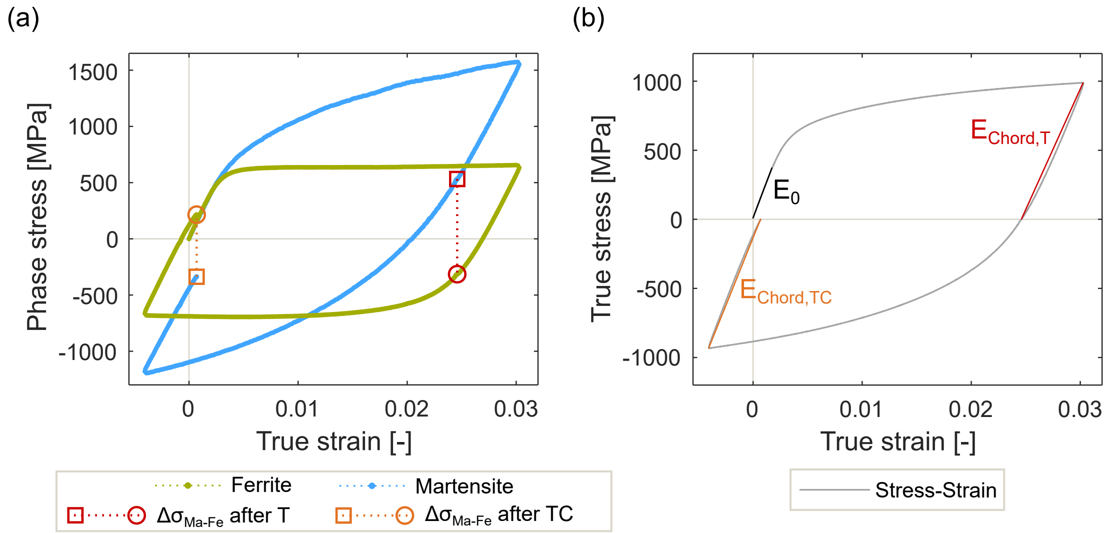

Figure 8.4: DP1000 - (a) Martensite and ferrite phase stresses during TC test and $\Delta\sigma_{Ma-Fe}$ at 0 MPa macroscopic stress after tension (T) and tension-compression (TC). (b) Macroscopic stress-strain curve with initial loading modulus (E_0), chord modulus after tension ($E_{Chord,T}$) and after tension-compression ($E_{Chord,TC}$).

Table 8.3: Interphase stresses after tension and after TC and corresponding elastic modulus values.

$\Delta\sigma_{\text{Ma-Fe}}$ after T	$E_{\text{Chord,T}}$	$\Delta\sigma_{\text{Ma-Fe}}$ after TC	$E_{\text{Chord,TC}}$
846 MPa	173.4 GPa	-552 MPa	191.7 GPa

9 Summary and Outlook

The importance of accurate numerical simulation for production technology was discussed. Complex phase compositions and microstructures of high-strength steels nowadays make it possible to achieve high formability at high strengths. However, this complex material composition results in material-specific characteristics, which prove to be a major challenge for modeling. This work addressed that issue. The overall objective was to improve numerical simulation. To achieve this goal, the present work focused on deepening the understanding of steel sheet materials by advanced experimental investigations and improving material characterization in this way. Figure 9.1 summarizes the idea behind this research project and illustrates the particular steps in form of a cycle.

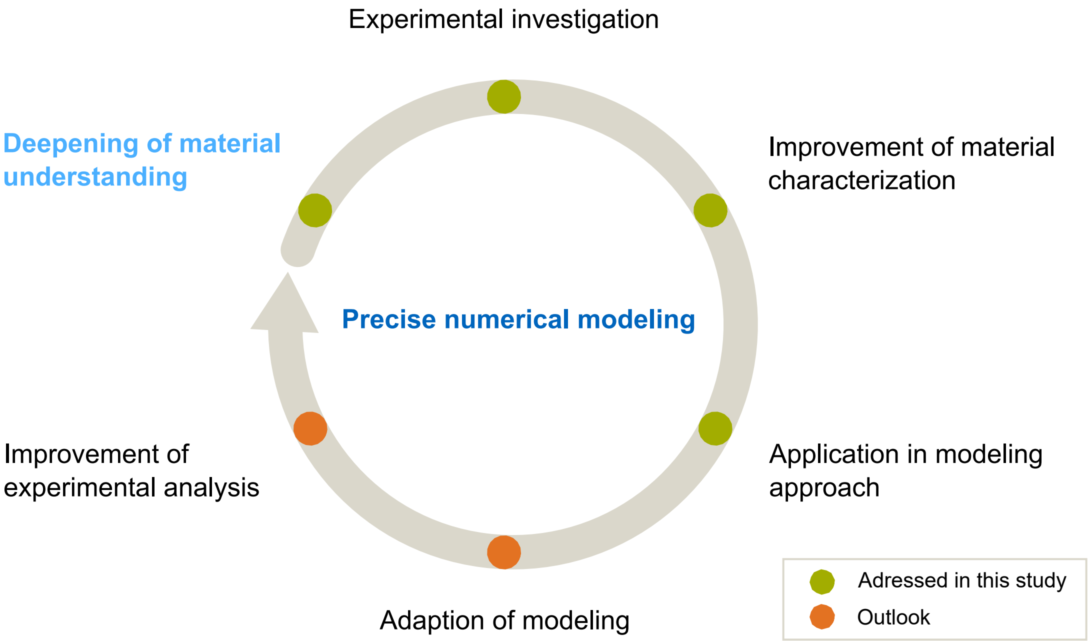

Figure 9.1: Illustration of a cycle for continuous improvement of numerical simulation.

By developing new and sophisticated experimental methods, it is possible to generate new material data and correlations. These make it possible to expand and improve material characterization, for example by introducing new evaluation methods and parameters. The next step is to transfer these parameters into models and to investigate their influence. Based on the knowledge gained, existing models can be adapted and extended or new models can be developed.

With continuous improvement of the experimental methods and measurement technologies, this procedure closes a cycle.

An experimental procedure has been conducted that allows the investigation of the materials at macro and micro levels. More precisely, an in-situ diffraction analysis for tensile and tension-compression tests was set up, which includes a time-synchronous measurement of macroscopic and microstructural material behavior. Cyclic tension tests as well as tension-compression tests were developed and carried out for this purpose in a particle accelerator under synchrotron radiation. In this way, it was possible to correlate macroscopic elastic-plastic material characteristics, such as the onset of plastic yielding and the elastic modulus as well as anelastic behavior and early re-yielding, with the microstructural behavior. Lattice strains and phase stresses calculated by the peak shift and dislocation densities calculated by the peak broadening of diffraction profiles were evaluated for different lattice planes. On the macroscopic level, load, strain and the specimen temperature were measured precisely. This experimental approach made the following analyses and results possible.

Based on the thermoelastic effect, a temperature-based determination method for both the onset of yielding and elastic loading modulus was developed. Therefore, temperature measurement during uniaxial tensile and TC tests was studied comprehensively for its accuracy, sensitivity and robustness. Findings on the thermal behavior were collected, which enabled a reliable evaluation of the temperature signal. The parameters yield stress at zero plastic strain YS_0 and yield stress at temperature minimum YS_{Tmin} have been introduced. Correlations with the microstructural behavior confirmed that the material is already plastically deformed at the stress value YS_{Tmin}. However, it could be shown that this parameter is significantly closer to the onset of yielding than the conventionally used parameter $YS_{0.2\%}$. Furthermore, no evaluation is necessary, since the value can be measured directly. Thus, it is less user-dependent. An extensive study on the measurement of the temperature minimum in tensile tests showed that the minimum can be measured very precisely with standard deviations of less than 2.5 %. This parameter is ideally suited for implementation in testing software and thus for industrial application.

The relationship between the thermoelastic effect and specimen temperature was investigated and the meaningfulness of the temperature-based onset of yielding YS_0 was demonstrated by correlation with microstructural behavior. The newly found parameter YS_0 reflects the onset of yielding with good accuracy for both the single-phase ferritic material HC260Y and the dual-phase steel DP1000. Lattice strains and especially the dislocation density, which increased significantly, when YS_0 was exceeded, showed this. By accurately determining the onset of plastic yielding, a physically based upper limit for determining the elastic modulus was found.

Thus, a new determination method for the loading modulus (E_{YS0}) could be introduced. The comparison with other determination methods, for example the procedure according to the standard, showed that the newly found method provided values that are more reasonable. In addition, the user interference is low with the new method, so that there is good reproducibility and robustness.

Using a sophisticated TC test rig, it was possible to determine the re-yielding (YS_{re}) of HC260Y in compression after initial tensile loading, also via temperature. The newly found parameter YS_{re} was also validated with the dislocation density. In DP steel, this was not possible at the time due to the significant Bauschinger effect. This must be implemented in future work by further improving the test rig and the temperature measurement.

Besides the microstructural validation of the thermoelastic effect and the newly defined parameters, material understanding was deepened using advanced synchrotron measurements. The following bullet points summarize the main findings on elastic-plastic microstructural material behavior.

- *Grain-to-grain yielding*
  It was shown that individual lattice planes do not plasticize simultaneously, but differ in their onset of yielding. This behavior is referred to grain-to-grain yielding (Tomota et al., 2003). Especially at initial loading, a significant grain-to-grain yielding was observed. After initial plasticization, i.e. activation of the slip systems, the grain-to-grain yielding was lower. A particularly significant grain-to-grain yielding was found after changing the loading direction. Thus, it could not only be shown that the initial activation of the slip systems has an influence on the plasticization, but that a certain directional dependence prevails. A correlation of the smooth elastic-plastic transition with intergranular stresses due to different grain behavior is conceivable. The comparison with the temperature-based parameters showed that YS_0 approximately reflects the start time and YS_{Tmin} the end time of grain-to-grain yielding.

- *Annihilation of dislocations*
  In literature, anelastic behavior is mainly attributed to dislocation motion and microstructural inhomogeneities. Dislocation motion is difficult to determine, but it was possible to determine the dislocation density for the single-phase material HC260Y. It has been shown that the peak width decreases and it is assumed that this means the dislocation density decreases during elastic unloading. It has also been shown that during reloading, there is a further marginal decrease until it increases again. Furthermore, the behavior in the dislocation density differed in the transversal and longitudinal directions. These

results suggest dislocation motion during elastic deformation. According to the definition of D. Li and Wagoner (2021), anelastic strain corresponds to reversible plastic strain. The decrease in dislocation density indicates that this reversible plastic deformation must be present. Another indication is that the density after reloading was lower than before previous unloading.

- *Interphase stresses as the main driver for anelasticity and early re-yielding*
  Neither of the two most plausible reasons for anelastic behavior, namely dislocation motion and microstructural inhomogeneities, can be excluded. This is because the single-phase material, where interphase stresses cannot occur, still exhibited anelastic behavior. Inhomogeneities due to inclusions or microstructural anisotropy in form of intergranular strains were also investigated for this material and no correlation was found. The comparison of the anelastic and re-yielding behavior of the single-phase and dual-phase steel showed that the phenomena are much more pronounced in the DP steel. The evaluation of the behavior of ferrite and martensite phase stresses during tensile and tension-compression loading made it possible to analyze interphase stresses. A correspondence between interphase stress and anelastic behavior was demonstrated. The hard martensite plasticizes at higher plastic strains than the ferrite. Thus, the interphase stresses increase significantly at the beginning of plastic deformation, where ferrite is already plasticized and martensite is still elastic. When the martensite plasticizes as well, the interphase stress saturates. This behavior reflects the decreasing chord modulus and thus anelastic behavior. The interaction of the two phases causes the martensite to preload ferrite in such a way that the latter already re-yields under macroscopic tensile load depending on the plastic strain. It can be assumed that this property, together with a significant microstructural anisotropy and grain-to-grain yielding, leads to the significant Bauschinger effect. This microstructural behavior resembles a shift in the ferrite yield locus relative to the macroscopic behavior. Thus, it can be compared to kinematic hardening. These findings were possible due to the separate evaluation of the martensite and ferrite phases. Existing evaluation approaches were taken up, adapted and further improved.

It was possible to show in a one-element simulation that the existing isotropic-kinematic hardening model introduced by Yoshida and Uemori (2002) could be improved by using the temperature-based determined parameters for its calibration. Thus, the parameters were not only investigated for their physical meaningfulness, but their positive influence on a widely used material model. With this, the potential for modeling in general was demonstrated.

9.1 Adaption of Modeling

In order to discuss implementation possibilities of the results in simulation models, a classification of the results and models is necessary. A distinction must be made between microscopic and macroscopic results and models. Figure 9.2 gives an overview and classifies the key results of this study. On the one side, there are crystal plasticity models, which allow to implement microstructural information, like dislocation behavior (Roters et al., 2010). On the other side, there are macroscopic models, which consider the material to be macroscopically homogeneous. These models try to reproduce the material behavior on basis of their stress-strain behavior, for example. The overall objective of this study was to create an experimental basis to be able to improve numerical springback prediction in future. Considering this, the simulation of real components is significant.

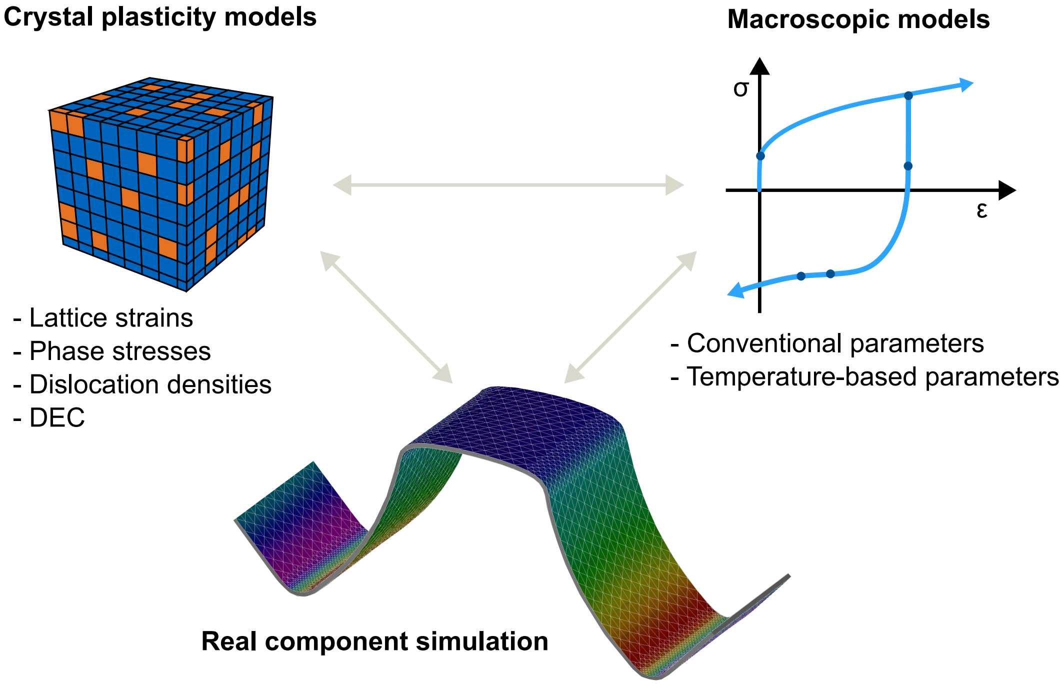

Figure 9.2: Representation of implementation possibilities of the listed results in models.

The temperature-based determined parameters are purely macroscopic parameters whose relationship with microstructural behavior could be demonstrated in this study. The great advantage is that these parameters can be determined with a simple macroscopic tensile and tension-compression test. The parameter YS_{Tmin} can be measured directly. YS_0 and E_{YS0} can be determined automatically by means of a suitable evaluation script. Furthermore, it was possible to determine a value for YS_{re} for the single-phase material.

In most of the mentioned macroscopic models, the elastic modulus is included. Instead of the elastic modulus determined according to the standard, the temperature-based determined elastic modulus can be used directly. The effect of the onset of yielding regarding the simulation result is often considered small, but the investigation in the one-element test showed that especially in kinematic hardening models the influence can be large. For the onset of yielding, conventionally the equivalent yield strength at 0.2 % plastic strain is used. Here, the parameters YS_0 and YS_{Tmin} do not necessarily have to substitute $YS_{0.2\%}$, but can complement it for modeling purposes. It is conceivable that materials with a pronounced yield strength or stagnation behavior after initial plasticization can be modeled more precisely using all three parameters. Furthermore, their ratio can already provide information on the behavior under load change. These ideas need to be examined in future studies.

Besides this implementation of the temperature-based determined parameters in macroscopic models, it is conceivable to use the microstructural results in crystal plasticity models. In Zecevic et al. (2016), a crystal plasticity model was introduced, which reproduced the macroscopic behavior of a DP steel under cyclic tension-compression. Assumptions and estimations based on mathematical relations were used to calibrate the model and good results were obtained. It is conceivable to use the dislocation density, lattice strain and phase stress data for the calibration of such models to improve the accuracy. The findings and results of this study provide a broad basis for the calibration of crystal plasticity models.

One possible and interesting way to bring the results of the work together is to use interface approaches such as those offered by DAMASK (Roters et al., 2019). DAMASK is a crystal plasticity simulation package, which can be connected to FE simulation software via an interface. Such multi-scale modeling approaches have to be studied in future work. In doing this, it becomes clearer, which data are valuable and the experimental approach can be adapted and specified. This results in the cycle shown in Figure 9.1.

9.2 Improvement of Microstructural Material Characterization

In this research study, an experimental setup was developed to enable time-synchronous in-situ analyses of microstructural and macroscopic material behavior. However, it can be seen in Figure 6.5 (b) that the limited instrumental resolution of the used DESY beamline P07B does not allow a more detailed evaluation of the Bragg peaks. In addition, the periphery in the experimental hutch does not allow a more precise adjustment of the settings for the DP material, since, for example, the xyz stage does not have enough degrees of freedom. Accordingly, the next step is to perform experiments on a beamline with higher instrumental resolution.

For better evaluation of the overlapping reflections for martensite and ferrite, implementation of additional boundary conditions is needed. In particular in the TC test, it was found that the martensite peak shifts from the left side of the ferrite peak to the right side in the 2 Θ range during load changes, which makes the evaluation particularly difficult. Transmission electron microscopy (TEM) and EBSD measurements would be suitable for this. Absolute values can be detected with these optical analyses at least localized, which is not possible with the in-situ diffraction experiments. So, the history of the material processing could be considered for the evaluations as well. Possibly information could be derived which can be used for the evaluation of the diffraction reflections. The results of TEM and EBSD measurements could be compared or correlated with the results presented in this thesis. In this way, it is conceivable that even more information can be found from peak broadening.

Neutron sources like the Forschungs-Neutronenquelle Heinz Maier-Leibnitz (FRMII) offer further possibilities for studying the material. At FRMII, an investigation with positrons would be conceivable. The use of positrons enables more precise investigation of the origin and type of dislocations, for example.

9.3 Concluding Statement

The present research work is a multidisciplinary project involving mechanical engineering, experimental physics and modeling. During the research project, it became apparent that these individual disciplines also implied different ways of thinking. Through good communication, close cooperation and mutual support, it was possible to unite these different ways of thinking for the scope of this research work. This has generated results that are valuable for all three disciplines. Materials science is a linking point between materials modeling and forming technology and further study of the interrelationships is desirable. The correlation of experimental macroscopic and microscopic material knowledge and their application in numerical models should in the end lead to the best possible production technology, respectively to the best possible component.

A List of Figures

B List of Tables

C Bibliography

AGNEW, S. R., R. P. MULAY, F. J. POLESAK, C. A. CALHOUN, J. J. BHATTACHARYYA, and B. CLAUSEN (2013). “In situ neutron diffraction and polycrystal plasticity modeling of a Mg–Y–Nd–Zr alloy: Effects of precipitation on individual deformation mechanisms”. In: *Acta Materialia* 61.10, pp. 3769–3780.

ARECHABALETA, Z., P. VAN LIEMPT, and J. SIETSMA (2016). “Quantification of dislocation structures from anelastic deformation behaviour”. In: *Acta Materialia* 115, pp. 314–323.

ASHBY, M. F. (1970). “The deformation of plastically non-homogeneous materials”. In: *Philosophical Magazine* 21.170, pp. 399–424.

BABA, A. and Y. TOZAWA (1964). “Effect of Tensile Force in Stretch-Forming Process on the Springback”. In: *Bulletin of JSME* 7.28, pp. 834–843.

BACHMANN, F., R. HIELSCHER, and H. SCHAEBEN (2010). “Texture Analysis with MTEX – Free and Open Source Software Toolbox”. In: *Solid State Phenomena* 160, pp. 63–68.

BAILEY, J. E. and P. B. HIRSCH (1960). “The dislocation distribution, flow stress, and stored energy in cold-worked polycrystalline silver”. In: *Philosophical Magazine* 5.53, pp. 485–497.

BAKER, J. (2009). “Die Bragg’sche Gleichung”. In: *50 Schlüsselideen Physik*. Ed. by J. BAKER. Heidelberg: Spektrum Akademischer Verlag, pp. 68–71.

BANABIC, D. (2010). *Sheet metal forming processes: Constitutive modelling and numerical simulation*. Berlin and Heidelberg: Springer.

BANABIC, D. and K. PÖHLANDT (2000). *Formability of metallic materials: Plastic anisotropy, formability testing, forming limits*. Engineering materials. Berlin and Heidelberg: Springer.

BARGEL, H.-J. (2022). *Werkstoffkunde*. Berlin, Heidelberg: Springer Berlin Heidelberg.

BARLAT, F., G. VINCZE, J. J. GRÁCIO, M.-G. LEE, E. F. RAUCH, and C. N. TOMÉ (2014). “Enhancements of homogenous anisotropic hardening model and application to mild and dual-phase steels”. In: *International Journal of Plasticity* 58.9, pp. 201–218.

BARLAT, F., J. J. GRACIO, M.-G. LEE, E. F. RAUCH, and G. VINCZE (2011). “An alternative to kinematic hardening in classical plasticity”. In: *International Journal of Plasticity* 27.9, pp. 1309–1327.

BARLAT, F., J. HA, J. J. GRÁCIO, M.-G. LEE, E. F. RAUCH, and G. VINCZE (2013). “Extension of homogeneous anisotropic hardening model to cross-loading with latent effects”. In: *International Journal of Plasticity* 46.136–141, pp. 130–142.

BARLAT, F., S.-Y. YOON, S.-Y. LEE, M.-S. WI, and J.-H. KIM (2020). “Distortional plasticity framework with application to advanced high strength steel”. In: *International Journal of Solids and Structures* 202, pp. 947–962.

BARNES, H. A. (1999). “The yield stress–a review”. In: *Journal of Non-Newtonian Fluid Mechanics* 81.1-2, pp. 133–178.

BAUSCHINGER, J. (1886). “Über die Veränderung der Elastizitätsgrenze und die Festigkeit des Eisens und Stahls durch Strecken und Quetschen, durch Erwärmen und Abkühlen und durch oftmals wiederholte Beanspruchungen”. In: *Mitteilungen aus dem Mechanisch-Technischen Laboratorium der K. Technischen Hochschule in Munchen* Vol. 13.

BELGEN, M. H. (1967). “Structural Stress Measurements with an Infrared Radiometer”. In: *ISA Trans* 6, pp. 49–53.

BERGSTRÖM, Y., Y. GRANBOM, and D. STERKENBURG (2010). “A Dislocation-Based Theory for the Deformation Hardening Behavior of DP Steels: Impact of Martensite Content and Ferrite Grain Size”. In: *Journal of Metallurgy* 2010.10, pp. 1–16.

BERNHARD, F. (2004). *Technische Temperaturmessung*. Berlin, Heidelberg: Springer Berlin Heidelberg.

BERNS, H. and W. THEISEN (2008). *Eisenwerkstoffe - Stahl und Gusseisen*. Berlin, Heidelberg: Springer Berlin Heidelberg.

BEVER, M. B., D. L. HOLT, and A. L. TITCHENER (1973). “The stored energy of cold work”. In: *Progress in Materials Science* 17.No. 9, pp. 5–177.

BINDU, P. and S. THOMAS (2014). “Estimation of lattice strain in ZnO nanoparticles: X-ray peak profile analysis”. In: *Journal of Theoretical and Applied Physics* 8.4, pp. 123–134.

BINGHAM, E. C. (1916). “An investigation of the laws of plastic flow”. In: *Bulletin of the Bureau of Standards* Vol. 13, pp. 309–353.

BIOT, M. A. (1955). “Theory of Elasticity and Consolidation for a Porous Anisotropic Solid”. In: *Journal of Applied Physics* 26.2, pp. 182–185.

BLACK, D. R., M. H. MENDENHALL, C. M. BROWN, A. HENINS, J. FILLIBEN, and J. P. CLINE (2020). “Certification of Standard Reference Material 660c for powder diffraction”. In: *Powder Diffraction* 35.1, pp. 17–22.

BLANTER, M. S., I. S. GOLOVIN, H. NEUHÄUSER, and H. SINNING, eds. (2007). *Internal Friction in Metallic Materials: A Handbook*. Vol. 90. Berlin, Heidelberg: Springer.

BODE, R., G. HARTMANN, K.-P. IMLAU, R. KOTHE, W. MÜSCHENBORN, and T. STEGEMANN (2000). *Stahlfeinbleche für den Automobilbau: Herstellung, Verarbeitung und Einsatzbereiche*. Vol. 202. Die Bibliothek der Technik. Landsberg am Lech: Verlag Moderne Industrie.

BÖGE, A. and W. BÖGE (2021). *Handbuch Maschinenbau*. Wiesbaden: Springer Fachmedien.

BOLEY, B. A. and J. H. WEINER (2012). *Theory of Thermal Stresses*. Dover Civil and Mechanical Engineering. Newburyport: Dover Publications.

BORCHARDT-OTT, W. and H. SOWA (2013). *Kristallographie*. Berlin, Heidelberg: Springer.

BOTTANI, C. E. and G. CAGLIOTI (1982). “Thermal emission: A probe to identify the critical point of the elastoplastic transition”. In: *Materials Letters* 1.3-4, pp. 119–121.

BRAGG, W. H. and W. L. BRAGG (1913). “The Reflection of X-rays by Crystals”. In: *Proceedings of the Royal Society A: Mathematical, Physical and Engineering Sciences* 88.605, pp. 428–438.

BRANDENBURGER ISOLIERTECHNIK GMBH & CO. KG (2022). “KV 3”. In: URL: `https://brandenburger-isoliertechnik.com/produkte/kv-3/` (visited on 09/07/2022).

CALLISTER, W. D. and D. G. RETHWISCH (2008). *Fundamentals of Materials Science and Engineering*. 3rd. John Wiley and Sons Ltd.

CAO, J., W. LEE, H. S. CHENG, M. SENIW, H.-P. WANG, and K. CHUNG (2009). “Experimental and numerical investigation of combined isotropic-kinematic hardening behavior of sheet metals”. In: *International Journal of Plasticity* 25.5, pp. 942–972.

CARDONA, M., P. FULDE, H.-J. QUEISSER, G. BENEDEK, H. BILZ, and R. ZEYHER (1983). *Statics and Dynamics of Nonlinear Systems*. Vol. 47. Berlin, Heidelberg: Springer.

CHABOCHE, J. L. and G. ROUSSELIER (1983). “On the Plastic and Viscoplastic Constitutive Equations—Part I: Rules Developed With Internal Variable Concept”. In: *Journal of Pressure Vessel Technology* 105.2, pp. 153–158.

CHANG, Y., B. T. WANG, X. D. LI, C. Y. WANG, K. M. ZHAO, and H. DONG (2020). “A new continuous tensile-compressive testing device with friction-counteracting and anti-buckling supporting mechanism for large strain”. In: *Journal of Materials Processing Technology* 278.41, p. 116540.

CHEN, P. and M. KOÇ (2007). “Simulation of springback variation in forming of advanced high strength steels”. In: *Journal of Materials Processing Technology* 190.1-3, pp. 189–198.

CHEN, Z., H. J. BONG, D. LI, and R. H. WAGONER (2016). “The elastic–plastic transition of metals”. In: *International Journal of Plasticity* 83.351, pp. 178–201.

CHEN, Z., U. GANDHI, J. LEE, and R. H. WAGONER (2016). “Variation and consistency of Young’s modulus in steel”. In: *Journal of Materials Processing Technology* 227.31 & 32, pp. 227–243.

CHOI, Y., W. YONG CHOO, and D. KWON (2001). “Analysis of mechanical property distribution in multiphase ultra-fine-grained steels by nanoindentation”. In: *Scripta Materialia* 45.12, pp. 1401–1406.

CHRISTIEN, F., M. T. F. TELLING, K. S. KNIGHT, and R. LE GALL (2015). “A method for the monitoring of metal recrystallization based on the in-situ measurement of the elastic energy release using neutron diffraction”. In: *Review of Scientific Instruments* 86.5, p. 053901.

CLAUSEN, B., T. LORENTZEN, and T. LEFFERS (1998). “Self-consistent modelling of the plastic deformation of f.c.c. polycrystals and its implications for diffraction measurements of internal stresses”. In: *Acta Materialia* 46.9, pp. 3087–3098.

CLEAR, J. (2022). “First Principles: Elon Musk on the Power of Thinking for Yourself”. In: URL: `https://jamesclear.com/first-principles` (visited on 06/20/2022).

CLEMENS, H., S. MAYER, and C. SCHEU (2017). “Microstructure and Properties of Engineering Materials”. In: *Neutrons and Synchrotron Radiation in Engineering Materials Science*. Ed. by P. STARON, A. SCHREYER, H. CLEMENS, and S. MAYER. Vol. 2a/2b, 6/7, 15. Weinheim, Germany: Wiley-VCH Verlag GmbH & Co. KGaA, pp. 1–20.

CLEVELAND, R. M. and A. K. GHOSH (2002). “Inelastic effects on springback in metals”. In: *International Journal of Plasticity* 18, pp. 769–785.

COMPTON, K. T. and D. B. WEBSTER (1915). “Temperature Changes Accompanying the Adiabatic Compression of Steel”. In: *Physical Review* 5.2, pp. 159–166.

CONG, Z. H., N. JIA, X. SUN, Y. REN, J. ALMER, and Y. D. WANG (2009). “Stress and Strain Partitioning of Ferrite and Martensite during Deformation”. In: *Metallurgical and Materials Transactions A* 40.6, pp. 1383–1387.

DALBY, W. E. (1921). “IV. Researches on the elastic properties and the plastic extension of metals”. In: *Philosophical Transactions of the Royal Society of London. Series A, Containing Papers of a Mathematical or Physical Character* 221.582-593, pp. 117–138.

DAYMOND, M. R., BOURKE, M. A. M., VON DREELE, R. B., B. CLAUSEN, and T. LORENTZEN (1997). “Use of Rietveld refinement for elastic macrostrain determination and for evaluation of plastic strain history from diffraction spectra”. In: *Journal of Applied Physics* 82.4, pp. 1554–1562.

DEAN, G. D., M. S. LOVEDAY, P. M. COOPER, B. E. READ, B. ROEBUCK, and R. MORRELL (1995). “Aspects of modulus measurement”. In: *Materials Metrology and Standards for Structural Performance*. Ed. by B. F. DYSON, M. S. LOVEDAY, and M. G. GEE. Vol. 38. Dordrecht: Springer Netherlands, pp. 150–209.

DEBYE, P. and P. SCHERRER (1916). “Interferenzen an regellos orientierten Teilchen im Röntgenlicht. I.” In: *Nachrichten von der Gesellschaft der Wissenschaften zu Göttingen, Mathematisch-Physikalische Klasse* Volume 1916, pp. 1–15.

DEUTSCHES ELEKTRONEN-SYNCHROTRON (2022). “PETRA III: Röntgenstrahlungsquelle PETRA III”. In: URL: `https://www.desy.de/forschung/anlagen__projekte/petra_iii/index_ger.html` (visited on 08/29/2022).

DOEGE, E. and B.-A. BEHRENS (2010). *Handbuch Umformtechnik: Grundlagen, Technologien, Maschinen*. 2. Aufl. VDI-Buch. Springer-Verlag.

DRONEY, B. E. and R. KLINMAN (1982). “Ultrasonic techniques for determining the mechanical properties of steels”. In: *AIP Conference Proceedings* 84, pp. 210–228.

DYE, D., H. J. STONE, and R. C. REED (2001). “Intergranular and interphase microstresses”. In: *Current Opinion in Solid State and Materials Science* 5.1, pp. 31–37.

EGGERTSEN, P.-A. and K. MATTIASSON (2009). “On the modelling of the bending–unbending behaviour for accurate springback predictions”. In: *International Journal of Mechanical Sciences* 51.7, pp. 547–563.

EGGERTSEN, P.-A., K. MATTIASSON, and J. HERTZMAN (2011). “A Phenomenological Model for the Hysteresis Behavior of Metal Sheets Subjected to Unloading/Reloading Cycles”. In: *Journal of Manufacturing Science and Engineering* 133.6, p. 804.

ESTEVES, G., K. RAMOS, C. M. FANCHER, and J. L. JONES (2017). “LIPRAS: Line-Profile Analysis Software”. In: *Technical Report*.

FALTA, J. (2010). *Forschung mit Synchrotronstrahlung: Eine Einführung in die Grundlagen und Anwendungen*. 1. Aufl. Wiesbaden: Vieweg + Teubner.

FREDERICK, C. O. and P. J. ARMSTRONG (2007). “A mathematical representation of the multiaxial Bauschinger effect”. In: *Materials at High Temperatures* 24.1, pp. 1–26.

GADALIŃSKA, E., A. BACZMAŃSKI, S. WROŃSKI, L. LE JONCOUR, C. BRAHAM, M. FRANÇOIS, B. PANICAUD, and K. WIERZBANOWSKI (2021). “Direct determination of phase stress evolution in duplex steel using synchrotron diffraction”. In: *Materials Science and Engineering: A* 801, p. 140355.

GARDEY, B., S. BOUVIER, and B. BACROIX (2005). “Correlation between the macroscopic behavior and the microstructural evolutions during large plastic deformation of a dual-phase steel”. In: *Metallurgical Transactions A* 36.11, pp. 2937–2945.

GAU, J.-T. and G. L. KINZEL (2001). “An experimental investigation of the influence of the Bauschinger effect on springback predictions”. In: *Journal of Materials Processing Technology* 108.3, pp. 369–375.

GENG, L. and R. H. WAGONER (2000). “Springback Analysis with a Modified Hardening Model”. In: *SAE Technical Paper Series*. SAE Technical Paper Series. SAE International400 Commonwealth Drive, Warrendale, PA, United States.

GOVIK, A., R. RENTMEESTER, and L. NILSSON (2014). “A study of the unloading behaviour of dual phase steel”. In: *Materials Science and Engineering: A* 602, pp. 119–126.

GRUBENMANN, M., K. BARTH, J. HEINGÄRTNER, N. MANOPULO, P. HORA, A. TORK-ABADI, T. VAN DEN BOOGAARD, and H. RÖSEN (2018). “Analysis of yield locus description on springback behaviour of CR700Y980T-DP steel”. In: *IOP Conference Series: Materials Science and Engineering* 418, p. 012108.

GUO, Y. Q., W. GATI, H. NACEUR, and J. L. BATOZ (2002). “An efficient DKT rotation free shell element for springback simulation in sheet metal forming”. In: *Computers & Structures* 80.27-30, pp. 2299–2312.

HALILOVIČ, M., M. VRH, and B. ŠTOK (2007). “Impact Of Elastic Modulus Degradation On Springback In Sheet Metal Forming”. In: *AIP Conference Proceedings* 908, pp. 925–930.

HAMA, T., N. KITAMURA, and H. TAKUDA (2013). “Effect of twinning and detwinning on inelastic behavior during unloading in a magnesium alloy sheet”. In: *Materials Science and Engineering: A* 583.5, pp. 232–241.

HAMMERSLEY, A. P. (1997). “FIT2D: An Introduction and Overview”. In: *ESRF Internal Report*.

HART, E. W. (1984). “A Micromechanical Basis for Constitutive Equations With Internal State Variables”. In: *Journal of Engineering Materials and Technology* 106.4, pp. 322–325.

HARTMANN, C., L. MAIER, and W. VOLK (2021). “Springback and compensation in sheet metal forming reconsidered as an ill-posed problem”. In: *IOP Conference Series: Materials Science and Engineering* 1157.1, p. 012044.

HASEGAWA, T., T. YAKOU, and S. KARASHIMA (1975). “Deformation behaviour and dislocation structures upon stress reversal in polycrystalline aluminium”. In: *Materials Science and Engineering* 20.No. 2, pp. 267–276.

HATTALLI, V. L. and S. R. SRIVATSA (2018). “Sheet Metal Forming Processes – Recent Technological Advances”. In: *Materials Today: Proceedings* 5.1, pp. 2564–2574.

HAUK, V. (1997). *Structural and residual stress analysis by nondestructive methods: Evaluation, application, assessment*. Amsterdam and New York: Elsevier.

HAUPT, P. (2002). *Continuum Mechanics and Theory of Materials*. Berlin, Heidelberg: Springer Berlin Heidelberg.

HEINZ, P. (1976). *Thermoelasticity*. Second revised and enlarged edition. Vienna: Springer.

HEINZE, T., O. HALLONSTEN, and S. HEINECKE (2017). "Turning the Ship: The Transformation of DESY, 1993–2009". In: *Physics in Perspective* 19.4, pp. 424–451.

HENCKY, H. (1924). "Zur Theorie plastischer Deformationen und der hierdurch im Material hervorgerufenen Nachspannungen". In: *ZAMM - Zeitschrift für Angewandte Mathematik und Mechanik* 4.4, pp. 323–334.

– (1928). "Über die Form des Elastizitätsgesetzes bei ideal elastischen Stoffen". In: *Zeitschrift für technische Physik* 9, pp. 215–220.

– (1929). "Das Superpositionsgesetz eines endlich deformierten relaxationsfähigen elastischen Kontinuums und seine Bedeutung für eine exakte Ableitung der Gleichungen für die zähe Flüssigkeit in der Eulerschen Form". In: *Annalen der Physik und Chemie* 394.6, pp. 617–630.

HESSE, B., H.-M. SONNE, and G. ROBILLER (1991). "Zuverlässige Dehngrenzen im rechnergesteuerten Zugversuch ermitteln / Reliable proof stress determination with computerized tensile test". In: *Materials Testing* 33.7-8, pp. 208–211.

HETZ, P. and M. MERKLEIN (2019). "Characterization of temperature-dependent tension-compression asymmetry for high-strength aluminium alloys". In: *Production at the leading edge of technology*. Ed. by J. P. WULFSBERG, W. HINTZE, and B.-A. BEHRENS. Berlin, Heidelberg: Springer, pp. 103–110.

HEYN, E. (1914). "Internal strains in cold-wrought metals, and some troubles caused thereby". In: *Journal of the Institute of Metals*.

HILL, R. (1950). *The mathematical theory of plasticity*. Oxford: Clarendon Press.

HOELZEL, M., W. M. GAN, M. HOFMANN, C. RANDAU, G. SEIDL, P. JÜTTNER, and W. W. SCHMAHL (2013). "Rotatable multifunctional load frames for neutron diffractometers at FRM II—design, specifications and applications". In: *Nuclear Instruments and Methods in Physics Research Section A: Accelerators, Spectrometers, Detectors and Associated Equipment* 711.3–4, pp. 101–105.

HOLDEN, T. M., C. N. TOMÉ, and R. A. HOLT (1998). "Experimental and theoretical studies of the superposition of intergranular and macroscopic strains in Ni-based industrial alloys". In: *Metallurgical Transactions A* 29.12, pp. 2967–2973.

HOOKE, R. (1676). *A description of helioscopes and some other instruments made by Robert Hooke, Fellow of the Royal Society*. Printed by T.R. for John Martyn.

HORNBOGEN, E., H. WARLIMONT, and B. SKROTZKI (2019). *Metalle*. Berlin, Heidelberg: Springer.

HOU, Y., J. MIN, J. LIN, Z. LIU, J. E. CARSLEY, and T. B. STOUGHTON (2017). "Springback prediction of sheet metals using improved material models". In: *Procedia Engineering* 207.1, pp. 173–178.

JACKSON, A. G. (1991). *Handbook of crystallography: For electron microscopists and others*. New York: Springer-Verlag.

JANDRLIĆ, I., S. REŠKOVIĆ, T. BRLIĆ, and V. FURLAN (2018). “Effect of deformation rate on low carbon steels mechanical properties”. In: *IOP Conference Series: Materials Science and Engineering* 461, p. 012030.

JANDRLIĆ, I., S. REŠKOVIĆ, F. VODOPIVEC, and P. LAVA (2016). “Dependence of thermoelastic effect on volume change by elastic deformation”. In: *Metals and Materials International* 22.3, pp. 407–412.

JIA, N., Z. H. CONG, X. SUN, S. CHENG, Z. H. NIE, Y. REN, P. K. LIAW, and Y. D. WANG (2009). “An in situ high-energy X-ray diffraction study of micromechanical behavior of multiple phases in advanced high-strength steels”. In: *Acta Materialia* 57.13, pp. 3965–3977.

JOCHAM, D., S. VITZTHUM, T. SUSUMU, W. ANNIKA, and V. WOLFRAM (2016). “Yield locus determination of DX56 on a testing apparatus with link mechanism using thermoelectrical effect and equivalent plastic work”. In: *9th Forming Technology Forum*.

JOULE, J. P. and W. THOMSON (1852). “LXXVI. On the thermal effects experienced by air in rushing through small apertures”. In: *The London, Edinburgh, and Dublin Philosophical Magazine and Journal of Science* 4.28, pp. 481–492.

KESSLER, L., J. GERLACH, and M.-S. AYDIN (2008). “Springback Simulation with Complex Hardening Material Models”. In: *LS-DYNA Anwenderforum, Bamberg*.

KIM, J., J. JUNG, T. PARK, D. KIM, Y. H. MOON, F. POURBOGHRAT, and J. H. KIM (2022). “Characterisation of Compressive Behaviour of Low-Carbon and Third Generation Advanced High Strength Steel Sheets with Freely Movable Anti-buckling Bars”. In: *Metals* 12.1, p. 161.

KIM, J. H., D. KIM, F. BARLAT, and M.-G. LEE (2012). “Crystal plasticity approach for predicting the Bauschinger effect in dual-phase steels”. In: *Materials Science and Engineering: A* 539.443, pp. 259–270.

KLOECKNER METALS (2021). “DP Steel: Why is Dual Phase Steel Important to Autos?” In: ed. by KLOECKNER METALS. URL: `https://www.kloecknermetals.com/blog/dp-steel-why-is-dual-phase-steel-important-to-autos/` (visited on 09/05/2022).

KOIZUMI, T. and M. KURODA (2018). “Evaluation of tension-compression asymmetry of a low-carbon steel sheet using a modified classical compression test method”. In: *Journal of Physics: Conference Series* 1063, p. 012167.

KUBLI, W., A. KRASOVSKYY, and M. SESTER (2008). “Modeling of reverse loading effects including workhardening stagnation and early re-plastification”. In: *International Journal of Material Forming* 1.S1, pp. 145–148.

KUPKE, A., L. MADEJ, P. D. HODGSON, and M. WEISS (2019). “Experimental in-situ verification of the unloading mechanics of dual phase steels”. In: *Materials Science and Engineering: A* 760, pp. 134–140.

KUWABARA, T., Y. KUMANO, J. ZIEGELHEIM, and I. KUROSAKI (2009). “Tension–compression asymmetry of phosphor bronze for electronic parts and its effect on bending behavior”. In: *International Journal of Plasticity* 25.9, pp. 1759–1776.

LANDESBERGER, M. (2022). “Characterization and Design of Enhanced Ductile Irons”. Dissertation. Munich: Technische Universität München.

LEE, H. and J. CHEN (1991). “Temperature effect induced by uniaxial tensile loading”. In: *Journal of Materials Science* 26.21, pp. 5685–5692.

LEE, S. and D. YANG (1998). “An assessment of numerical parameters influencing springback in explicit finite element analysis of sheet metal forming process”. In: *Journal of Materials Processing Technology* 80-81, pp. 60–67.

LEHMANN, T., Z.-H. GUO, and H. LIANG (1991). “The conjugacy between Cauchy stress and logarithm of the left stretch tensor”. In: *European Journal of Mechanics A-solids* 10, pp. 395–404.

LEMS, W. (1962). “The change of Young’s modulus of copper and silver after deformation at low temperature and its recovery”. In: *Physica* 28.4, pp. 445–452.

LI, D. and R. H. WAGONER (2021). “The nature of yielding and anelasticity in metals”. In: *Acta Materialia* 206.1958, p. 116625.

LI, K. P., W. P. CARDEN, and R. H. WAGONER (2002). “Simulation of springback”. In: *International Journal of Mechanical Sciences* 44.1, pp. 103–122.

LI, L. and M. HAN (2017). “Molecular dynamics simulations on tensile behaviors of single-crystal bcc Fe nanowire: effects of strain rates and thermal environment”. In: *Applied Physics A* 123.6.

LI, X., Y. YANG, Y. WANG, J. BAO, and S. LI (2002). “Effect of the material-hardening mode on the springback simulation accuracy of V-free bending”. In: *Journal of Materials Processing Technology* 123.2, pp. 209–211.

LIU, W., J. LIAN, N. ARAVAS, and S. MÜNSTERMANN (2020). “A strategy for synthetic microstructure generation and crystal plasticity parameter calibration of fine-grain-structured dual-phase steel”. In: *International Journal of Plasticity* 126.

LOU, X. Y., M. LI, R. K. BOGER, S. R. AGNEW, and R. H. WAGONER (2007). “Hardening evolution of AZ31B Mg sheet”. In: *International Journal of Plasticity* 23.1, pp. 44–86.

LUO, L. and A. K. GHOSH (2003). “Elastic and Inelastic Recovery After Plastic Deformation of DQSK Steel Sheet”. In: *Journal of Engineering Materials and Technology* 125.3, p. 237.

MACIOLEK, A., R. WAGENER, and T. MELZ (2021). “Review of and a new approach to elastic modulus evaluation for fatigue design of metallic components”. In: *International Journal of Fatigue* 151.2, p. 106325.

MAEDA, T., N. NOMA, T. KUWABARA, F. BARLAT, and Y. P. KORKOLIS (2017). “Experimental Verification of the Tension-Compression Asymmetry of the Flow Stresses of a High Strength Steel Sheet”. In: *Procedia Engineering* 207, pp. 1976–1981.

MARCINIAK, Z. (1961). “Influence of the sign change of the load on the strain hardening curve of a copper test subject to torsion”. In: *Archiwum mechanici Stosowanej* 13, pp. 743–751.

MCKEIGHAN, P. C. and B. M. HILLBERRY (1991). “An algorithm for determining tensile properties from digitally recorded tensile test data”. In: *Experimental Techniques* 15.6, pp. 27–30.

MEHRABI, H., R. YANG, and B. WANG (2020). “Effects of Tension–Compression Asymmetry on Bending of Steels”. In: *Applied Sciences* 10.9, p. 3339.

MENDIGUREN, J., F. CORTÉS, X. GÓMEZ, and L. GALDOS (2015). “Elastic behaviour characterisation of TRIP 700 steel by means of loading–unloading tests”. In: *Materials Science and Engineering: A* 634, pp. 147–152.

MILLER, W. H. (1839). *A Treatise on Crystallography*. Deighton.

MITTEMEIJER, E. and U. WELZEL (2008). “The “state of the art” of the diffraction analysis of crystallite size and lattice strain”. In: *Zeitschrift für Kristallographie* 223.9, pp. 552–560.

MIYAUCHI, K. (1992). “Deformation path effect on stress-strain relation in sheet metals”. In: *Journal of Materials Processing Technology* 34.1-4, pp. 195–200.

MOMPIOU, F., D. CAILLARD, M. LEGROS, and H. MUGHRABI (2012). “In situ TEM observations of reverse dislocation motion upon unloading in tensile-deformed UFG aluminium”. In: *Acta Materialia* 60.8, pp. 3402–3414.

MONAVARI, M. and M. ZAISER (2018). “Annihilation and sources in continuum dislocation dynamics”. In: *Materials Theory* 2.1, p. 761.

MORESTIN, F., M. BOIVIN, and C. SILVA (1996). “Elasto plastic formulation using a kinematic hardening model for springback analysis in sheet metal forming”. In: *Journal of Materials Processing Technology* 56, pp. 619–630.

MORESTIN, F. and M. BOIVIN (1996). “On the necessity of taking into account the variation in the Young modulus with plastic strain in elastic-plastic software”. In: *Nuclear Engineering and Design* 162, pp. 107–116.

MÜNSTERMANN, S. (2004). “Einflußgrößen auf den Elastizitätsmodul von Stählen für den Fahrzeugbau: (AVIF A 188)”. In: *FAT-Schriftenreihe* FAT-182.

MURÁNSKY, O., C. J. HAMELIN, M. C. SMITH, P. J. BENDEICH, and L. EDWARDS (2012). “The effect of plasticity theory on predicted residual stress fields in numerical weld analyses”. In: *Computational Materials Science* 54, pp. 125–134.

NOWICK, A. S. and B. S. BERRY (1972). *Anelastic relaxation in crystalline solids*. Materials science series. New York: Academic Press.

OLIFERUK, W., M. MAJ, R. LITWINKO, and L. URBAŃSKI (2012). “Thermomechanical coupling in the elastic regime and elasto-plastic transition during tension of austenitic steel, titanium and aluminium alloy at strain rates from 10−4 to 10−1 s−1”. In: *European Journal of Mechanics - A/Solids* 35.4, pp. 111–118.

OLIVER, W. C. and G. M. PHARR (2004). “Measurement of hardness and elastic modulus by instrumented indentation: Advances in understanding and refinements to methodology”. In: *Journal of Materials Research* 19.1, pp. 3–20.

PANDEY, K. N. and S. CHAND (2003). “Deformation based temperature rise: a review”. In: *International Journal of Pressure Vessels and Piping* 80.10, pp. 673–687.

PANG, J. W. L., T. M. HOLDEN, and T. E. MASON (1998). “The development of intergranular strains in a high-strength steel”. In: *The Journal of Strain Analysis for Engineering Design* 33.5, pp. 373–383.

PAPELEUX, L. and J.-P. PONTHOT (2002). “Finite element simulation of springback in sheet metal forming”. In: *Journal of Materials Processing Technology* 125-126, pp. 785–791.

PATIL, P., K. THIYAGARAJAN, R. V. PRAKASH, and K. BALASUBRAMANIAM (2009). “Damage characterization in SS 304 due to monotonic loading using infrared thermography”. In: *The International Journal of Advanced Manufacturing Technology* 37.1, p. 853.

PECHARSKY, V. and P. ZAVALIJ (2003). *Fundamentals of Powder Diffraction and Structural Characterization of Materials*. New York: Springer-Verlag.

PÉREZ, R., J. A. BENITO, and J. M. PRADO (2005). “Study of the Inelastic Response of TRIP Steels after Plastic Deformation”. In: *Metallurgical Transactions A* 45.12, pp. 1925–1933.

POPOVIĆ, S. (2020). “Quantitative Phase Analysis by X-ray Diffraction—Doping Methods and Applications”. In: *Crystals* 10.1, p. 27.

PRAGER, W. (1955). “The Theory of Plasticity: A Survey of Recent Achievements”. In: *Proceedings of the Institution of Mechanical Engineers* 169.1, pp. 41–57.

PRAKASH, R. V., T. PRAVIN, T. KATHIRVEL, and K. BALASUBRAMANIAM (2011). “Thermo-mechanical measurement of elasto-plastic transitions during cyclic loading”. In: *Theoretical and Applied Fracture Mechanics* 56.1, pp. 1–6.

REPPER, J. (2010). “Einfluss mikroskopischer Eigenspannungen auf die makroskopische Eigenspannungsanalyse mittels Neutronenbeugung”. Dissertation. Munich: Technische Universität München.

ROCCA, R. and M. B. BEVER (1950). “The thermoelastic effect in iron and nickel as a function of temperature”. In: *JOM* 2.2, pp. 327–333.

ROEBUCK, B., J. D. LORD, P. M. COOPER, and L. N. MCCARTNEY (1994). “Data Acquisition and Analysis of Tensile Properties for Metal Matrix Composites”. In: *Journal of Testing and Evaluation* 22.1, p. 63.

ROTERS, F., M. DIEHL, P. SHANTHRAJ, P. EISENLOHR, C. REUBER, S. L. WONG, T. MAITI, A. EBRAHIMI, T. HOCHRAINER, H.-O. FABRITIUS, S. NIKOLOV, M. FRIÁK, N. FUJITA, N. GRILLI, K. JANSSENS, N. JIA, P. KOK, D. MA, F. MEIER, E. WERNER, M. STRICKER, D. WEYGAND, and D. RAABE (2019). “DAMASK – The Düsseldorf Advanced Material Simulation Kit for modeling multi-physics crystal plasticity, thermal, and damage phenomena from the single crystal up to the component scale”. In: *Computational Materials Science* 158.2, pp. 420–478.

ROTERS, F., P. EISENLOHR, L. HANTCHERLI, D. D. TJAHJANTO, T. R. BIELER, and D. RAABE (2010). “Overview of constitutive laws, kinematics, homogenization and multiscale methods in crystal plasticity finite-element modeling: Theory, experiments, applications”. In: *Acta Materialia* 58.4, pp. 1152–1211.

SALLAT, G. (1988). “Theoretische und experimentelle Untersuchungen zum Fliessverhalten von Blechen im Zweiachsigen”. Dissertation. Chemnitz: Technische Universität Karl-Marx-Stadt.

SCARDI, P., M. LEONI, and R. DELHEZ (2004). “Line broadening analysis using integral breadth methods: a critical review”. In: *Journal of Applied Crystallography* 37.3, pp. 381–390.

SCIBETTA, M. and J. SCHUURMANS (2004). “Development and Qualification of an Algorithm for the Determination of the Initial Linear Portion of a Force Versus Displacement Record”. In: *Journal of Testing and Evaluation* 32.6, p. 12618.

SHARPE, W. N. (2008). *Springer handbook of experimental solid mechanics*. Springer handbooks. New York: Springer.

SIEGERT, K. (2015). *Blechumformung: Verfahren, Werkzeuge und Maschinen*. VDI. Berlin, Heidelberg: Springer.

SONNE, H. M. (1999). “Bestimmung des Elastizitäsmoduls im Zugversuch”. In: *Vortrags- und Diskussionstagung, Bad Nauheim*, pp. 219–230.

SPIESS, L., G. TEICHERT, R. SCHWARZER, H. BEHNKEN, and C. GENZEL (2019). *Moderne Röntgenbeugung: Röntgendiffraktometrie für Materialwissenschaftler, Physiker und Chemiker*. 3., überarbeitete Auflage. Springer eBook Collection. Wiesbaden: Springer Spektrum.

STAHL GMBH, voestalpine (2018a). “Dualphasen-Stähle: Der Klassiker mit Zugfestigkeiten bis 1000 MPa und exzellenten Zieheigenschaften”. In: URL: `file:///C:/Users/ga56job/Downloads/Dualphasen-St%C3%A4hle-voestalpine-DE-28092018%20(2)-1.pdf` (visited on 09/05/2022).

– (2018b). “Höherfeste IF-Stähle: Höherfeste Stähle mit bester Umformbarkeit”. In: URL: `file:///C:/Users/ga56job/Downloads/Datenblatt_HF-IF_1608_DE-1.pdf` (visited on 09/05/2022).

STANLEY, P. (2008). “Beginnings and Early Development of Thermoelastic Stress Analysis”. In: *Strain* 44.4, pp. 285–297.

STONE, H. J., T. M. HOLDEN, and R. C. REED (1999). “On the generation of microstrains during the plastic deformation of Waspaloy”. In: *Acta Materialia* 47.17, pp. 4435–4448.

SUN, L. and R. H. WAGONER (2011). “Complex unloading behavior: Nature of the deformation and its consistent constitutive representation”. In: *International Journal of Plasticity* 27.7, pp. 1126–1144.

SUTTNER, S. and M. MERKLEIN (2017). “A new approach for the determination of the linear elastic modulus from uniaxial tensile tests of sheet metals”. In: *Journal of Materials Processing Technology* 241, pp. 64–72.

TAYLOR, G. I. and H. QUINNEY (1931). “The plastic distortion of metals”. In: *Philosophical Transactions of the Royal Society of London*. Series A, Containing Papers of a Mathematical or Physical Character 230.681-693, pp. 323–362.

TEKKAYA, A. E. (2000). “State-of-the-art of simulation of sheet metal forming”. In: *Journal of Materials Processing Technology* 103.1, pp. 14–22.

TEKKAYA, A. E., K. PÖHLANDT, and K. LANGE (1982). “Determining Stress-Strain Curves of Sheet Metal in the Plane Torsion Test”. In: *CIRP Annals* 31.1, pp. 171–174.

THAWEESAK PHONGSAI, WEERAPONG JULSRI, BUNYONG CHONGTHAIRUNGRUANG, SURASAK SURANUNTCHAI, SUWAT JIRATHEARANAT, and VITOON UTHAISANGSUK (2016). "Identification of material parameters for springback predictionusing cyclic tensioncompression test". In: *Journal of Science and Technology* 38.5.

THOMSON, W. (1853). "XV.— On the Dynamical Theory of Heat, with numerical results deduced from Mr Joule's Equivalent of a Thermal Unit, and M. Regnault's Observations on Steam". In: *Transactions of the Royal Society of Edinburgh* 20.2, pp. 261–288.

TOMOTA, Y., P. LUKAS, S. HARJO, J.-H. PARK, N. TSUCHIDA, and D. NEOV (2003). "In situ neutron diffraction study of IF and ultra low carbon steels upon tensile deformation". In: *Acta Materialia* 51.3, pp. 819–830.

TOMOTA, Y., H. TOKUDA, Y. ADACHI, M. WAKITA, N. MINAKAWA, A. MORIAI, and Y. MORII (2004). "Tensile behavior of TRIP-aided multi-phase steels studied by in situ neutron diffraction". In: *Acta Materialia* 52.20, pp. 5737–5745.

TORKABADI, A. (2018). "Towards an Accurate Springback Prediction: Experiments and Modeling". Dissertation. Twente: University of Twente.

TORKABADI, A., E. S. PERDAHCIOĞLU, V. T. MEINDERS, and A. H. VAN DEN BOOGAARD (2018). "On the nonlinear anelastic behavior of AHSS". In: *International Journal of Solids and Structures* 151.56, pp. 2–8.

UPADHYAY, M. V., J. CAPEK, T. PANZNER, and H. VAN SWYGENHOVEN (2019). "Microstructure evolution of stainless steel subjected to biaxial load path changes: In-situ neutron diffraction and multi-scale modeling". In: *International Journal of Plasticity* 122, pp. 49–72.

VAN PETEGEM, S., J. WAGNER, T. PANZNER, M. V. UPADHYAY, T. TRANG, and H. VAN SWYGENHOVEN (2016). "In-situ neutron diffraction during biaxial deformation". In: *Acta Materialia* 105, pp. 404–416.

VERMA, R. K. and A. HALDAR (2007). "Effect of normal anisotropy on springback". In: *Journal of Materials Processing Technology* 190.1-3, pp. 300–304.

VITZTHUM, S., M. EDER, C. HARTMANN, and W. VOLK (2018). "Investigation on strain dependent elastic behavior for accurate springback analysis". In: *Journal of Physics: Conference Series* 1063, p. 012118.

VITZTHUM, S., C. HARTMANN, M. EDER, and W. VOLK (2019). "Temperature-based determination of the onset of yielding using a new clip-on device for tensile tests". In: *Procedia Manufacturing* 29, pp. 490–497.

VITZTHUM, S., C. HARTMANN, H. WEISS, G. BAUMGARTNER, M. HOFMANN, and W. VOLK (2017). "Determination of crystallographic young's modulus for sheet metals by in situ neutron diffraction". In: *Journal of Physics: Conference Series* 896, p. 012123.

VOLK, W., P. GROCHE, A. BROSIUS, A. GHIOTTI, B. L. KINSEY, M. LIEWALD, L. MADEJ, J. MIN, and J. YANAGIMOTO (2019). "Models and modelling for process limits in metal forming". In: *CIRP Annals* 68.2, pp. 775–798.

VOLK, W. and P. HORA (2011). "New algorithm for a robust user-independent evaluation of beginning instability for the experimental FLC determination". In: *International Journal of Material Forming* 4.3, pp. 339–346.

WAGNER, L., M. WALLNER, P. LAROUR, K. STEINEDER, and R. SCHNEIDER (2021). “Reduction of Young’s modulus for a wide range of steel sheet materials and its effect during springback simulation”. In: *IOP Conference Series: Materials Science and Engineering* 1157.1, p. 012031.

WAGONER, R. H., H. LIM, and M.-G. LEE (2013). “Advanced Issues in springback”. In: *International Journal of Plasticity* 45.11/12, pp. 3–20.

WEBER, W. (1830). “Ueber die specifische Wärme fester Körper, insbesondere der Metalle”. In: *Annalen der Physik und Chemie* 96.10, pp. 177–213.

WEINMANN, K. J., A. H. ROSENBERGER, L. R. SANCHEZ, and B. F. von TURKOVICH (1988). “The Bauschinger Effect of Sheet Metal Under Cyclic Reverse Pure Bending”. In: *CIRP Annals* 37.1, pp. 289–293.

WEISSBACH, W., M. DAHMS, and C. JAROSCHEK (2015). *Werkstoffkunde*. Wiesbaden: Springer Fachmedien Wiesbaden.

WIEDEMANN, H. (2003). *Synchrotron Radiation*. Springer eBook Collection. Berlin and Heidelberg: Springer.

WILLIAMSON, G. K. and W. HALL (1953). “X-ray line broadening from filed aluminium and wolfram”. In: *Acta Metallurgica* 1.1, pp. 22–31.

WILLIAMSON, G. K. and R. E. SMALLMAN (1956). “III. Dislocation densities in some annealed and cold-worked metals from measurements on the X-ray debye-scherrer spectrum”. In: *Philosophical Magazine* 1.1, pp. 34–46.

WOLFENDEN, A. and W. R. SCHWANZ (1995). *An Evaluation of Three Methods to Measure the Dynamic Elastic Modulus of Steel*. ASTM International.

WOO, W., V. T. EM, E.-Y. KIM, S. H. HAN, Y. S. HAN, and S.-H. CHOI (2012). “Stress–strain relationship between ferrite and martensite in a dual-phase steel studied by in situ neutron diffraction and crystal plasticity theories”. In: *Acta Materialia* 60.20, pp. 6972–6981.

XU, W. L., C. H. MA, C. H. LI, and W. J. FENG (2004). “Sensitive factors in springback simulation for sheet metal forming”. In: *Journal of Materials Processing Technology* 151.1-3, pp. 217–222.

YAMAGUCHI, K., H. ADACHI, and N. TAKAKURA (1998). “Effects of plastic strain and strain path on youngs modulus of sheet metals”. In: *Metals and Materials* 4.3, pp. 420–425.

YIN, Q., A. E. TEKKAYA, and H. TRAPHÖNER (2015). “Determining cyclic flow curves using the in-plane torsion test”. In: *CIRP Annals* 64.1, pp. 261–264.

YOSHIDA, F. (2018). “Description of non-linear unloading curve and closure of cyclic stress-strain loop based on Y-U model”. In: *Journal of Physics: Conference Series* 1063, p. 012094.

– (2022). “Description of elastic–plastic stress–strain transition in cyclic plasticity and its effect on springback prediction”. In: *International Journal of Material Forming* 15.2, p. 769.

YOSHIDA, F. and T. AMAISHI (2020). “Model for description of nonlinear unloading-reloading stress-strain response with special reference to plastic-strain dependent chord modulus”. In: *International Journal of Plasticity* 130, p. 102708.

YOSHIDA, F. and T. UEMORI (2002). “A model of large-strain cyclic plasticity and its application to springback simulation”. In: *International Journal of Mechanical Sciences* 45.10, pp. 1687–1702.

YOSHIDA, F., T. UEMORI, and K. FUJIWARA (2002). “Elastic–plastic behavior of steel sheets under in-plane cyclic tension–compression at large strain”. In: *International Journal of Plasticity* 18.5-6, pp. 633–659.

YU, M.-H. (2018). *Unified Strength Theory and Its Applications*. Singapore: Springer.

ZECEVIC, M., Y. P. KORKOLIS, T. KUWABARA, and M. KNEZEVIC (2016). “Dual-phase steel sheets under cyclic tension–compression to large strains: Experiments and crystal plasticity modeling”. In: *Journal of the Mechanics and Physics of Solids* 96.4, pp. 65–87.

ZENER, C. (1948). *Elasticity and Anelasticity of Metals*. Chicago University Committee on Publications in the Physical Sciences. University of Chicago Press.

ZHANG, X. X., H. ANDRÄ, S. HARJO, W. GONG, T. KAWASAKI, A. LUTZ, and M. LAHRES (2021). “Quantifying internal strains, stresses, and dislocation density in additively manufactured AlSi10Mg during loading-unloading-reloading deformation”. In: *Materials & Design* 198, p. 109339.

ZHANG, Z. T. and D. LEE (1995). “Effect of Process Variables and Material Properties on the Springback Behavior of 2D-Draw Bending Parts”. In: *SAE Technical Paper Series*. SAE Technical Paper Series. SAE International 400 Commonwealth Drive, Warrendale, PA, United States.

ZHAO, Y. and J. ZHANG (2008). “Microstrain and grain-size analysis from diffraction peak width and graphical derivation of high-pressure thermomechanics”. In: *Journal of Applied Crystallography* 41.6, pp. 1095–1108.

ZHONG, Z. Y., H.-G. BROKMEIER, W. M. GAN, E. MAAWAD, B. SCHWEBKE, and N. SCHELL (2015). “Dislocation density evolution of AA 7020-T6 investigated by in-situ synchrotron diffraction under tensile load”. In: *Materials Characterization* 108, pp. 124–131.

ZHOU, A. G., S. BASU, and M. W. BARSOUM (2008). “Kinking nonlinear elasticity, damping and microyielding of hexagonal close-packed metals”. In: *Acta Materialia* 56.1, pp. 60–67.

ZHUANG, Z., Z. LIU, and Y. CUI (2019). “Dislocation-Based Single-Crystal Plasticity Model”. In: *Dislocation Mechanism-Based Crystal Plasticity*. Elsevier, pp. 91–119.

D Standards

ASTM E 111-17 (2017). *Test Method for Youngs Modulus, Tangent Modulus, and Chord Modulus*. West Conshohocken, PA.

DIN 50125 (2009). *Prüfung metallischer Werkstoffe - Zugproben*. Berlin.

DIN EN 10268 (2013). *Kaltgewalzte Flacherzeugnisse aus Stählen mit hoher Streckgrenze zum Kaltumformen –Technische Lieferbedingungen: Deutsche Fassung EN 10268:2006+A1:2013*. Berlin.

DIN EN 10338 (2015). *Warmgewalzte und kaltgewalzte Flacherzeugnisse ohne Überzug aus Mehrphasenstählen zum Kaltumformen –Technische Lieferbedingungen: Deutsche Fassung EN 10338:2015*.

DIN EN 60751 (2009). *Industrielle Platin-Widerstandsthermometer und Platin-Temperatursensoren (IEC 60751:2008): Deutsche Fassung EN 60751:2008*. Berlin.

DIN EN ISO 21432 (2021). *Zerstörungsfreie Prüfung – Standardprüfverfahren zur Bestimmung von Eigenspannungen durch Neutronenbeugung (ISO 21432:2019): Deutsche Fassung EN ISO 21432:2020*. Berlin.

DIN EN ISO 6892-1 (2020). *Metallic materials – Tensile testing: Part 1: Method of test at room temperature*. Berlin.

VDA 239-100 (2016). *Flacherzeugnisse aus Stahl zur Kaltumformung*.

E Appendix

E.1 SEM Settings

Table E.1 shows the settings for the SEM analyses explained in Section 6.2.4. The SEM analysis was performed at the University of Mondragon in Spain.

Table E.1: Settings of SEM analyses.

Feature	Setting
Acceleration voltage	30 kV
Working distance	7 mm
Tilting angle	70°
Area	170 µm × 120 µm
Step size	16 µm
Exposure time	4.02 ms

E.2 Results - YS_0 Sensitivity

This chapter presents supplementary information for Section 7.1.2.

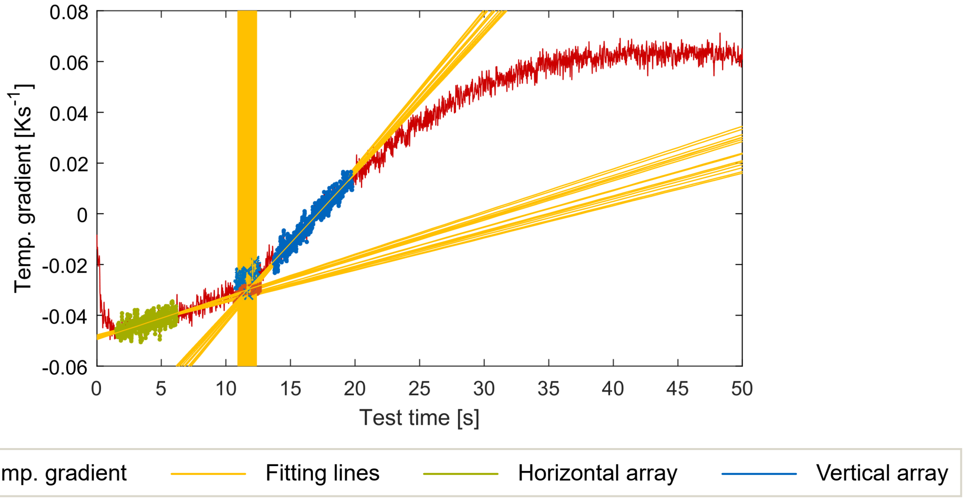

Figure E.1: DP1000 - Example plot for full factorial sensitivity analysis for the parameter YS_0*. The intersection of 225 combinations of the horizontal and vertical fit are calculated and plotted for the initial loading.*

E.3 Results - Onset of Yielding

This chapter presents supplementary information for Section 7.2.2.

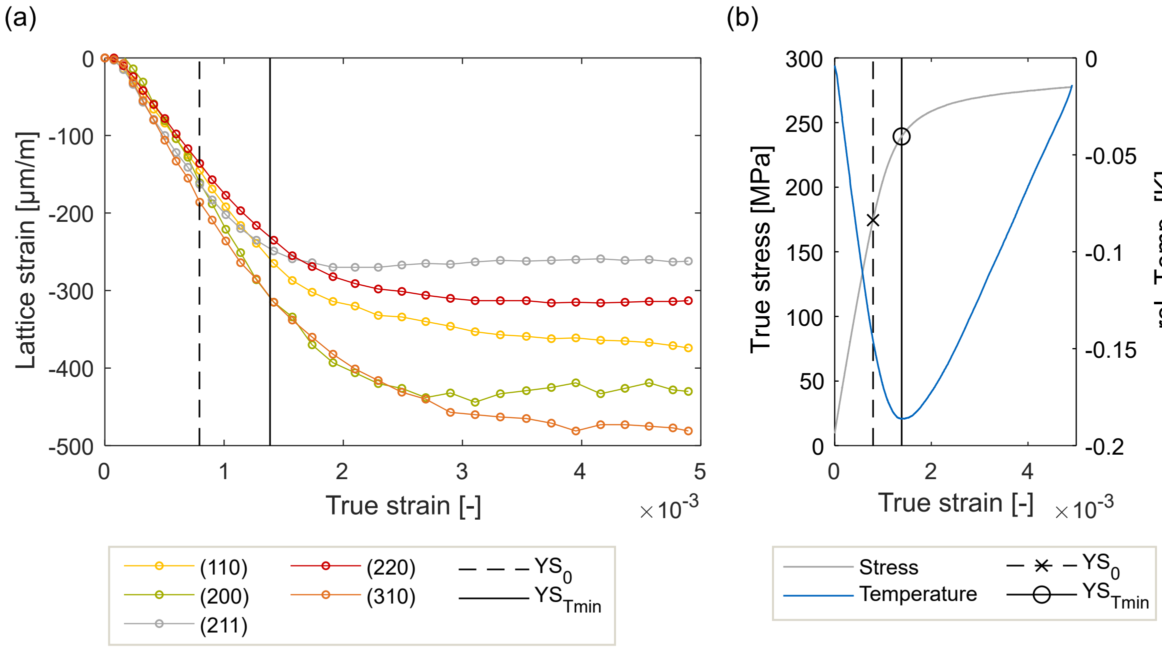

Figure E.2: HC260Y - (a) Lattice strain versus true strain for five lattice planes in transversal direction for the initial tensile loading. Marked are the parameters YS_0 and YS_{Tmin}. (b) True stress versus true strain and corresponding temperature with YS_0 and YS_{Tmin} marked.

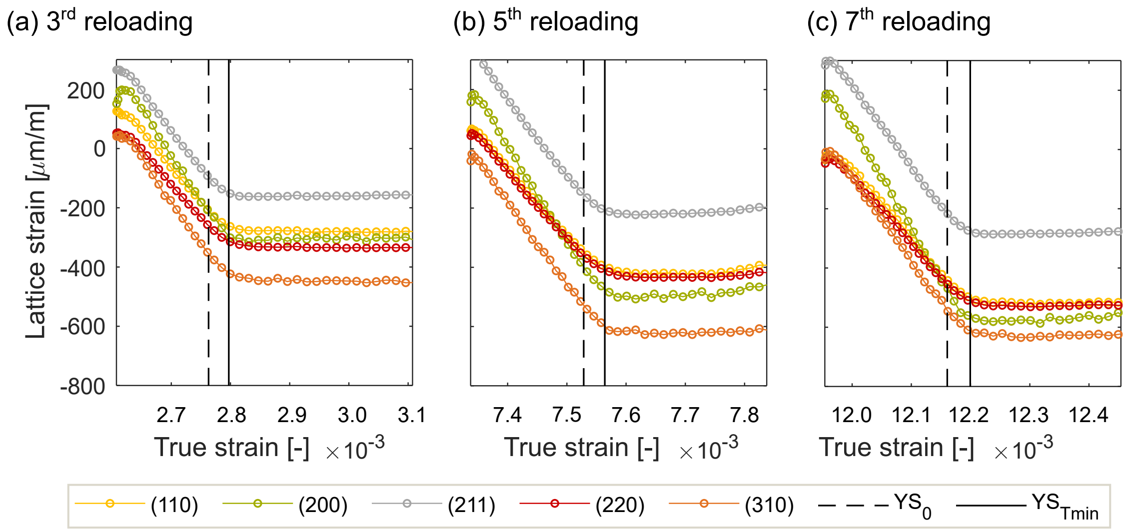

Figure E.3: HC260Y - Lattice strain versus true strain for five lattice planes in transversal direction for the (a) 3rd, (b) 5th and (c) 7th reloading. Marked YS$_0$ and YS$_{Tmin}$.

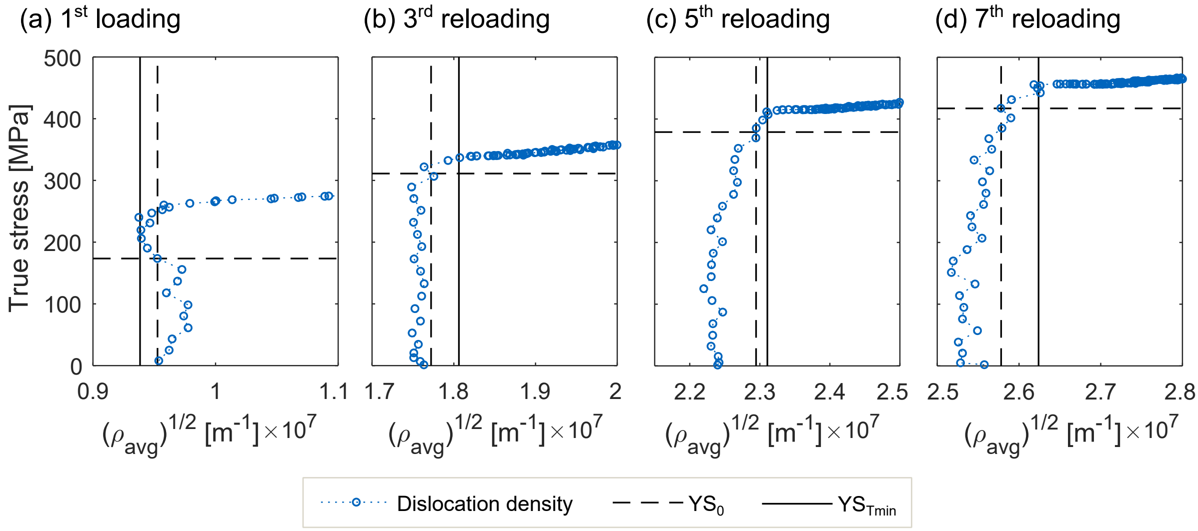

Figure E.4: HC260Y - True stress versus the root square of the dislocation density ρ_{avg} in transversal direction for the initial loading (a) and three reloadings (b-d).

E.4 Results - Elastic Loading Modulus

This chapter presents supplementary information for Section 7.2.3.

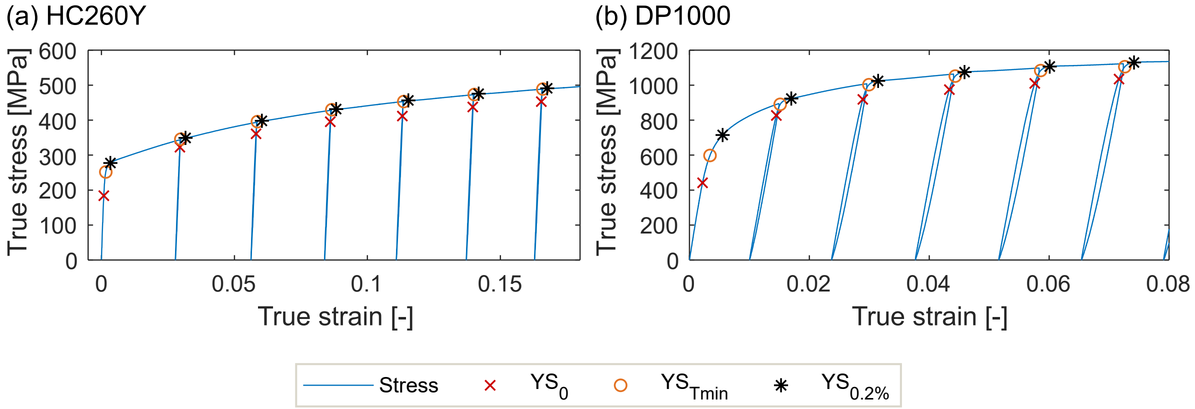

Figure E.5: Comparison of the values for YS_0*,* YS_{Tmin} *and* $YS_{0.2\%}$ *of a cyclic tensile test for (a) HC260Y and (b) DP1000.*

Dissertationen des Lehrstuhls für Umformtechnik und Gießereiwesen, Prof. Dr.-Ing. Wolfram Volk

01 *Felix Zimmermann*
Generierung von maßgeschneiderten Bauteileigenschaften in
PHS-Bauteilen durch Anlassen mittels Flamme;
2014; ISBN: 978-3-95884-007-2

02 *Christopher Joseph Thoma*
Simulationsgestützte Optimierung der Maßhaltigkeit in der Prozesskette Druckguss;
2015; ISBN: 978-3-73699-009-8

03 *Joung Sik Suh*
Verbesserung der Kaltumformbarkeit von AZ31 Mg-Blech
durch Equal Channel Angular Pressing (ECAP);
2015; URN: http://nbn-resolving.de/urn/resolver.pl?urn:nbn:de:bvb:91-diss-20151215-1271570-1-8

04 *Robert Ramakrishnan*
3-D-Drucken mit einem anorganischen Formstoffsystem;
2016; URN: http://nbn-resolving.de/urn/resolver.pl?urn:nbn:de:bvb:91-diss-20160129-1276474-1-5

05 *Patrick Saal*
Quantitative Phasenanalyse von ausferritischem Gusseisen
mithilfe der Neutronendiffraktometrie;
2017; URN: http://nbn-resolving.de/urn/resolver.pl?urn:nbn:de:bvb:91-diss-20170125-1304161-1-8

06 *Peter Sachnik*
Methodik für gratfreie Schnittflächen beim Scherschneiden;
2017; URN: http://nbn-resolving.de/urn/resolver.pl?urn:nbn:de:bvb:91-diss-20160406-1304184-1-8

07 *Thomas Martin Kopp*
Einfluss der Werkzeugsteifigkeit auf Scherschneidprozess
und Werkzeugverschleiß beim offenen Schnitt;
2017; URN: http://nbn-resolving.de/urn/resolver.pl?urn:nbn:de:bvb:91-diss-20170426-1327352-1-7

08 *Simon Josef Maier*
Inline-Qualitätsprüfung im Presswerk durch intelligente Nachfolgewerkzeuge
2018; ISBN: 978-3-95884-004-1

09 *David Jocham*
Bestimmung der lokalen Einschnürung nach linearer und nichtlinearer Umformhistorie
sowie Ermittlung dehnungs- und geschwindigkeitsabhängiger Materialkennwerte;
2018; ISBN: 978-3-95884-012-6

10 *Christoph Kaiser*
Effiziente Produkt- und Prozessabsicherung für gefalzte Karosseriebauteile
durch ein metamodellbasiertes Assistenzsystem;
2018; ISBN: 978-3-95884-018-8

11 *Daniel Marian Opritescu*
Risikominimale Überbrückung von Kapazitätsengpässen
im Presswerksverbund der Automobilindustrie;
2018; ISBN: 978-3-95884-020-1

12 *Maria Anna Hiller*
Fügen durch Clinchen mit rotierender Werkzeugbewegung;
2019; ISBN: 978-3-95884-024-9

13 *Hannes Alois Weiss*
Fertigung effizienter Elektromotoren;
2019; ISBN: 978-3-95884-037-9

14 *Wan-Gi Cha*
Formability Consideration in Bead Optimization to stiffen Deep Drawn Parts;
2019; ISBN: 978-3-95884-036-2

15 *Sven Peter Jansen*
Methodik zur Auslegung konturnaher Temperiersysteme in Druckgusswerkzeugen;
2019; ISBN: 978-3-95884-035-5

16 *Georg Baumgartner*
Das mikromechanische Verhalten von binären Aluminium-Silizium-Legierungen unter Last;
2019; ISBN: 978-3-95884-032-4

17 *Simon Vogt*
Entwicklung eines Verfahrens zur Herstellung von
verpressten Spulen für effizientere E-Traktionsantriebe;
2019; URN: http://nbn-resolving.de/urn/resolver.pl?urn:nbn:de:bvb:91-diss-20191001-1483133-1-0

18 *Patrick Thomas Helmut Woisetschläger*
Beitrag zur Optimierung der Schichtanbindung bei
thermisch gespritzten Zylinderlaufflächen im Verbrennungsmotor;
2020; ISBN: 978-3-95884-042-3

19 *Michael Walter Krinninger*
Ansätze zur Reduzierung der prozessbedingten Flitterbildung
beim Scherschneiden von Aluminiumblechen im offenen Schnitt;
2020; ISBN: 978-3-95884-045-4

20 *Tim Benkert*
Blechradkörper für Leichtbauzahnräder – Eine Machbarkeitsstudie zur Herstellung von
tiefgezogenen und feingeschnittenen Innenteilen mehrteiliger Zahnräder;
2020; ISBN: 978-3-95884-046-1

21 *Benjamin Himmel*
Material Jetting of Aluminium – Analysis of a Novel Additive Manufacturing Process;
2020; ISBN: 978-3-95884-049-2

22 *Florian Martin Hofbauer*
Großserientaugliche Umsetzung von dünnwandigem Stahlguss für den Automobilbau;
2020; ISBN: 978-3-95884-050-8

23 *Annika Weinschenk*
Simulative und experimentelle Untersuchungen zur Detektion und Prävention von
Einfallstellen in Außenhautbauteilen;
2020; ISBN: 978-3-95884-052-2

24 *Florian Heilmeier*
Ermittlung schwindungsbedingter Gussteilspannungen mit Hilfe
eingegossener, faseroptischer Dehnungssensoren;
2020; ISBN: 978-3-95884-053-9

25 *Ferdinand Neumayer*
Ermittlung und Auswirkung der Durchbruchkraft beim Scherschneiden;
2020; URN: http://nbn-resolving.de/urn/resolver.pl?urn:nbn:de:bvb:91-diss-20200729-1530885-1-5

26 *Manuel Pintore*
Gießtechnische Herstellung und technologische Charakterisierung
von Kupfer-Aluminium-Schichtverbunden;
2021; ISBN: 978-3-95884-059-1

27 *Tim Mittler*
Verbundstranggießen von Kupferwerkstoffen;
2021; ISBN: 978-3-95884-058-4

28 *Christoph Hartmann*
Spatio-Temporal Optical Flow Methods for Process Analysis
– Robust Strain, Strain Rate, and Crack Propagation Measurement in Shear Cutting;
2021; ISBN: 978-3-95884-066-9

29 *Marco Raupach*
Simulationsbasierte Konstruktionsmethodik zur Herstellung markanter
Bauteilradien im Karosseriebau;
2021; ISBN: 978-3-95884-068-3

30 *Fabian Zgoll*
Methodik zur maschinenoptimalen Werkzeugeinarbeitung durch
virtuelle Kompensation der Werkzeug- und Pressendurchbiegung;
2021; ISBN: 978-3-95884-067-6

31 *Phillipp Johnathan Lechner*
A Material Model for Foundry Cores
– The Brittle Fracture Behaviour of Chemically-Bound Foundry Sands;
2021; ISBN: 978-3-95884-073-7

32 *Martin Feistle*
Edge-Fracture-tensile-Test – Neues Kantenrissprüfverfahren für duktile metallische Werkstoffe;
2021

33 *Thomas Greß*
Vertical Continuous Compound Casting of Copper Aluminium Semi-Finished Products
– Design of a Resource-Efficient Production Technology for
the Formation of Metallurgically Bonded Bilayer Parts;
2021; URN: http://nbn-resolving.de/urn/resolver.pl?urn:nbn:de:bvb:91-diss-20210721-1579499-1-7

34 *Jens-Michael Stahl*
Residual stresses induced by shear cutting – Targeted use for manufacturing
functional surfaces with an improved fatigue behavior;
2021; URN: http://nbn-resolving.de/urn/resolver.pl?urn:nbn:de:bvb:91-diss-20210802-1593943-1-2

35 *Florian Ettemeyer*
Charakterisierung des Entkernverhaltens anorganisch gebundener Sand-Binder-Systeme;
2021; URN: http://nbn-resolving.de/urn/resolver.pl?urn:nbn:de:bvb:91-diss-20211011-1601398-1-3

36 *Lucas Schulte-Vorwick*
In-Line-Richten von Fahrzeugstrukturteilen aus Leichtmetalldruckguss;
2021; URN: http://nbn-resolving.de/urn/resolver.pl?urn:nbn:de:bvb:91-diss-20211015-1585266-0-9

37 *Martin Günther Landesberger*
Characterization and Design of Enhanced Ductile Irons;
2022; ISBN: 978-3-9820746-9-6

38 *Nikolas Viktor Beulich*
Entwicklung einer Methodik zur Auslegung und Absicherung des Freiformbiegens
mit bewegter Matrize für dreidimensionale Biegegeometrien;
2022; URN: http://nbn-resolving.de/urn/resolver.pl?urn:nbn:de:bvb:91-diss-20221219-1652106-1-5

39 *Philipp Maximilian Tröber*
Adhäsionsentstehung beim Scherschneiden und Tiefziehen unter Berücksichtigung von
Temperatur und thermoelektrischen Strömen;
2023; URN: http://nbn-resolving.de/urn/resolver.pl?urn:nbn:de:bvb:91-diss-20230130-1688200-1-4

40 *Matthias Eder*
Validierung von Materialmodellen
– Der MUC-Test als Methodik zur Qualifizierung von Materialmodellen für Blechwerkstoffe;
2023; ISBN: 978-3-9820746-8-9

41 *Simon Josef Vitzthum*
In-situ Analysis of Elastic-Plastic Characteristics of Steel Sheets
2023; ISBN: 978-3-9820746-7-2